



UNIVERSITEIT VAN PRETORIA  
UNIVERSITY OF PRETORIA  
YUNIBESITHI YA PRETORIA

# **USING BRILLOUIN FREQUENCY SHIFT TO DETECT UNDERGROUND PIPE LEAKS**

**JASON DANIEL BARRY**

**A dissertation submitted in fulfilment of the requirements for the degree of**

**MASTER OF ENGINEERING (GEOTECHNICAL ENGINEERING)**

**In the**

**FACULTY OF ENGINEERING, BUILT ENVIRONMENT AND INFORMATION**

**TECHNOLOGY**

**UNIVERSITY OF PRETORIA**

**November 2021**

**Supervisor: Professor S.W. Jacobsz**

# ABSTRACT

**Title:** Using Brillouin Frequency Shift to Detect Underground Pipe Leaks

**Author:** Jason Daniel Barry

**Supervisor:** Professor S.W. Jacobsz

**Department:** Civil Engineering

**University:** University of Pretoria

**Degree:** Master of Engineering (Geotechnical Engineering)

Underground pipe-networks and pipeline mains provide water to communities and industry, but some water is lost between the purification plant and the end user as Non-Revenue Water (NRW). A significant contributor to NRW is pipe leaks. Due to the fact that pipes are submerged underground, pipeline leaks are difficult to detect as there are potentially few to no visual indicators at ground level. Leaking pipes are the greatest contributing factor to the loss of purified water, accounting for more than 69% of NRW in South Africa, and accounting for between 25-50% of the total global water outlet from water purification plants, with the global average being 35%. Identifying leaking pipes to protect pipeline infrastructure and conserve water requires a sub-surface leak detection system.

An investigation was conducted on the performance of a potential leak detection system based on Distributed Fibre Optic Sensing using Fibre Optic Brillouin Frequency Shift Strain Interrogation. Brillouin Frequency Shift (BFS) is a phenomenon that occurs in optical fibres and is dependent on the fibres' stress and temperature state.

Five different fibre optic cables were buried and monitored using the BFS phenomenon, measured along the length of the fibre optic cables at a spatial resolution of 50mm. Artificial leak experiments were conducted by introducing water into standpipes discharging at the depth of the fibre optic cables to invoke an artificial leak response. The introduction of water into the standpipes caused the moisture content of the soil surrounding the fibre optic cables to change. This change in soil moisture content caused strain and temperature changes to occur in the soil surrounding the fibre optic cables, which was in turn imposed onto the fibre optic cables. This resulted in changes in BFS in the fibre optic cables at the leak location. Monitoring fibre optic cables for changes in BFS therefore provides for a means of leak detection.

It was found from this study that it was possible to confidently detect moisture content changes resulting from the imposed artificial water leaks with each of the different fibre optic cable types tested, i.e. each cable worked as a functional leak detection sensor. The leak-induced-change in the optical fibres' BFS was significant relative to that caused by natural temperature fluctuations and soil movements where no soil moisture content change took place. By analysing the BFS in the time domain it was also possible to determine the time of origin of the induced leaks in the experimental setup.

# DECLARATION

I, the undersigned hereby declare that:

- I understand what plagiarism is and I am aware of the University's policy in this regard;
- The work contained in this thesis is my own original work;
- I did not refer to work of current or previous students, lecture notes, handbooks or any other study material without proper referencing;
- Where other people's work has been used this has been properly acknowledged and referenced;
- I have not allowed anyone to copy any part of my thesis;
- I have not previously in its entirety or in part submitted this thesis at any university for a degree.

## DISCLAIMER:

The work presented in this thesis is that of the student alone. Students were encouraged to take ownership of their projects and to develop and execute their experiments with limited guidance and assistance. The content of the research does not necessarily represent the views of the supervisor or any staff member of the University of Pretoria, Department of Civil Engineering. The supervisor did not read or edit the final report and is not responsible for any technical inaccuracies, statements or errors. The conclusions and recommendations given in the report are also not necessarily that of the supervisor, sponsors or companies involved in the research.

**Signature of student:**



**Name of student:**

Jason Daniel Barry

**Student number:**

16078901

**Date:**

22 November 2021

**Number of words in report:**

35534 words

## **ACKNOWLEDGEMENTS**

I wish to express my appreciation to the following organisations and persons who made this project report/dissertation/thesis possible:

- To the Water Research Commission of South Africa for the research opportunity and funding they provided.
- To Professor S.W. Jacobsz for sharing his experience and wisdom and providing guidance throughout the study.
- To my mom for proofreading my dissertation.
- To my family for their support and encouragement through the endless hours of work
- To the LORD for His providence from the start of the study through to the end.

# TABLE OF CONTENTS

1	INTRODUCTION	1
1.1	Background	1
1.1.1	Problem Definition	1
1.1.2	Relevance of this Research	1
1.2	Objectives of the Study	2
1.3	Scope of the Study	2
1.4	Methodology	3
1.5	Organisation of the Report	3
2	LITERATURE REVIEW	4
2.1	Introduction	4
2.2	Water Loss From Distribution Networks	4
2.2.1	Non-Revenue Water	4
2.2.2	The State Of Non-Revenue Water In South Africa	6
2.2.3	Factors Affecting Water Distribution Network Conditions	7
2.2.4	Factors Affecting Pipe Leakage	7
2.2.5	Soil Behaviour Surrounding Leaking Pipes	8
2.2.6	Negative Impacts of Pipeline Failures	9
2.2.7	Reducing NRW	10
2.2.8	Benefits of Reducing NRW	11
2.3	Soil-Water Interaction	12
2.3.1	Shrink-SWell Behaviour of Soil	13
2.3.2	Damage to Infrastructure Due to Expansive Soil	14
2.3.3	Relationship Between Soil Strength and Water Content	16
2.4	Pipe Leak Detection Methods	17
2.4.1	Active Leak Detection Methods	17
2.4.1.1	Water Audits	17
2.4.1.2	Leak-Detection Surveys	18
2.4.1.3	Tracer Gas	18

2.4.1.4	Thermagraphy	18
2.4.1.5	Ground Penetrating Radar	19
2.4.2	Passive Leak Detection Techniques	19
2.4.2.1	Acoustic Leak Detection	19
2.5	Fibre Optic Cables and Distributed Sensing	21
2.5.1	Fibre Optic Basics	21
2.5.2	Fibre Optic Sensing Technology	23
2.5.2.1	Electrostriction, Acoustic Phonon Development and Backscattering	24
2.5.2.2	Brillouin Backscatter in Fibre Optic Sensing	25
2.5.3	Structural Health Monitoring using Fibre Optics	26
2.5.3.1	Fibre Optic Leak Detection	27
2.6	Summary	28
3	EXPERIMENTAL SETUP	29
3.1	Introduction	29
3.2	Measuring Instrumentation	29
3.2.1	Fibre Optic Cables Used	29
3.2.2	Brillouin Frequency Shift Fibre Optic Interrogator	30
3.3	Field Setup	31
3.3.1	Trench	31
3.3.2	Soil Properties	33
3.3.3	FO Instrumentation of a Working Pipeline	36
3.4	Artificial leak tests	39
4	EXPERIMENTAL RESULTS	40
4.1	Introduction	40
4.2	Fibre Optic BFS Baseline Behaviour	40
4.2.1	Output From The Bfs Interrogator	40
4.2.2	BFS in the Time Domain	42
4.2.2.1	Seasonal Variation	46
4.2.3	Average BFS Profiles and Relative BFS Profiles	48

4.2.4	Comparison of Various Cables	52
4.2.4.1	72F-6C-LC-to-Strain Cable	52
4.2.4.2	6F-TB Cable	54
4.2.4.3	4F-DC-LC Cable	56
4.2.4.4	2F-TB Cable	58
4.3	Leak Tests Results	60
4.3.1	Data Processing Methodology	60
4.3.2	Cleaning Relative Profiles using a Centred Moving Average	61
4.3.3	Zeroing Relative Profile	61
4.3.4	Squared Relative Profile	63
4.3.5	Comparison Against Expected Minimum And Maximum BFS Response	64
4.3.6	Repeatability of Detection	66
4.4	BFS Response in the Time Domain	67
4.5	Comparison of the Response of Different FO Cables	69
4.5.1	Strain to 72F-6C-LC cable	69
4.5.2	4F-DC-LC cable	70
4.5.3	2F-TB cable	71
4.5.4	6F-TB to 72F-6C-LC cables	72
4.6	Detection of an Unknown Leak Location and Time of Occurrence	73
4.6.1	Unknown Leak Detection Methodology	73
4.6.2	Comparison of Performance of Different Cables	79
4.6.2.1	Strain to 72F-6C-LC CABLE	79
4.6.2.2	4F-DC-LC CABLE	80
4.6.2.3	2F-TB cable	82
4.6.2.4	6F-TB to 72F-6C-LC cables	82
4.7	Prolonged Leak Test	84
4.7.1	Long Term Leak BFS behaviour	85
4.7.2	Effect of Prolonged Leak on the Change in BFS	89
4.7.3	Comparison of the Different FO Cable Types	93

4.7.3.1	Strain to 72F-6C-LC	93
4.7.3.2	4F-DC-LC	97
4.7.3.3	2F-TB	101
4.7.3.4	6F-TB to 72F-6C-LC	104
4.8	Buried Pipeline Conditions	108
4.9	Discussion of results	111
5	CONCLUSIONS AND RECOMMENDATIONS	113
5.1	Conclusions	113
5.2	Recommendations	115
	REFERENCES	116
	APPENDIX A SGS MATROLAB HILLCREST CAMPUS CLAY TEST RESULTS	119
	APPENDIX B 6F-TB and 2F-TB CABLE SPEC SHEET	121
	APPENDIX C STRAIN CABLE SPEC SHEET	125
	APPENDIX D 72F-6C-LC CABLE SPEC SHEET	127
	APPENDIX E 4F-DC-LC SPEC SHEET	131
	APPENDIX F FIBRISTERRE FTB SERIES FIBRE-OPTIC SENSING BFS INTERROGATOR SPECIFICATION SHEET	135

## LIST OF FIGURES

Figure 2.1. Linear attenuation of an optical signal as a function of the light signal's wavelength. Taken from Curran and Shirk (2018).	22
Figure 2.2. Acoustic phonon development in an optical fibre invoked by the Stimulated Brillouin technique. Taken from Motil et al. (2015).	26
Figure 3.1. Bird's eye view of the 150m trench dug on the University of Pretoria Hillcrest Campus.	32
Figure 3.2. Standing point view of the trench prior to installation of the fibre optic cables.	32
Figure 3.3. Schematic long section of the trench (not drawn to scale) depicting the three 50m segments.	33
Figure 3.4. Schematic bird's eye view diagram of the trench showing the orientation of the laid cables.	33
Figure 3.5. Particle size distribution for the Hillcrest Campus clay measured by SGS Matrolab.	34
Figure 3.6. Soil-water retention curve for the Hillcrest Campus clay showing suctions measured using tensiometers.	35
Figure 3.7. A WP4C dewpoint potentiometer.	35
Figure 3.8. Soil-water retention curve for the Hillcrest Campus clay showing the suctions measured both by the tensiometers and the WP4C. The labelled data point is outside the region of accurate suction measurement.	36
Figure 3.9. A bird's eye view of Rietondale showing Tom Jenkins Drive, and the two adjacent streets, Kameel and Buffels.	37
Figure 3.10. Bird's eye view of Rietondale showing the region where the FO cable was laid.	37
Figure 3.11. Photograph showing the position of the FO cable relative to the laid pipeline.	38
Figure 3.12. Photograph of one of the standpipes leading down to the level of the FO cable installed along the pipeline laid in Tom Jenkins Drive.	38
Figure 4.1. BFS profile of the cable with the 50m segment of strain cable spliced to it. The segment of the cable buried in the trench is highlighted by the blue rectangle.	40
Figure 4.2. Two BFS profiles taken at two different times during the day for the same cable showing how temperature variation affects the BFS output.	41
Figure 4.3. Difference between the two BFS profiles plotted in Figure 4.2.	42
Figure 4.4. A curve of the BFS plotted against time for the length-ordinate $L = 240\text{m}$ along the cable to which the strain cable was spliced.	42

Figure 4.5. A depiction of the development of a moving average BFS value as time progresses at length-ordinate $L = 240\text{m}$ of the 72F-6C to strain spliced cable.	43
Figure 4.6. BFS vs time plot of the 72F-6C to strain cable. Curves are plotted for length-ordinates 240m, 280m, 340m, and 400m occurring in the 72F-6C section, and 530m, occurring in the strain cable section.	44
Figure 4.7. BFS vs time curves for the 72F-6C to strain cable, plotted from 240m to 580m, every 20m for the 72F-6C cable, and every 5m for the strain cable segment.	44
Figure 4.8. Zeroed set of BFS vs time curves from Figure 4.7.	45
Figure 4.9. Zeroed set of BFS vs time curves from Figure 4.7 showing only those of the 72F-6C-LC cable.	45
Figure 4.10. Zeroed set of BFS vs time curves from Figure 4.7 showing only those of the strain cable.	46
Figure 4.11. BFS measurements produced by the 4F-DC-LC cable from the Hillcrest Campus trench at length-ordinates with buried depths of 0.5m, 1.0m and 1.5m, from the 23 <sup>rd</sup> of February 2021 until the 25 <sup>th</sup> of August 2021.	47
Figure 4.12. BFS measurements produced by the 2F-TB cable from the Hillcrest Campus trench at length-ordinates with buried depths of 0.5m, 1.0m and 1.5m, from the 23 <sup>rd</sup> of February 2021 until the 25 <sup>th</sup> of August 2021.	47
Figure 4.13. BFS vs time for the 2F-TB cable zeroed with respect to the each first BFS reading on the 23 <sup>rd</sup> of February.	48
Figure 4.14. Set of BFS profiles of the 72F-6C-to-strain cable logged over a period of 24 hours at 2 hour intervals.	49
Figure 4.15. An average BFS profile created by averaging 12 profiles logged over a 22 hour time span at 2 hour intervals.	49
Figure 4.16. A set of average BFS profiles plotted for the 72F-6C-to-strain cable.	50
Figure 4.17. Set of average BFS profiles from Figure 4.16 plotted relative to the 2020/12/15 average BFS profile.	50
Figure 4.18. Average, minimum and maximum BFS value logged from 14 to 31 December 2020 for the 72F-6C-to-strain cable.	51
Figure 4.19. Minimum and maximum BFS values logged, as per Figure 4.18, relative to the average BFS profile.	51
Figure 4.20. Set of relative BFS profiles of the 72F-6C-LC-to-strain cable.	52

Figure 4.21. Set of relative BFS profiles of the 72F-6C-LC-to-strain cable focusing on the strain cable section.	53
Figure 4.22. Maximum and minimum boundaries of the BFS output logged for the 72F-6C-to-strain cable relative to the average BFS profile.	53
Figure 4.23. Set of daily average BFS profiles for the 72F-6C-to-6F-TB cable from 15/12/2020 to 31/12/2020.	54
Figure 4.24. Set of daily average BFS profiles for the 72F-6C-to-6F-TB cable focused on the 6F-TB section.	55
Figure 4.25. Set of daily average BFS profiles relative to the 15/12/20 profile for the 72F-6C-to-6F-TB cable from 15/12/2020 to 31/12/2020.	55
Figure 4.26. Minimum-maximum envelope of the 72F-6C-to-6F-TB cable.	56
Figure 4.27. Set of daily average BFS profiles for the 4F-DC-LC cable from 15/12/2020 to 31/12/2020.	56
Figure 4.28. Set of daily average BFS profiles relative to the 15/12/20 profile for the 4F-DC-LC cable from 15/12/2020 to 31/12/2020.	57
Figure 4.29. Minimum-maximum envelope of the 4F-DC-LC cable.	57
Figure 4.30. Set of daily average BFS profiles for the 2F-TB cable from 15/12/2020 to 31/12/2020.	58
Figure 4.31. Set of daily average BFS profiles relative to the 15/12/20 profile for the 2F-TB cable from 15/12/2020 to 31/12/2020.	59
Figure 4.32. Minimum-maximum envelope of the 2F-TB cable.	59
Figure 4.33. Relative BFS plot generated by subtracting the dry baseline from the wet baseline (leak points are highlighted by boxes).	60
Figure 4.34. A plot of the raw relative profile output as well as the 25-point moving centred average created from the raw data output.	61
Figure 4.35. A set of curves representing the raw relative BFS output profile, a 25-point CMA and a 601 point CMA.	62
Figure 4.36. 25-point CMA relative profile before being zeroed and after being zeroed.	63
Figure 4.37. Zeroed raw output and 25pt CMA profiles generated by subtracting the 601 point CMA.	63
Figure 4.38. Squared 25-point CMA relative profile.	64
Figure 4.39. Leak test result shown against the minimum and maximum expected bounds of the 72F-6C-LC to 6F-TB cable.	65

Figure 4.40. Regions of the zeroed 25-point CMA relative profile that exceeded the minimum-maximum expected BFS boundary.	65
Figure 4.41. Results of the first (24 March) and second (1 April) leak occurrence plotted relative to the dry baseline. The curve labelled 02-Apr is indicative that it is generated from a baseline logged on the 2 <sup>nd</sup> of April after the second leak occurrence had taken place on the 1 <sup>st</sup> of April.	67
Figure 4.42. Time domain plot of the $\Delta$ BFS at the three leak points for the two cables (72F-6C-LC and 6F-TB) as the leak test was conducted.	68
Figure 4.43. Results of the second leak test measured using the strain to 72F-6C-LC FO cable.	69
Figure 4.44. Results of the second leak test measured using the 4F-DC-LC FO cable.	70
Figure 4.45. Results of the second leak test measured using the 2F-TB FO cable.	71
Figure 4.46. Results of the second leak test measured using the 6F-TB to 72F-6C-LC FO cable.	72
Figure 4.47. Bar graph showing the maximum $\Delta$ BFS <sup>2</sup> caused by a leak registered in each cable type.	72
Figure 4.48. Comparison of two 24-hour average BFS profiles. The orange times formulate the baseline and the blue times are the latest observation. Every 2 hours the data used to formulate the baseline and the latest observation shifts forward by 2 hours.	74
Figure 4.49. Maximum $\Delta$ BFS <sup>2</sup> obtained for each time step (2F-TB).	74
Figure 4.50. Relative BFS profile that occurs at time $t = 13.25$ days (2F-TB).	75
Figure 4.51. Plot of length-ordinate where the maximum $\Delta$ BFS <sup>2</sup> occurs against time (2F-TB).	75
Figure 4.52. Replot of Figure 4.49 highlighting the 24 hours surrounding the leak-peak (2F-TB).	76
Figure 4.53. Replot of Figure 4.51 highlighting the 24 hours surrounding the leak (2F-TB).	76
Figure 4.54. 3D plot of the $\Delta$ BFS <sup>2</sup> for the 2F-TB cable plotted against time and length, excluding $\Delta$ BFS <sup>2</sup> values below $1e-7$ (GHz) <sup>2</sup> . The detected leak is highlighted by the rectangle. The blue section corresponds to the first 150m of the cable and the red section to the second 150m of the cable.	77
Figure 4.55. Raw BFS output and a 24-hour moving average computed at the length-ordinate $L = 119.53$ m.	78
Figure 4.56. 24 hour difference computed for the raw BFS and 24-hour moving average shown in Figure 4.55.	78
Figure 4.57. Maximum $\Delta$ BFS <sup>2</sup> for each time step along the 72F-6C-LC cable segment.	79
Figure 4.58. Length-ordinate of the maximum $\Delta$ BFS <sup>2</sup> at each time step along the 72F-6C-LC cable segment.	80
Figure 4.59. $\Delta$ BFS <sup>2</sup> along the 72F-6C-LC cable at time $t = 13.25$ days.	80
Figure 4.60. Maximum $\Delta$ BFS <sup>2</sup> for each time step along the 4F-DC-LC cable.	81

Figure 4.61. Length-ordinate of the maximum $\Delta\text{BFS}^2$ at each time step along the 4F-DC-LC cable.	81
Figure 4.62. $\Delta\text{BFS}^2$ along the 4F-DC-LC cable at time $t = 13.25$ days.	82
Figure 4.63. Maximum $\Delta\text{BFS}^2$ for each time step along the 6F-TB to 72F-6C-LC cable.	83
Figure 4.64. Length-ordinate of the maximum $\Delta\text{BFS}^2$ at each time step along the 6F-TB to 72F-6C-LC cable.	83
Figure 4.65. $\Delta\text{BFS}^2$ along the 6F-TB to 72F-6C-LC cable at time $t = 13.25$ days.	84
Figure 4.66. The BFS for 72F-6C-LC cable segment of the 72F-6C-LC to strain cable that occurs at standpipe 5 and another length ordinate 10m away before, during and after the first prolonged leak test.	85
Figure 4.67. The BFS for 72-6C-LC cable segment of the 72F-6C-LC-to-strain cable that occurs at standpipe 2 and another length ordinate 15m away before, during and after the second prolonged leak test.	86
Figure 4.68. BFS output by the strain cable segment of the 72F-6C-LC-to-strain cable at standpipe 2 and a length-ordinate 10m away during the second prolonged leak test.	87
Figure 4.69. Zeroed BFS output by the strain cable segment of the 72F-6C-LC-to-strain cable at standpipe 2 and a length-ordinate 10m away during the second prolonged leak test.	87
Figure 4.70. BFS recorded by the 4F-DC-LC cable at standpipes 2, 5, and 8 from the 23 <sup>rd</sup> of February 2021 until the 25 <sup>th</sup> of August 2021.	88
Figure 4.71. BFS recorded by the 2F-TB cable at standpipes 2, 5, and 8 from the 23 <sup>rd</sup> of February 2021 until the 25 <sup>th</sup> of August 2021.	89
Figure 4.72. Maximum $\Delta\text{BFS}^2$ vs time plot for the strain to 72F-6C-LC cable during the first prolonged leak test. The solid black line signifies the start of the leak test, and the dashed line represents the end of the leak test.	90
Figure 4.73. Maximum $\Delta\text{BFS}$ , plotted using a logarithmic scale, vs time for the strain to 72F-6C-LC cable.	91
Figure 4.74. Length-ordinate of the maximum $\Delta\text{BFS}$ along the strain to 72F-6C-LC cable after being separated into two segments (excluding the strain cable segment).	92
Figure 4.75. $\Delta\text{BFS}^2$ plotted along the length of the strain to 72F-6C-LC FO cable at time = 16 days and 6 hours.	92
Figure 4.76. A 3-Dimensional plot of the $\Delta\text{BFS}^2$ output (excluding values less than $1e-8$ (GHz) <sup>2</sup> ) from the 72F-6C-LC to strain cable against time and length during the first prolonged leak test. The detected leak is highlighted by the blue boxes. Blue corresponds to the strain cable, and the orange and green plots are the output of the 72F-6C-LC cable.	93

Figure 4.77. Maximum $\Delta\text{BFS}^2$ plotted against time for the strain to 72F-6C-LC cable during the second prolonged leak test.	94
Figure 4.78. Maximum $\Delta\text{BFS}^2$ plotted on logarithmic scale against time for the strain to 72F-6C-LC cable during the second prolonged leak test.	94
Figure 4.79. Length-ordinate of the maximum $\Delta\text{BFS}$ occurring along the strain to 72F-6C-LC cable during the second prolonged leak test.	95
Figure 4.80. $\Delta\text{BFS}^2$ plotted against the length of the 4F-DC-LC cable at time: $t = 15$ days and 10 hours from the second leak test.	96
Figure 4.81. A 3-Dimensional plot of the $\Delta\text{BFS}^2$ against time and length produced by the strain to 72F-6C-LC cable during the second leak test. The detected leak is highlighted by the blue boxes. The blue portion represents the 72F-6C-LC cable, and the red the strain cable.	97
Figure 4.82. Maximum $\Delta\text{BFS}$ plotted against time for the 4F-DC-LC cable during the first prolonged leak test.	98
Figure 4.83. Maximum $\Delta\text{BFS}^2$ plotted against time for the 4F-DC-LC cable using a logarithmic vertical scale during the first prolonged leak test.	98
Figure 4.84. Length-ordinate of the maximum $\Delta\text{BFS}$ occurring along the 4F-DC-LC cable during the first prolonged leak test.	99
Figure 4.85. $\Delta\text{BFS}^2$ plotted against the length of the 4F-DC-LC cable at time: $t = 16$ days and 6 hours during the first prolonged leak test.	99
Figure 4.86. $\Delta\text{BFS}^2$ plotted on a logarithmic scale against the length of the 4F-DC-LC cable at time: $t = 16$ days and 6 hours during the first prolonged leak test.	100
Figure 4.87. A 3-Dimensional plot of the $\Delta\text{BFS}^2$ (excluding values less than $1\text{e-}8$ (GHz) <sup>2</sup> ) against time and length for the 4F-DC-LC cable during the first prolonged leak test.	101
Figure 4.88. Maximum $\Delta\text{BFS}^2$ output by the 2F-TB cable plotted against time.	102
Figure 4.89. Maximum $\Delta\text{BFS}^2$ , plotted on a logarithmic scale, produced by the 2F-TB cable against time.	102
Figure 4.90. Length-ordinate of the Maximum $\Delta\text{BFS}$ output by the 2F-TB cable for each time step.	103
Figure 4.91. $\Delta\text{BFS}^2$ plotted against length for time instant, $t = 16$ days and 2 hours along the 2F-TB cable. There was greater strain in the soil corresponding to $L = 225\text{m}$ than at $L = 75\text{m}$ .	103
Figure 4.92. A 3-Dimensional plot of the $\Delta\text{BFS}^2$ (excluding values less than $1\text{e-}8$ (GHz) <sup>2</sup> ) against time and length for the 2F-TB cable during the first prolonged leak test.	104
Figure 4.93. Maximum $\Delta\text{BFS}^2$ output by the 6F-TB to 72F-6C-LC cable plotted against time.	105

Figure 4.94. Maximum $\Delta\text{BFS}^2$ , plotted on a logarithmic scale, output by the 6F-TB to 72F-6C-LC cable, against time.	106
Figure 4.95. Length-ordinate of the Maximum $\Delta\text{BFS}$ output by the 6F-TB to 72F-6C-LC cable for each time step.	106
Figure 4.96. $\Delta\text{BFS}^2$ plotted against length for the 6F-TB and the 72F-6C-LC cables at time instant, $t = 16$ day and 8 hours.	107
Figure 4.97. A 3-Dimensional plot of the $\Delta\text{BFS}^2$ (excluding values less than $1\text{e-}8$ (GHz) <sup>2</sup> ) against time and length for the 6F-TB to 72F-6C-LC cable during the first prolonged leak test.	108
Figure 4.98. Maximum $\Delta\text{BFS}^2$ measured along Tom Jenkins Drive plotted against time. The solid line corresponds to the start of the influx of water, and the dashed line to the end of the induced leak.	109
Figure 4.99. Length-ordinate of the maximum $\Delta\text{BFS}^2$ that occurred along Tom Jenkins Drive plotted against time.	109
Figure 4.100. Plot of the $\Delta\text{BFS}^2$ plotted against distance at time $t = 17$ days and 14 hours along at Tom Jenkins Drive.	110
Figure 4.101. 3-Dimensional plot of the $\Delta\text{BFS}^2$ (excluding values below $1\text{e-}6$ (GHz) <sup>2</sup> ) produced at Tom Jenkins Drive plotted against both time and length. The $\Delta\text{BFS}^2$ -peaks due to the induced leak are highlighted by blue boxes. The five other non-induced-leak events are numbered chronologically.	111

## LIST OF TABLES

Table 4.1. Summary of the length-ordinates, trench segment depths, cable types and standpipe number at the 3 leak points.	68
---	----

## **LIST OF ABBREVIATIONS**

$\Delta$ BFS	Change in Brillouin Frequency Shift
BFS	Brillouin Frequency Shift
DAS	Distributed acoustic sensing
DC	Drop Cable
EM	Electro-Magnetic
FO	Fibre Optic
FOBFSI	Fibre Optic Brillouin Frequency Shift Strain Interrogation
LC	Loose Core
NRW	Non-Revenue Water
OTDR	Optical Time Domain Reflectometry
SA	South Africa
SHM	Structural Health Monitoring
SNR	Signal-to-Noise Ratio
TB	Tight Buffered

# **1 INTRODUCTION**

## **1.1 BACKGROUND**

Underground pipe-networks and pipeline mains provide water to communities. However, not all purified water reaches the end user. The water that is lost between the purification plant and the end user is called Non-Revenue Water (NRW) (González-Gómez et al. 2011). One contributor to NRW is pipe leaks. Due to the fact that they are submerged underground, pipeline failures are difficult to detect as there are potentially few to no visual indicators at ground level. Leaking pipes are the greatest contributing factor to the loss of purified water accounting for more than 70% of NRW (Van Zyl and Clayton, 2007), and accounting for between 25-50% of the total water outlet from water purification plants (Pedersen et al., 2013) with the global average being 35% (Van Zyl et al., 2013). Identifying leaking pipes in order to protect pipeline infrastructure and conserve water, requires a sub-surface leak detection system. The leak detection system proposed for this research is based on Distributed Fibre Optic Sensing (Grattan and Sun, 2000) using Fibre Optic Brillouin Frequency Shift Strain Interrogation (FOBFSSI). The Brillouin Frequency Shift (BFS) is a phenomenon that occurs in optical fibres and is dependent on the fibres' stress state (Galindez-Jamioy and Lopez-Higuera, 2012).

### **1.1.1 PROBLEM DEFINITION**

When a pipe leaks, the surrounding soil moisture content changes. This change in moisture content causes a change in stress state within the soil (Khademi and Budiman, 2016). Due to the change in stress state, the soil undergoes strain. If left unchecked, the strains that develop in the soil could cause damage to surrounding infrastructure (Li et al., 2013). However, this strain can be detected by fibre optic cables buried along the pipe length using FOBFSSI. This system is also influenced by temperature change (Motil et al., 2015). Therefore, the system must be calibrated to take account of temperature variation and only alert a user when a leaking pipe is detected. The aim of this research is to assess the operational legitimacy of this leak detection system.

### **1.1.2 RELEVANCE OF THIS RESEARCH**

A substantial loss occurs due to leaking pipes, both financially and as an essential resource. The cost of purifying water is borne by the end user. Thus, the cost of any water losses incurred directly impacts the financial state of consumers. Therefore, a pipe leak detection system has the potential to reduce the financial cost of delivering purified water to communities by timeously alerting those responsible for the maintenance of pipeline networks.

## **1.2 OBJECTIVES OF THE STUDY**

The primary objective of this research is to develop a leak detection system that will determine whether a buried pipeline is leaking and also pinpoint the location of the leak. This will be achieved by investigating how the BFS behaves within a fibre optic cable buried underground before and after moisture content change occurs in the surrounding soil.

The secondary objective is to determine which type of fibre optic cable is best suited to use as a leak detection sensor. Various types of fibre optic cables were used in the experimental setup and compared for efficacy. Fibre optic cables differ due to the type of sheath protecting the optical fibre and the friction interaction between the sheath and the optical fibre.

## **1.3 SCOPE OF THE STUDY**

The study consisted of:

- Four different fibre optic cables buried within a 150m long trench. The trench contained fibre optic cables and no pipeline. These cables were connected to leads which carry their signals to a BFS interrogator. Each cable had a different protective sheath. The sheaths' stiffness changed the amount of stress experienced by the optical fibre within the sheath under changing soil moisture conditions.
- Nine evenly spaced standpipes were placed along the length of the buried cables. These standpipes were used to introduce water directly into the soil, level with the cables.
- To measure the baseline cable behaviour before water is introduced into the system, the BFS of the fibres was monitored over a number of weeks, taking readings every 2 hours. Readings were taken at these time intervals to measure the variation in BFS due to temperature variation. Once a baseline was firmly established, water was introduced via the standpipes. BFS readings were then taken and a new baseline was established post-wetting.

The test conducted using the 150m long trench did not fully replicate the environment that a FO cable would be placed in under working conditions. Therefore, a second experimental setup along a working pipeline was incorporated into the study as follows:

- A working pipeline was instrumented with a tight-buffered fibre optic cable and downpipes were installed along its length which could be used to trigger a leak. The same methodology as stated previously, i.e. obtaining baseline behaviour both before and after wetting takes place, was used to obtain data to assess the efficacy of the pipeline leak detection system.

The limitation of the study was that in both the trench setup and along the pipeline water was introduced to the level of the FO cable via standpipes and not via cracks in pipe walls.

## **1.4 METHODOLOGY**

Reading an optical fibre using a BFS interrogator yields a BFS profile. This profile depicts the BFS along the entire fibre length. These profiles are temperature and strain dependent. When an optical fibre is buried in a soil medium it experiences temperature variation, thus its BFS reading will change throughout the day as the ambient temperature varies. These temperature variations are accounted for by taking readings throughout the day over a period of many days and averaging all the measured BFS readings to create one averaged BFS profile.

If the soil in which an optical fibre is buried is wetted, the soil stress state would change due to the soil-water interaction that takes place. The soil moisture content change would also cause the soil to swell or shrink, if it is an expansive soil, due to the change in stress state. The strain that occurs in the expansive soil will be imposed onto the optical fibre, which in turn locally affects the BFS of the cable at the point where it was strained.

If an average profile is established for an optical fibre before a leak occurs, it can be used to determine if a leak has taken place. This is achieved by comparing subsequent BFS readings against the averaged baseline profile. A significant deviation in subsequent readings from the average profile indicates that a leak at a specific location along the pipeline has occurred.

## **1.5 ORGANISATION OF THE REPORT**

### **1. Chapter 1 – Introduction**

The Introduction to the dissertation contains the background, problem statement, objectives, and methodology of the research topic.

### **2. Chapter 2 – Literature Review**

The Literature Review contains a review of previous literature pertaining to the current research topic to familiarize both the researcher and the reader of the dissertation with information regarding the research topic.

### **3. Chapter 3 – Experimental Setup**

The testing equipment, the manner in which it was set up and the purpose of the equipment used is explained in this chapter.

### **4. Chapter 4 – Data Analysis**

In this chapter the data obtained from the testing equipment is discussed. The following is explained: the output, the processing method, how the data was analysed, and how it could be implemented in a working leak detection system.

### **5. Chapter 5 – Conclusions (September 2021)**

The outcomes of the research are outlined and discussed. Recommendations for further research are given.

## **2 LITERATURE REVIEW**

### **2.1 INTRODUCTION**

This literature review discusses the background knowledge that is required both to justify the research that has been conducted, and to enlighten the reader concerning the fundamental principles that are employed in the operation of the proposed leak detection system. This literature review addresses the loss of water from distribution networks and the impacts thereof. Existing leak detection methods which have been developed to determine if a distribution system is leaking water are discussed. The behaviour of soil-water interaction is explained so that the behaviour of soil is understood when it is influenced by a leaking pipe. Fibre optic technology is also discussed and the Brillouin Frequency Shift (BFS) effect in optical fibres as a method of distributed sensing is explained.

### **2.2 WATER LOSS FROM DISTRIBUTION NETWORKS**

A water distribution network comprises of the facilities involved in the cleansing and purification of raw water and the infrastructure that brings the purified water to the consumer, i.e. the pipeline distribution network. Modern pipeline networks were conceived in the late 19<sup>th</sup> century (Martinez-Espineira et al., 2017), with some operating pipeline segments being over 150 years old (Clayton et al., 2010). This high age of pipeline networks, however, is a major proponent that contributes to pipeline failures in developing countries (Gonzalez-Gomez et al., 2011). The American Water Works Association has estimated that there are about 237600 pipeline breaks/failures per year in the USA (Gonzalez-Gomez et al., 2011). This is attributed to the poor maintenance of an aging distribution system and consequently great volumes of precious water are lost from these break points.

According to Gonzalez-Gomez et al. (2011), it is estimated that 47% of the world's population shall live in regions subject to severe water stress by the year 2030. With the growing world population, the annual volume of world-water-usage is projected to grow to 6275km<sup>3</sup> by the year 2050. With the advent of population growth and water scarcity on the horizon, mitigation of pipe network leakages must become a global priority.

#### **2.2.1 NON-REVENUE WATER**

Non-revenue water (NRW) is water that is purified and fed into a water distribution system by a water treatment facility which does not bring in revenue to the supplier (Gonzalez-Gomez et al., 2011). This is because some of the water that is introduced into the distribution system is lost from the distribution network before it can be metered and billed. The worldwide average calculated quantity of NRW is estimated as 36.6% of all purified water fed into distribution systems (Mckenzie et al., 2012). Kingdom et al. (2006) stated that worldwide 32 billion m<sup>3</sup> of treated water is leaked from urban supply systems yearly. Another 16 billion m<sup>3</sup> of treated water is consumed by end users, but is not paid for, also contributing to the loss of income to water utilities. The American Water Work Association

recommended in their guidelines that NRW as a percentage should be less than 10% for developed countries and less than 23% in developing countries. Given that the world average is 36.6% these recommendations have not been met.

NRW is categorised into three categories and components: real losses, apparent losses and unbilled authorised consumption (Gonzalez-Gomez, 2011).

Real losses, also referred to as physical losses, are the losses that occur due to water leaking from operating pipelines as a result of structural failure of the pipe itself. These losses are caused by a poor operations and maintenance regime, lack of an active leak control system and poor quality underground pipeline assets (Pederson et al., 2013). Real losses are the main contributors to the total NRW volume in developed countries due to the high age of the distribution networks.

Apparent losses are losses in water volume in cases where water has not been metered and billed, yet it has been used. It has not been leaked from the pipe itself, instead a party has obtained it through fraudulent means such as meter tampering or through corruption, or devious institutional management in the water supply agency. Apparent losses can also be attributed to illegal connections made to pipelines by informal settlements, or by devious means to circumvent payment for using supplied water. Data handling and customer registration errors also play a part in apparent losses.

Unbilled authorised use is defined as water used by consumers who are given concession with regard to payment. An example of this would be a fire fighting crew tapping into a fire hydrant to douse a fire, or a community to whom a governing body has gifted a supply of free water.

NRW has financial consequences that reach beyond the loss of income due to lost water. Because water is being lost from the system, additional water needs to be introduced into the system to compensate for the water that is lost (Gonzalez-Gomez, 2011). This causes excess working load to be imposed onto the water treatment plants. Along with this comes an increased operating cost as more water is being treated than what is needed. This cost must then be borne by the paying consumers to whom metered water comes via the correct route, and not illegitimately. In addition, paying consumers also pay for the water consumed by parties who do not pay for their water. NRW therefore has a negative feedback effect, in that greater leakage and illegitimate use of water over-stresses the purification system, raises operating costs and requires the paying consumers to bear the increased levies.

The increased need for water, due to the loss thereof, exerts extra stress on the existing available water sources from which raw water for purification is acquired. This worsens the water deficit in water scarce regions, resulting in more rapid depletion of existing local sources. This forces water supply agencies to search for alternative water sources which increases their catchment channelling costs. A risk associated with searching for alternative sources of water is that the water that is found may be of inferior quality. Therefore, the treatment plants that treat this water will require extra purification processes. This further increases the cost of the water that is produced by the water purification facility, which again must be borne by the end paying-users.

It is the responsibility of a water supply agency to minimise leakage from their water distribution network. One method to achieve this is by improving the water network pressure management. Working pipelines are subjected to substantial pressure fluctuations. These pressure variations play a major role in the failures of pipelines. By minimising the variations of pressure that occur throughout the network, pipelines' lives may be extended, reducing maintenance costs incurred in the future. The problem, however, is that water utilities are profit driven. Thereafter, the intent is to purify the water and introduce it into the distribution system to be used by paying consumers. The more water is introduced into the network, the more consumers must pay. Even if all the input-water is not used, the costs of the treatment facility must still be covered. Therefore, if a network contains leaks, more water must be introduced into the distribution system, which results in a higher income to the water supply agency. It is thus more profitable not to repair leaks in the network unless the leaks are causing physical damage to surrounding infrastructure. Consequently there is a lack of interest to mitigate leaks due to the benefit of increased revenue associated with them (Gonzalez-Gomez, 2011).

### **2.2.2 THE STATE OF NON-REVENUE WATER IN SOUTH AFRICA**

The figure representing the state of NRW in South Africa (SA) in 2012 by Mckenzie et al. (2012) was determined as 36.8%. This statistic was obtained by assessing 132 of the 237 municipalities responsible for the supply of water in SA. The 132 municipalities accounted for 75% of the total water volume supplied in SA. SA's NRW figure is in line with the global average of 36.6%. This corresponded to a volume, in 2012, of 1580 million m<sup>3</sup>/annum lost as NRW, equating to a financial loss of R7 Billion in that year. It was also found that the components of the three NRW categories were spread among the South African NRW as 25.4% for real losses, 6.4% commercial/apparent losses, and 5% unbilled authorised losses.

Bhagwan et al. (2014) have stated that SA is regarded as a water stressed country. The inadequate distribution of precipitation, and the high rate of evaporation renders SA vulnerable to extreme climate variability. To combat these effects, the Water Research Commission (WRC) of SA has developed software models and tools that are able to assist water suppliers in reducing water distribution network leaks.

SA is a country that has both developed and developing regions. The water audits conducted in 2012 (Mckenzie et al., 2012) showed that the developed regions of SA had NRW levels as low as the best countries in the world. However, in the developing regions, NRW was reported to be as high as 90% of the total water volume input into the distribution network. The discrepancy in NRW levels in countries like SA must be addressed to ensure that the water resources that are available can be used as efficiently as possible.

### **2.2.3 FACTORS AFFECTING WATER DISTRIBUTION NETWORK CONDITIONS**

There are a number of factors which influence the effectiveness with which a water distribution network provides customers with water and how efficiently they are billed. The initial quality of the pipeline plays an important role in how the pipeline will perform for the rest of its life (Georgia Environmental Protection Division Watershed Protection Branch, 2007). A poorly constructed water distribution network will deteriorate with more rapidity than one that is constructed with rigorous quality checks and high quality pipelines and equipment. Once a water distribution network has been constructed, the causes of NRW include inaccurate billing and metering systems, deteriorating water distribution infrastructure that is not being maintained, excessive water pressure in pipelines, overflowing reservoirs, unnecessary flushing of pipelines and illegal connection, to name but a few (Pederson et al., 2013).

The main contributor to the high rate of physical leakage from a network is its age (Martinez-Espineira et al., 2011). With the introduction of modern water supply networks being implemented in the mid-19<sup>th</sup> century, many systems have undergone substantial wear and tear without maintenance, repair or replacement. This poor state of network repair allows leaks to abound, wasting precious water, and making way for external contaminants to enter the pipes through break points. Old networks were originally constructed using iron and lead pipes. These materials are today considered inferior quality materials for pipeline construction. Current pipelines are constructed and maintained using ductile cast iron, steel and polyethylene based pipes. These materials are more resistant to wear and less vulnerable to corrosion. Existing pipelines consisting of these iron and lead pipes should therefore be subject to rigorous maintenance, or replaced by a new alternative material. However, the pace of investment into improving current water distribution networks is insufficient in many countries due to a lack of economic incentive.

Pipeline networks are required to operate in punishing conditions. Extreme weather such as frequent and heavy rainfall, temperature variations due to day and night and seasonal cycles, wetting up and drying of surrounding soil, and dynamic water supply rates in the pipelines themselves impose significant stresses on the materials constituting the pipes. These environmental forces cause the pipe material to degrade and wear over time. If they continue to degrade unchecked, this leads to pipe failures. The pipe networks that are in the worst conditions are located in countries with extreme climates, high temperature variability and heavy rainfall. Additionally, a trend exists that the longer a pipe network is, the greater the population size that uses it. The more intensively it is used, the poorer its condition will be.

### **2.2.4 FACTORS AFFECTING PIPE LEAKAGE**

The volume of water exiting a working pipeline is dependent on the shape and size of the crack releasing water, as well as the pressure of the water within the pipeline. Leakage is primarily influenced by the

water pressure within the pipeline (Van Zyl et al., 2007). The flow rate,  $Q$ , of water flowing through an orifice is governed by the orifice equation:  $Q = ch^\alpha$ . Here  $c$  is the orifice energy loss discharge coefficient,  $h$  is the pressure head, in meters, and  $\alpha$  is a theoretically derived exponent, having no units, obtained in the mathematical derivation of the expression.

The mathematically derived value of  $\alpha$  is 0.5. The value of  $\alpha$ , however, when tested experimentally on pipes does not come out as 0.5 (Van Zyl et al., 2007). Field studies have shown that  $\alpha$  can be both slightly less and significantly greater than 0.5.  $\alpha$  ranges between the values of 0.42 and 2.79, a value of 1.15 being the median observed value. These exponents are dependent upon the shape of the orifice in the pipe wall. Pipe material also has a role to play in the value of  $\alpha$ , as the highest  $\alpha$  values occur in corroded steel pipes.

The variability of  $\alpha$  arises from the shape and orientation of the crack in the pipe wall. The orifice shape that achieves values of  $\alpha$  closest to 0.5 are round holes and holes with aspect ratios that are close to a 1:1 ratio. The crack shapes that give rise to  $\alpha$  values that stray from 0.5 are thin-line cracks with high aspect ratios. These cracks have areas that are dependent upon the pressure that is present within the pipe. A thin-line longitudinal crack (a crack that propagates in the same direction as the flow of water in the pipe) will open wider as the water pressure in the pipe increases due to circumferential pressure acting upon the pipe wall (Van Zyl et al., 2013). In contrast, a vertical thin-line crack will be stretched and closed by the circumferential pressure acting within the pipe.

When a pipe crack is tested, the orifice area is measured before the pressure in the pipe is increased. Water is allowed into the pipe under pressure, increasing the orifice area, and the flow rate out of the crack is measured. The area, however, is not corrected, but instead  $\alpha$  is calibrated using the original orifice area and the measured flow rate. Technically, this lack of an area correction is in practice incorrect. But what can be learned from the higher empirically derived values of  $\alpha$  is that in pressurised pipelines cracks are able to leak far more water than what their original size should allow.

## **2.2.5 SOIL BEHAVIOUR SURROUNDING LEAKING PIPES**

Most water distribution systems are buried underground. Soil is therefore the typical medium surrounding a leaking pipe. How the water exiting a pipe break interacts with the surrounding soil can have a huge impact on the infrastructure built upon that soil.

There are three possible zones that can develop around a pipe break. These are the fluidised zone, the mobile bed zone and the static zone (Van Zyl et al., 2013).

The fluidised zone is characterised by particles that are free to move with the pore fluid, or water that is leaked out of a pipe. The inter-particle forces become negligible as the soil particles are suspended and move with the leaking water. The fluidised zone size is a function of the pipe leak's flow rate. Thus this zone could not be present if the flow rate is too low. It is possible for a fluidised zone to develop, but for the water therein to never reach the ground surface, rendering the leak unnoticeable. The danger of

a fluidised zone is that the zone's strength is governed by the properties of water which has virtually no shear strength. The fluidised zone is therefore subject to collapse if too great a load is imposed onto the soil surrounding it.

The mobile bed zone surrounds the fluidised zone. Like the fluidised zone, the mobile bed zone is characterised by moving particles, except that there are no inter-particle gaps present. The particles move steadily about the fluidised zone toward the orifice opening, guided by the direction of the flow of water.

The static bed zone lies outside the mobile bed zone. Particles in this zone remain stationary and are unaffected by the water jet, except for the water that ingresses into the soil pores.

The soil that constitutes these zones around a pipe leak will be prone to allowing structural failures of surrounding infrastructure. The most dangerous of all these zones is the fluidised zone, as this zone does not have any shear strength due to the absence of inter-particle forces existing between soil particles.

## **2.2.6 NEGATIVE IMPACTS OF PIPELINE FAILURES**

Although NRW is comprised of three components i.e. physical leakage, apparent losses and unbilled authorised consumption, leakage constitutes the greatest portion of the three (Burn et al., 1999). Pipes leaking underground are not readily detectable without specialised equipment, and therefore they can go unchecked for extended periods of time. The loss of water from pipe breaks does not only contribute to financial loss, in the form of lost water, but also has consequences extending to the surrounding environment and infrastructure surrounding leaking pipelines.

The most immediate effect that a leaking pipe has on the surrounding environment is on the pipe bedding. Depending on what the mineralogy and of the pipe bedding is, the soil could either be collapsible or expansive, or have no expansive potential. Whether the soil shrinks or swells around the pipe, there will be additional stresses imposed onto the pipe. Clayton et al. (2009) reported that soil movement due to water ingress into and out of the soil surrounding a pipeline can impose additional stresses of up to 30MPa. These high stresses repeatedly imposed on pipelines can cause them to fatigue and cracks can form in weakened regions of the pipe material.

Leaking pipes can also cause their own bedding to be washed away as a result of the constant out-gushing of water. When a pipe is no longer resting on the bedding provided for it, it will be subjected to bending stresses in the hanging regions likened to a supported beam with fixed ends. In addition, the water leaked out of a damaged pipe, if severe enough, can impact the soil upon which the foundations of infrastructure surrounding the pipeline are constructed. The ingress of water into the soil may weaken it, or it could generate swelling which causes excessive pressures to act on foundations.

Water can also ingress through the soil by forming soil cracks along planes of weakness and flowing preferentially along these cracks (Van Zyl et al., 2007). This could allow water to flow much farther than if it was only seeping through the soil. Gas mains, telephones, roadways and buildings can all be

damaged by an unchecked leaking pipe situated below the surface. It is in the water utilities' best interest to be able to prevent such damages from taking place.

A crack in a pipe usually expels water, but there are instances when the pipe pressure becomes negative and the pipe is able to suck external substances into it (Van Zyl et al., 2007). If a pipeline is surrounded by a hazardous substance and it has a rupture, it is very possible for contaminants to be sucked into the working pipeline when the pressure thereof becomes negative. If ingested by end users, these substances would undoubtedly be detrimental to the consumers' health.

Pipe breaks can also occur along sewage transport lines, and although the losses from these pipes do not affect purified-water consumers, the waste water leaked by sewage lines can cause serious environmental damage. The eutrophication of bodies of water and soils can occur, causing the environment to become toxic toward plant and wildlife living in the affected region. Faecal coliforms can use up the available oxygen in bodies of water, resulting in the death of fish and other creatures who live in that water. Pipeline leakage therefore not only has monetary costs, but can also affect the quality of life of people and animals in the immediate environment of working pipelines.

### **2.2.7 REDUCING NRW**

Reducing NRW is a necessary action that all countries should invest in. The task, however, is not only a technical issue, but must overcome political hurdles, economic restraints and address the repair of deteriorated infrastructure (Kingdom et al., 2006). The task of a utility reducing NRW to half its state is a realistic goal that is achievable within a one to two year timeframe with major benefits (Pederson et al., 2013). In order to assess a network so that the NRW components of the system can be reduced, the following must be considered: lack of system pressure, frequency of pipe failures and breakdowns, the state of deterioration of the accessories, the losses due to the present leaks. Based on these criteria the distribution network can be rated as a well-operating system, or as a poor one (Martinez-Espineira et al., 2011).

Pederson et al. (2013) laid out a master plan that was developed to counter-act the NRW challenges that were plaguing Denmark. To reduce NRW in a given distribution network, the network must be analysed using available data and supplementary collected data to provide a complete level of information surrounding the distribution network state. Water audits are used in this regard to acquire a detailed account of water flowing into and out of the distribution system (Burn et al., 1999). These can help to identify parts of the system that have excessive leakage if the input and the output are vastly different. The information gained from this process can then be used to optimise and prioritise the NRW reduction activities that must be done. Once the data analysis has been completed, a NRW baseline and a breakdown of the water balances, including NRW losses, can be establish from which subsequent results can be compared.

Management and repair systems must then be implemented and data bases and modelling tools must be developed to track the management systems' progress. These management systems include pressure

management, based on output obtained from the hydraulic modelling and data analysis. This can be achieved through intelligent pumping operations. Leakage reduction through pressure management can be a powerful tool which can save up to 1000m<sup>3</sup>/hour in a system the size of the Unicity of Cape Town, South Africa (Water Wheel, 2005). At night when the water demand is low, due to few people and industries operating, dripping taps drip faster and weak points in the main distribution system are prone to bursting. By monitoring the distribution system pressure sector by sector, off-peak pressures can be reduced to a level adequate for users who require water at non-busy times. This will lower the stresses in worn tap washers and weak points in the distribution system.

District metering systems must be put in place so that measurement of water fed into and used by districts can be quantified (Burn et al., 1999). Importantly, a leak detection system must be installed so that pipe failure can be detected and located. To reduce the NRW level as quickly as possible, work to be completed must be prioritised. NRW hotspot areas require the most immediate action as these regions are the greatest contributors to the NRW level. The party responsible for the reduction of NRW must propose a budget of all the costs that they will incur and thereafter they must procure the funds necessary to achieve their goal.

Once the necessary remedial action has been done on the pipeline distribution network, the NRW reduction scheme then moves into its operational phase. The reduction and control of leakage is a long-term ongoing process. The operational phase of the NRW reduction project involves active pipe replacement and a rehabilitation plan, again targeting NRW hotspots. Active leak control is achieved through an operational emergency leak repair system. An alert-system must be in place to trigger an alarm whenever a leak in the distribution network is detected. Repairing physical leaks as quickly as possible after an alarm has been triggered is crucial to mitigating water loss from distribution systems.

The reality of NRW is that all systems will have certain amounts of water that are unpaid for. Water distribution systems have designed overflow points to relieve pressure in pipes when their capacity is exceeded (Burn et al., 1999) and it is impossible to find every leak point and metering error. The well run utilities in the world have NRW levels in the teens and the best ones have single digit NRW percentages. The lowest NRW levels of the most efficient systems in the world are recorded as 3% (Pederson et al., 2013) in countries such as Germany and the Netherlands (Martinez-Espineira et al., 2011). The city of Copenhagen in Denmark, after implementing a stringent NRW reduction programme was able to reduce their NRW level to 5% even with pipe network infrastructure that was over 100 years old (Pederson et al., 2013).

Low quality poorly maintained systems, having a NRW level of 40% or above, must be addressed worldwide to mitigate the loss of precious drinking water and to encourage economic development.

## **2.2.8 BENEFITS OF REDUCING NRW**

NRW is a challenge faced by both developing and developed countries. By reducing the NRW of a country to half, a boost in income can be generated for the water supply agency as more water would

reach the end user (Pederson et al., 2013). Increased revenues can be generated as more people will be billed for the water they consume. The water utility shall also have reduced operating costs, because they will not be required to treat unnecessary volumes of water to supply the needs of consumers.

The total global annual financial loss attributed to NRW in 2006 was \$14 billion (Kingdom et al. 2006). Kingdom et al. (2006) conducted a study on the NRW levels in developing countries and found that the NRW level of developing countries ranges from 40% to 50% of water input into distribution networks. The total daily leakage due to pipe breaks in developing countries in 2006 was 45 million m<sup>3</sup>. The volume was calculated to be enough water to serve 200 million people daily. In addition to the water that was leaked daily, the unaccounted for water (water used but not billed) was determined as 30 million m<sup>3</sup>. The NRW financial loss of the developing world constitutes one third of the annual total global NRW loss of \$14 billion.

Kingdom et al. (2006) calculated that if the NRW of developing countries could be reduced by a half, then the extra revenue that could be generated in a year would amount to \$2.9 billion. In addition, 90 million extra persons would be able to be served by the water supply agencies. These two benefits would be possible without any further investment into finding new water resources. The reduction of NRW by a half would require significant capital investment into existing pipeline resources that would need to be repaired. However, the available water resources would remain unchanged. The investment would be well worth it as, in 2006, \$215 to \$500 would have been saved per m<sup>3</sup> of water saved (Kingdom et al., 2006).

There are also benefits that do not relate to financial gain, but to the infrastructure quality, by looking after a water distribution network (Pederson et al., 2013). By optimising water distribution the quality of the water can be improved as less water is treated with the same resources, resulting in a cleaner finished product. By managing the pressure, water hammer can be reduced and negative pressures that suck contaminants into the pipelines from the surrounding environment can be avoided. Also the energy consumption of pump stations can be minimised as pressure is adapted to meet the instantaneous demand. This would also make the water supply more stable. Stress on water resources would be reduced as the same number of people can be served by using and treating less raw water. Reducing underground leaks would help to protect civil infrastructure by mitigating the damage that water could do to building foundation and street pavements. Lastly, a good leak reduction programme can significantly improve the relationship between the water supply agency and the public who consume the supplied water (Georgia Environmental Protection Division Watershed Protection Branch, 2007).

## **2.3 SOIL-WATER INTERACTION**

Soils comprises of a medium of soil particles with pore spaces between them. These pore spaces can accommodate water and air to fill the void between soil particles. Due to the surface tension that water possesses, the interaction of soil, water and air, gives rise to stress states within the soil that are a function

of the mineralogy of the soil particles and the amount of water (moisture content) and air present between the particles.

### **2.3.1 SHRINK-SWELL BEHAVIOUR OF SOIL**

Soils that undergo changes in volume due to changes in their moisture content are called expansive soils (Adem and Vanapalli, 2014). These soils are prone to swelling and shrinking if their moisture content is either increased or decreased and are therefore sensitive to changes in moisture content. The volume change is attributed to water being absorbed into the soil to fill the available pore spaces of the soil, and is thus dependent on the soil water content (Khademi and Budiman, 2016). The stress in the soil between the soil particle and the water is called matric suction and arises because of the surface tension of the water.

Volume change due to changes in soil moisture content are most notable in unsaturated soils containing clay particles. Expansive soils are most commonly found in countries with arid and semi-arid conditions (Mokhtari and Dehghani, 2012). Soils that contain a high percentage of clay are capable of absorbing vast quantities of water. Their shrinking and swelling potential are governed by their initial water content, initial void ratio, the soil internal structure, and the external vertical stresses being imposed on the soil, and the type and amount of clay minerals present. Smectite, montmorillonite, nontronite, vermiculite, illite and chlorite are minerals that have an impact on the expansive potential of a soil (Mokhtari and Dehghani, 2012). The swelling potential of each clay mineral, however, differs. Montmorillonite (Khademi and Budiman, 2016) and smectite (Mokhtari and Budiman, 2012), for example, are the clay minerals with the greatest volume change potential of all clay minerals.

The reason why clays are capable of absorbing vast amounts of water is due to their high surface area to volume ratio (Ross, 1978). They are shaped like flat platelets, because the minerals comprising the clay particles arrange themselves into sheets (Khademi and Budiman, 2016). These sheets are thin and their length and breadth are great in comparison to their thickness. Clay particles are smaller than 0.002mm, constituting the smallest particles in a medium of soil. Clay particles have such expansive power that if a soil contains 5% clay particle content or more, its behaviour is dominated by the clay particles (Mokhtari and Dehghani, 2012).

The shrinking and swelling potential of soil is dependent upon how much water a soil is capable of absorbing (Ross, 1978). The clay particles in a soil, with their large surface areas, are adept at holding large quantities of water between clay platelets. In addition, these clay platelets are also reluctant to give up the water which they are holding between themselves. This is attributed to the nature of the surface of clay particles as they have a certain charge density with which they can attract water molecules. There are also exchangeable ions in clay platelets which can attract water due to the salts dissolved within the water.

At the particle level there are two phenomena that cause the swelling and shrinking of a soil medium, one being mechanical, and the other physiochemical (Gens and Alonso, 1992). The mechanical

phenomenon is the negative pore pressures associate with capillary water in the soil. These play a role in the interconnected pores of the clay macrostructure. The physiochemical phenomenon is the water linked to individual clay platelets with larger units of closely packed particles. These two phenomena work together to suck water into the spaces between the clay platelets. The eagerness of the absorption of water into the inter-clay-platelet spaces gives rise to the reactivity of clay within a soil to cause the soil as a whole to be expansive.

The macroscopic in-situ factors that influence an expansive soil's swelling potential is its stress history, loading conditions and the soil profile (Mokhtari and Budiman, 2012). Expansive soils may be hindered in their expansive ability if they are being acted upon by large loads. However, instead of expanding, the expansive soils will develop large stresses, which are then imposed onto the objects confining them from swelling. The expansiveness of clays is also diluted by the presence of non-swelling material such as quartz and carbonate. These materials could even be used to treat a soil that is too expansive, but that may become costly.

The environmental conditions can also play a role in the shrink-swell behaviour of a soil. Expansive soils in climates where moisture varies greatly such as hot, heavy rainfall areas will undergo many expansion and contraction cycles. Tree roots in the vicinity of an expansive soil can also cause the soil to shrink and swell through multiple cycles due to evapotranspiration (Li et al., 2013). The groundwater and drainage conditions will have an influence on the soil's initial moisture content, which in turn affects its expansive potential. If a structure is to be built on an expansive soil all these factors must be taken into account so that the structure can be designed to be safe against failure due to soil movement.

### **2.3.2 DAMAGE TO INFRASTRUCTURE DUE TO EXPANSIVE SOIL**

All infrastructure is founded upon soil and it is inevitable that some structures will be built upon clayey soils. Non-expansive clays do not exist and some clays are even capable of swelling to multiple times their dry volume (Khademi and Budiman, 2016). Swelling clays are a hazard to structures because structures built upon expansive soils are prone to high stresses due to soil heave (Mokhtari and Dehghani, 2012). Expansive soils are capable of causing tremendous pressure when their soil moisture content increases while they are confined (Mokhtari and Budiman, 2012). If unaccounted for, these heave stresses can cause major damage to structures, resulting in large financial costs to repair such infrastructure.

Buildings, roads and pipelines are all prone to damage incurred by being overstressed due to heave caused by expansive soils (Khademi and Budiman, 2016). The worldwide costs of infrastructural damage caused by expansive soils is twice that of damage caused by floods, hurricanes, earthquakes and tornadoes combined. Adem and Vanipalli (2014) reported that the cost of expansive soil damage in the USA, in 2009, amounted to \$13 billion, and has been ever increasing.

Structural damage is caused by differential heaving of the foundation subsoil (Jennings and Kerrich, 1962). Heaving of structural foundations can cause the supported structure to crack and distort, exposing

structural steel to the air through cracks, and imposing unnecessary stresses through distortion. One of the causes of soil heave is the failure of underground pipelines. Pipelines leaking copious amounts of water are prime candidates for the supply of water to allow expansive soils to swell to their full potential. As the swell of an expansive clay is a function of its water content, by soaking up large volumes of water, excessive swelling will occur and the heave generated imposes significant stresses on the surrounding environment and infrastructure. Soil heave is capable of exceeding the tensile strength of foundation concrete of 2.7MPa and yield the foundation rebar (Li et al., 2013). Once the concrete is cracked, water can also ingress into the foundation footing and corrode the structural steel.

The swelling of expansive soils is not the only problem, however. The shrinkage of soil can be just as devastating. An expansive soil that loses water content during a dry spell can undergo significant shrinkage, so much so that it can cause differential settlement to form beneath the foundations of a structure (Mokhtari and Dehghani, 2012). Thus, the loads of the structure would be unevenly distributed among its foundations. The overloaded foundations will in turn be prone to failure, resulting in failure of the structure itself.

The shrinkage of expansive soil also brings about the formation of cracks in the soil medium (Khademi and Budiman, 2016). These cracks allow water to penetrate further into the soil, enabling a deeper layer of soil to expand and contract, amplifying the effect of heave. In addition, when these cracks open, they are filled with other soil material and therefore do not close when the soil expands again with the advent of water ingress. The original volume of the soil medium is therefore increased and the soil is able to expand to a greater volume, further enhancing the heave stresses imposed onto structures due to the soil swell.

There is, therefore, much concern about the design, protection and operation of structural systems as even moderately expansive soils can cause major damage to structures, let alone highly expansive soils (Khademi and Budiman, 2016). The foremost problem that is encountered with expansive soil is that deformations are considerably greater than those predicted using elastic theory. In order to design a reliable structure on an expansive soil, the soil movement must be able to be anticipated (Adem and Vanipalli, 2014). Assessments must be made during the design process of structures, taking into account environmental factors such as climate, vegetation, botanical feature watering and soil cover type to predict how the soil will respond so that a structure can be designed to operate safely.

In order for a structure to be safely constructed on an expansive soil, excavations may need to bypass the soil layer so that the structure can be founded upon bedrock or a deeper layer of stable soil. The most reactive layer of clayey soil is the top 3m below the ground surface, as this region is exposed to the most water content variation. It is important for construction agencies to monitor the interaction between the ground and foundations during and after construction has been completed.

### **2.3.3 RELATIONSHIP BETWEEN SOIL STRENGTH AND WATER CONTENT**

Soil strength increases in a non-linear manner as it desaturates (Vanapalli et al., 1996). This also implies that its strength decreases as its moisture content increases. This is a result of the change in matric suction within the soil structure. The shear strength of a soil is thus a function of the amount of water that is held in the voids of the soil.

Soils therefore have the potential to collapse if their moisture content is raised too high (Li et al., 2016). This collapse upon wetting is triggered by the loss of capillary tension that attracts the soil particles to one another. Unsaturated soils derive strength from this capillary tension, and the addition of this water destroys the capillary tension. As the attractive force is decreased between particles, the shear strength of the soil decreases due to the lack of inter-particle friction generated by the normal forces between soil grains. This reduction in strength is what triggers a soil's collapse.

Collapsibility of a soil is dependent upon the initial water content of the soil and the vertical stress under which wetting occurs. Soils that are compacted at dry of optimum moisture content exhibit collapsible behaviour upon wetting. Soils compacted at wet of optimum moisture content show no collapsibility. Soil collapse upon wetting is attributed to the metastable nature of an open flocculated structure associated with dry of optimum water conditions. The contact relation, the ease with which particles can slip over each other, also contributes to the collapsibility of a soil.

Collapse of unsaturated soils typically occurs before the soil can reach a fully saturated condition. This is dangerous for buildings constructed on highly unsaturated material. Significant collapse begins to occur at a critical water content. As the water content increases beyond the critical value, the bonding strength within the soil fails to support the soil fabric. Thus the soil structure as a whole fails and a particle rearrangement occurs that transforms the initial stable open structure into a remoulded close structure. This is the collapse process.

It is therefore evident that a spaced pore structure constitutes a favourable spatial condition in which collapse is allowed to occur. When a soil gets wet, the bonding strength between particles weakens and overhanging particles are free to fall into open spaced pores.

The volume change of collapsible soils is attributed to a change in net normal stress and matric suction. It is believed that collapsible soils experience their maximum settlement as their degree of saturation approaches 100%. The collapse settlement at the saturated condition of soil is of concern and interest for geotechnical engineers. The collapse of a soil beneath a foundation supporting a building can have devastating consequences, both financial and life threatening to the people inside the supported structure.

## **2.4 PIPE LEAK DETECTION METHODS**

Leaking pipes are a worldwide problem that have led to the development of an array of pipeline leak detection methods and technologies. Many of these leaks are below the surface and can go unnoticed for extended periods of time (Georgia Environmental Protection Division Watershed Protection Branch, 2007). These leaks can therefore take time to become apparent as water penetrates through ground layers above the damaged pipe to become visible at the ground surface (Blazevic et al., 2005). The time that a leak could take to become visible at the surface depends on the depth of the damaged pipeline, the dimensions of the crevice through which the water is escaping from the pipeline, the water pressure and the type of soil beneath which the pipe is buried.

Apparent leakage is easy to detect. Regular patrols along the pipelines constituting a water distribution network can easily establish visual contact with the location where a pipe is leaking. The leaking pipe can then be excavated and repaired accordingly. Hidden leakages are not detectable by visual inspection and therefore require specialised technology to detect them. These leaks can last many years without being noticed and contribute heavily to NRW.

Pipe leak detection methods are grouped into two sub-categories: active and passive methods. Active detection methods are those that involve personnel performing inspections on a pipeline to determine if a pipe failure has occurred and where it is located. Passive detection methods involve measuring instrumentation that is installed onto or near the working pipeline that sends out an alert if the instrument detects an anomaly such as a leak.

### **2.4.1 ACTIVE LEAK DETECTION METHODS**

#### **2.4.1.1 WATER AUDITS**

Water audits are used to determine the amount of loss that occurs in a water distribution system (Osama, 2000). This is done by processing the available metering data to determine what volume of water flows into a section of the distribution system and how much volume is used out of that section. By processing this collection of data an overview of the quality of the network, characterised by the distribution losses, is gained for the distribution network. This can help to identify problem areas of the network that have excessive leakage so that resources can be diverted to the leak hotspots.

If data is not available it can be collected using ultrasonic flow meters and pressure loggers (Blazevic et al. 2005). Ultrasonic flow meters determine the accurate quantity of water flowing through a pipeline. If a measured flow rate is above the expected flow rate, or if the volume of water flowing in differs from the volume of water flowing out, then it can be implied that a leak has occurred downstream in the region being monitored as more water enters the pipeline than what flows out. This is known as the Compensated Volume Balance method (Sandberg et al., 1989).

Another measurement that can be performed to acquire data on a pipeline is pressure measurement. A pressure logger is used to log a pipeline's pressure at specified time intervals (Blazevic et al., 2000). The effect that leakage has on the pressure in a pipeline is that it experiences a reduction in operating pressure. Therefore, if a significant pressure drop is registered in a pipeline it may be due to a pipe failure leaking water.

The water auditing process does not provide any precise leak locations, but only provides information about the state of the regions into which the network is divided (Osama, 2000). Water auditing is therefore a great tool to use so that an overall picture of the network performance can be acquired and for the efficient tasking of available resources to specific problem areas.

#### **2.4.1.2 LEAK-DETECTION SURVEYS**

Leaks are commonly pinpointed using acoustic devices that detect vibrations induced along a pipeline (Osama, 2000). A leaking pipeline will induce vibrations in the pipe wall which travel along the length of the pipeline. These vibrations can be detected by acoustic listening devices. To bracket the leak region two listening devices can be placed on two separate valves or fire-hydrants encompassing a region of the distribution network.

Once the region of the leak has been determined the leak can be pinpointed using a ground microphone or listening rods. A ground microphone or geophone detects the micro location of a leak by listening for the leak noise (Blazevic et al., 2005). The operator lays the geophone directly on the ground and listens for a signal. The operator then searches for where the loudest signal occurs which reveals where the leak that he/she is looking for is located.

#### **2.4.1.3 TRACER GAS**

Tracer gas is a non-toxic, water soluble, lighter than air gas that gets injected into a section of pipeline to locate a pipe fault (Osama, 2000). The pipeline must be sectioned off by closing the appropriate valves and then drained so that the gas can fill the isolated pipeline section. The gas is free to escape from the pipe where the pipe wall has an opening, i.e. at leak points. The location where escaping gas is exiting the pipe is detected using a gas detector which scans the ground surface above the pipe.

#### **2.4.1.4 THERMAGRAPHY**

The water that flows within a pipeline has different thermal characteristics to the surrounding soil (Osama, 2000). Therefore, when water leaks from a pipeline the thermal characteristics of the soil surrounding the pipeline will inevitably change. By scanning a pipeline network using thermal imaging, the locations where the soil thermal characteristics deviate from their expected behaviour can be determined. These regions of abnormal thermal soil behaviour in turn give away the locations of pipe leaks.

### **2.4.1.5 GROUND PENETRATING RADAR**

Leaking pipes are able to create voids in the surrounding soil medium (Osama, 2000). These voids in the soil can be detected using ground penetrating radar as the seismic wave propagation characteristics of a void will be different to that of the soil surrounding the void. In addition, when the soil surrounding a pipeline becomes saturated due to a leak, the dielectric constant of the soil surrounding the pipeline increases. This causes the pipeline to appear deeper than what it actually does when scanned using ground penetrating radar. Thus, the detection of a pipeline that appears to be deeper than expected by ground penetrating radar is a possible indicator that the scanned pipeline has a leak.

## **2.4.2 PASSIVE LEAK DETECTION TECHNIQUES**

### **2.4.2.1 ACOUSTIC LEAK DETECTION**

Active acoustic leak detection instruments include listening rods, aquaphones, geophones and ground microphones (Osama, 2000). These however, all require personnel to operate them and to interpret the data output. An example of a passive acoustic leak detector is a leak noise correlator. This device is capable of pinpointing leaks automatically using the cross correlation method.

The cross correlation method functions by registering two acoustic signals, generated by the same source, using two different listening devices in different locations (Osama, 2000). The acoustic signal source is a leaking pipe. The leak will be asymmetrically located between the two acoustic signal registration points, and thus there will be a time lag between the measured signals, calculated by the cross correlation function. The cross correlation function outputs a distinct peak at the time shift between the leak signals. The location of the leak is then found using the relationship relating the time lag, the distance separating the two sensors and the sound wave propagation velocity in the pipe wall.

The effectiveness of acoustic leak detection methods is dependent upon the characteristics of the pipe in which the leak occurs and the sensing equipment used to detect the leaks (Osama, 2000). The pipe material and diameter have a significant effect on the acoustic signal that travels through the pipe. Acoustic signals are carried farther by metal pipes, but the signals are greatly attenuated by plastic pipes. This is due to the fact that plastic is less rigid than metal and acoustic signals attenuate faster in less rigid materials than stiffer ones. In addition, a larger pipe diameter also causes the acoustic signal travelling along the pipe to attenuate more rapidly. In conjunction herewith, leaks in large diameter pipes which have less rigidity are characterised by lower predominant frequencies. Acoustic detection equipment was developed for metal pipes, and because plastic pipes are quieter than metal ones, the equipment developed is not as efficient in plastic pipe networks. Thus, highly sensitive equipment is required when the pipe material is less rigid and when a pipe's diameter is large.

The depth to which a pipe is buried, the type of soil surrounding the pipe and the soil conditions themselves also influence the performance of the acoustic leak detection system (Osama, 2000). Leak

signals are more audible in sandy soils than in clayey ones, and an acoustic signal is muffled if it occurred below the level of a water table.

A greater pipeline operating pressure also causes a leak to emit a stronger acoustic signal, and splits, corrosion pits and failures in the pipe wall generate stronger signals than leaks that occur from joints and valves (Osama, 2000). Any interfering noise that causes a low frequency vibration, such as pumps and road traffic can negatively impact the listening devices ability to hear the acoustic signal output caused by a leak. It is therefore necessary that acoustic equipment be used that is highly sensitive with a large frequency range, and that working conditions give high signal-to-noise ratios so that smaller leaks can be detected even in large plastic pipes.

One way in which acoustic listening devices can detect leaks is described by Wang et al. (2019). Wang et al. developed an acoustic leak detection system which is based on model-free isolation of abnormal signals. To achieve this, the acoustic signal received by a listening device is decomposed into its sub-signals using signal decomposition methods such as Fourier Transformation. The function between signal-to-noise-ratio (SNR) is established and from this, positions of abnormal sub-signals are obtained. Operational sub-signals, acoustic signals produced by the working pipeline, are filtered out and the precise location of the leak can be acquired. This method of analysing the data put forth by Wang et al. (2019) was able to reduce the impact of operational sub signals on the leak detection process and it was able to provide higher leak location precision. The false alarm rate was also lowered as compared to more conventional acoustic sensing techniques.

The acoustic leak detection equipment proposed by Wang et al. (2019) consisted of a piezoelectric pressure sensor which listened to and captured the acoustic signals, and then converted them into electrical signals. Instead of exporting the signals to a computer, a signal conditioning circuit was integrated into the setup to filter and process the acquired acoustic signal. This method increases the rapidity with which data can be processed. Thereafter, the processed signals were transmitted to terminal units from multiple acoustic listening devices placed upstream and downstream from acquired signals. The synchronous acquisition of data, synchronised using GPS timing, was then combined and used to successfully calculate the locations of leaks.

To make a truly passive acoustic leak detection system, acoustic listening devices must be installed at strategic locations throughout a pipeline distribution network. This must be done so that a leak that arises anywhere in the network can be detected by two corresponding listening devices. To optimise the layout of acoustic sensors Li et al. (2011) formulated an algorithm that uses the geographic information of a distribution network to place the minimum number of listening devices in a network with the maximum leak detection coverage of the network. The algorithm was tested on the city of Beijing over the course of 2007 to 2009, installing 11243 acoustic devices on the distribution network. The test was a success as 728 leaks were found over the course of the two year period and the amount of water saved totalled  $2.385 \times 10^6 \text{ m}^3$ .

Acoustic leak detection is a powerful tool which can be used for structural health monitoring to detect pipeline leaks. Its shortcoming, however, is that it is not a distributed sensing method, but relies on acoustic signals registered at discrete points. The interference due to noise surrounding the operation of pipeline can hinder an acoustic leak detection system's ability to detect a leak signal, leading to the need for more specialised equipment and highly skilled personal to interpret the data output. In addition all sensors need to be connected to a network of electric cables to be monitored.

## **2.5 FIBRE OPTIC CABLES AND DISTRIBUTED SENSING**

### **2.5.1 FIBRE OPTIC BASICS**

Fibre optics is the science of the transmission of light through very fine glass or plastic tubes/fibres (Curran and Shirk, 2018). Fibre optics are primarily used to transfer information over long distances by converting electrical information into an optical signal, which can be conveyed through the glass or plastic fibre. Fibre optics are readily replacing copper as a primary communication medium due to the major advantages that optical fibres have over copper with regard to information carrying capacity.

Optical fibres have very high bandwidth, allowing them to carry a vast array of signals at once. Multimode optical fibres have bandwidths that range between 200 and 600 MHz-km, whereas electrical conductors, such as copper, have bandwidths in the range of 10 to 25 MHz-km. Single mode optical fibres offer even greater bandwidths, being greater than 10GHz-km. Another massive advantage that optical fibres have over electrical conductors is their immunity to electromagnetic (EM) interference. Electrical conductors convey their signals using the flow of electricity. This electrical flow is prone to disturbance from EM radiation due to the nature of the negatively charged electrons which constitute the flow of electricity. In optical fibres, however, the information is carried as light, which is unaffected in the presence of EM radiation near the optical fibre. In addition, optical fibres do not emit any form of radiation while they are operating, unlike electrical conductors.

Optical fibres are also much smaller and compact than electrical conductors. Optical fibres are so proficient at carrying information that an optical fibre cross section requires only a fraction of the cross section of an electrical conductor to achieve the equivalent information transfer capacity. FO cables are therefore small in size, light weight, and because they are made of glass or plastic, are much cheaper than electrical conductors. Their low signal attenuation allows them to carry light signals over long distances without the information contained therein getting lost.

The light signal carried by optical fibres does however attenuate as the light travels through the fibre. This is because the light signal is constantly being reflected within the fibre and each reflection results in an energy loss. To achieve minimum attenuation of the light signal, optimal wavelengths which provide minimum attenuation of the signal are used to transfer the information. These wavelengths have been experimentally determined to be 850nm, 1300nm and 1550nm. The relationship between attenuation of an optical signal and its wavelength is depicted in Figure 2.1.

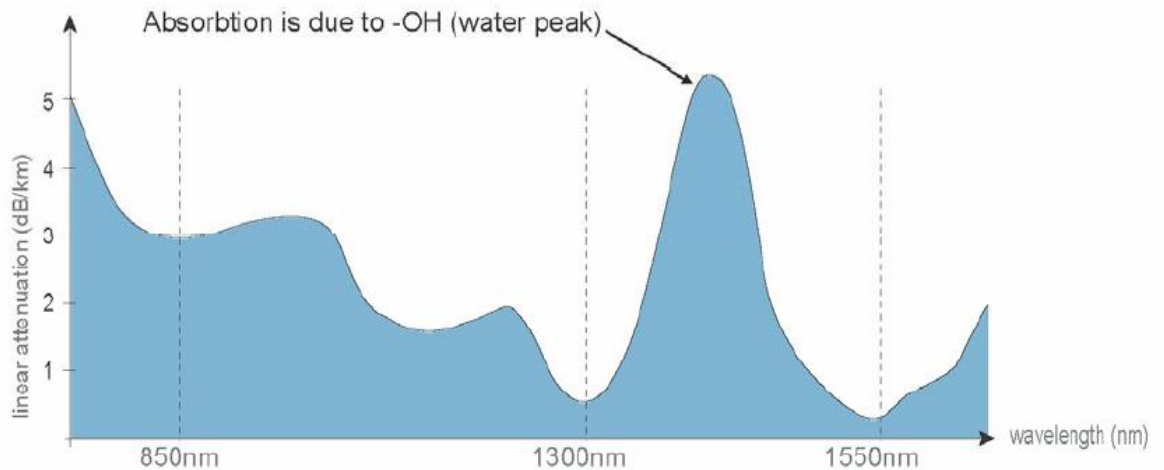


Figure 2.1. Linear attenuation of an optical signal as a function of the light signal's wavelength. Taken from Curran and Shirk (2018).

Optical fibres are themselves fragile due to the fact that they are extremely thin and made of glass or plastic. They are therefore constructed into fibre optic (FO) cables. The FO cable is constructed into a structure consisting of concentric layers. The innermost layer of the FO cable is the core. This is the light transmitting region of the fibre, made of either silica or doped silica, and is fragile if unprotected. The next layer around the core is the cladding. The cladding is also made of silica, although it is not the same silica as that of the core. The reason for the difference in the core and cladding silica is so that their refractive indices can differ from each other (the refractive index of a material is the ratio of the velocity of light in a vacuum to the velocity of light in the specified medium). The cladding performs the job of an optical wave guide by confining the optical signal using total internal reflection at the core-cladding interface. The lower refractive index of the cladding traps the light signal, forcing it to propagate along the length of the optical fibre. Hence, the cladding prevents any light from escaping from the FO cable and also prevents unwanted light from entering in.

The coating is placed over the cladding. This is the first non-optical layer around the cladding and is comprised of one or more layers that protects the optical fibre from physical or environmental damage. Lastly, the buffer, or sheath layer protects the optical fibre from being damaged during installation. The most stressful part of a FO cable's life is the installation process. It is therefore necessary that a strong protective layer keeps the optical fibre contained within the FO cable from being broken, which would render the FO cable unusable.

There are various construction configurations used to make FO cables. Some of these configurations include tight buffered, loose tube/gel filled cables. Tight buffered (TB) cables have a nylon, or similar material, strength member running along the length of the FO cable to provide resilience to the FO cable. The deformations that are felt by the sheath of TB cables are transmitted into the optical fibres themselves. However, these deformations, if the cable is handled properly, are far below those needed to damage the optical fibre housed inside the cable. Loose tube and gel filled cables are constructed so

that the stresses imposed onto the sheath do not get transmitted to the optical fibre. This is achieved by having the optical fibre surrounded by a gel matrix, which mitigates the frictional forces that occur between the sheath and the optical fibre coating.

The components required in the operation of a FO cable are an optical transmitter, an optical fibre, connectors, and an optical receiver. The optical transmitter is the device that renders, or converts, an electrical signal into an optical signal to be injected into the optical fibre. The optical receiver is the device that converts the optical signal back into an electrical signal. The electrical to optical signal conversion is performed in both the transmitter and the receiver by a photodiode. The optical transmitter and the receiver need to be able to encode and decode the signal with the same encoding scheme, otherwise the light signal will be meaningless when it reaches the optical receiver. Connectors are required to plug the FO cable into the optical transmitter and receiver. These connectors are constructed with high precision as the transmitter and receiver need to input and receive signals from fibres with tubes that are as small as 9 $\mu\text{m}$ .

## **2.5.2 FIBRE OPTIC SENSING TECHNOLOGY**

In the early 1970s the first experiments were done on low-loss optical fibres for use as measuring sensors (Grattan and Sun, 2000). FO cables are able to both sense the measurand they are measuring and transmit the measured data via the same wavelength. Thus, the need for a measuring instrument and a data sender and receiver becomes redundant as the FO cable acts as both (Motil et al., 2015). Due to their compact, lightweight structure, their ability to be multiplexed effectively on a single fibre network, and their durability to survive in harsh, punishing environments makes FO cables very attractive sensors for measurement.

Sensor devices that utilise FO cables discriminate in the spatial mode, and with this, measurements can be made along the length of the optical fibre (Grattan and Sun, 2000). This is termed “distributed sensing”, and is employed widely in the measurement of temperature and strain, using non-linear backscattering effects in optical fibres. The ability to make distributed measurements on extended civil structures is of increasing importance, given the complexity of the structures that are being constructed today.

One technique that distributed sensors operate on is optical time domain reflectometry (OTDR) using the method of location of local loss in the fibre. This technique was first used for fault detection, but thereafter it evolved into a measurement technique. Knowledge of the propagation time of a pulse at a particular wavelength along a fibre of specific refractive index enables the position of interaction to be located. This is used for sensing purposes to determine the measurand perturbation on the fibre.

The development of distributed FO sensor systems relies on the employment of methods, which are well-established and reproducible, by which a measurand can interact with the light travelling in the fibre core. These methods make use of the non-linear effects that occur in the optical fibre silica that exhibit varied and distinctive responses to external disturbances that act upon an optical fibre. The most

popular approach uses backscatter of light in the optical fibre that has different properties to the light that is injected into the optical fibre. The three main backscattering techniques used are Rayleigh, Raman and Brillouin backscattering. Rayleigh backscattering is used to detect vibrations in an optical fibre and thus is used for distributed acoustic sensing (DAS) (Tanimola and Hill, 2009). This acoustic sensing is not to be confused with the acoustic measurement devices discussed in Section 2.4.2.1. Raman backscattering is used in temperature sensing systems as Raman backscatter is insensitive to optical fibre strain. Lastly, Brillouin sensing is used to measure both temperature and strain simultaneously.

Backscattering is popular due to the advantages that it holds over other measurement techniques. The spatial resolution to which measurements can be made using backscattering is very fine, with only a few centimetres separating two consecutive measurement points. Backscattering techniques also provide very sensitive measurement capabilities, being able to measure even small changes in external disturbances that act upon the optical fibre. This furthermore makes FO sensing even more attractive for structural health monitoring (SHM), as the fine spatial resolution and the high sensitivity allow for close monitoring of structural behaviour. The downside to measurement using backscattering is the low signal due to non-linear coefficients in silica. The low signal requires many backscattering iterations to be performed and then combined to formulate the measurement result along the length of the fibre. The need for multiple iterations and the time taken for the compilation of the output, results in a long system response time for a single measurements to be made (Grattan and Sun, 2000).

### **2.5.2.1 ELECTROSTRICTION, ACOUSTIC PHONON DEVELOPMENT AND BACKSCATTERING**

When the optical power of the light passing through an optical fibre overcomes a given power threshold, non-linear phenomena occur (Galindez-Jamioy and Lopez-Higuera, 2012). The interaction between an EM wave (light) and matter generates variations in the molecular structure of the material over which the light passes. The incident light wave generates acoustic waves, modulations in the density of the material through the electrostriction effect. Electrostriction is the densification of a material in the presence of an EM field. The acoustic waves in the material result in a periodic modulation of the refractive index of the material due to the modulation in the material density.

As a consequence of the elasto-optic effect, these optically induced acoustic waves act as moving refractive index (Bragg) gratings (Motil et al., 2015). The regions with altered refractive indices in turn, like Bragg gratings, reflect light backward in the opposite direction to the original optical signal. This reflected light is the backscattered light, and is reflected back with a downshifted frequency due to the Doppler shift associated with the gratings moving at the acoustic velocity of the optical fibre material.

This scattering process can only occur if the intensity of the light can locally modify the density of the solid. The material must be able to absorb part of the energy from the electromagnetic wave and generate the periodic acoustic phonon structure. In addition, there must be sufficient energy left over for the generation of the downshifted backscattered light.

### **2.5.2.2 BRILLOUIN BACKSCATTER IN FIBRE OPTIC SENSING**

The research conducted in this study made use of Brillouin scattering in FO cables. Therefore, a detailed explanation is given of the Brillouin backscattering process, but Rayleigh and Raman backscattering will not be discussed in detail. It is important for the reader, however, to be aware that other backscattering techniques, besides Brillouin backscattering, exist.

When a section of fibre is strained, either due to an applied mechanical stress, or by thermal expansion or contraction, the physical length of the fibre changes and the refractive index along the strained section is altered (Motil et al., 2015). This alteration has a direct impact on the phase of optical wave propagation in the fibre, which can be measured to quantify the strain that the optical fibre has undergone. In addition, the applied strain also affects the speed of sound in the fibre due to a slight change in the silica density, which affects the speed of the acoustic phonons that develop.

In the non-linear Brillouin backscattering process, acoustic phonons scatter a forward propagating optical wave into a backward propagating wave. The forward propagating wave is termed the probe wave, and the backward propagating wave is termed the pump wave. The light that is backscattered from this interaction between the pump and the probe wave has a characteristic frequency shift from that of the pump wave. This frequency shift is termed the Brillouin Frequency Shift (BFS). The BFS lies approximately in the range of 10-11 GHz, using an incident light wavelength of 1550nm.

The BFS of the optical fibre material is a function of the acoustic phonon, medium structure and constituents of the optical fibre. These are in turn altered by perturbation from the external environment, temperature and strain effects (Galindez-Jamioy and Lopez-Higuera, 2012). The BFS is therefore a function of the mechanical strain state and temperature of the optical fibre. These measurands, however, cannot be measured independently. To separate the strain and temperature components measured by the BFS, temperature must be quantified concurrently and independently by a temperature measuring instrument. Because the BFS is a measure of an optical fibre's instantaneous strain and temperature state, if the BFS is known beforehand subsequent readings can be compared to previous readings to determine the change in strain and temperature state of the optical fibre. As a distributed sensing technique, the BFS can sense along FO cables that extend up to 100km with centimetric spatial resolution (Motil et al., 2015).

There are two methods in which Brillouin scattering can be invoked: spontaneous Brillouin scattering and stimulated Brillouin scattering.

Stimulated Brillouin scattering is invoked by injecting two light waves, a pump and a probe wave, into opposite ends of an optical fibre. These counter propagating light waves create the moving optical intensity pattern at the points where they interfere with one another, caused by the electrostriction effect. The electrostriction of the optical fibre material creates an acoustic wave that travels in the same direction as the pump wave, as shown in Figure 2.2. These induced acoustic wave Bragg gratings reflect the downshifted light back to be read by the measuring instrument, called an interrogator. , However,

due to the need for light to be injected into both ends of the optical fibre, the total length of fibre, comprising the loop extending from and back to the interrogator, can extend up to 100km in total. Thus the farthest measurand that the FO cable can measure is 50km away from the interrogator. Stimulated Brillouin scattering is a very attractive distributed sensing technique due to the low threshold power needed to induce acoustic phonons and acquire backscatter and the high conversion efficiency giving the method high sensitivity (Jiang et al., 2020).

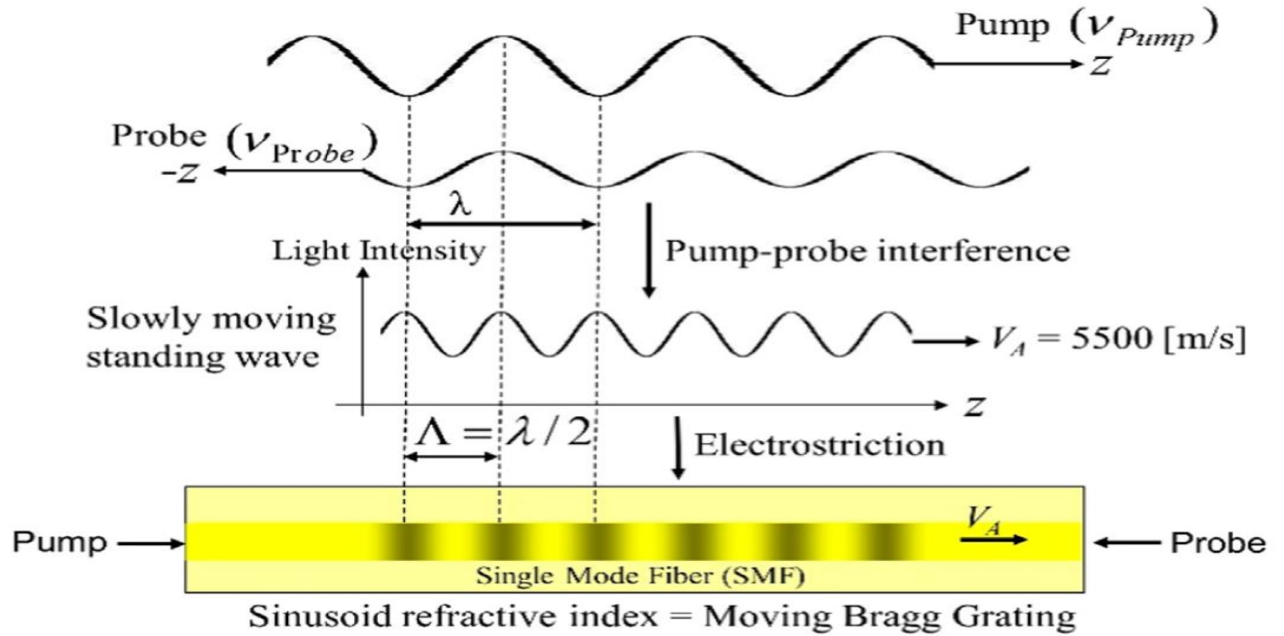


Figure 2.2. Acoustic phonon development in an optical fibre invoked by the Stimulated Brillouin technique. Taken from Motil et al. (2015).

Spontaneous Brillouin scattering utilises only one incident light wave that is injected into one end of the fibre. This light wave interacts with the thermally initiated acoustic waves, caused by electrostriction, which function as the Bragg gratings. The backscattered light is again reflected and downshifted by the acoustic waves propagating in the direction of the incident light wave. As only one end of the fibre is injected with an incident light wave there is no need for an optical fibre to form a closed loop to return back to the interrogator. Thus the maximum usable length, 100km, of a FO cable can be used for sensing. The trade off, however, is that Spontaneous Brillouin backscattering is less sensitive than Stimulated Brillouin backscattering.

### 2.5.3 STRUCTURAL HEALTH MONITORING USING FIBRE OPTICS

Optical fibre sensing has become popular and has been employed in an array of civil engineering SHM applications (Zheng, 2020). These include the monitoring of deformation of bridges under traffic loading, measuring the displacement of railways under trains, assessing the ground movement of geotechnical structures, and early warning systems for leaking pipes that carry both gas and liquids (Galindez-Jamioy and Lopez-Higuera, 2012). The primary goal of SHM is to assess structures for deteriorations, damage, and to predict occurrences such as collapses in geotechnical structures (Cheng-

Yu et al., 2017). SHM is thus a powerful tool to ensure the structural integrity, stability and reliability of structures and to prevent disastrous failures of structures.

### **2.5.3.1 FIBRE OPTIC LEAK DETECTION**

Pipeline monitoring, instead of monitoring the pipeline structural integrity to prevent pipeline failures, searches for pipeline failures so that they can be remedied. Physical or chemical properties surrounding the pipeline are monitored, such as soil temperature and strain, or the air temperature around a suspended pipe, to determine if a pipeline has developed a fault (Ren et al., 2018). Once a change has been detected, an alarm is triggered and the exact location of the change is determined, revealing the leak location (Tanimola and Hill, 2009).

Fibre optic leak detection is superior to acoustic leak detection because the pipeline is being continuously monitored along its entire length instead of at discrete points (Tanimola and Hill, 2009). The FO cables are non-obtrusive to the appearance of a working pipeline, and their installation requires no shut down of the working pipeline.

By utilising the sensitivity of FO cables to variations in temperature, strain and vibrations, regions where gas or fluid are escaping a pipeline can be detected. There are various ways that fibre optics can be employed in leak detection applications. As previously discussed, when substances leak from a working pipeline, they cause acoustic vibrations to travel through the pipeline. These vibrations can be detected by a FO cable being interrogated by a Rayleigh backscatter interrogator. In addition, the FO cable can detect the acoustic signal at the source, instead of requiring two acoustic listening devices to locate the leak using the cross correlation method. Tanimola and Hill (2009) reported that DAS, using Rayleigh backscatter, can successfully detect leaks to within 1-10m and with more certainty than that of acoustic cross correlation.

The properties of the fluid or gas escaping from a pipeline, in relation to the external environment, can also be used to detect a pipe breach. The Joule-Thompson effect states that the temperature of a fluid or gas travelling through a pipe under confined pressure is normally lower than the temperature of the immediate surrounding environment. Thus, fluid or gas escaping a pipe breach will induce a drop in the temperature of the FO sensing cable. This drop in temperature can be measured using either Raman or Brillouin backscatter to reveal the location of an existing leak (Zou and Landolsi, 2014).

Pipeline pressure variation can also be measured as a means of leak detection. Direct pressure exposure, which does not necessarily need to be in the lateral direction, induces changes in the optical fibre properties (Schenato et al., 2020). This can be utilised in hydraulic transient based leak detection techniques. Hydraulic transient leak detection is performed by introducing an incident pressure wave into a pipeline, which is reflected back to the source by physical anomalies such as leaks and deteriorated pipe sections (Zeng et al., 2020). An in-pipe FO sensor array can be used for hydraulic transient measurement to successfully detect leaks, as has been demonstrated by Gong (2018).

A new and promising method of underground pipeline leak detection, proposed by Jacobsz and Jahnke (2020), is to instrument a pipeline by burying the FO cables in the soil adjacent to the pipeline. Due to the characteristics of water-soil interaction, a leaking pipeline is able to induce significant changes in effective stress in the soil surrounding the pipe, which results in ground deformation. The leaking water will also typically have a temperature that differs from the surrounding soil in which the FO cable is buried. By monitoring for soil deformations and temperature changes simultaneously, using Brillouin scattering, a sensitive and robust leak detection method can be formulated.

Due to the low cost and ease of installation and the resilience of FO cables, leak detection using FO sensing is considered a potentially economic, user-friendly and effective method of pipeline protection. The FO sensing interrogator, however, can be costly, and is sensitive to small particles entering the FO input plugs. Careful installation of an interrogator is required and thorough cleaning of the plugs before use is necessary.

## **2.6 SUMMARY**

Billions of m<sup>3</sup> of water are leaked from pipeline networks worldwide every year. Much of the leaked water escapes from pipelines that are buried underground and therefore these leaks cannot be detected by visual inspection. The loss of water results in great financial losses to the water utilities that are supplying purified water which is borne by the water utilities' end users. Leak points of underground pipelines also pose a threat to infrastructure, as the soil bearing the infrastructure has the potential to collapse or change volume due to increased soil moisture content. Breaches in pipelines are also prone to contamination via ingress of external contaminants that enter pipelines in negative pressure states. All of these factors negatively affect the communities making use of water utilities and the reduction of water loss and repair of pipeline failures would benefit all the affected parties.

There are an array of pipeline leak detection methods which can be implemented in a pipeline protection programme to mitigate water loss. Both active, labour-intensive methods and passive, highly sophisticated measuring instrument dependent methods exist. With the advent of FO distributed sensing becoming popular and widely available, pipeline monitoring systems incorporating fibre optics to sense for pipe leaks are being researched and are showing great promise as leak detection systems.

There is a well-established relationship that soil shares with water. The water content of a soil plays a role in determining its volume characteristics and the strength that a soil can generate. In addition, water being added to a soil medium is likely to have a different thermal signature to the soil it is being added to. This volume change and temperature alteration due to the ingress of water into soil can be exploited to develop a pipeline leak detection system. Using Brillouin backscattering, by monitoring for changes in BFS, caused by strains and temperature change in soil near operational pipelines, locations along operational pipelines where leaks are gushing out water can be determined. Thus a sensitive BFS pipeline leak detection system can be developed using the interaction between water, soil and FO cables.

## **3 EXPERIMENTAL SETUP**

### **3.1 INTRODUCTION**

This chapter discusses the experimental setup that was created on the Hillcrest campus of the University of Pretoria to simulate the effects of water ingress through the soil surrounding a fibre optic cable buried in the ground, i.e., the environment that a pipeline would be placed into. The purpose of this fieldwork was to determine the optimal type of FO cable for use in a fibre optic leak detecting system. The FO leak detection system would operate by detecting strain and temperature changes in the surrounding soil characteristic of water ingress into the soil. If installed along a working pipeline, measurements would be made along the entire length of a FO cable buried in the pipe trench alongside the water pipe. The measuring instrumentation and the testing methodology used are presented in this chapter.

The instrumentation used included five different fibre optic cables, a BFS (Brillouin Frequency Shift) FO interrogator, and a fibre optic multi-channel four-way splitter. The five cables were buried in a trench that was 150m long, with FO cables running in both directions along the trench. The FO cables entered from the one end of the trench, turned around at the opposite end of the trench, and exited from the same end where they entered.

### **3.2 MEASURING INSTRUMENTATION**

#### **3.2.1 FIBRE OPTIC CABLES USED**

Five different fibre optic cables were used in the experimental setup to investigate which type of cable is best suited to be used as a leak detection sensor. The five different cables included four different telecommunication cables and one cable specifically designed to measure mechanical strain. The primary difference between the five cables is that each cable had a different protective sheath that houses the optical fibres contained within them. The most important difference between the classes of cables tested is that some of them were made to have the optical fibres free-sliding within the protective surround (referred to as loose core (LC) cables), while others had a tightly surrounding sheath (referred to as tight buffered (TB) cables). The five cables were:

- A 6-fibre Tight Buffered Field Deployable Cable (6F-TB)
- A 2-fibre Tight Buffered Field Deployable Cable (2F-TB)
- A BRUsens strain V9 cable (strain-TB)
- An Aerial Self Support (industrial strength) 72-fibre, 6-core cable with loose cores (72F-6C-LC)
- A 4-fibre Loose Core Dual Purpose Drop Cable (4F-DC-LC)

The 6F-TB and 2F-TB cables, see APPENDIX B, are cables designed for re-usable, temporary or mobile point to point links in military applications. The sheath housing the fibre is composed of Hytrel, a strong, flexible, cut resistant rubber like material suitable for harsh environments. The optical fibres

housed inside are surrounded by Aramid yarn to provide tensile strength. There is no gel present to provide lubrication between the sheath and the fibres. This implies that the fibres would be sensitive to external effects as the transfer of strains from the sheath onto the fibres would not be hindered. This would be advantageous in leak detection applications as a change in strain state in the soil would be imposed into the fibre via the sheath. However, this type of cable would be more prone to other unwanted disturbances, such as soil deformations caused by non-leak events that could affect the baseline behaviour of the cable.

The strain cable, see APPENDIX C, as its name suggests, is a cable specially designed to measure strain. This is done by forming close contact between the fibre and the sheath. The sheath is made of Nylon Plastic (PA) which is directly attached to a steel tube interlocked with a buffer and transfer layer the surrounds the optical fibre. Thus, any strain that is imposed onto the sheath will be transferred to the optical fibre. The strain cable is, however, not insensitive to temperature changes, as the thermal expansion and contraction of the sheath induces strains onto the optical fibre housed inside.

The 72F-6C-LC cable is a multicore cable designed for telecommunication networks with many communication channels which branch out and span over great distances. The 72F-6C-LC cable specifications are given in APPENDIX D. The structural composition of the cable is as follows: a polyethylene sheath houses and protects 6 tubes that surround a glass reinforced plastic strength member. Within these tubes there are 12 optical fibres surrounded by a lubricant. This ensures that the optical fibres are not tensioned or compressed by the movement of the sheath or tubes, altering the passage of optical signals carried by the fibres. The advantage of using such a cable is the ability to create a branched network of cables leading out from and back to the 72F-6C cable. However, the lubricant surrounding the fibres significantly reduces the transfer of longitudinal stress from the sheath to the optical fibres, which may impair the ability of the cable to perform as a leak detection sensor with regard to strain measurement.

The 4F-DC-LC, see APPENDIX E, cable is comprised of a high density Polyethylene sheath that houses 4 optical fibres surrounded by a lubricant, and Aramid yarn to provide extra tensile resistance. Like the 72F-6C-LC cable, because of the lubricant the external effects from the sheath would be expected to be less pronounced upon the fibres housed inside. However, the effects of unwanted disturbances acting on the cable would be less pronounced, which may be beneficial in establishing the baseline behaviour of the cable.

### **3.2.2 BRILLOUIN FREQUENCY SHIFT FIBRE OPTIC INTERROGATOR**

The FO interrogator used in the experimental setup was a fibrisTerre fTB series fibre-optic sensing system, see APPENDIX F. In addition, the interrogator was connected to a fibrisTerre optical fibre multi-channel splitter. Four of the five different fibre optic cables could therefore be connected to the interrogator at the same time. The interrogator model uses Stimulated Brillouin Scattering to determine

the BFS at a specific point along the length of a fibre optic cable. To perform distributed sensing, the interrogator employs Brillouin optical frequency domain analysis to create a BFS profile of the entire cable length. A software package, fTView, was used to control the interrogator and interpret the results.

The BFS profile is created as follows: the interrogator first determines the length of the cable it is monitoring by injecting an optical signal into one end of the optical fibre and measuring the time it takes for the signal to be received at the other end.

The interrogator then performs a process called a frequency sweep. In this process two optic signals (a pump and probe) of different frequencies, are injected into the optical fibre, one at each end. The two optic signals are injected into the fibre at different times so that they coincide with each other at a specific ordinate along the fibre length. When the optic signals coincide, Stimulated Brillouin Scattering occurs at that point. The downshifted light travels back to the interrogator and the BFS is logged for the specific ordinate. The interrogator repeats this process every 5cm along the cable length. The specific interrogator model used can measure BFS in a cable up to 50km in length. For an 800m FO cable the interrogation process takes between 90 and 120 seconds

The intensity of the backscattered light is dependent on the frequency difference between the pump and the probe wave. Therefore, an array of frequency differences is used, and hence the term: frequency sweep. Multiple iterations of measuring the BFS along the entire cable length must therefore be completed using the array of frequency differences. The strongest BFS response at each length ordinate is used to determine the BFS response at that length ordinate.

Once the BFS has been logged for the entire length of the cable, the interrogator sends the logged data to fTView and a BFS profile can be plotted. FTView can export BFS profiles to a text file format, which can then readily be imported into a data analysis package, such as Excel or Python.

### **3.3 FIELD SETUP**

#### **3.3.1 TRENCH**

To mimic the environmental conditions that a buried pipeline would be subjected to, a 150m trench was excavated on the University of Pretoria's Hillcrest campus, which was further divided into three 50m sections. The collection of fibre optic cables investigated in this study were laid long the base of the trench. The three trench sections were excavated to depths of 0.5m, 1.0m and 1.5m respectively. The three different depths were chosen to investigate how varying depths would affect the temperature variation experienced by each cable. Temperature variation is an important factor in establishing the baseline behaviour of a cable over time. The cables were expected to undergo more pronounced temperature variation if buried closer to the surface, and less temperature variation when buried deeper underground. The trench was backfilled without a specified compaction. An aerial view of the trench can be seen in Figure 3.1 and Figure 3.2.



Figure 3.1. Bird's eye view of the 150m trench dug on the University of Pretoria Hillcrest Campus.



Figure 3.2. Standing point view of the trench prior to installation of the fibre optic cables.

Within the three 50m segments, standpipes were inserted into the soil leading down to the level of the fibre optic cables. These standpipes served as points of introduction for water into the soil to simulate pipe leaks during the leak test phase of the experiment. Three standpipes, spaced 15m apart were installed in each of the three trench sections. These standpipes are depicted in the schematic diagram shown in Figure 3.3.

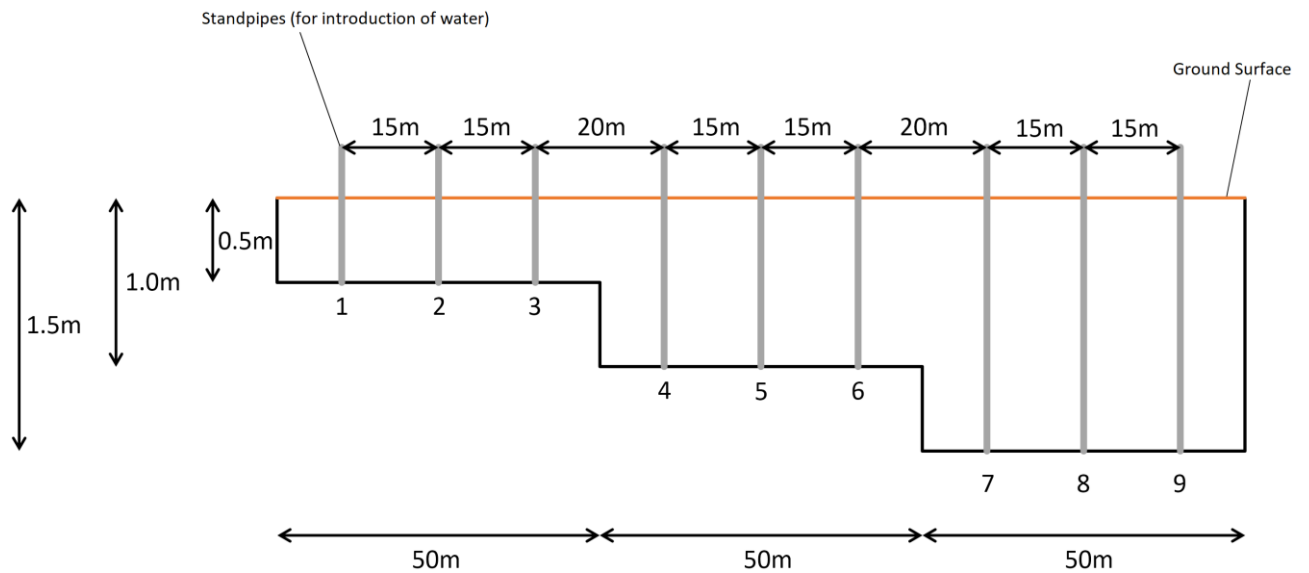


Figure 3.3. Schematic long section of the trench (not drawn to scale) depicting the three 50m segments.

The arrangement of the cables is illustrated in Figure 3.4 which shows a schematic diagram of the cables' layout in the trench.

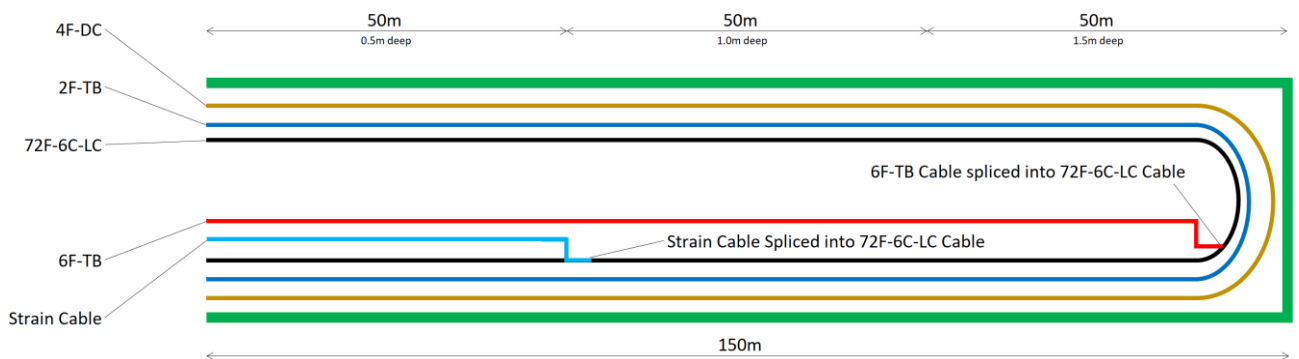


Figure 3.4. Schematic bird's eye view diagram of the trench showing the orientation of the laid cables.

As can be seen in Figure 3.4, the cables were laid along the trench in both directions, entering at the shallow end (0.5m depth), running the length of the trench to the deep end (1.5m depth), and then looping around, running back along the trench and exiting at the shallow end. The ends of the cable segments buried in the trench were spliced to a single multicore cable leading to the BFS interrogator housed in the server room of the University of Pretoria Engineering 4 building, approximately 150m away.

Due to limited availability of the lengths of the strain cable and the 6F-TB cable, 60m of strain cable and 145m of 6F-TB cable were spliced into two of the fibres of the 72F-6C-LC cable.

### 3.3.2 SOIL PROPERTIES

The soil in which the trench was dug on the Hillcrest Campus is a red clayey soil of hill wash origin. Clayey soils are highly sensitive to soil moisture content changes as they are more likely to undergo volume changes during moisture content fluctuation than coarser soil types. Therefore, they are supposedly best suited as a soil for housing fibre optic cables to be used as leak detection sensors as

clays will be able to impose greater strains onto the cables buried within them compared to more coarse-grained soils. However, expansive soils are avoided as bedding material for pipelines due to their expansive potential to impose unwanted stresses on pipelines.

A sample of the Hillcrest Campus clay was tested by SGS Matrolab, the results are given in APPENDIX A. The soil was classified as a sandy clay according to the Jennings and ASTM standards, and a clayey sand according to the British Standard. The unified soil classification given was **CL**, the soil having a liquid limit of 37% with a plasticity index of 17. The activity of the soil sample was determined to be 0.54, and thus the soil was of medium activity, and also of medium potential heave classification.

The particle size distribution of the soil is shown in Figure 3.5

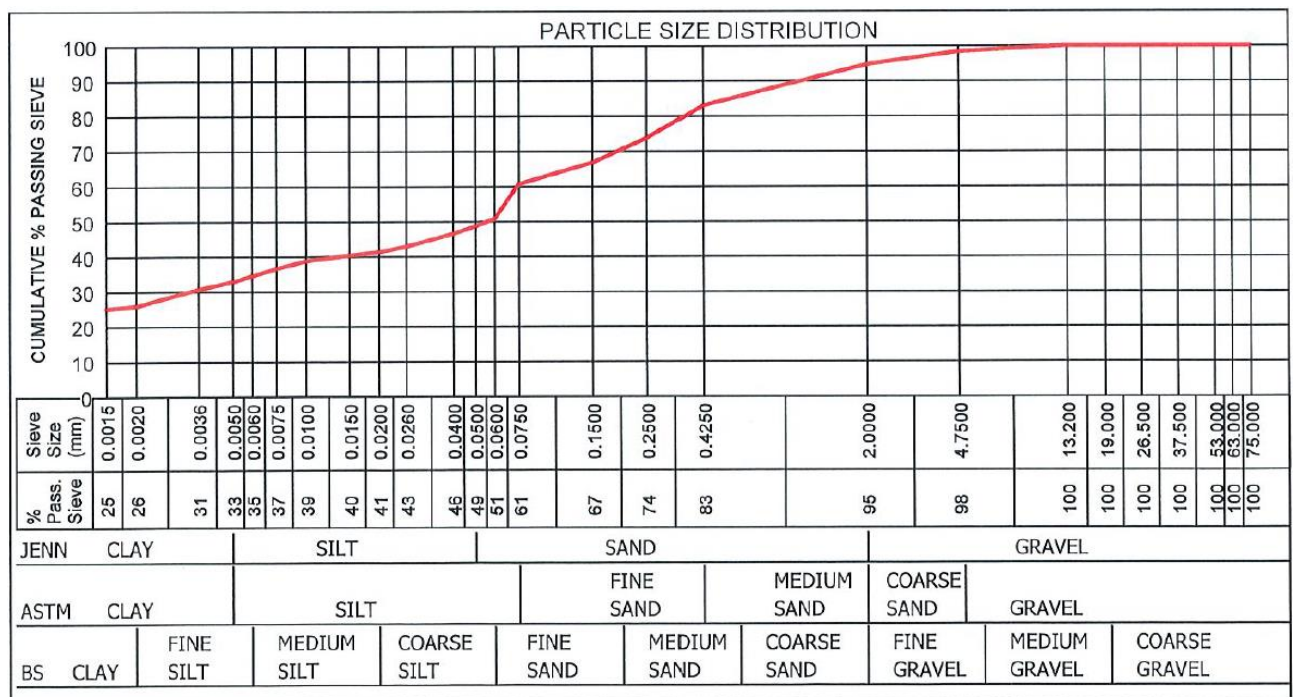


Figure 3.5. Particle size distribution for the Hillcrest Campus clay measured by SGS Matrolab.

As can be seen in Figure 3.5, the Hillcrest Campus clay is comprised of 39% particles that are smaller than 100µm. Furthermore 26% of the particles passed the 2µm sieve. This soil was therefore expected to have a high affinity for water and a change in moisture content would induce large changes in suction pressures.

To assess how the Hillcrest Campus clay’s matric suction responds to changes in moisture content, a soil water retention curve (SWRC) was measured for the soil using two tensiometers. Tensiometers are able to measure suctions within soils until the water around the tensiometers cavitates. Cavitation is the formation of vapour inside a liquid causing the static pressure of the liquid to reduce below its vapour pressure. Once cavitation has occurred suctions within the soil can no longer be measured using tensiometers. The soil water retention curve for the Hillcrest Campus clay measured using tensiometers is shown in Figure 3.6.

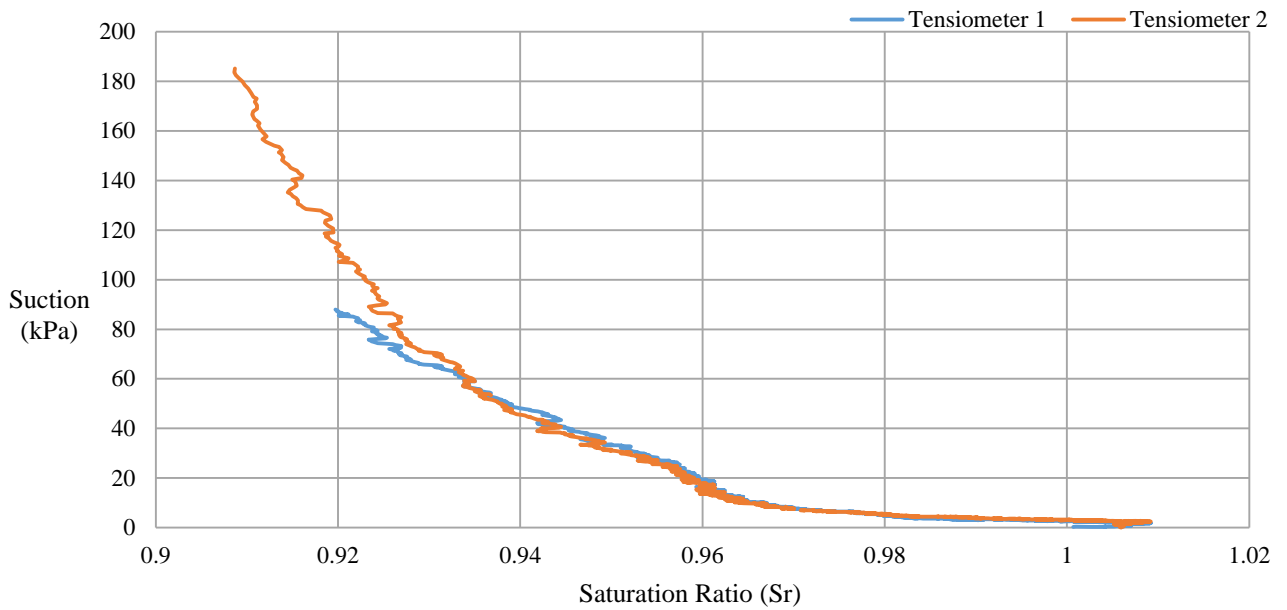


Figure 3.6. Soil-water retention curve for the Hillcrest Campus clay showing suctions measured using tensiometers.

The matric suctions in the Hillcrest Campus clay underwent a substantial suction increase before the tensiometers cavitated. Unfortunately, Tensiometer 1 cavitated prematurely as opposed to tensiometer 2. However, Tensiometer 2 measuring a suction of 185.22kPa at a saturation ratio ( $S_r$ ) of 0.908 implies that a significant amount of matric suction is experienced by the Hillcrest Campus clay even with a very small change in saturation ratio. These large suctions relative to the small change in  $S_r$  will give rise to noticeable strains with small changes in soil moisture content.

To measure the matric suctions of the soil at lower moisture contents a WP4C dewpoint potentiometer was used. A WP4C is shown in Figure 3.7.

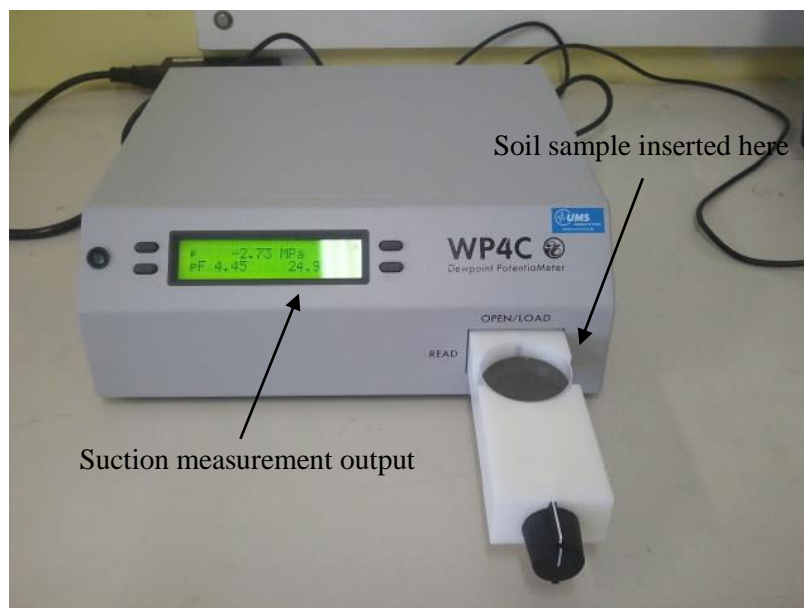


Figure 3.7. A WP4C dewpoint potentiometer.

As annotated in Figure 3.7 a soil sample is inserted into the device and the matric suction of the soil sample is measure and output to the display. The WP4C however, is only accurate at measuring suctions past 1MPa, and suctions around or just above 1MPa should be questioned. The SWRC plotted against water content ( $w$ ) of the Hillcrest Campus clay measured using the WP4C is shown in Figure 3.8.

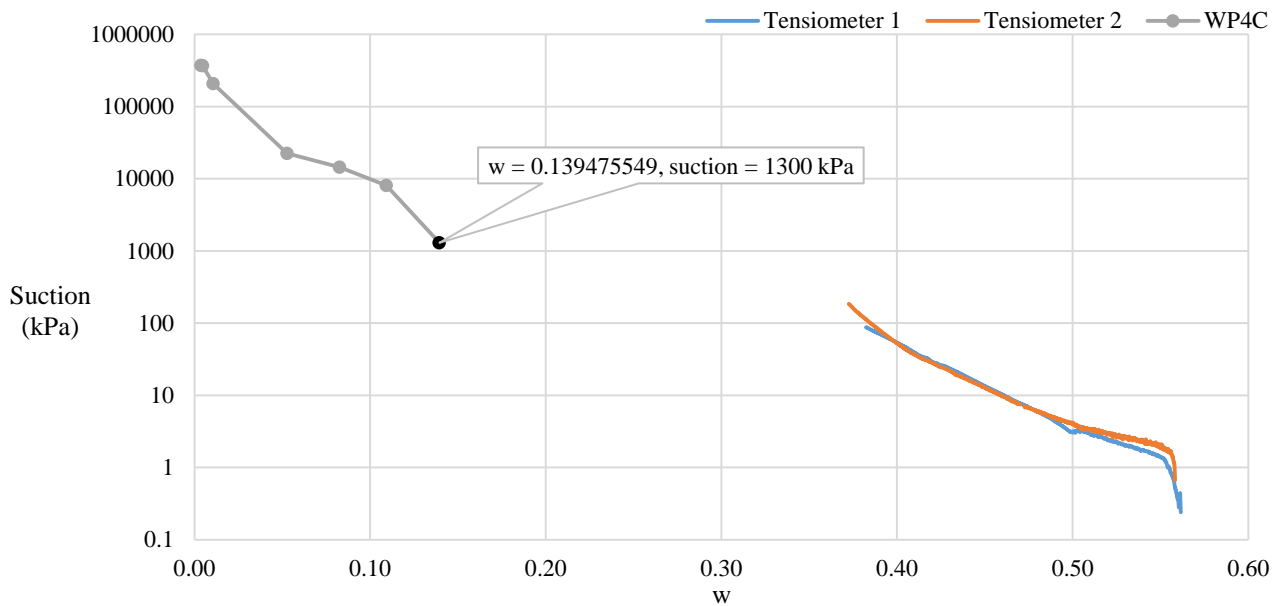


Figure 3.8. Soil-water retention curve for the Hillcrest Campus clay showing the suctions measured both by the tensiometers and the WP4C. The labelled data point is outside the region of accurate suction measurement.

The clay was generating suctions of about 10MPa at a water content of 0.1, which could cause substantial strains in the soil in-situ. The maximum matric suction of the clay at almost zero water content was measured as 370MPa, indicating that the Hillcrest Campus clay has a high affinity for water.

### 3.3.3 FO INSTRUMENTATION OF A WORKING PIPELINE

In addition to the trench setup created on the University of Pretoria Hillcrest Campus, a pipeline in Rietondale, Pretoria was instrumented with a length of 2F-TB cable. The FO cable was installed along a new pipeline that was being laid, thus the pipeline had never been operational before the FO cable was installed. A bird's eye view of Rietondale is shown in Figure 3.9.

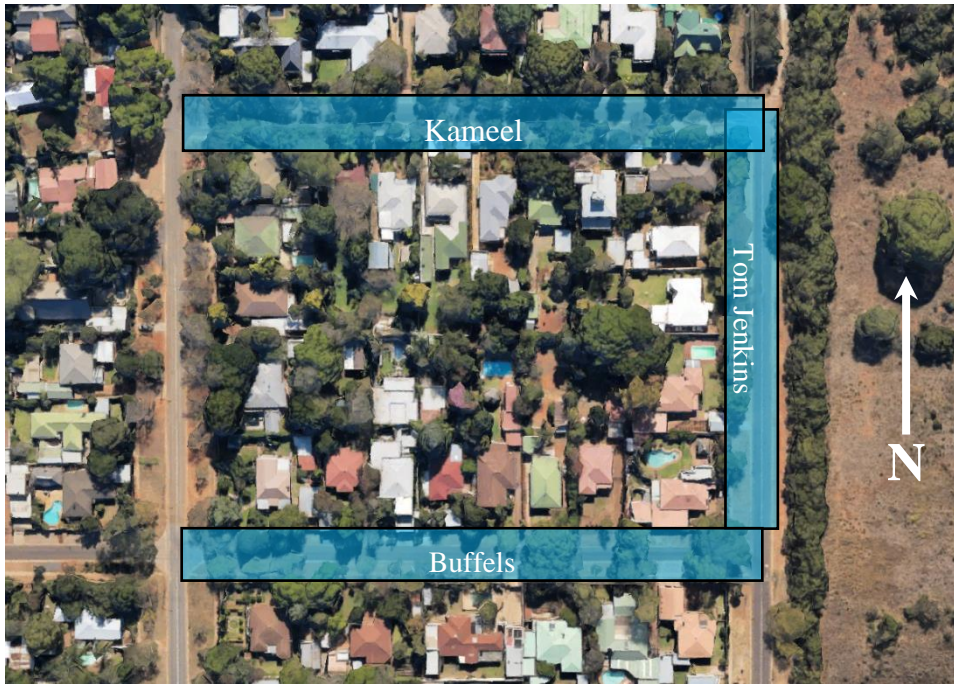


Figure 3.9. A bird's eye view of Rietondale showing Tom Jenkins Drive, and the two adjacent streets, Kameel and Buffels.

The FO cable was laid along a pipeline being installed in Tom Jenkins Drive as depicted in Figure 3.10.



Figure 3.10. Bird's eye view of Rietondale showing the region where the FO cable was laid.

The FO cable type used was the 2F-TB cable. This cable was chosen due to it being both strain and temperature sensitive to maximise the leak detection potential during the experiment. The cable was placed just next to the pipeline as can be seen in Figure 3.11.



Figure 3.11. Photograph showing the position of the FO cable relative to the laid pipeline.

To complete the installation along Tom Jenkins Drive, five artificial leak points were installed leading down to the level of the FO cable as shown in Figure 3.12



Figure 3.12. Photograph of one of the standpipes leading down to the level of the FO cable installed along the pipeline laid in Tom Jenkins Drive.

The BFS interrogator was hosted by one of the residents living in Tom Jenkins Drive. A section of FO cable 60m long was drawn from the pipeline into the residence and connected to the interrogator.

### **3.4 ARTIFICIAL LEAK TESTS**

To simulate a leak, water was required to be introduced into the experimental trench down to the level of the FO cables shown in Figure 3.4. The standpipes installed in the trench were used for this purpose, depicted in Figure 3.3, extending to the bottom of the trench (the level of the FO cables) for each 50m segment.

Three tests were performed on the FO cable trench setup, each to investigate a different aspect of the system. The first test involved the introduction of a volume of 50L of water down standpipes: 1, 4, and 7 at a known time. The results of this test were used to confirm that the FO cables were indeed able to be used to detect the introduction of water via the standpipes by giving a measurable system response. Using three different standpipes from each segment ensured that each different depth segment was tested so that the influence that depth has on the detectability of leaks could be assessed. No set flow rate was used as only a change in soil moisture content was required.

The second test was conducted as a blind leak test. In other words, water was introduced into the trench by an independent party, but the time and the location of the introduction was unknown. Again, 50L of water was used for the test, but only a single standpipe had water introduced into it. This goal of this test was to determine whether a leak could be found without knowing the time of the test and the location of occurrence.

The third and fourth tests that were performed was a prolonged leak test. In the first and second leak tests the volume of water used was a finite volume of 50L. In the third test, conducted between 27 May and 3 June, and fourth test, conducted between 5 August and 12 August, water was introduced into standpipe 5 and standpipe 2, respectively, at a constant flow rate of 40L/hour for 7 days from a tap next to the trench. As a leaking pipe constantly discharges water, this condition of a constant flow rate is more representative of a real-world leaking pipe scenario.

The method of water introduction was through the use of an irrigation pipe above ground. Water distribution pipes are buried below ground and are thus shielded against ambient air temperature changes. The use of a pipe above ground means that the water flowing into the standpipe would be influenced by the ambient air temperature change, giving rise to daily water temperature fluctuations.

The leak test conducted at Tom Jenkins Drive followed the same procedure as the prolonged leak tests. Water was introduced into one of the five standpipes at 40L/hour for 7 days and the response that the FO cable produced was assessed thereafter.

## 4 EXPERIMENTAL RESULTS

### 4.1 INTRODUCTION

This chapter discusses the results of the various tests that were conducted throughout the period of the study. This includes a discussion of the output that the BFS interrogator gives when reading a FO cable and how those readings are processed. An explanation of the baseline behaviour of the BFS that occurs inside the optical fibres is given and the results that were obtained from the conducted tests are discussed.

### 4.2 FIBRE OPTIC BFS BASELINE BEHAVIOUR

The baseline BFS field data, its analysis and the findings thereof are required to be understood so that subsequent analysis of the test results can be correctly interpreted. An overview of the output from the BFS interrogator is presented and thereafter an interpretation and method of analysis of the output are developed. The analysis method discussed here is focused on establishing the baseline behaviour of a FO cable buried underground.

#### 4.2.1 OUTPUT FROM THE BFS INTERROGATOR

A typical output of the BFS interrogator is shown in Figure 4.1.

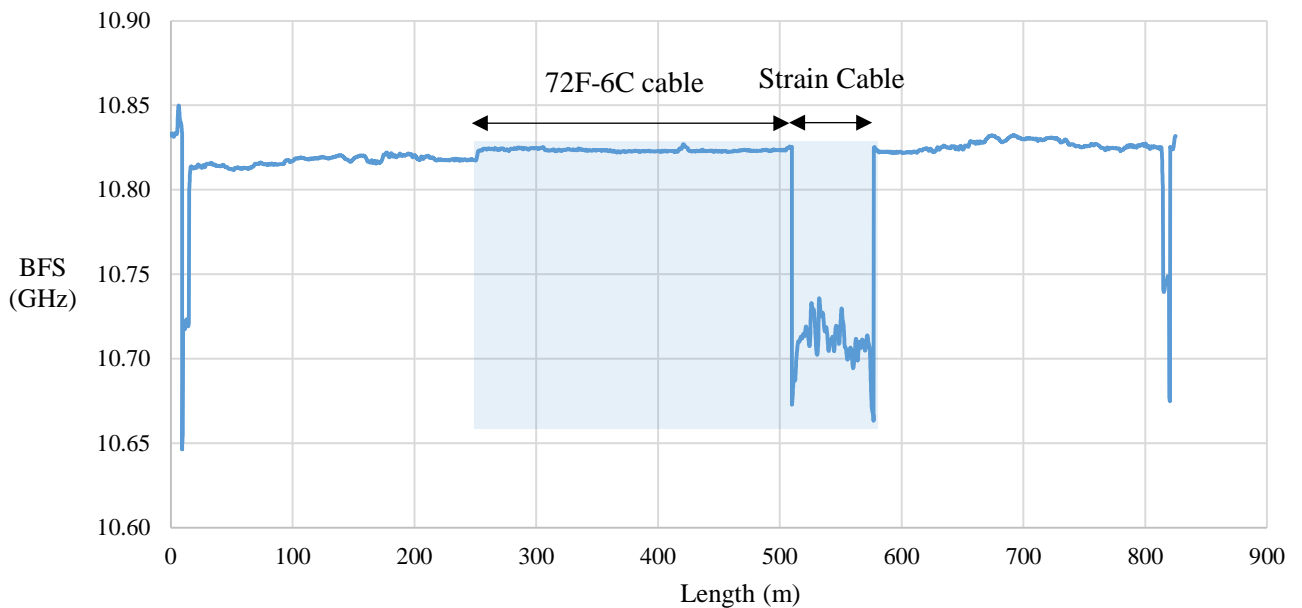


Figure 4.1. BFS profile of the cable with the 50m segment of strain cable spliced to it. The segment of the cable buried in the trench is highlighted by the blue rectangle.

The profile in Figure 4.1 shows the BFS in Giga Hertz (GHz) measured along the length of the optical fibre at a moment in time. In each BFS plot discussed in this report the midpoint of the profile corresponds to the location where the cable was looped about 180° at the end of the deep end (1.5m) of the trench. The section of the FO cable shaded in blue represents the part of the cable buried in the trench. The remainder of the profile flanking the trench represents the communications cable linking the

cable in the trench to the interrogator which was housed in the server room of the nearby Engineering 4 building. Only the section shaded blue is therefore relevant in this study.

Each BFS profile logged for a given optical fibre at different times is dissimilar, due to fluctuations in ambient temperature around the cable. This phenomenon is demonstrated in Figure 4.2, where two BFS profiles registered 12 hours apart are shown together.

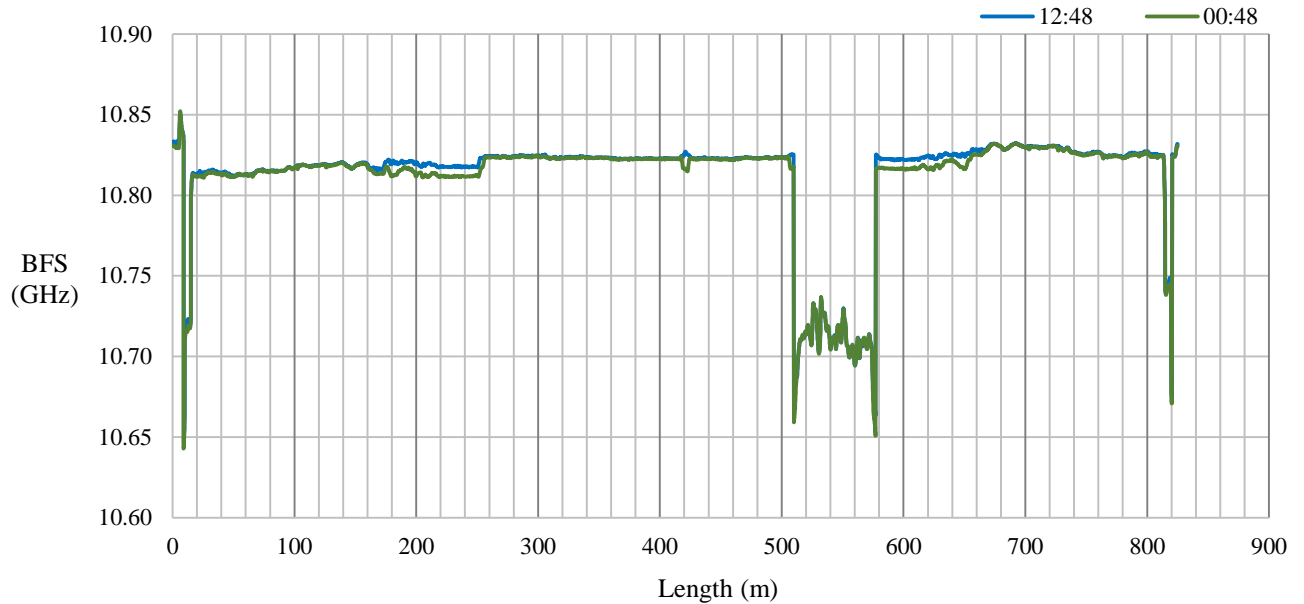


Figure 4.2. Two BFS profiles taken at two different times during the day for the same cable showing how temperature variation affects the BFS output.

In Figure 4.2 the two profiles seem to lie one on top the other for the majority of the profile, except for the two instances seen around 200m and 600m. The difference between the two profiles can be more explicitly seen by subtracting one profile from another. Figure 4.3 shows a plot of the difference between the two profiles plotted in Figure 4.2, namely the 00:48 profile subtracted from the 12:48 profile.

The two regions in Figure 4.2 and Figure 4.3 where the difference between the profiles was pronounced are segments of the cable which are surrounded by air and not by soil, as the temperature fluctuations in ambient air are greater than the temperature variations in soil. The segments at the sides of the profiles correspond to sections that are running in underground ducts leading to the server room housing the BFS interrogator, but are not part of the area of interest.

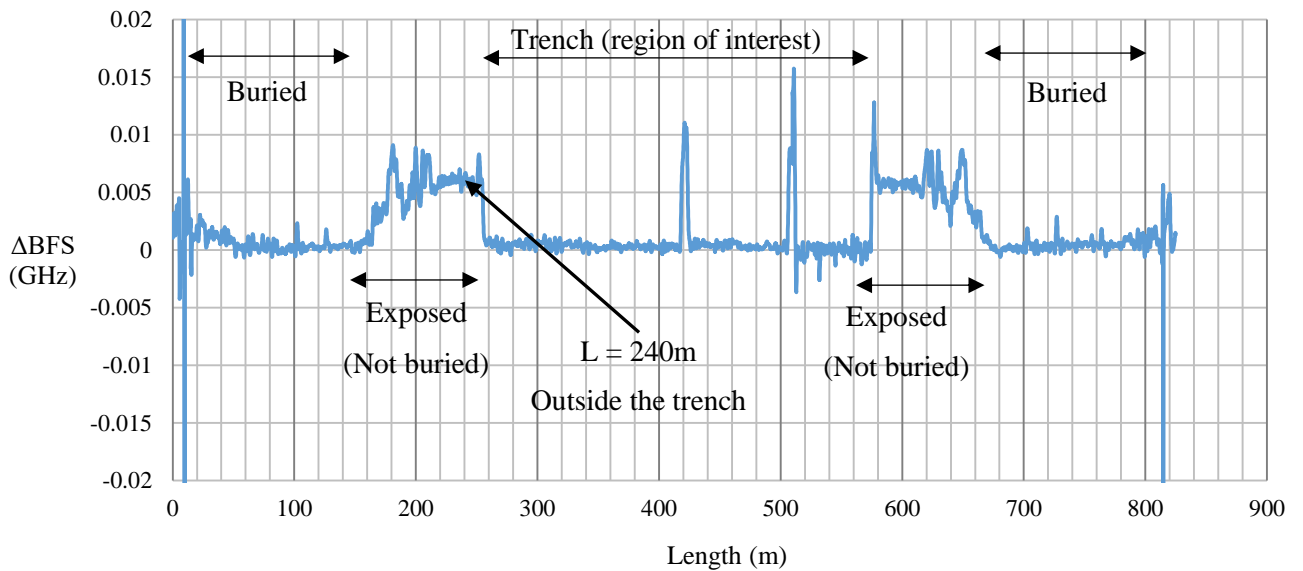


Figure 4.3. Difference between the two BFS profiles plotted in Figure 4.2.

## 4.2.2 BFS IN THE TIME DOMAIN

It was illustrated in Figure 4.2 that the BFS measured along the length of an optical fibre changes over time. In order to determine a baseline against which data from a leak test is to be compared, it is important that the fluctuation in BFS be understood for the different types of optical fibres investigated. By shifting the focus from plotting the BFS of the cable along its entire length to plotting the BFS of a specific length-ordinate in the time domain, a plot such as that shown in Figure 4.4 can be created.

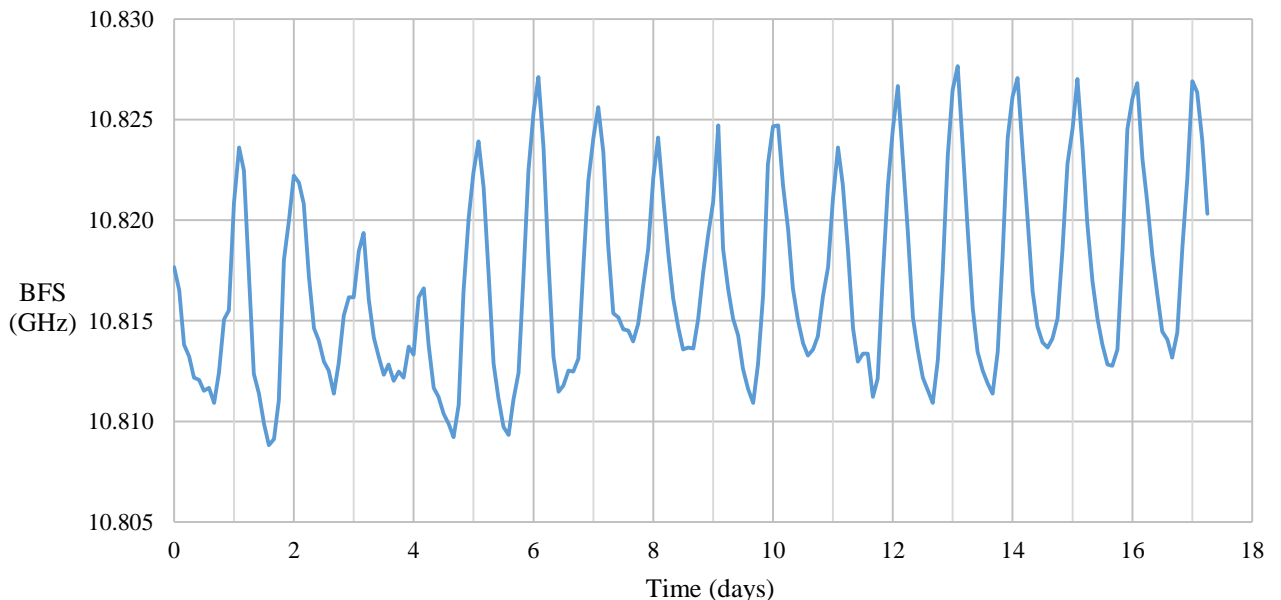


Figure 4.4. A curve of the BFS plotted against time for the length-ordinate  $L = 240\text{m}$  along the cable to which the strain cable was spliced.

The BFS vs Time curve in Figure 4.4 was plotted using the BFS readings taken at the length-ordinate  $L = 240\text{m}$  from the 72F-6C-LC cable segment outside of the trench. The variation in the BFS with time as the ambient temperature changes is an unwanted occurrence and it is useful to eliminate the variation of the BFS output.

In order to circumvent the problem of variable BFS readings, based on the ambient temperature, a moving average BFS reading with respect to time can be calculated incorporating 24 hours of the available data to calculate the average. The average BFS value as time progresses is demonstrated in Figure 4.5

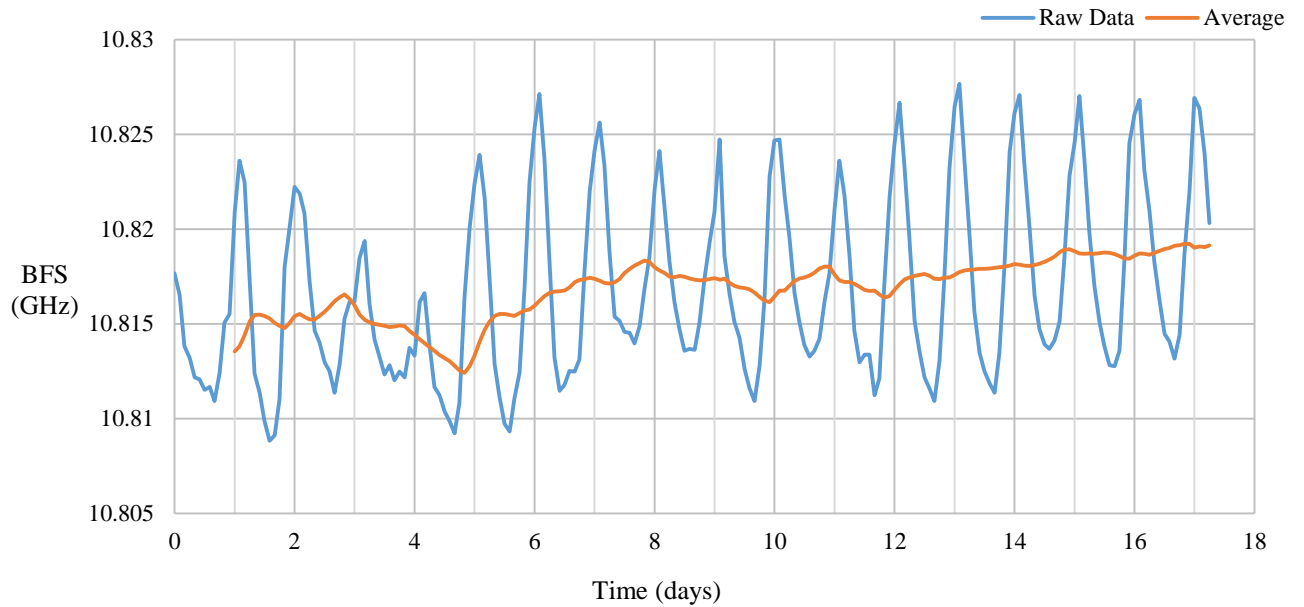


Figure 4.5. A depiction of the development of a moving average BFS value as time progresses at length-ordinate  $L = 240\text{m}$  of the 72F-6C to strain spliced cable.

The data and the development of the average BFS value shown in Figure 4.5 occur over the course of 17 days. As time progresses the moving average BFS curve is following the trend of the BFS output, but the variation in daily temperature is mitigated. Instead the moving average BFS is giving an indication of how the average temperature of any given day is varying with time.

Referring to Figure 4.3 the length-ordinate  $L = 240\text{m}$  is in the non-buried segment of the cable. This is the reason why this segment of the optical fibre shows a much greater change in BFS ( $\Delta\text{BFS}$ ) output 12 hours apart. A FO cable undergoes greater temperature variation when it is in an air medium above ground as opposed to being underground. The soil lying 0.5m below the ground will undergo less temperature variation than the environment at ground level because it is protected from the ambient temperature change by 0.5m of soil. This is demonstrated in Figure 4.6, showing BFS profiles recorded at 280m (0.5m depth), 340m (1.0m depth) and 400m (1.5m depth) in the 72F-6C-LC cable and in the strain cable at 530m (0.5m depth) respectively.

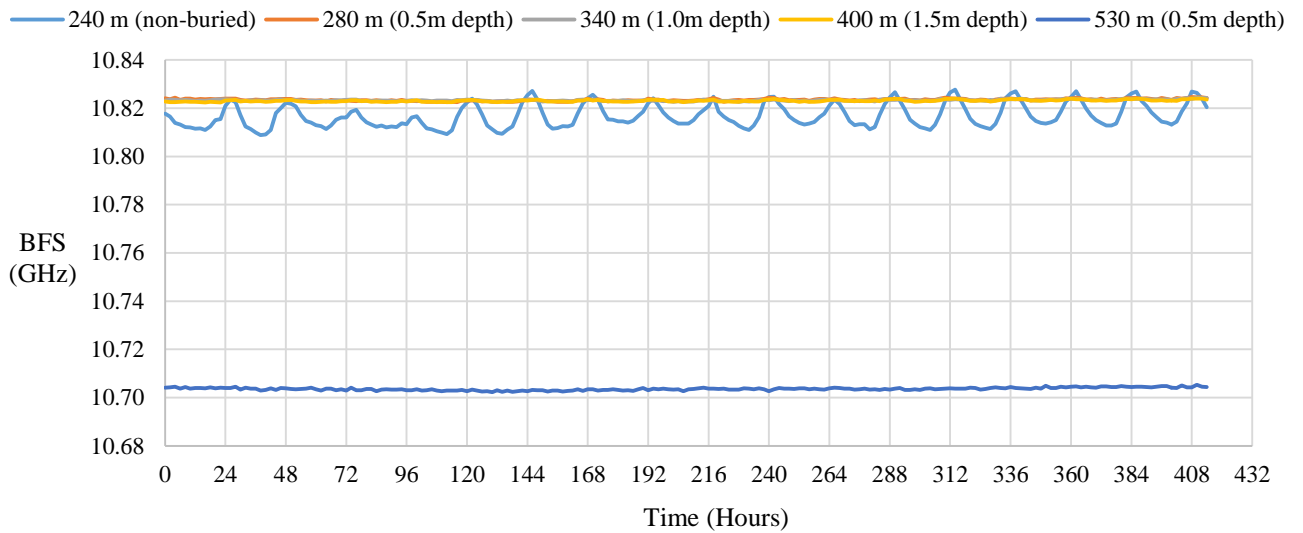


Figure 4.6. BFS vs time plot of the 72F-6C to strain cable. Curves are plotted for length-ordinates 240m, 280m, 340m, and 400m occurring in the 72F-6C section, and 530m, occurring in the strain cable section.

In Figure 4.6 the BFS vs time curves labelled 340m and 530m are taken from segments of the 72F-6C and the strain cable, respectively, which are buried in the trench. The BFS vs time plots from length-ordinates where the cable is buried are clearly distinguishable from BFS vs time curves plotted for ordinates that are not buried. The cables within the trench experience less BFS variation over time relative to non-buried cables, and this indicates that the cables within the trench undergo less temperature variation as they are separated from the ambient environment by the soil. A set of BFS vs time curves is shown in Figure 4.7 for the 72F-6C-to-strain cable.

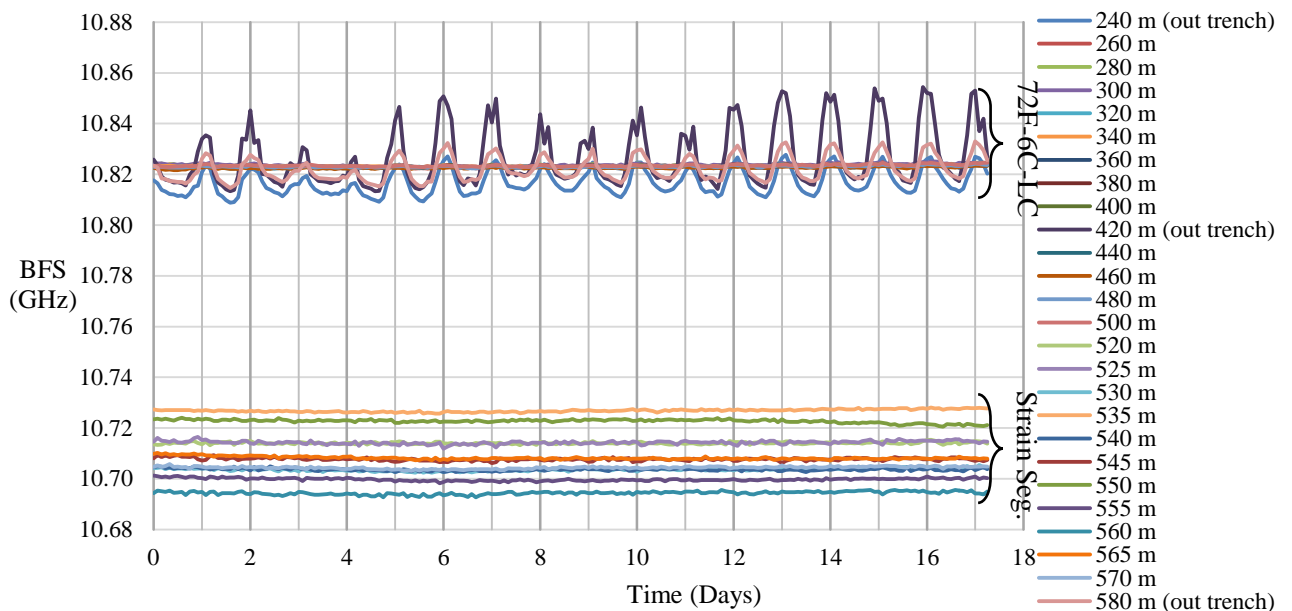


Figure 4.7. BFS vs time curves for the 72F-6C to strain cable, plotted from 240m to 580m, every 20m for the 72F-6C cable, and every 5m for the strain cable segment.

It is notable that the BFS of the strain cable is different to that of the 72F-6C cable. This is because the BFS is also a function of the material composition of the glass of which the fibre is composed. Thus, the BFS of the 72F-6C-LC and the strain cable are different due to the different structural make-up of

the optical fibres. This is where the process of developing an average BFS value for each length-ordinate, explained in Figure 4.5, becomes useful. By calculating an average BFS value for each length-ordinate with respect to time, each BFS vs time curve can be normalised, or zeroed, relative to its own respective average BFS value. By zeroing the set of curves shown in Figure 4.7, Figure 4.8 can be generated.

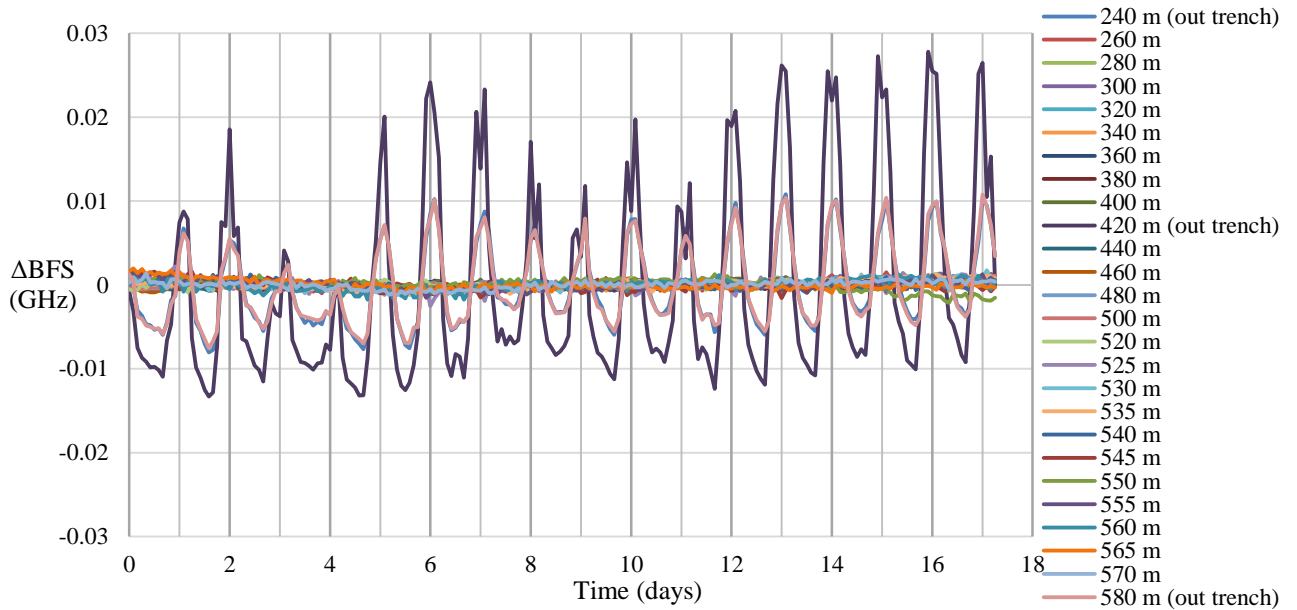


Figure 4.8. Zeroed set of BFS vs time curves from Figure 4.7.

The set of curves shown in Figure 4.8 do not clearly show how the 72F-6C-LC and strain cables differ one from another over time when they are zeroed. The 72F-6C-LC and strain cables are separated out into Figure 4.9 and Figure 4.10 respectively to show how the  $\Delta$ BFS of each cable behaves over time.

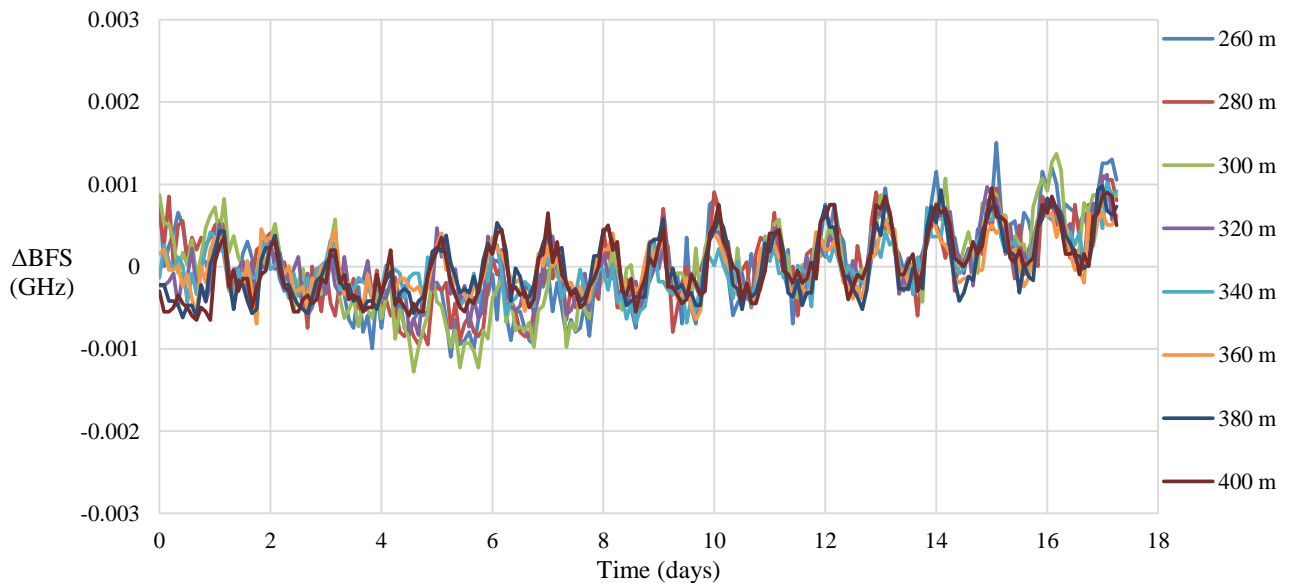


Figure 4.9. Zeroed set of BFS vs time curves from Figure 4.7 showing only those of the 72F-6C-LC cable.

The 72F-6C-LC cable displays a daily fluctuation behaviour, with the BFS peaking at the hottest time of the day and troughing at the coldest time of the day. The 72F-6C-LC cable is able to output this result as the optical fibres inside the sheath are not restricted longitudinally, and are thus able to elongate with temperature variation.

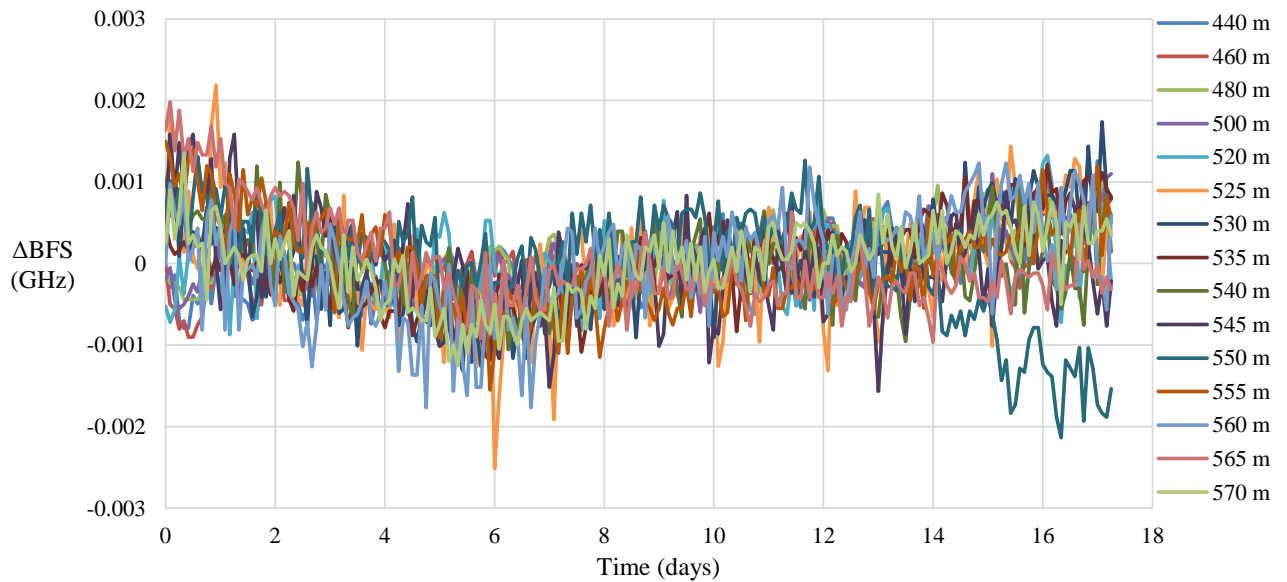


Figure 4.10. Zeroed set of BFS vs time curves from Figure 4.7 showing only those of the strain cable.

From Figure 4.9 and Figure 4.10 it is clear that the 72F-6C-LC cable behaves differently from the strain cable.

The strain cable on the other hand does not display a daily fluctuation behaviour. This is because the optical fibres in the sheath do not have the ability to expand and contract longitudinally as they are fixed to the surrounding sheath. Thus the daily temperature variation does not have as great an effect on the strain cable due to the fixity of the optical fibres to the sheath.

#### 4.2.2.1 SEASONAL VARIATION

Due to the fact that the BFS is affected by temperature it would be expected that the BFS would undergo seasonal changes in the BFS output. The BFS output by the 4F-DC-LC at standpipes 2, 5, and 8, at buried depths of 0.5m, 1.0m and 1.5m respectively from the 23<sup>rd</sup> of February 2021 to the 25<sup>th</sup> of August 2021 is shown in Figure 4.11.

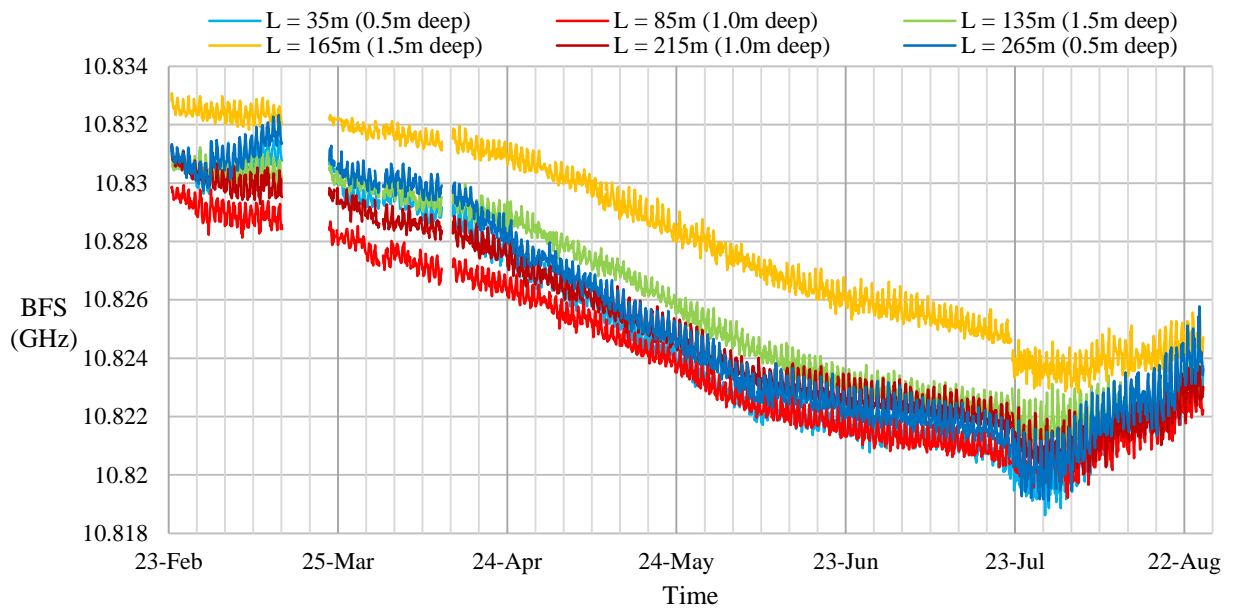


Figure 4.11. BFS measurements produced by the 4F-DC-LC cable from the Hillcrest Campus trench at length-ordinates with buried depths of 0.5m, 1.0m and 1.5m, from the 23<sup>rd</sup> of February 2021 until the 25<sup>th</sup> of August 2021.

As can be seen in Figure 4.11 the BFS during summer on 23<sup>rd</sup> of February is at its highest output of the entire time period. As time progressed towards winter the BFS output at each length-ordinate decreased. The lowest BFS was recorded at the end of July and into the beginning of August where it began to increase again.

The 4F-DC-LC cable being primarily influenced by temperature effects does not give an indication of how strain effects play a role in the seasonal variation of a FO cable. Figure 4.12 shows the BFS output from the 2F-TB cable from the 23<sup>rd</sup> of February 2021 until the 25<sup>th</sup> of August 2021 at the same length-ordinates as Figure 4.11.

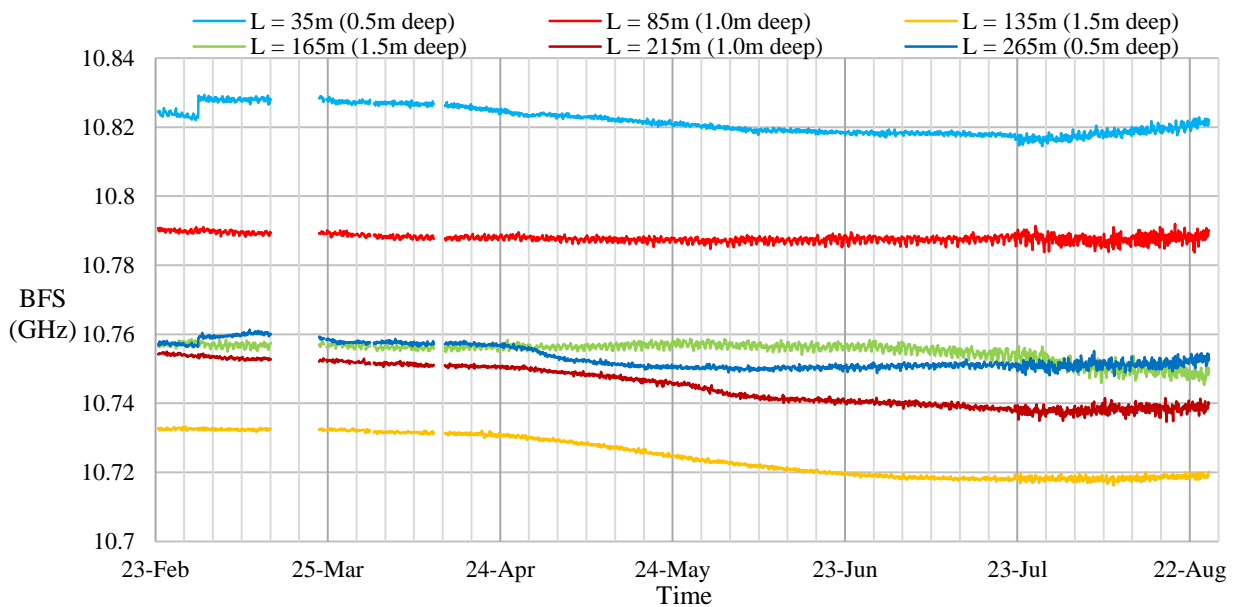


Figure 4.12. BFS measurements produced by the 2F-TB cable from the Hillcrest Campus trench at length-ordinates with buried depths of 0.5m, 1.0m and 1.5m, from the 23<sup>rd</sup> of February 2021 until the 25<sup>th</sup> of August 2021.

In contrast to Figure 4.11, the curves depicted in Figure 4.12 of the 2F-TB cable occur over a much broader BFS range than the 4F-DC-LC cable. This is attributed to the different initial strain states that different sections of the 2F-TB cable are in as a different strain state results in a different initial BFS. To better examine the seasonal variation of the 2F-TB cable each BFS vs time curve from Figure 4.12 can be zeroed with respect to their first BFS taken on the 23<sup>rd</sup> of February. This is done in Figure 4.13.

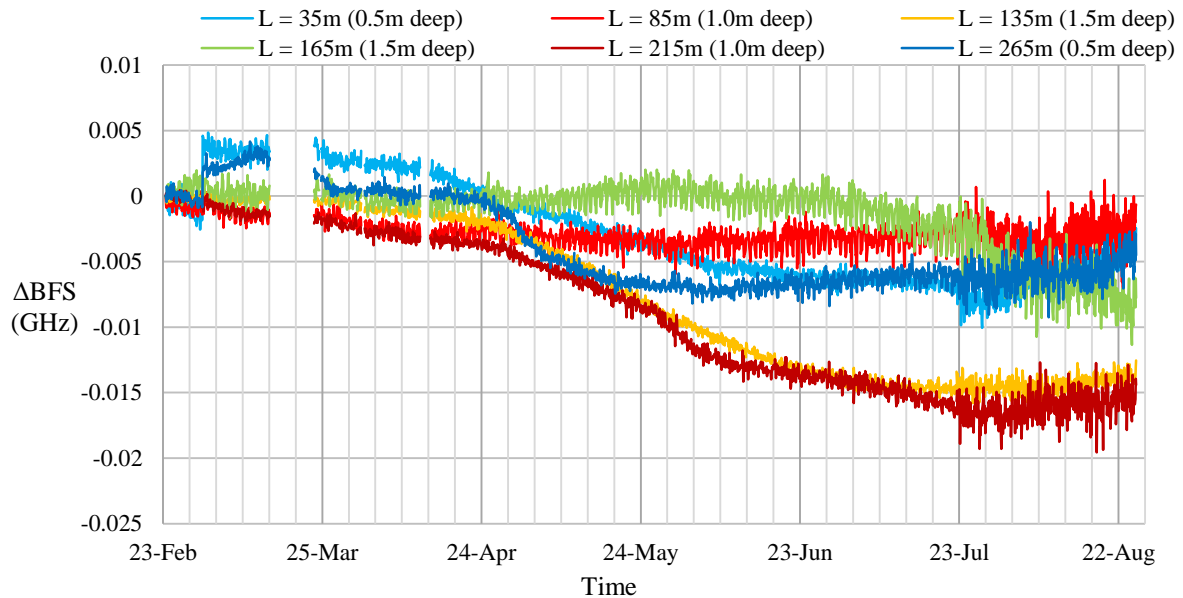


Figure 4.13. BFS vs time for the 2F-TB cable zeroed with respect to the each first BFS reading on the 23<sup>rd</sup> of February.

As can be seen in Figure 4.13 the 2F-TB cable also exhibits seasonal variation behaviour, yet not the same as the 4F-DC-LC cable. At different length ordinates along the 2F-TB cable the changes in BFS from summer (February) to winter (August) are different. Again this may be attributed to the optical fibre being constrained unevenly by the sheath along the cable length allowing certain segments to thermally contract more than others.

### 4.2.3 AVERAGE BFS PROFILES AND RELATIVE BFS PROFILES

Consider the set of BFS profiles shown in Figure 4.14 showing BFS for the 72F-6C-LC-to-strain cable logged over a period of 24 hours at 2 hour intervals.

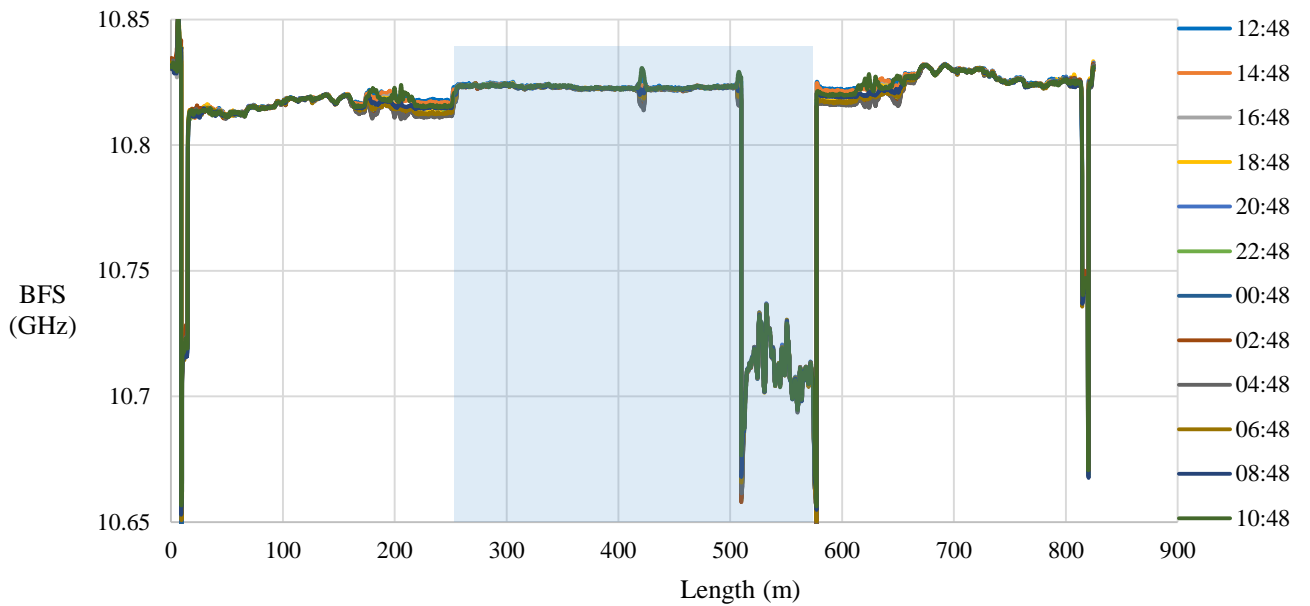


Figure 4.14. Set of BFS profiles of the 72F-6C-to-strain cable logged over a period of 24 hours at 2 hour intervals.

As has been demonstrated in Section 4.2.2, this set of BFS profiles can be condensed into a single average BFS profile, by averaging the BFS readings with respect to time for each length-ordinate. In doing so a profile such as the one seen in Figure 4.15 can be generated.

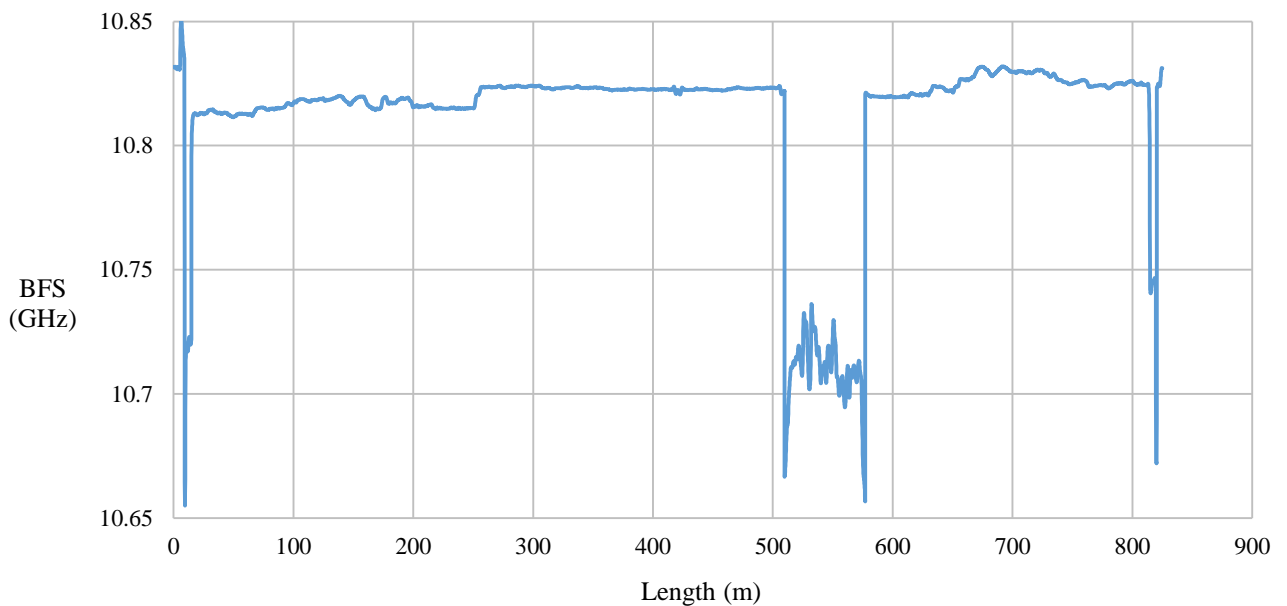


Figure 4.15. An average BFS profile created by averaging 12 profiles logged over a 22 hour time span at 2 hour intervals.

An average BFS profile looks similar to any other BFS profile that was logged at an instant in time. It is, however, a visual summary of BFS profiles taken over a set period of time conglomerated into a single curve. The greater the time span over which BFS profiles are logged, the more stable the resulting average BFS profile will be, as was demonstrated in Figure 4.5. For example, one week's sample of profiles, logged every 2 hours, will create a more stable profile than one day's sample of profiles, logged every 2 hours. The process of logging profiles to create a stable average BFS profile is establishing a baseline.

A set of average BFS profiles from a preliminary data set from the 15<sup>th</sup> to the 31<sup>st</sup> of December 2020 is shown in Figure 4.16.

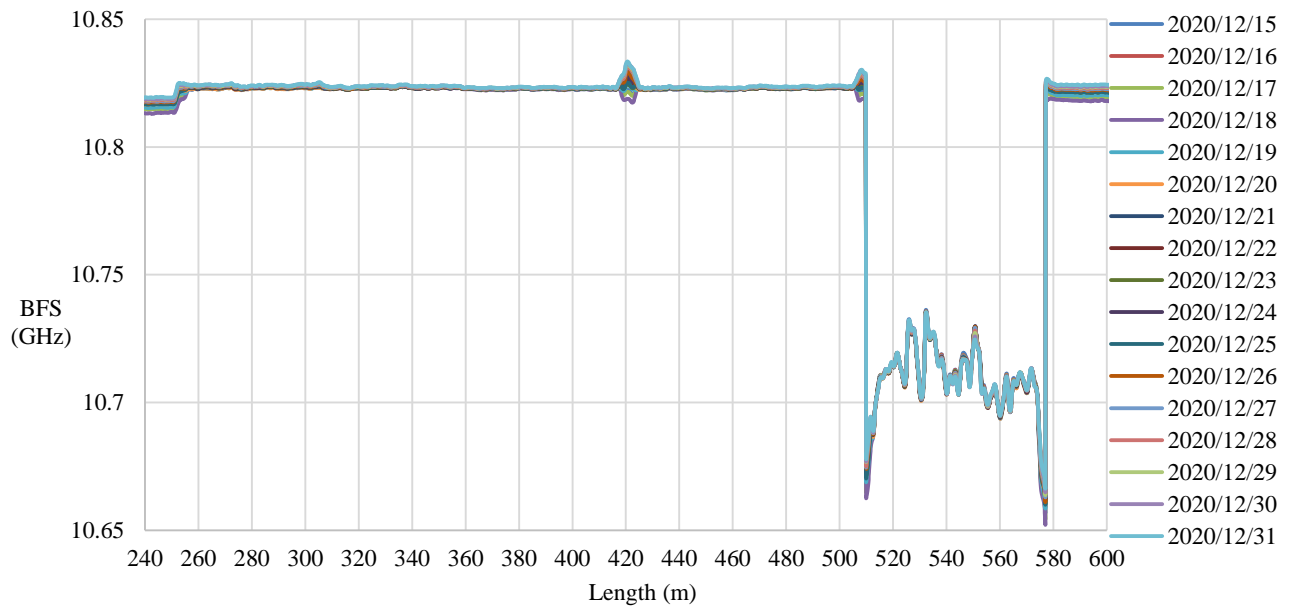


Figure 4.16. A set of average BFS profiles plotted for the 72F-6C-to-strain cable.

The set of profiles shown in Figure 4.16 is difficult to distinguish between one profile and another. This is where a relative BFS profile becomes useful. In like manner to what was done in Figure 4.3, an average BFS profile can be chosen as a baseline and can be subtracted from any other profile to generate a relative BFS plot. Choosing the average BFS profile labelled 2020/12/15 from Figure 4.16 as the baseline and subtracting it from the remainder of the set of average BFS profiles, yields Figure 4.17.

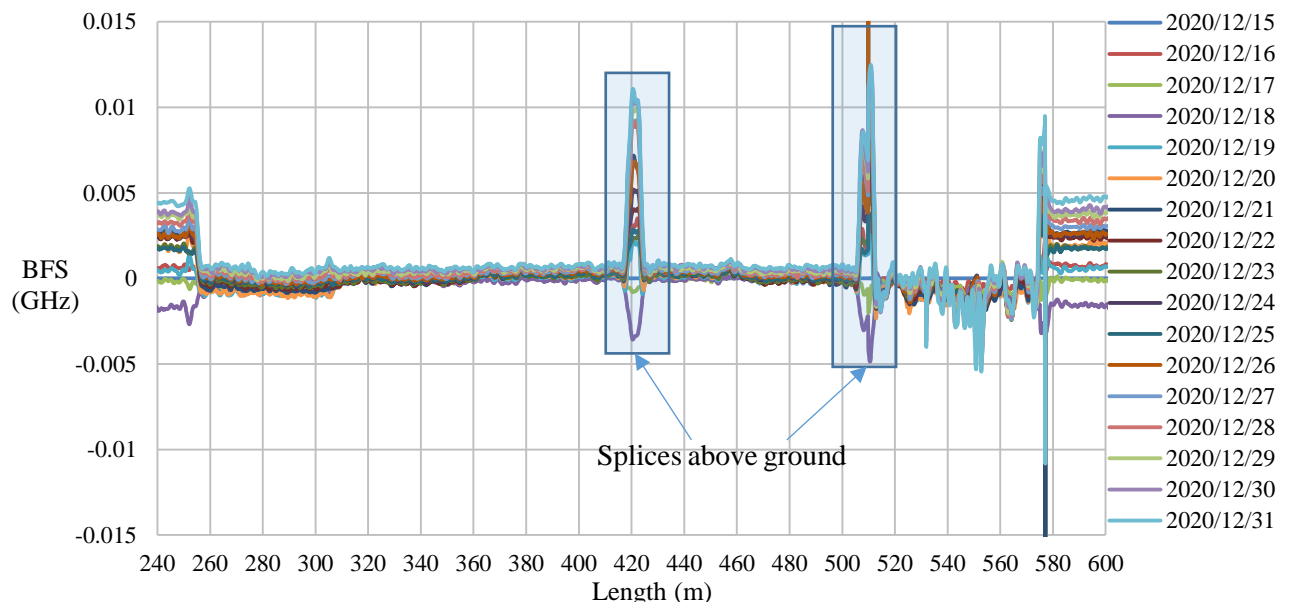


Figure 4.17. Set of average BFS profiles from Figure 4.16 plotted relative to the 2020/12/15 average BFS profile.

As in Figure 4.3, it is easy to see in Figure 4.17 which sections of the cable undergo large temperature variations. Due to the fact that these profiles are daily averages, they give an indication of the average temperature over the course of a day compared to that of a different day. For example, if an average

profile lies above another profile, then the higher profile indicates it experienced a higher average temperature over its day than the lower profile.

Establishing a firm baseline is of utmost importance because it is against this baseline that subsequent readings must be compared in order to detect a disturbance such as a leaking pipe. It is also important to know what the expected BFS output boundaries are for a specific optical fibre, as a value that lies outside of this range can also be a flag to indicate a disturbance to the FO cable. Figure 4.18 and Figure 4.19 demonstrate this argument by showing the average BFS plot and plots of the minimum and maximum BFS values obtained from the 14<sup>th</sup> to the 31<sup>st</sup> of December 2020 for the 72F-6C-to-strain cable.

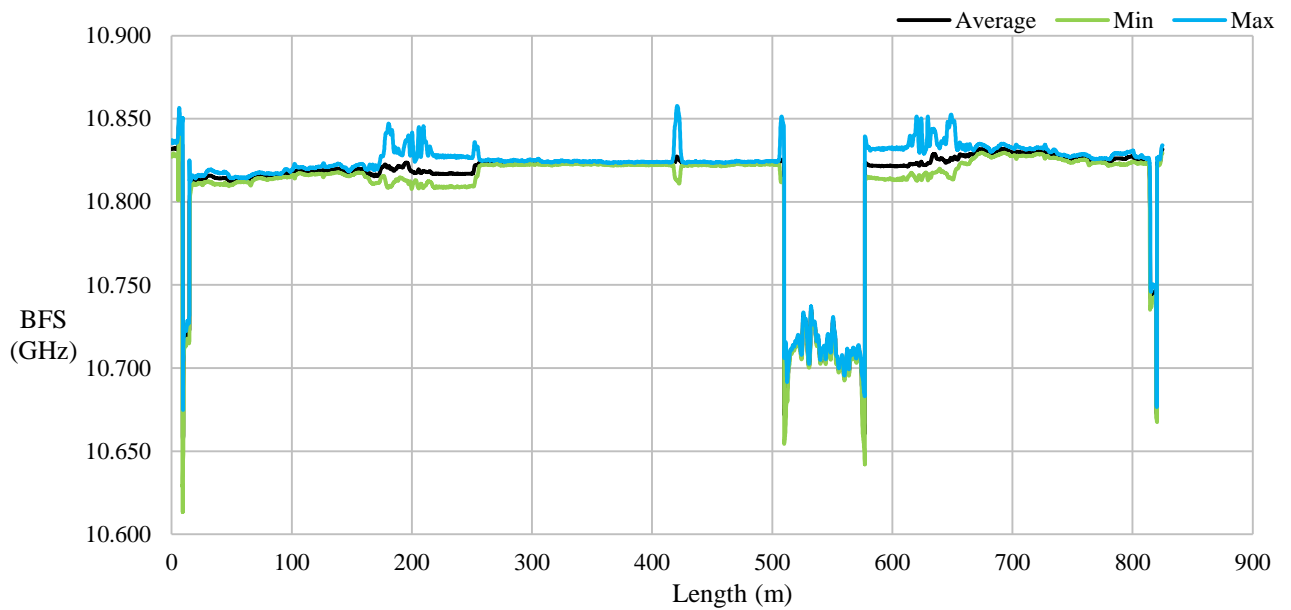


Figure 4.18. Average, minimum and maximum BFS value logged from 14 to 31 December 2020 for the 72F-6C-to-strain cable.

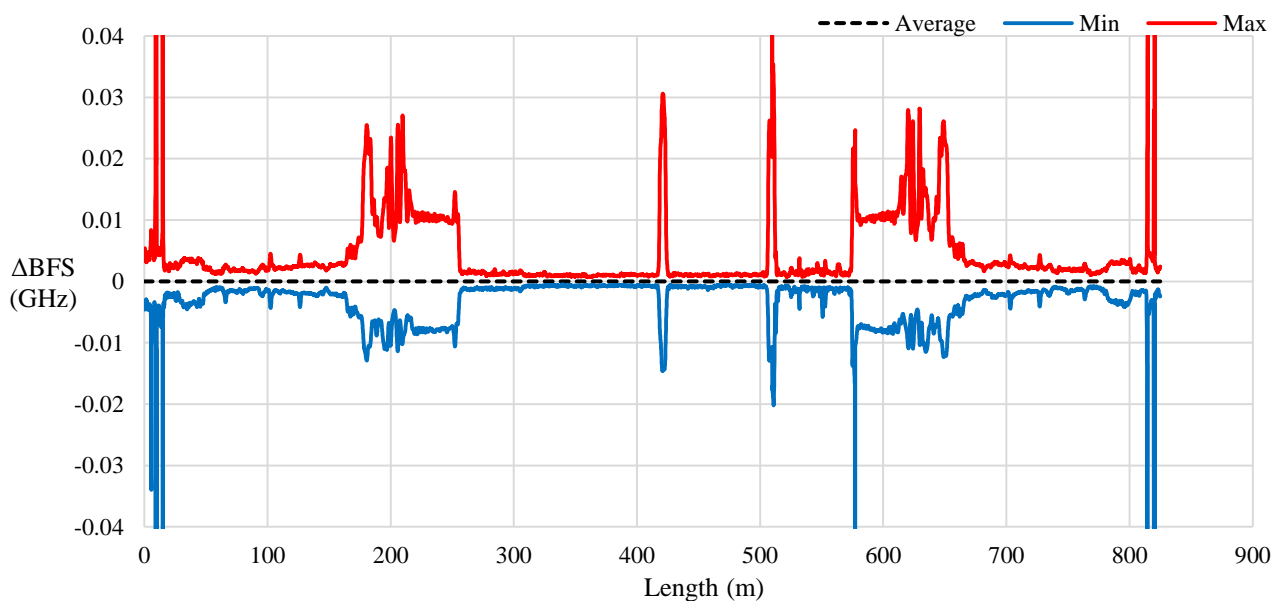


Figure 4.19. Minimum and maximum BFS values logged, as per Figure 4.18, relative to the average BFS profile.

## 4.2.4 COMPARISON OF VARIOUS CABLES

The discussions of Sections 4.2.1 to 4.2.3 have only dealt with the 72F-6C-LC-to-strain cable to explain the basic concepts pertaining to the baseline analysis of the data. In this section the results and performance of the various cables are discussed.

### 4.2.4.1 72F-6C-LC-TO-STRAIN CABLE

Consider Figure 4.20, which is repeat of Figure 4.17 with a legend of annotations. The relative BFS profiles of the 72F-6C section of the cable, from 260m to 500m, plot very smoothly, excluding the splices at 420m and 510m. This is due to the ability of the optical fibre in the 72F-6C-LC cable to slide smoothly within the sheath. Thus, it does not experience and register significant changes in BFS due to strains occurring in the soil, and due to the sliding the deformation can distribute evenly along the length of the optical fibre. The shapes of each BFS profile consecutively logged at a specified time interval are therefore very similar to one another. This is advantageous when establishing a baseline for a cable as the consecutive BFS profiles that are logged are consistent over time and therefore erratic readings will not negatively impact the average calculated for each length-ordinate.

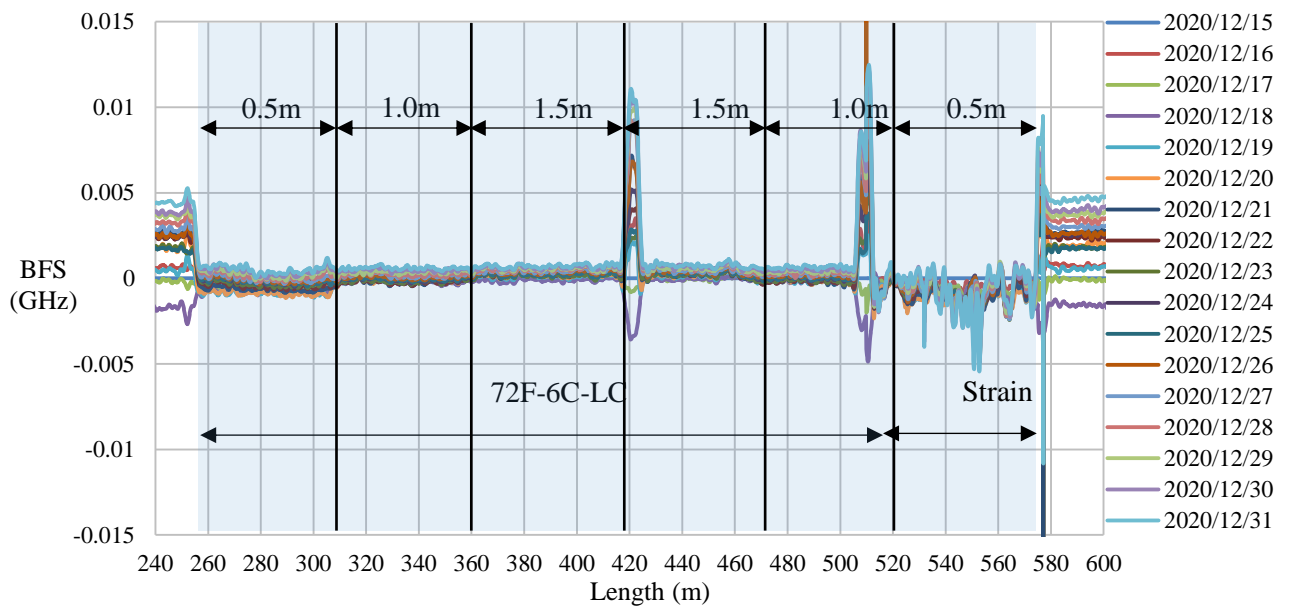


Figure 4.20. Set of relative BFS profiles of the 72F-6C-LC-to-strain cable.

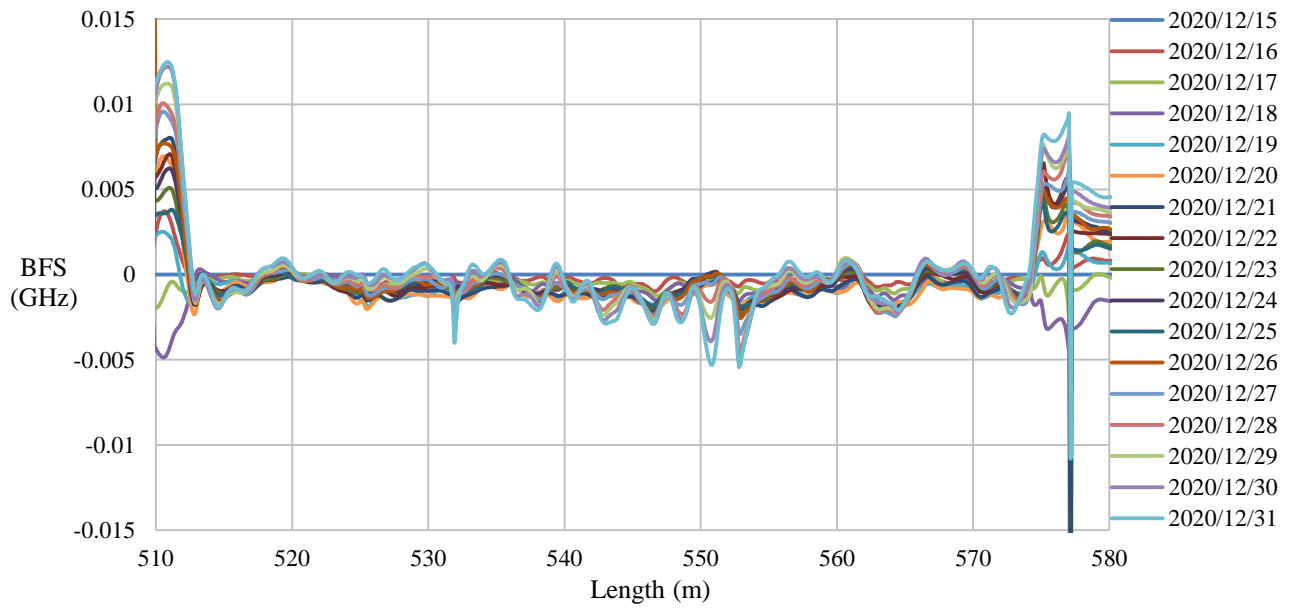


Figure 4.21. Set of relative BFS profiles of the 72F-6C-LC-to-strain cable focusing on the strain cable section.

Considering the strain segment of the relative BFS profile in Figure 4.20, which is focused upon in Figure 4.21, from 520m to just before 580m, it can be seen that this segment of the profile does not plot as smoothly as the 72F-6C-LC segment. This is due to the tight buffered contact between the sheath of the cable and the optical fibre it houses. Because the cable is a tight buffered design specifically developed to measure strain, it means that there is strain transferred onto the optical fibre from the sheath via frictional forces. Therefore, any strains that develop in the soil will have a more pronounced effect on the BFS of the strain cable than for the 72F-6C-LC cable. This statement is also substantiated by the curves of minimum and maximum registered BFS for the 72F-6C-to-strain cable shown in Figure 4.22.

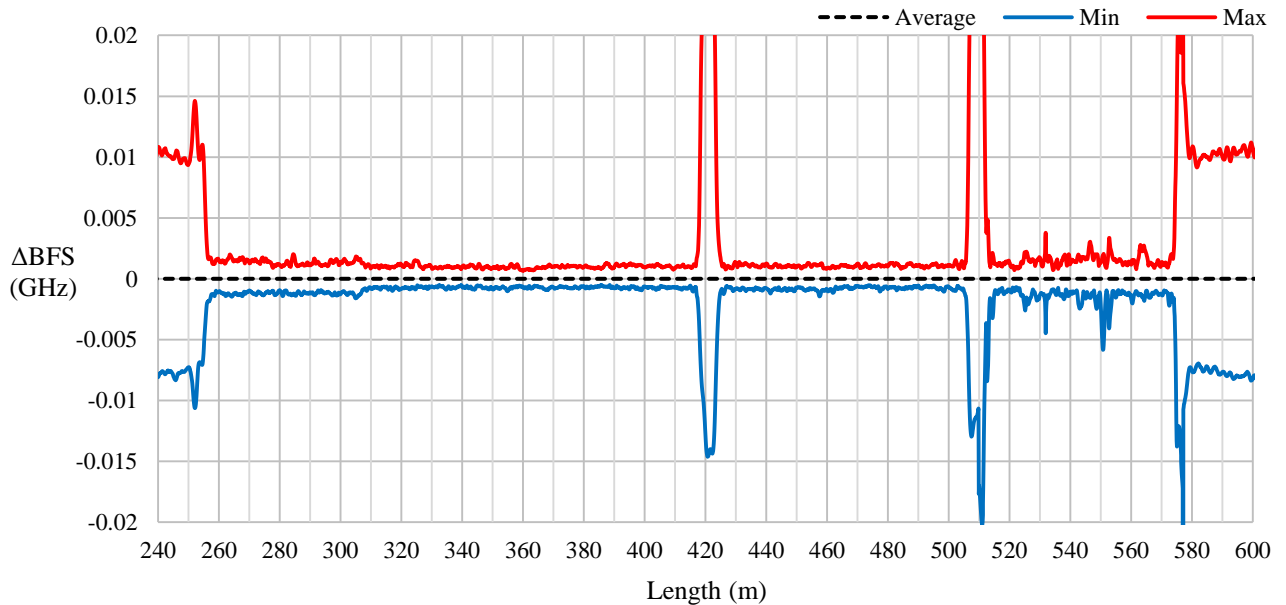


Figure 4.22. Maximum and minimum boundaries of the BFS output logged for the 72F-6C-to-strain cable relative to the average BFS profile.

The minimum to maximum envelope relative to the average BFS of the cable, Figure 4.22, is narrower and flatter for the 72F-6C-LC cable segment, and wider and more erratic for the strain cable segment.

This is because the  $\Delta$ BFS of the 72F-6C-LC cable is primarily caused by temperature variation within the soil, whereas in the strain segment, both temperature and strain play a role in the  $\Delta$ BFS that the optical fibre experiences.

#### 4.2.4.2 6F-TB CABLE

Figure 4.23 presents a set of daily average BFS profiles for the 6F-TB cable. Referring back to Figure 3.4, the 6F-TB cable ran the full length of the trench, but did not double back because of only 150m being available. The 6F-TB cable was spliced into a spare fibre of the 72F-6C-LC cable to complete the loop to the interrogator. In Figure 4.23 the 72F-6C-LC cable enters the trench just before 260m and at 420m the splice between the 72F-6C-LC cable and the 6F-TB cable is evident from the sudden jump in the profile. The 6F-TB cable runs from 420m to just before the 570m mark, where it is spliced back into the 72F-6C-LC cable to complete the loop.

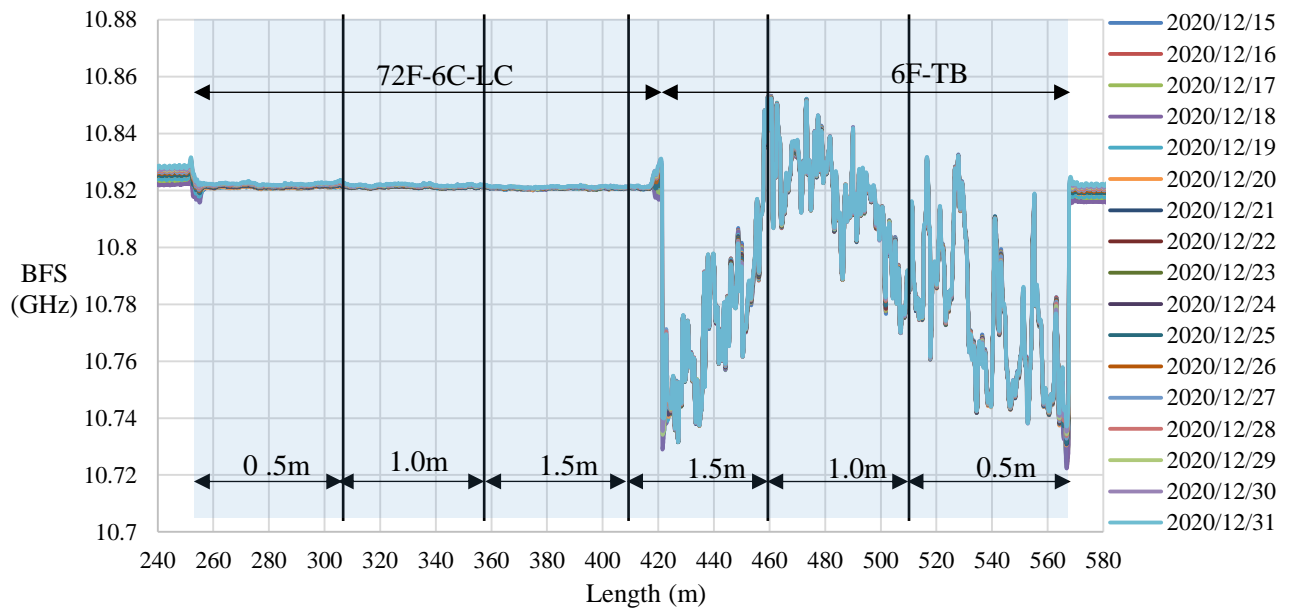


Figure 4.23. Set of daily average BFS profiles for the 72F-6C-to-6F-TB cable from 15/12/2020 to 31/12/2020.

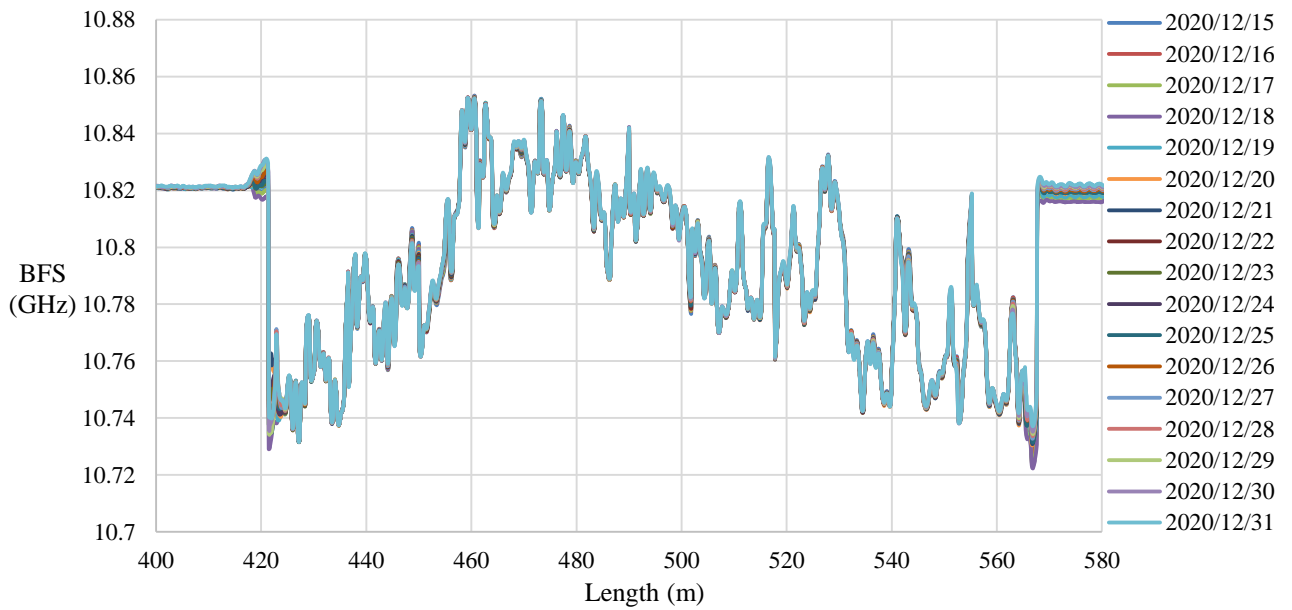


Figure 4.24. Set of daily average BFS profiles for the 72F-6C-to-6F-TB cable focused on the 6F-TB section.

Converting the data in Figure 4.23 into a plot of relative BFS profiles, relative to the 15/12/2020 profile, the set of relative BFS profiles shown in Figure 4.25 is created. Looking at Figure 4.25 and comparing the 72F-6C-LC cable against the 6F-TB cable, the 72F-6C-LC cable profiles are significantly more consistent than the profiles of the 6F-TB cable. The 6F-TB cable is a tight buffered cable, which means that the optical fibres housed by the surrounding sheath experience a significant amount of strain transfer, via friction, from the sheath onto the optical fibre. Like the strain cable, the baseline readings of a tight buffered cable will be affected both by temperature variation, and strains that develop in the surrounding soil. This gives rise to the more variable daily average BFS profiles of the 6F-TB cable, relative to the 15/12/2020 average profile.

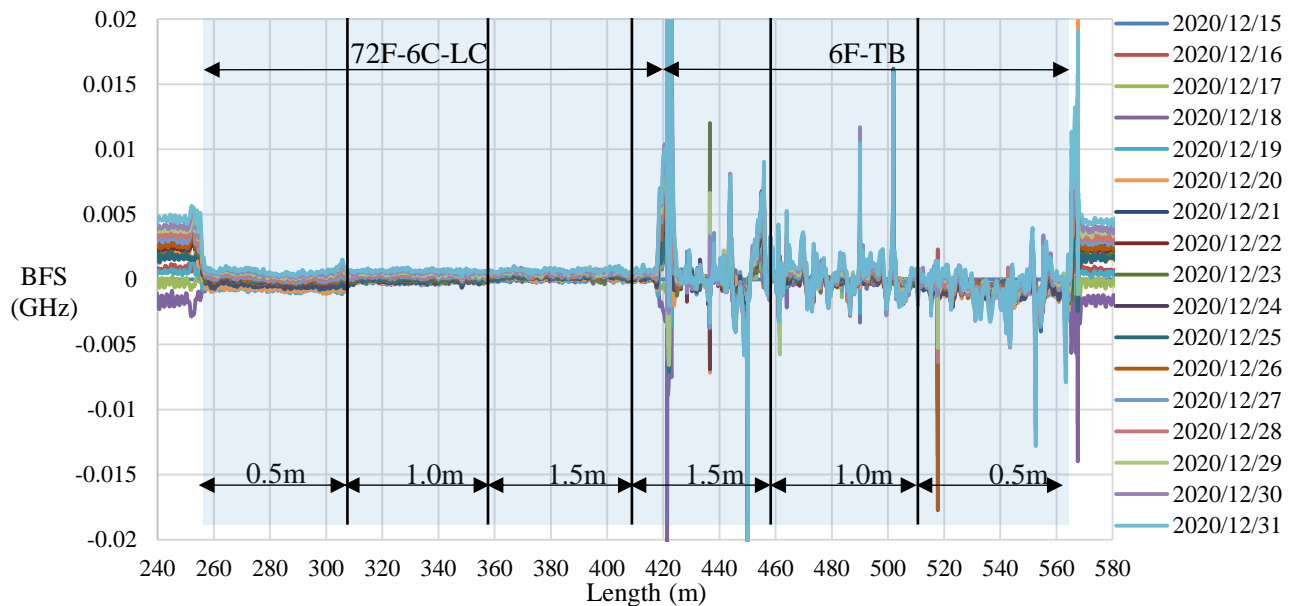


Figure 4.25. Set of daily average BFS profiles relative to the 15/12/2020 profile for the 72F-6C-to-6F-TB cable from 15/12/2020 to 31/12/2020.

Plotting the minimum-maximum envelope, relative to the average BFS profile, of the 72F-6C-to-6F-TB cable Figure 4.26 is obtained.

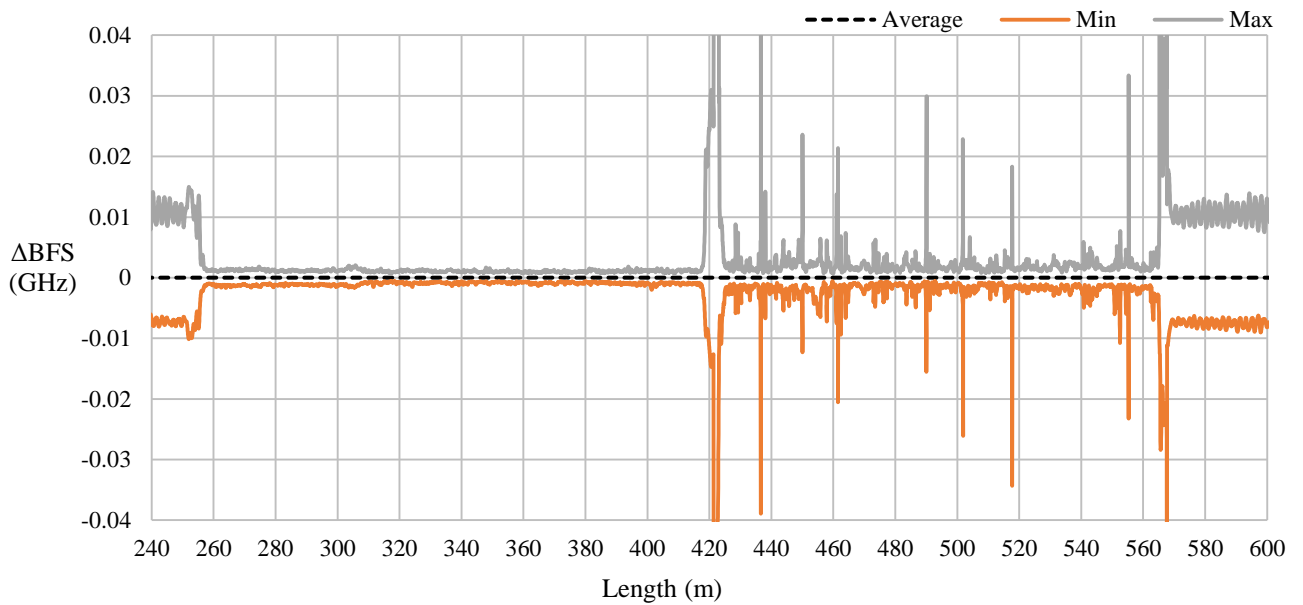


Figure 4.26. Minimum-maximum envelope of the 72F-6C-to-6F-TB cable.

The minimum-maximum envelope for the 6F-TB cable segment has a wider range than that of the 72F-6C-LC cable as expected. However, there are spikes on the envelope that do not fit within the expected boundaries of the envelope (not to be confused with the wider envelope where the splices are located). These outlying data points are the extreme values, but if they occur often enough they could possibly offset the average BFS value that is calculated over time at the length-ordinate where they occur.

#### 4.2.4.3 4F-DC-LC CABLE

The set of daily average BFS profiles for the 4F-DC-LC cable is shown in Figure 4.27

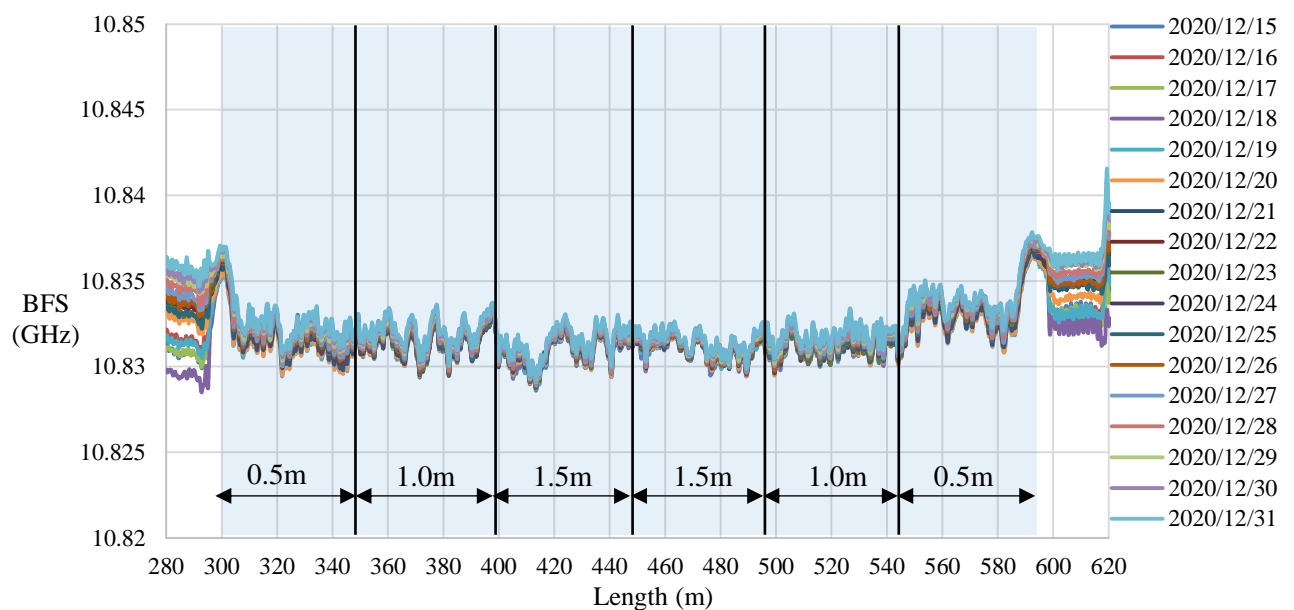


Figure 4.27. Set of daily average BFS profiles for the 4F-DC-LC cable from 15/12/2020 to 31/12/2020.

The BFS of the profiles of the 4F-DC-LC cable occur over a narrower range over the length of the cable as opposed to the 6F-TB. The 4F-DC-LC cable behaviour is more like that of the 72F-6C-LC cable, due to the gel surrounding the fibres reducing the effect of frictional force transfer from the sheath onto the optical fibres. Plotting the average BFS profiles from Figure 4.27 relative to the 15/12/2020 profile yields Figure 4.28.

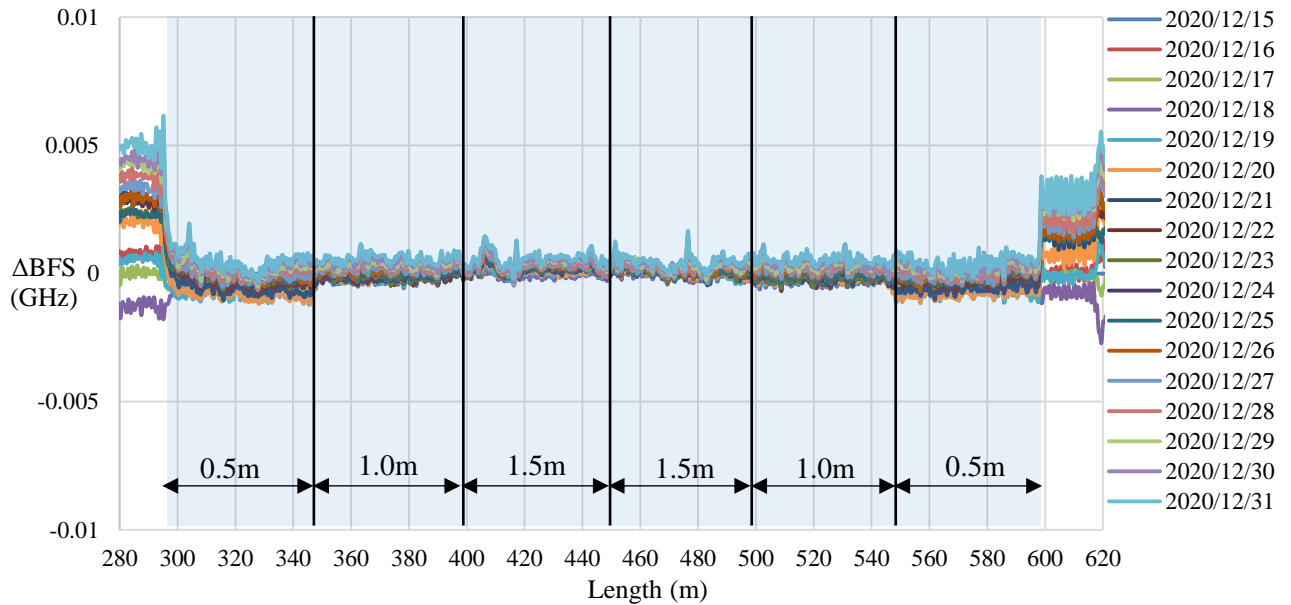


Figure 4.28. Set of daily average BFS profiles relative to the 15/12/20 profile for the 4F-DC-LC cable from 15/12/2020 to 31/12/2020.

As is illustrated in Figure 4.28 the  $\Delta$ BFS profiles of the 4F-DC-LC cable occur within a narrower band as compared to the 6F-TB (Figure 4.25) and the strain (Figure 4.21) cables. The profiles of the 4F-DC-LC cable therefore give near constant BFS profiles as time progresses. This is further reinforced when considering the minimum-maximum envelope of the 4F-DC-LC cable shown in Figure 4.29.

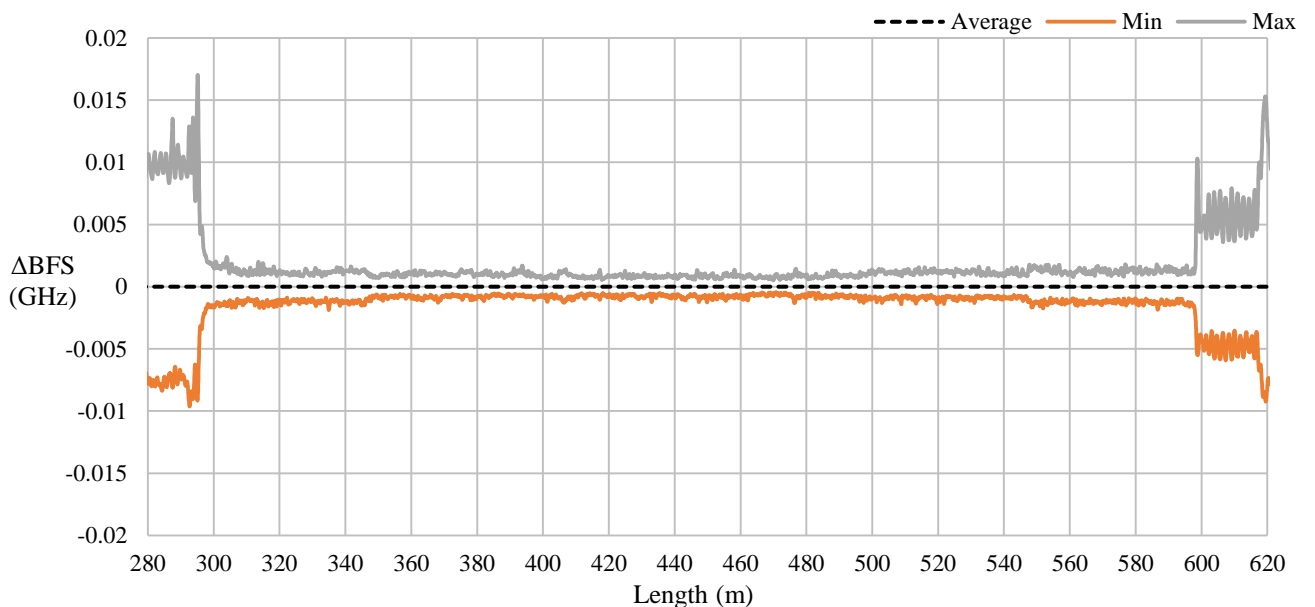


Figure 4.29. Minimum-maximum envelope of the 4F-DC-LC cable.

The minimum-maximum envelope of the 4F-DC-LC cable is flat and smooth like that of 72F-6C-LC cable, showing a consistent baseline.

The effect that buried depth has on the BFS output range can also be seen in Figure 4.28 and Figure 4.29. The range over which the BFS occurs is the widest in the 0.5m deep section, narrower in the 1.0m deep section, and it is the narrowest in the 1.5m deep section. This is to be expected as the effect that the ambient temperature change has on the soil surrounding the FO cables diminishes as the depth to which the cables are buried becomes greater.

#### 4.2.4.4 2F-TB CABLE

In Figure 4.30 the set of daily average BFS profiles for the 2F-TB cable is plotted.

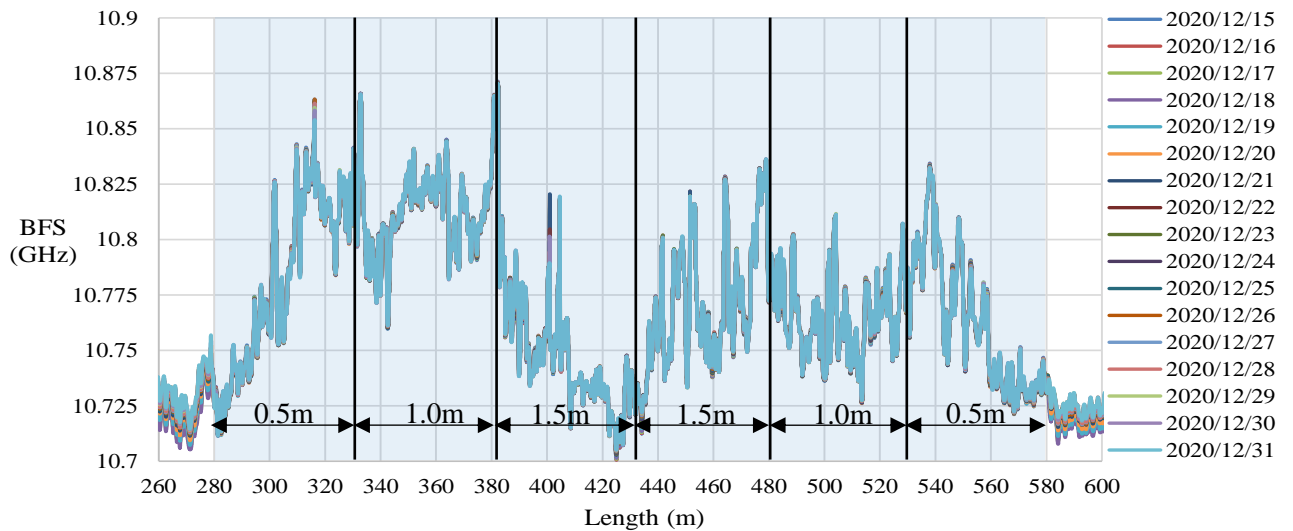


Figure 4.30. Set of daily average BFS profiles for the 2F-TB cable from 15/12/2020 to 31/12/2020.

Like the 6F-TB, the 2F-TB also has a wide range over which BFS outputs can be expected over the length of the cable. In addition to the wide variation of expected outputs, the profiles have regions with steep gradients between data points. These occurrences of steep gradients not aligning perfectly between consecutive readings could possibly give rise to the spikes seen in the relative BFS profiles shown in Figure 4.31.

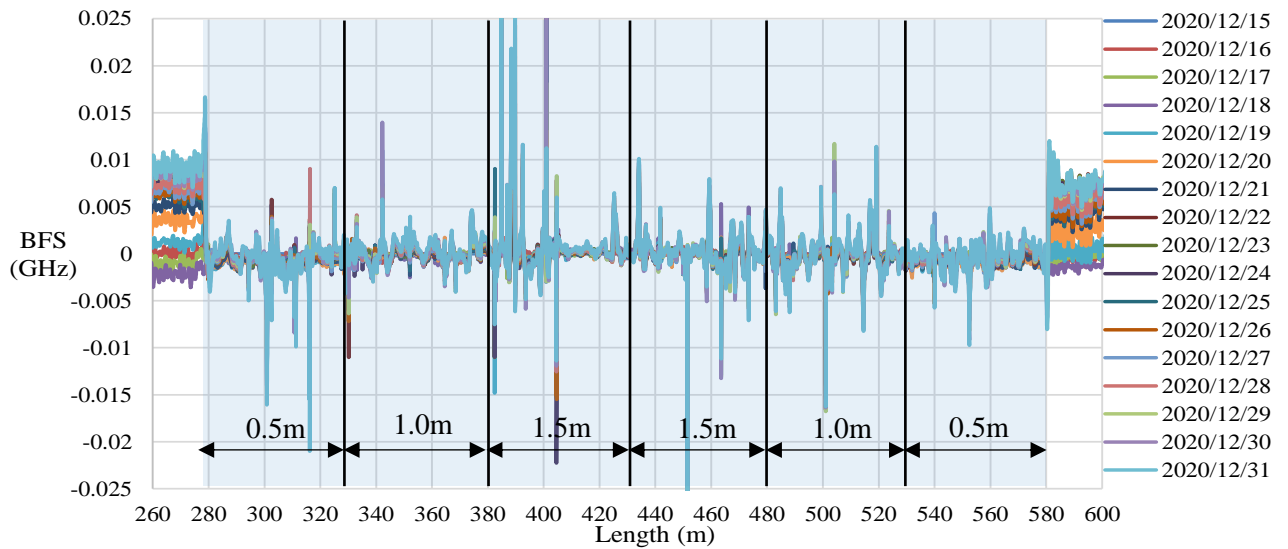


Figure 4.31. Set of daily average BFS profiles relative to the 15/12/20 profile for the 2F-TB cable from 15/12/2020 to 31/12/2020.

The tight buffered cables 6F-TB and 2F-TB both produce BFS profiles which are not consecutively perfectly consistent. For example, the strain interrogator produces a recording of the BFS along the FO cable’s length at a spatial resolution of 0.05m. It sometimes occurs that a given spike in the BFS record is not always register at the same length ordinate along the cable, but sometimes at an adjacent ordinate. When subtracting two BFS records, this results in unwanted spikes in the data. The problem associated with this inconsistency is that a well-established baseline would require much more data to develop and such a baseline may not be able to be developed from the BFS readings logged for these cables. As can be seen in Figure 4.32, there are again data spikes which lie outside of the expected boundaries of where the maximum and minimum BFS values are expected to occur.

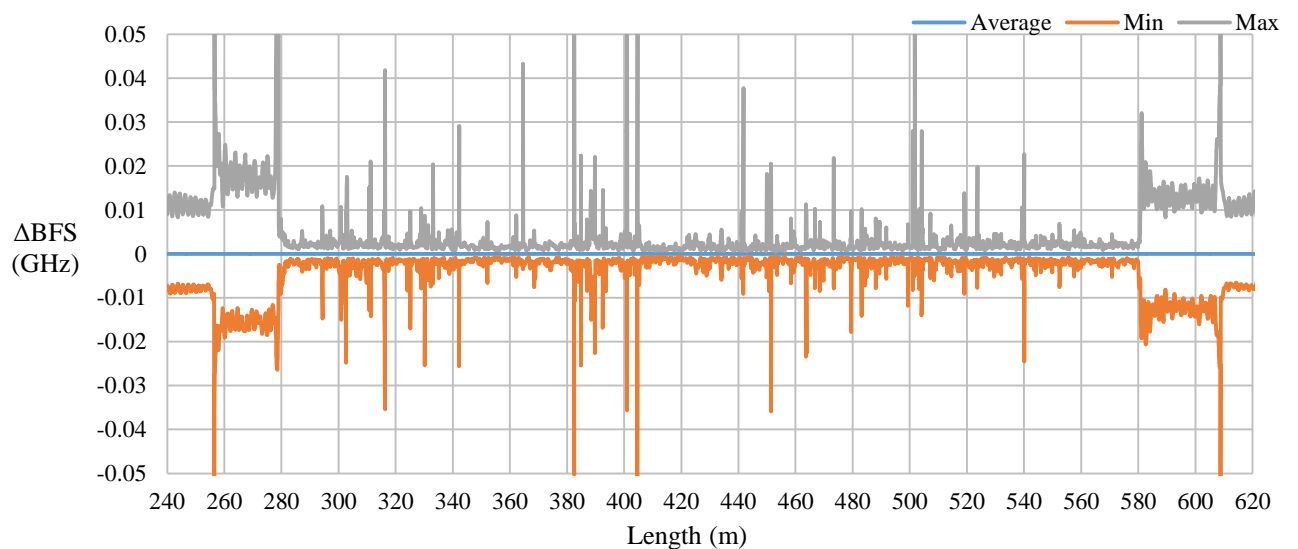


Figure 4.32. Minimum-maximum envelope of the 2F-TB cable.

### 4.3 LEAK TESTS RESULTS

To detect a change in the system using the FO cables, Brillouin Frequency Shift (BFS) output profiles must be compared. The  $\Delta$ BFS output must be used to indicate that an event, such as a leak, has taken place. In this chapter the computational methods developed and used to process the data acquired from the leak tests, enabling leaks to be detected, are discussed.

#### 4.3.1 DATA PROCESSING METHODOLOGY

One set of results from the first leak test is used to explain how the raw output data can be processed to show whether a leak has occurred. For explanation purposes the 6F-TB to 72F-6C-LC cable shall be used to explain the results and data processing. Thereafter, each cable's results are plotted and discussed for comparison.

The first leak test conducted, using standpipes 1, 4 and 7, was preceded by acquiring a 24-hour average BFS baseline over the course of a single day (a dry baseline) taking readings every 2 hours. After the water had been introduced into the trench, a 24 hour average baseline was acquired thereafter (a wet baseline). The result of subtracting the dry baseline from the wet baseline is a relative BFS profile depicting the change that occurred due to the ingress of water into the surrounding soil. The relative BFS profile is shown in Figure 4.33. The flat portion between 160m and 170m corresponds to the spliced region of the cable which was deleted from the data set

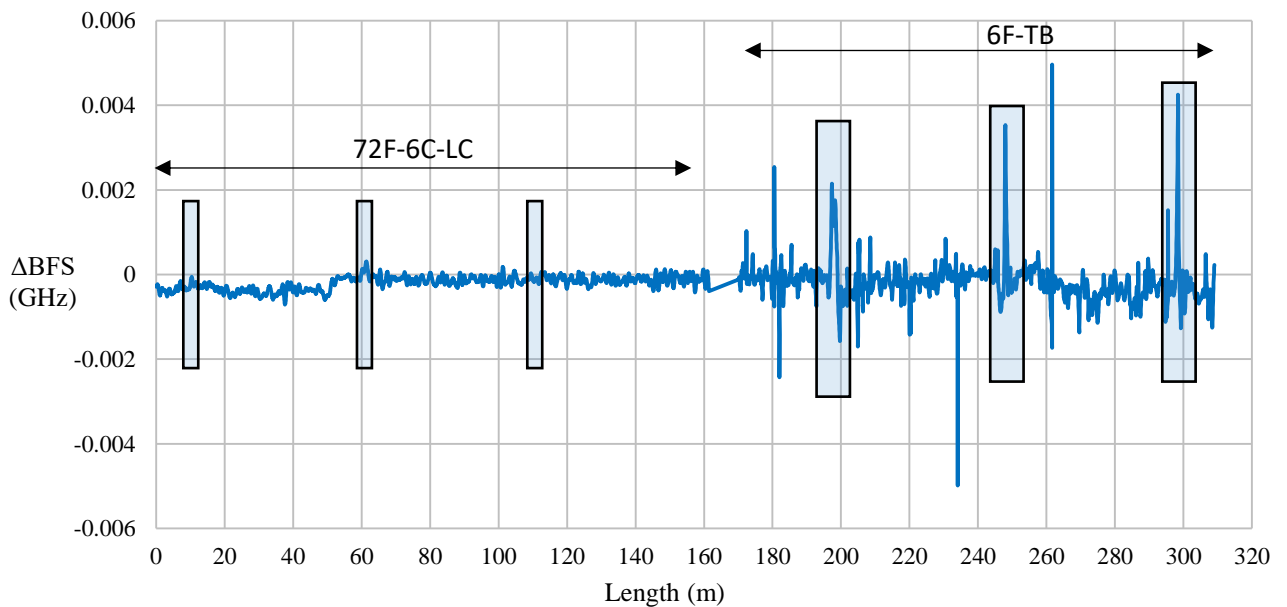


Figure 4.33. Relative BFS plot generated by subtracting the dry baseline from the wet baseline (leak points are highlighted by boxes).

### 4.3.2 CLEANING RELATIVE PROFILES USING A CENTRED MOVING AVERAGE

As can be seen in Figure 4.33, the output of the relative profile is noisy (there are unwanted, random sharp peaks that occur in the relative plot). The random noise that occurs in the relative profiles can hinder the system’s ability to detect leaks, as a sharp peak may be mistaken for a leak by a leak detection algorithm. To rid the profile of this noise, the output can be processed by applying a centred moving average (CMA) in the spatial domain. By using a CMA, the random noise of the output can be reduced significantly, generating a more consistent plot of the relative BFS profile. Figure 4.34 shows a comparison between the raw relative output and the “cleaned” CMA relative profile output using 25 points in the computation of the CMA.

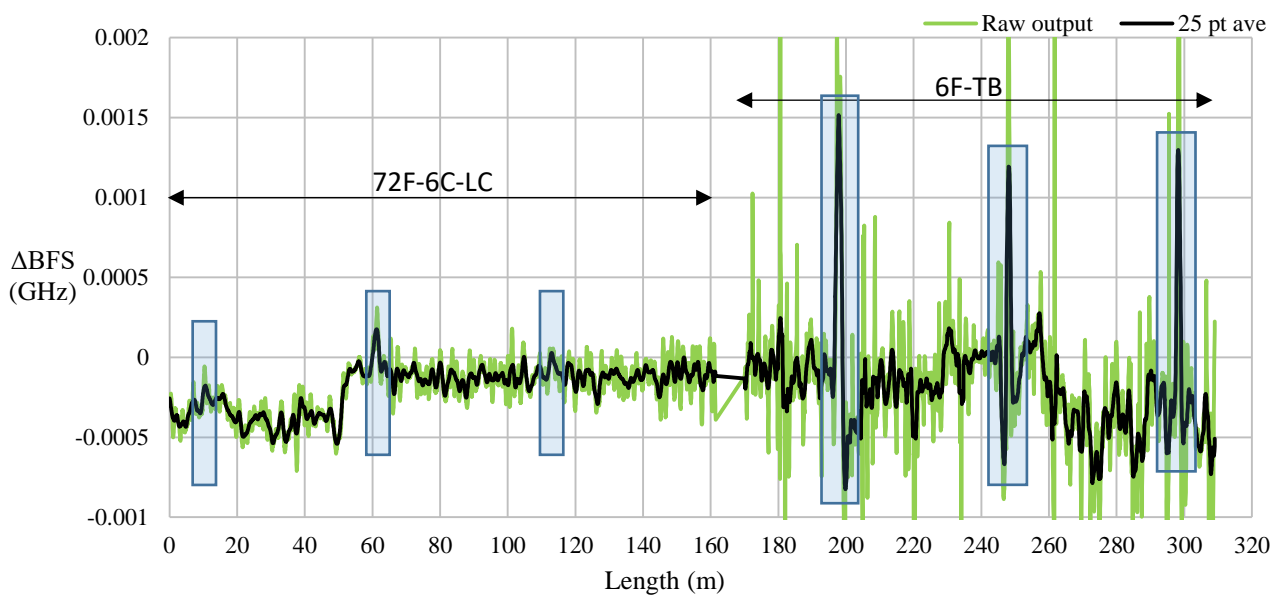


Figure 4.34. A plot of the raw relative profile output as well as the 25-point moving centred average created from the raw data output.

As can be seen in Figure 4.34, the random spikes that occur in the raw relative profile output have been smoothed by applying the CMA. There is a major benefit in applying the CMA as it makes the peaks where the leak occurred clearly detectable against the unaffected regions of the profile. The disadvantage of using the CMA, however, is that the peaks that denote a leak are reduced in height compared to their original raw output height. This is a side effect of applying the CMA as the points surrounding the leak-peak region affect the average value calculated in the leak-peak region. It is therefore crucial that enough points be used in the centred CMA so that the output is sufficiently cleaned with minimal reduction in the leak-peak heights.

### 4.3.3 ZEROING RELATIVE PROFILE

Although the profile in Figure 4.34 has undergone some noise reduction, the profile is not necessarily centred about the horizontal (length) axis. Having the profile centred about the length axis is useful as

the regions of the profile that would be further away from the length axis, and deviating away from the trend of the data, would represent possible leak points. To centre the data about the length axis another CMA can be generated from the zeroed relative BFS profile, but using significantly more points. In this case 601 points are used to generate a CMA that can be used to centre, or zero, the data about the length-axis. 601 data points corresponds to roughly 30m of FO cable length, as the spatial resolution of the interrogator output is around 5cm. By using 601 points the raw output profile is flattened, i.e. the curvature of the data is greatly smoothed out. The result is a smooth line that passes through the data with the same general shape as the original data. The raw relative output, the 25-point CMA and the 601-point CMA are represented in Figure 4.35.

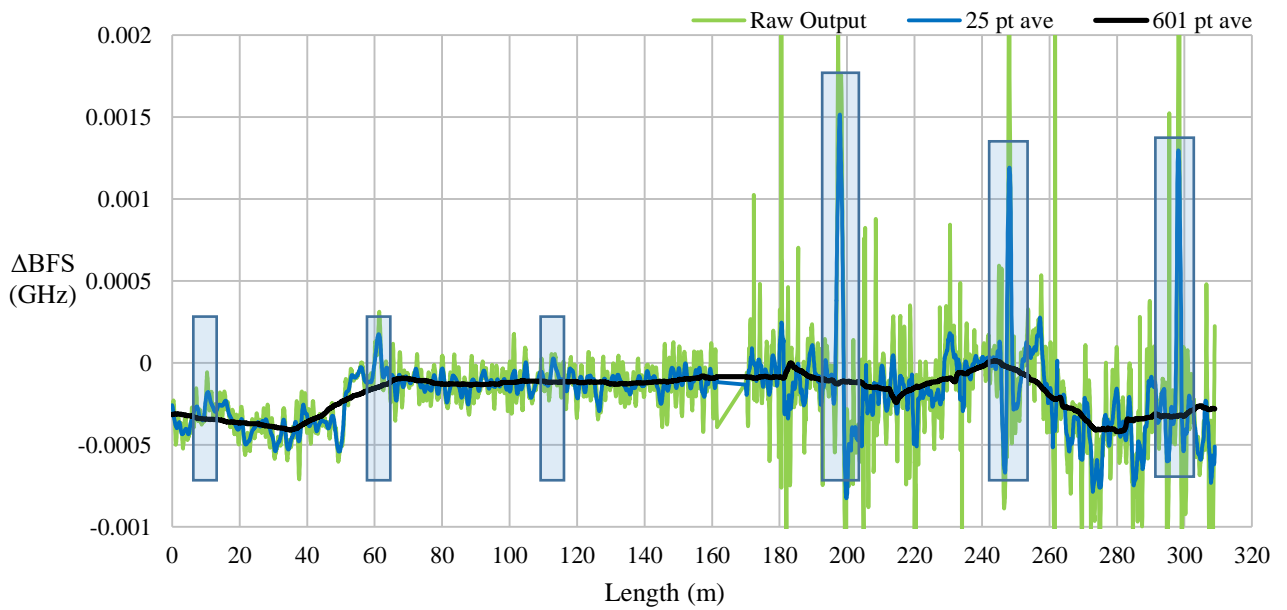


Figure 4.35. A set of curves representing the raw relative BFS output profile, a 25-point CMA and a 601 point CMA.

It is evident from Figure 4.35 that the 601-point CMA follows the shape of the raw output and the 25-point CMA. Thus if the 601-point CMA is subtracted from the raw output or the 25-point CMA the latter profiles will be centred, or zeroed, with respect to the length axis. A comparison of the 25-point CMA relative profile before and after being zeroed about the length axis is shown in Figure 4.36.

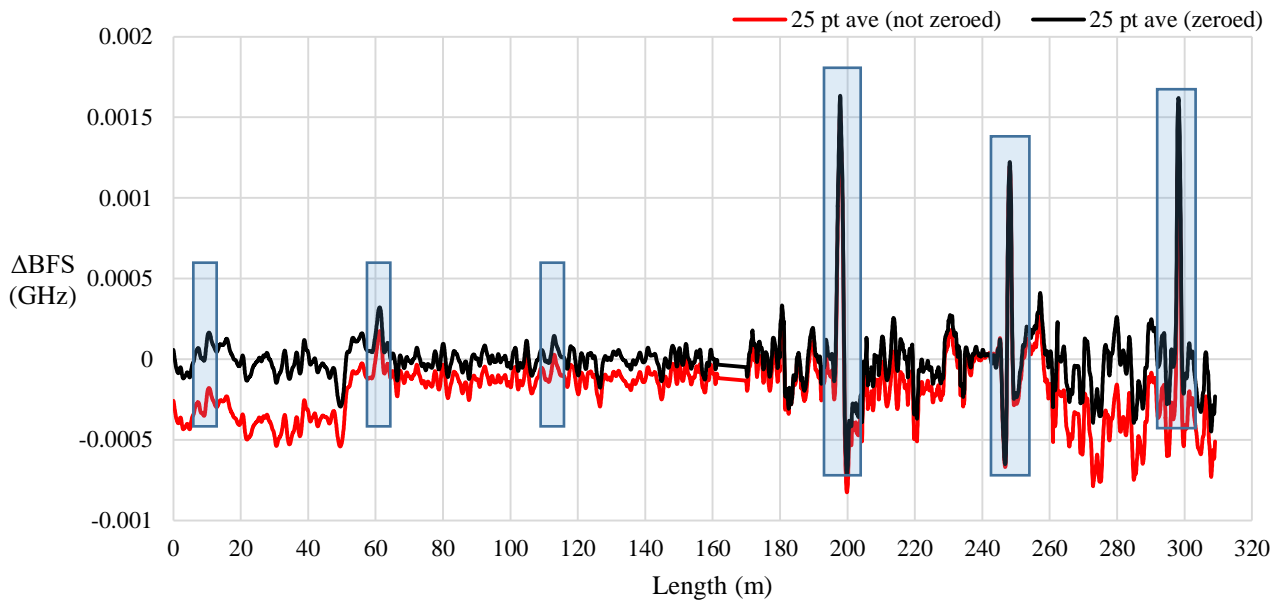


Figure 4.36. 25-point CMA relative profile before being zeroed and after being zeroed.

The zeroed raw and 25pt CMA relative profiles are both depicted in Figure 4.37.

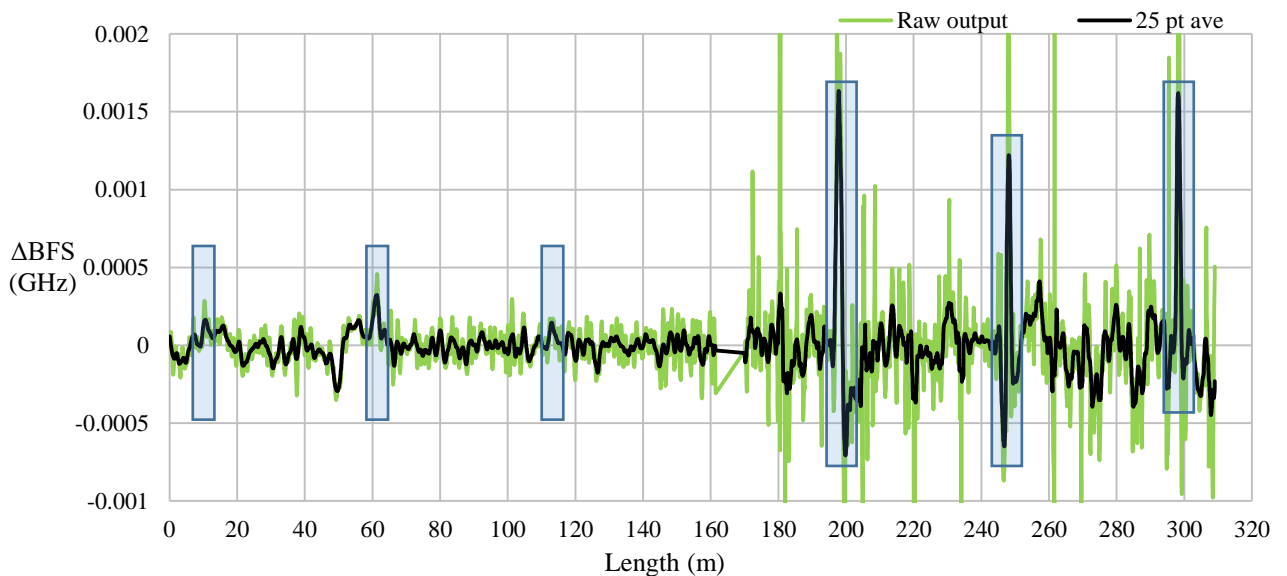


Figure 4.37. Zeroed raw output and 25pt CMA profiles generated by subtracting the 601 point CMA.

### 4.3.4 SQUARED RELATIVE PROFILE

The regions where leaks occurred along the 6F-TB FO cable length clearly stand out from the rest of the profile at length-ordinates 200m, 250m and 300m. The leak points on the 72F-6C-LC cable, however, are not as evident as the 6F-TB cable. This is because the 6F-TB cable is more sensitive to strain effects imposed by a soil moisture content change than the 72F-6C-LC cable. The leak points can, however, be made even more prominent. If the values comprising the 25-point CMA profile shown in Figure 4.37 are squared then the portions of the profile that show greater change in BFS, i.e. data points further from the length axis will be made even greater. In addition, the values lying below the length

axis will be made positive due to the nature of the squaring function. The squared 25-point CMA relative profile is shown in Figure 4.38.

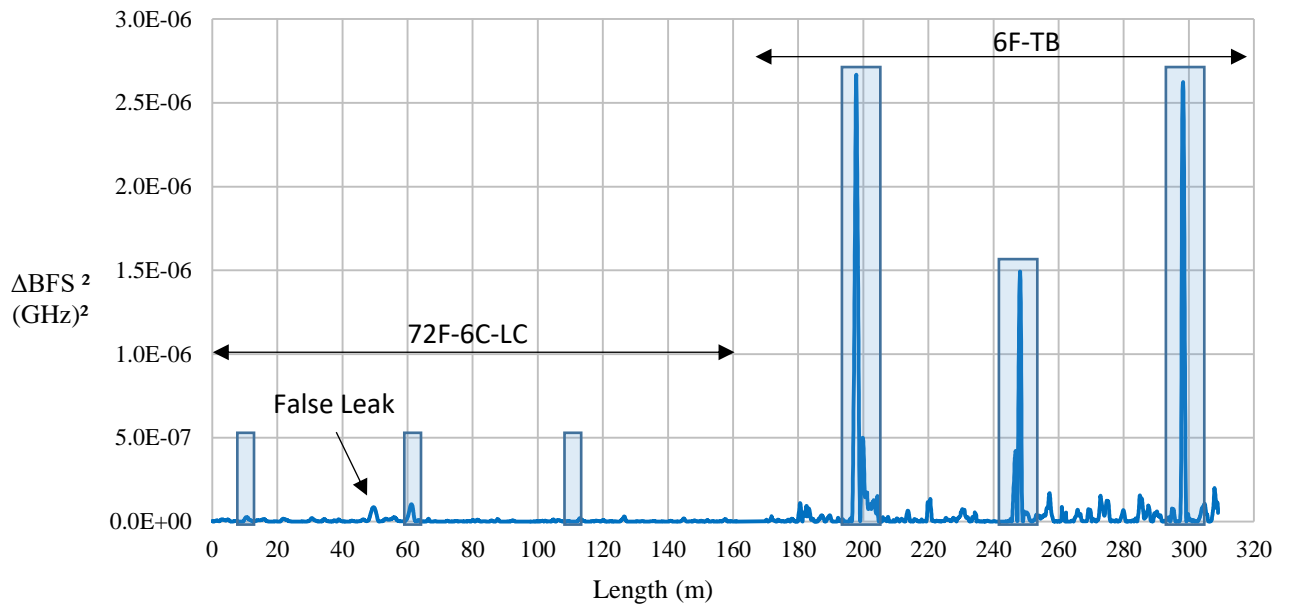


Figure 4.38. Squared 25-point CMA relative profile.

The peaks occurring at 200m, 250m and 300m have been made very distinct from the rest of the profile in Figure 4.38 by squaring the zeroed 25-point CMA relative profile. There is no doubt that these peaks in the 6F-TB segment of Figure 4.38 correspond to the leaks imposed in the trench, as the peaks line up with the locations of the standpipes where water was introduced.

The 72F-6C-LC cable, on the other hand, was only able to detect one leak in this instance at 60m. However, the leak signal that the 72F-6C-LC cable detected was very weak, and may be mistaken for noise in comparison to the false leak that was detected. The 72F-6C-LC cable should show peaks at 10m, 60m and 110m. Furthermore, a false leak was detected by the 72F-6C-LC cable at 50m.

#### 4.3.5 COMPARISON AGAINST EXPECTED MINIMUM AND MAXIMUM BFS RESPONSE

In reality however, it will not be known where, or if a leak has even occurred. An algorithm, or multiple algorithms, will need to be applied to the data from a FO cable monitoring a pipeline and a decision must be made, based on the output, whether a leak has occurred or not. One check is proposed as follows: if a leak occurs, the expected BFS might change such that the BFS response occurs outside the typically expected minimum or maximum BFS response. Therefore, if a BFS response occurs outside of the expected BFS response range it could be inferred that a leak has occurred at the length-ordinate where such an event has taken place in the data. This methodology is visualised in Figure 4.39.

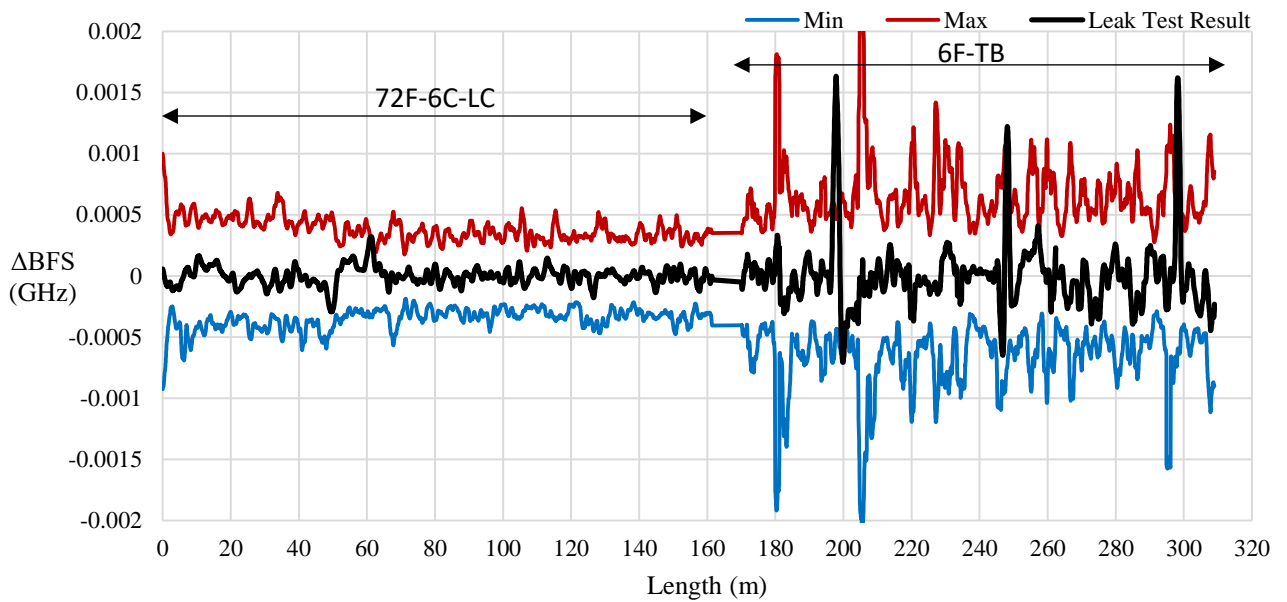


Figure 4.39. Leak test result shown against the minimum and maximum expected bounds of the 72F-6C-LC to 6F-TB cable.

The maximum-minimum envelope is derived from 24-hours' worth of BFS data taken before the leak test was conducted. The regions where leaks were induced into the trench are seen to exceed the maximum expected BFS boundary in the 6F-TB cable, but it is not clear in the segment of the 72F-6C-LC cable. To ascertain whether a boundary has been exceeded, a simple test can be performed: if the leak test result profile exceeds either boundary, maximum or minimum, then the absolute difference between the result and the respective boundary can be returned. This test is illustrated in Figure 4.40.

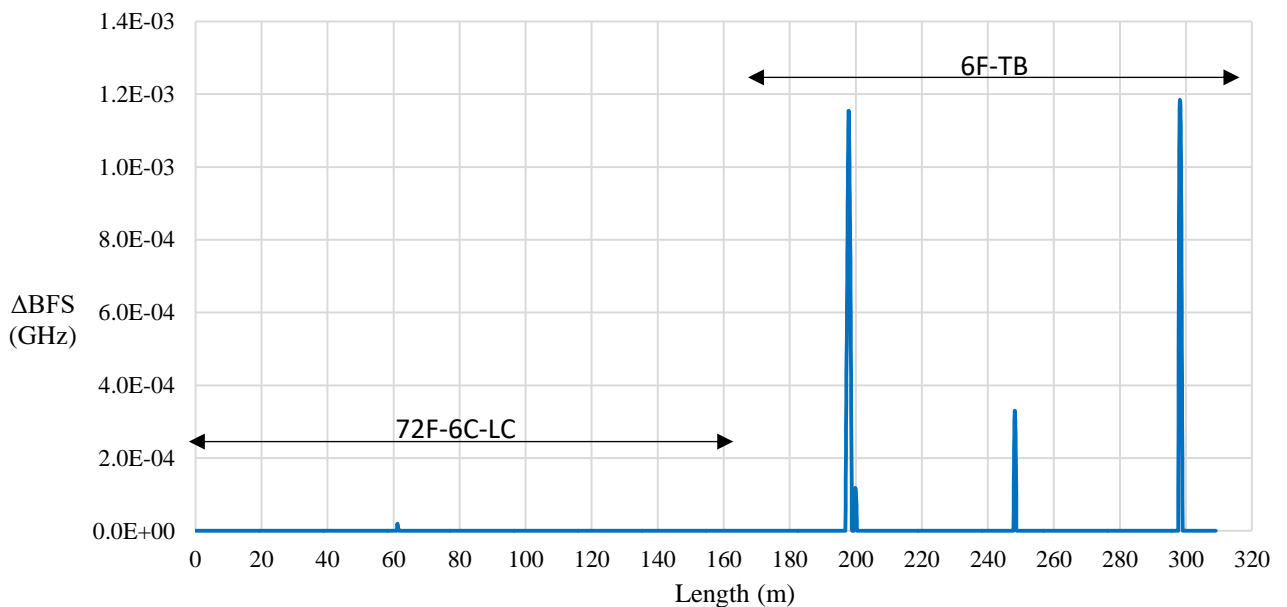


Figure 4.40. Regions of the zeroed 25-point CMA relative profile that exceeded the minimum-maximum expected BFS boundary.

As can be seen in Figure 4.39 and Figure 4.40, this detection method works when applied to the 6F-TB cable output. It has also been partially successful when applied to the output supplied by the 72F-6C-

LC cable, as seen by the small spike at the 60m length-ordinate in Figure 4.40. However, the  $\Delta$ BFS of the 6F-TB cable beyond the boundary was far greater than the 72F-6C-LC cable. This is because the method of comparing a result to the maximum and minimum boundaries is dependent on the mechanical properties of the cable. The maximum and minimum expected BFS boundary for a FO cable is dependent on the temperature fluctuation that the cable experiences. Cables that respond well to strain responses can exceed their maximum and minimum boundaries more easily when influence by a changing soil moisture content imposing strain on the cable. Cables that are dependent primarily on temperature changes for their BFS responses are less sensitive to imposed strain. Because the 6F-TB cable is more sensitive to soil strains than the 72F-6C-LC cable, the 6F-TB cable BFS response is more significantly affected by a leak and it is able to exceed the maximum-minimum boundary at all three leak points as demonstrated in Figure 4.40. The 72F-6C-LC cable only exceeded the maximum boundary at the 60m length-ordinate, but to a much lesser extent in comparison to the 6F-TB cable.

This comparison of the two cables types, loose-core (LC) versus tight-buffered (TB), shows that the performance of a FO cable is dependent on its structure. Although TB cables produce noisy raw data, their performance as leak detection sensors seems significantly better than that of LC cables, once a TB cable's output has been processed.

#### **4.3.6 REPEATABILITY OF DETECTION**

It has been shown that the FO cables are indeed capable of detecting changes in soil moisture contents that could occur along a length of the cable. However, it would be beneficial if the system could detect a recurring leak at the same length-ordinate even if a leak has previously occurred at that length-ordinate. To test this, a second introduction of water into standpipes 1, 4, and 7 was conducted seven days after the experiment had taken place. The results of both leak instances relative to the dry baseline are plotted in Figure 4.41.

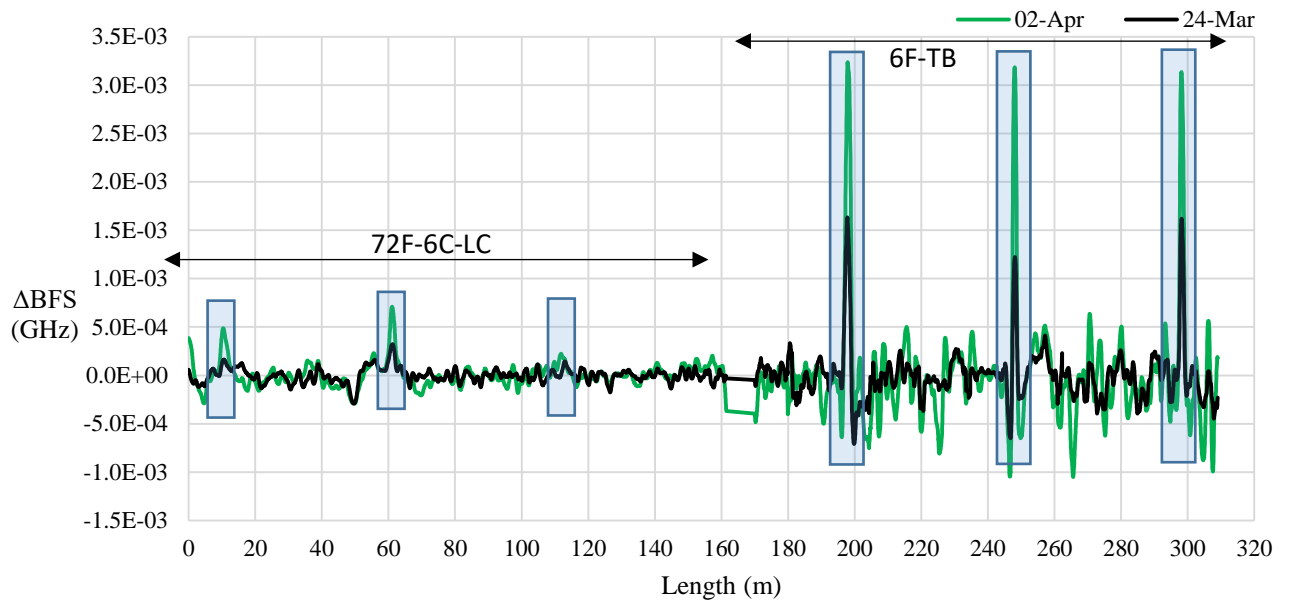


Figure 4.41. Results of the first (24 March) and second (1 April) leak occurrence plotted relative to the dry baseline. The curve labelled 02-Apr is indicative that it is generated from a baseline logged on the 2<sup>nd</sup> of April after the second leak occurrence had taken place on the 1<sup>st</sup> of April.

In Figure 4.41 the two curves, 24-Mar and 02-Apr, are both generated by subtracting a baseline measured over the course of the 23<sup>rd</sup> of March from baselines measured on the two curves' respective measuring dates. From Figure 4.41 the proposition that a leak can be detected at the same length-ordinate more than once has proven successful in both the 72F-6C-LC and the 6F-TB cables. In the 6F-TB segment it appears as though the results of the second leak occurrence (02-Apr) yielded peaks that are roughly double the height of the first leak occurrence (24-Mar). This is attributed to the fact that the result of the second leak occurrence, relative to the dry baseline is showing the combined effect of the two leak tests superimposed. Therefore, the two leak occurrences each generated independent changes in the BFS. The strain response from the second leak occurrence has been added to the strain response of the first leak test. The 72F-6C-LC cable was also able to register a response at two of the three leak points along the cable length. It can therefore be concluded that repeatability of detection is viable even after a section of soil has been wetted by a previous leak.

#### 4.4 BFS RESPONSE IN THE TIME DOMAIN

In order for a FO cable to detect a leak along a working pipeline a  $\Delta$ BFS output must be registered. It is therefore necessary to understand how the BFS response behaves in the time domain to assess how a  $\Delta$ BFS develops and whether there is any signal decay after a leak has occurred.

The result of the second leak occurrence, introducing 50L without a monitored flow rate, recorded by the 6F-TB cable is shown in Figure 4.41. The 6F-TB was able to again detect all three water leaks, whereas the 72F-6C-LC cable was only able to successfully detect two out of the three leaks at standpipes 1 and 4, and partially detected the leak at standpipe 7.

The result displayed in Figure 4.41, however, is a static plot of the  $\Delta$ BFS output displaying the locations where the leaks were detected. If the attention is shifted from the spatial domain to the time domain it can be seen how the BFS changes as a small leak (50L) occurs. A plot of the  $\Delta$ BFS at the three leak points for the 6F-TB cable and the 72F-6C-LC cable is shown in Figure 4.42.

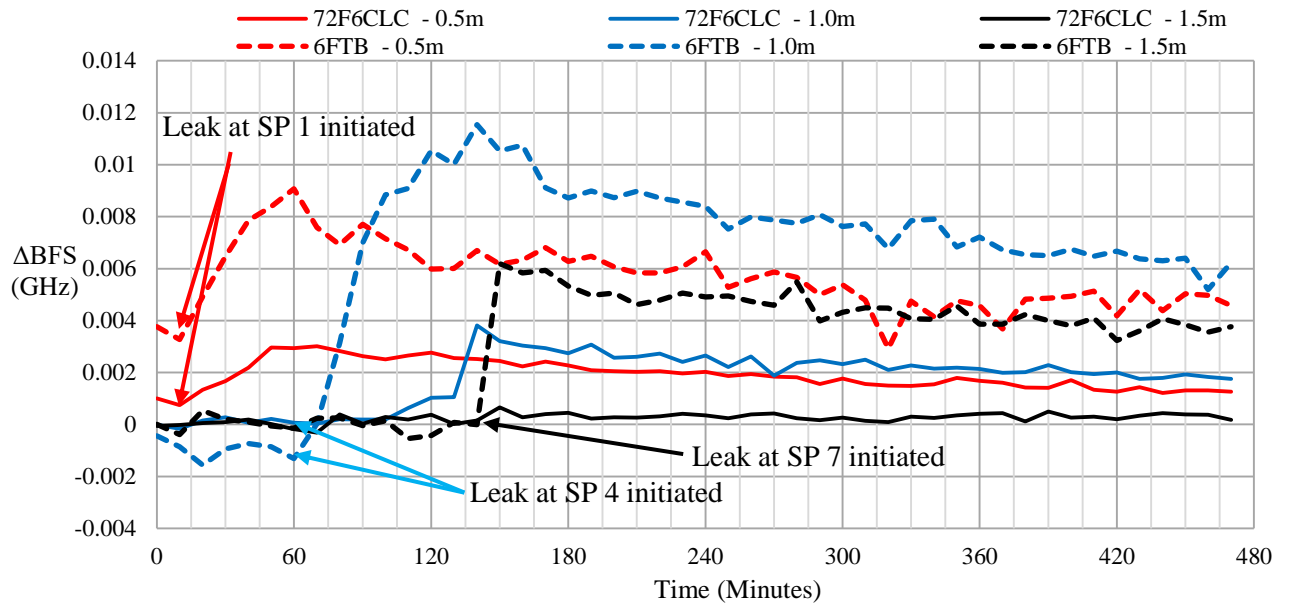


Figure 4.42. Time domain plot of the  $\Delta$ BFS at the three leak points for the two cables (72F-6C-LC and 6F-TB) as the leak test was conducted.

Figure 4.42 shows a change in the BFS at the three leak points for the two different cables as water is introduced to simulate three separate leaks. While water is being input into the trench the BFS undergoes a positive change, but after the introduction of water has ended the signal begins to decay. This is attributed to the fact that the water introduced into the trench is generating both a temperature effect as well as a strain effect in the soil. The temperature effect is only present while the water is being introduced into the soil and once the flow of water has ceased, the temperature effect dissipates until a temperature equilibrium has been reached in the soil. Once the temperature has equilibrated, only the strain effect present in the soil surrounding the FO cables remains.

Table 4.1 shows the cable type, length-ordinate and standpipe number for the leaks detected in **Error! Reference source not found.** and Figure 4.42.

Table 4.1. Summary of the length-ordinates, trench segment depths, cable types and standpipe number at the 3 leak points.

Cable Type	Trench Segment Depth	Length-ordinate (m)	Standpipe
72F6CLC	- 0.5m	8.52	1
72F6CLC	- 1.0m	59.25	4
72F6CLC	- 1.5m	109.71	7
6FTB	- 1.5m	196.24	7
6FTB	- 1.0m	245.87	4
6FTB	- 0.5m	296.39	1

Due to the nature of the experiment, the temperature effect attributed to the introduction of water dissipates after the inflow of water has ceased. However, on a working pipeline this would not be the case. A working pipeline would continue to leak until it is repaired. Therefore, the temperature effect demonstrated in Figure 4.42 would be present without dissipation taking place. This would, theoretically, make the detection of leaks more likely on a working pipeline as both the effect of strain and temperature would be prominent for detection by the FO cables.

## 4.5 COMPARISON OF THE RESPONSE OF DIFFERENT FO CABLES

To compare the results of the various cables the results of the second leak test conducted are discussed for each cable. In addition, due to the prominence given to the peaks by the squared relative plots, these shall be used in the discussion for the comparison between the different cables.

### 4.5.1 STRAIN TO 72F-6C-LC CABLE

The strain to 72F-6C-LC cable results are depicted in Figure 4.43. The order of the strain cable and the 72F-6C-LC cable were swapped due to the plugs in the interrogator being swapped around.

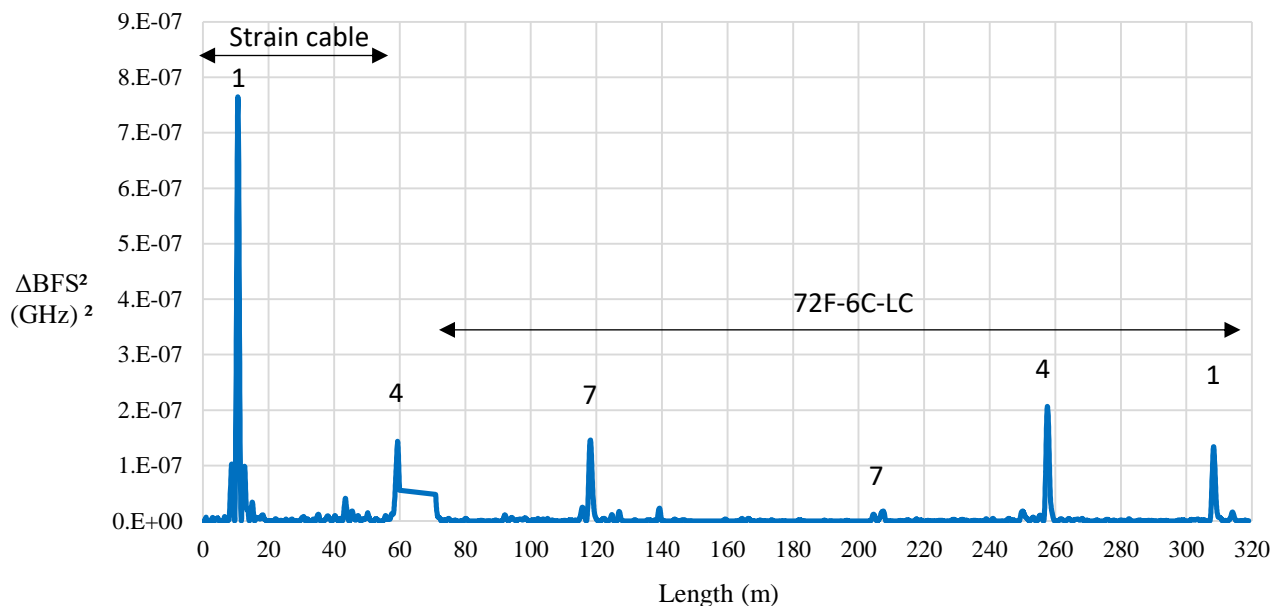


Figure 4.43. Results of the second leak test measured using the strain to 72F-6C-LC FO cable.

The strain FO cable worked well as a strain detection sensor, as it was able to give a stronger response when compared against the 72F-6C-LC cable. Due to the short length of the strain cable, this cable is only able to detect leaks that occurred in the first 50m segment. The peak occurring at 60m is a partial detection of a leak by the strain cable, but it is hindered by the highly variable BFS of the splice that also occurs in that region and is therefore ignored in this discussion.

The strain cable, however, when compared to the 6F-TB cable did not register as great a response as the 6F-TB cable. This occurrence is interesting because the strain cable, as its name implies, is a cable

designed to measure strain, typically for applications where it is embedded in concrete. As such, the cable is relatively stiff in bending. The lesser response registered by the strain cable is due to the stiffness of the sheath housing the strain cable's optical fibre. The 6F-TB cable has a more flexible protective sheath, allowing its optical fibres to undergo greater strain than the strain cable, due to soil displacement. The 72F-6C-LC cable registered a lesser response than that of both the strain cable and the 6F-TB cable. The 72F-6C-LC cable gave an interesting response to the leaks induced in the trench in this instance. In the latter half of the profile the 72F-6C-LC cable detected the leaks at standpipes 1 and 4 with significant certainty, but not at standpipe 7. However, in the first half of the profile it is clear that the 72F-6C-LC cable did detect the leak at standpipe 7. Referring to the experimental setup shown in (Figure 3.4), it can be seen that the 72F-6C-LC FO cable runs on opposite sides of the trench, looping around at the end of the trench. Therefore, the direction of the optic signal heads away from the interrogator on the input side, and returns to the interrogator after the loop, giving rise to a double detection response. The response registered at standpipe 7 with the 72F-6C-LC cable is attributed to the one half of the cable picking up the effect of water ingress on the one side of the trench, but not on the opposite side at the same standpipe location. It is therefore necessary that the FO cable be strategically placed along a pipeline to obtain maximum exposure to water due to a leaking pipe.

#### 4.5.2 4F-DC-LC CABLE

The results of the first leak test output by the 4F-DC-LC cable are displayed in Figure 4.44.

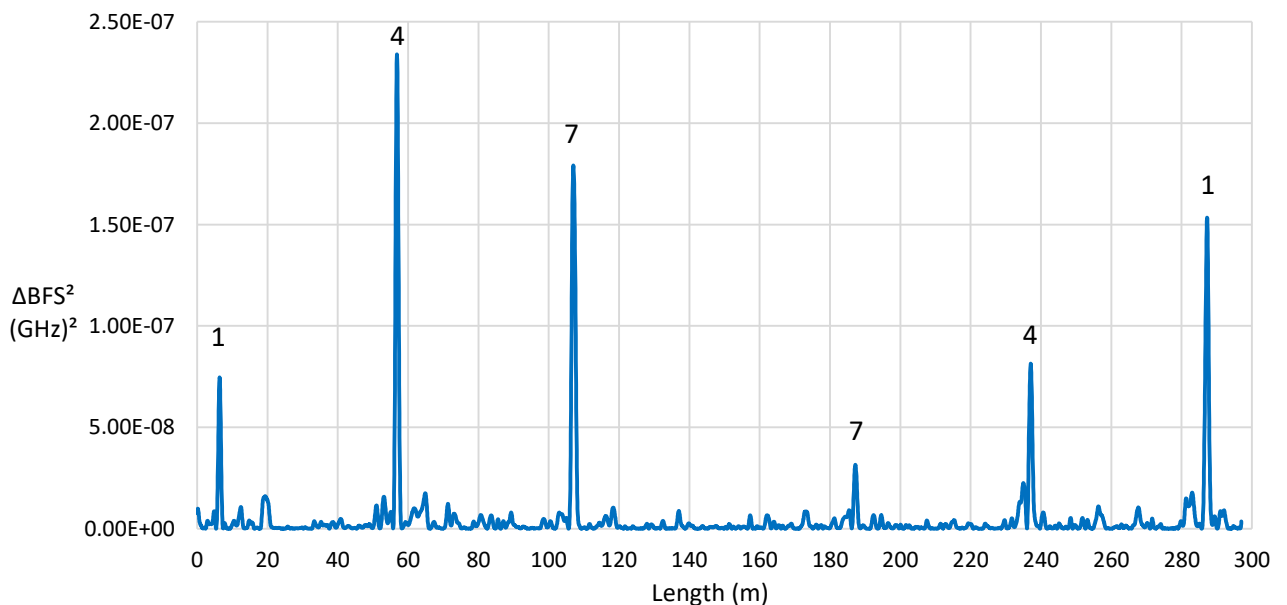


Figure 4.44. Results of the second leak test measured using the 4F-DC-LC FO cable.

The 4F-DC-LC cable, due to it being a loose core cable, gave a very similar performance to the 72F-6C-LC cable. The expected result would be that the 4F-DC-LC cable would give greater  $\Delta BFS$  responses due to it being thinner and less stiff, and therefore more affected by soil movement than the 72F-6C-LC cable. However, due to the gel matrix surrounding the fibre in the 4F-DC-LC cable, the

optical fibres are shielded from strain effects due to soil displacement around the FO cables. The two loose core cables therefore produced similar responses due to both being affected almost entirely by the temperature effect of the water introduction into the trench and hardly by the strain effects. Nonetheless, the 4F-DC-LC cable was able to detect each leak introduction point with certainty, despite its reduced sensitivity to strain effects.

### 4.5.3 2F-TB CABLE

The results of the first leak test from the 2F-TB cable are displayed in Figure 4.45.

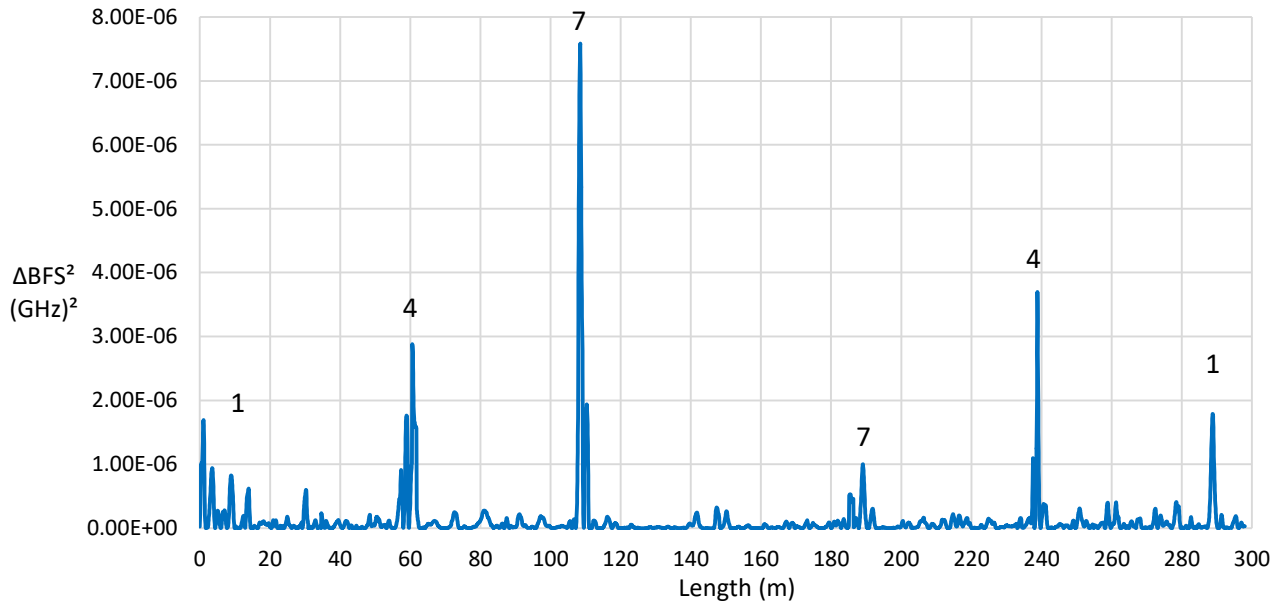


Figure 4.45. Results of the second leak test measured using the 2F-TB FO cable.

The 2F-TB cable and the 6F-TB cable both produced the largest responses of any of the cable types. The TB cables consistently yielded squared  $\Delta\text{BFS}$  responses which were an order of magnitude greater than the LC cables and the strain cable. A problem with the TB cables is that the random noise generated by the TB cables is significantly greater than the noise generated by the LC and strain cables. As can be seen in Figure 4.45 at standpipe 1 on the left side of the profile, the leak was not able to be detected because of a noisy output in the region of standpipe 1. The leak was, however detected at standpipe 1 on the right-hand-side of the profile at  $L = 290\text{m}$ . The TB cables performed the best as leak detection sensors. However, it is necessary that signal processing techniques be developed to mitigate noise and amplify the  $\Delta\text{BFS}$  response triggered by a leak.

The results of the second leak test produced by the 6F-TB to 72F-6C-LC FO cable are shown in Figure 4.46.

#### 4.5.4 6F-TB TO 72F-6C-LC CABLES

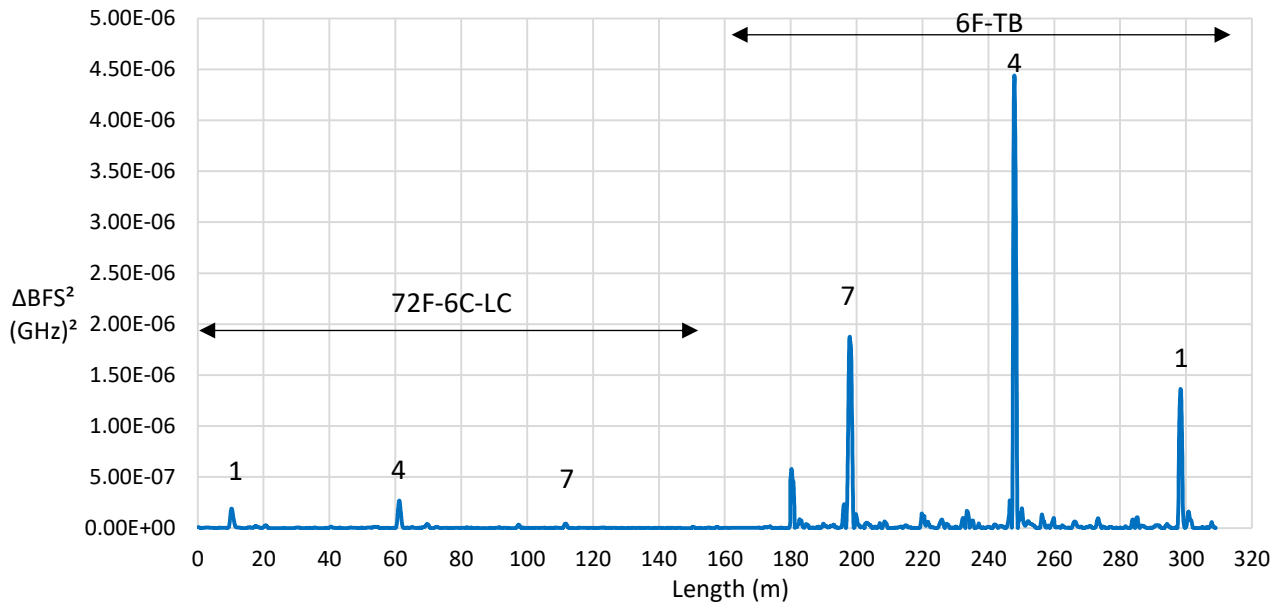


Figure 4.46. Results of the second leak test measured using the 6F-TB to 72F-6C-LC FO cable.

It is interesting to note in Figure 4.46 that the 6F-TB cable does not experience as much noise surrounding its peaks resulting from the leaks as the 2F-TB cable does. This may be attributed to the fact that the 6F-TB cable has 6 optical fibres as opposed to the 2 optical fibres in the 2F-TB cable, resulting in less optical fibre movement in the sheath of the 6F-TB cable. Figure 4.46 also gives a good perspective of the superior performance of the 6F-TB cable compared to the 72F-6C-LC cable.

Figure 4.47 summarises the maximum squared  $\Delta BFS$  response registered by each cable type, clearly demonstrating the superiority of the TB cables' performance as a leak detection sensor.

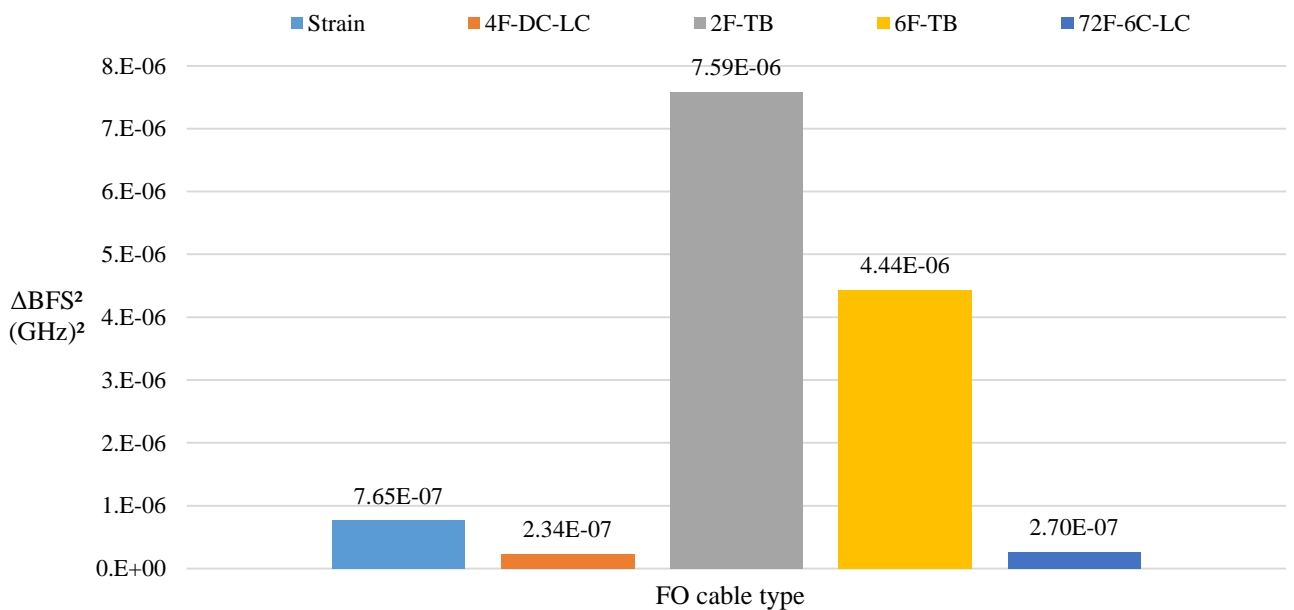


Figure 4.47. Bar graph showing the maximum  $\Delta BFS^2$  caused by a leak registered in each cable type.

## **4.6 DETECTION OF AN UNKNOWN LEAK LOCATION AND TIME OF OCCURRENCE**

The proposed BFS FO cable leak detection system is required to both detect where a leak has occurred, which has been successfully demonstrated, and when a leak starts. Unlike the first set of tests, the location and time of a leak occurrence may initially not be known, but instead will need to be detected. Given that a change in soil moisture content produces a  $\Delta$ BFS response registered by FO cables, an analysis of the data output by the BFS interrogator in the time domain should provide a means of detecting when a leak occurs. Thereafter, by analysing the data from the flagged time in the FO cable length domain, the location of the leak can be determined.

### **4.6.1 UNKNOWN LEAK DETECTION METHODOLOGY**

To simulate an unknown leak 50L of water was deposited into an unknown standpipe at an unknown time. This was a separate leak event to the first and second leak test.

A change in soil moisture content should cause a significant change in the BFS registered by a FO cable due to both changes in temperature and soil strain effects. By searching for a large  $\Delta$ BFS in the time domain that does not fit into the expected trend of the  $\Delta$ BFS output data, an unknown leak can be identified. The following method is proposed:

- BFS profiles can be logged every two hours for the FO cable being used as the sensor.
- Two 24-hour baselines can continuously be compared against one another every 2 hours, as depicted in Figure 4.48, by subtracting the previous average BFS profile from the latest average BFS profile.
- By comparing the two 24-hour baselines, a change in the behaviour of the FO cable can be detected as a large  $\Delta$ BFS output. A centred moving average can be applied to the relative BFS profile to rid the profile of unwanted noise and to zero the profiles with respect to the length axis. The  $\Delta$ BFS values can then be squared to make negative  $\Delta$ BFS values positive and to give more bias towards the larger  $\Delta$ BFS values.
- For every relative BFS profile created every 2 hours, the maximum  $\Delta$ BFS<sup>2</sup> value can be obtained for each time step.

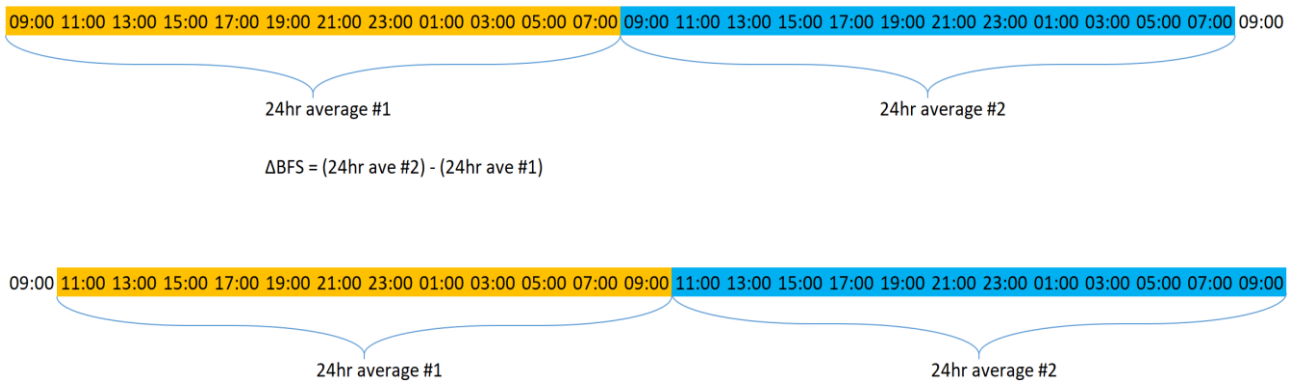


Figure 4.48. Comparison of two 24-hour average BFS profiles. The orange times formulate the baseline and the blue times are the latest observation. Every 2 hours the data used to formulate the baseline and the latest observation shifts forward by 2 hours.

The results of performing the preceding steps on a set of data from the 2F-TB cable from the 14<sup>th</sup> of April 2021 to the 11<sup>th</sup> of May 2021 is shown in Figure 4.49. The 2F-TB cable was chosen to demonstrate this methodology as the 2F-TB cable produced the strongest leak detection response.

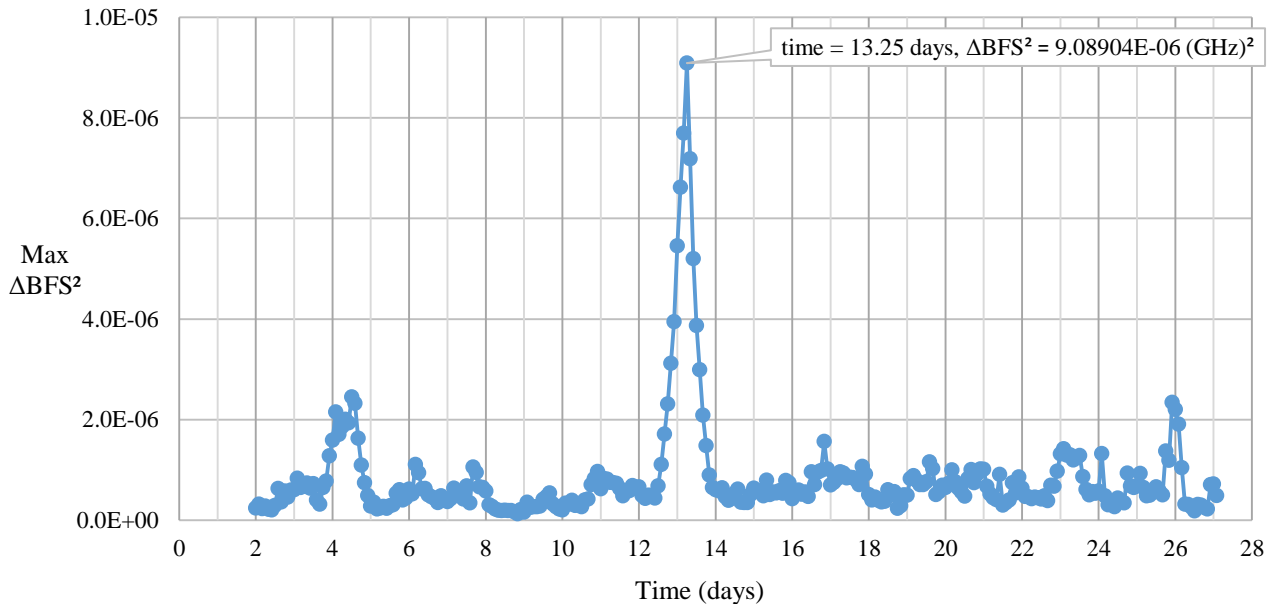


Figure 4.49. Maximum  $\Delta\text{BFS}^2$  obtained for each time step (2F-TB).

The peak in the maximum  $\Delta\text{BFS}^2$  vs time curve that occurs in Figure 4.49, centred about time  $t = 13.25$  days, clearly deviates from the values preceding and following it. The maximum  $\Delta\text{BFS}^2$  value depicted in Figure 4.49 can occur anywhere along the length of the FO cable. By investigating the relative BFS profile that occurs at time = 318 hours it can be determined whether or not the FO cable has detected a leak. A leak detected by the FO cable would appear as a peak in the  $\Delta\text{BFS}$  when plotted against the length of the FO cable. The plot of the relative BFS profile,  $\Delta\text{BFS}^2$  vs length, that occurs at time  $t = 318$  hours is shown in Figure 4.50.

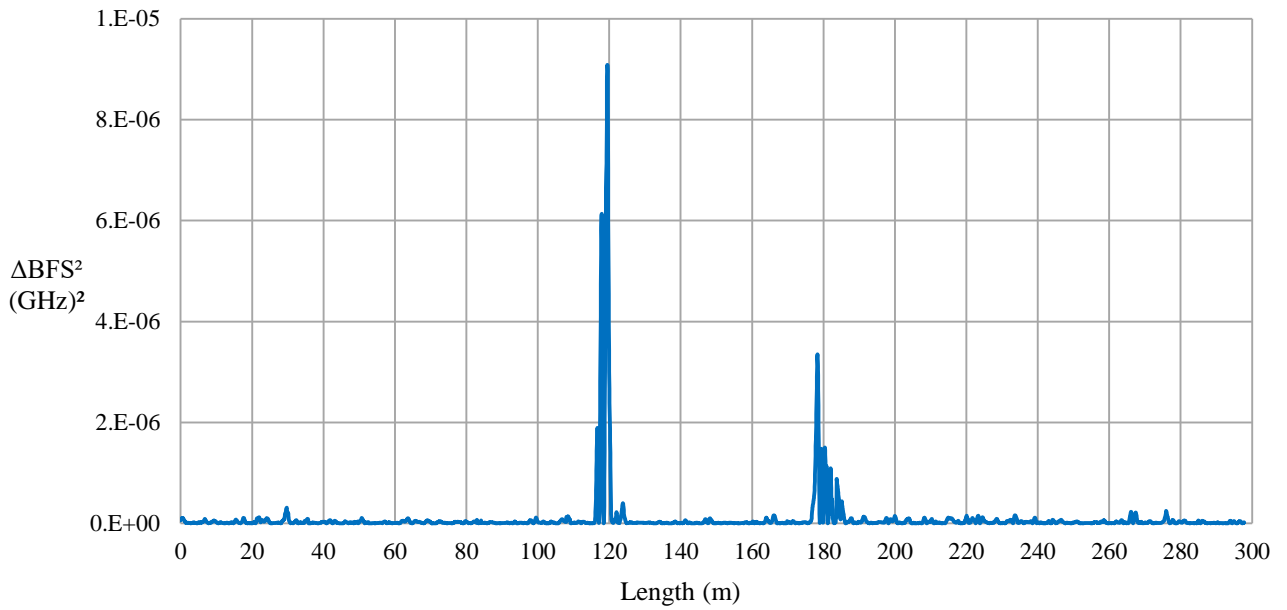


Figure 4.50. Relative BFS profile that occurs at time  $t = 13.25$  days (2F-TB).

As can be seen in Figure 4.50 there are definitive peaks in the  $\Delta\text{BFS}^2$  centred about length-ordinates 120m and 180m. These peaks correspond to the location of standpipe 8. As the experimental trench on the Hillcrest Campus is 150m long and the cable loops back along the trench, the cable gives a double response that is mirrored about the midpoint of the cable corresponding to the end of the trench. The response occurring about length-ordinates 120m and 180m is a good indicator that a change in soil moisture content has occurred in the soil surrounding the FO cable.

By acquiring the length-ordinate at which the maximum  $\Delta\text{BFS}^2$  occurs at each time step, the location of the maximum  $\Delta\text{BFS}$  can be determined along the length of the FO cable. The plot depicted in Figure 4.51 shows how the length-ordinate, at which the maximum  $\Delta\text{BFS}$  occurs, varies as time progresses.

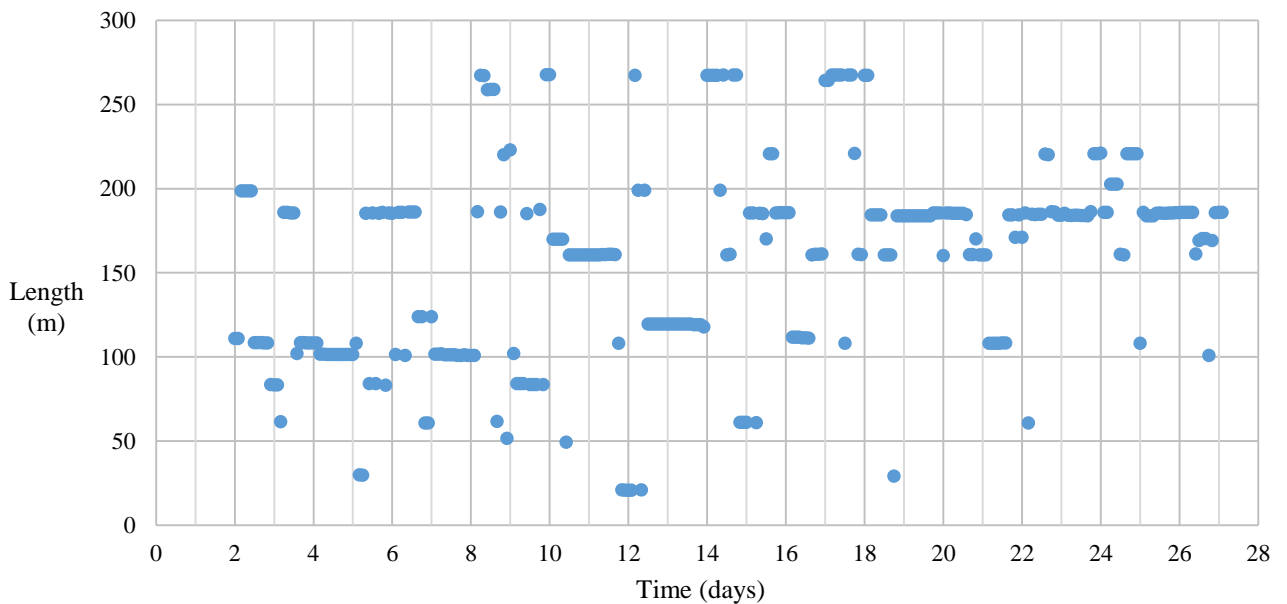


Figure 4.51. Plot of length-ordinate where the maximum  $\Delta\text{BFS}^2$  occurs against time (2F-TB).

The significance of Figure 4.51 is that it shows the extent of time for which the maximum  $\Delta BFS$  remains in a particular region. By observing the amount of time that the maximum  $\Delta BFS$  occurs in a specific region along the FO cable and noting whether the maximum  $\Delta BFS$  exceeds the expected range of maximum  $\Delta BFS$  values in that time frame, it can be inferred whether a leak has occurred in the region that is exhibiting the maximum  $\Delta BFS$ . Stated another way: if the maximum  $\Delta BFS$  occurs in the same region over a period of 24 hours (as the  $\Delta BFS$  peak due to a leak grows and decays over a period of 24 hours, shown in Figure 4.49), and the maximum  $\Delta BFS$  that occurs in that region is outside the expected range of maximum  $\Delta BFS$  values, then these simultaneous occurrences can indicate that a leak has occurred in the stipulated region. This is demonstrated in Figure 4.52 and Figure 4.53.

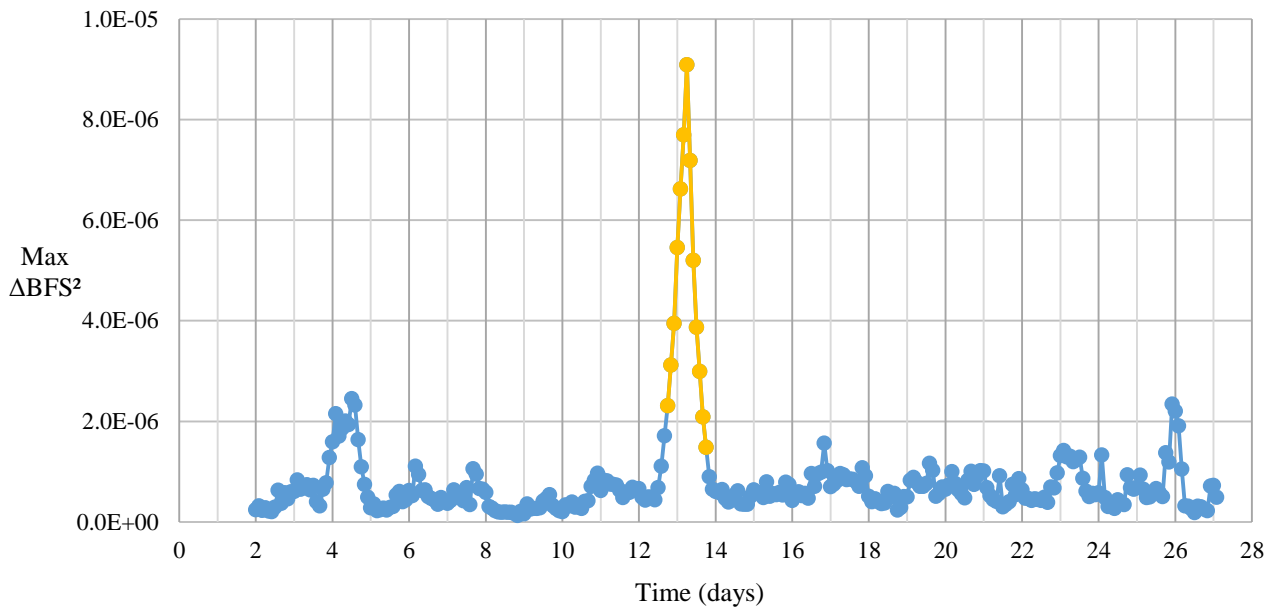


Figure 4.52. Replot of Figure 4.49 highlighting the 24 hours surrounding the leak-peak (2F-TB).

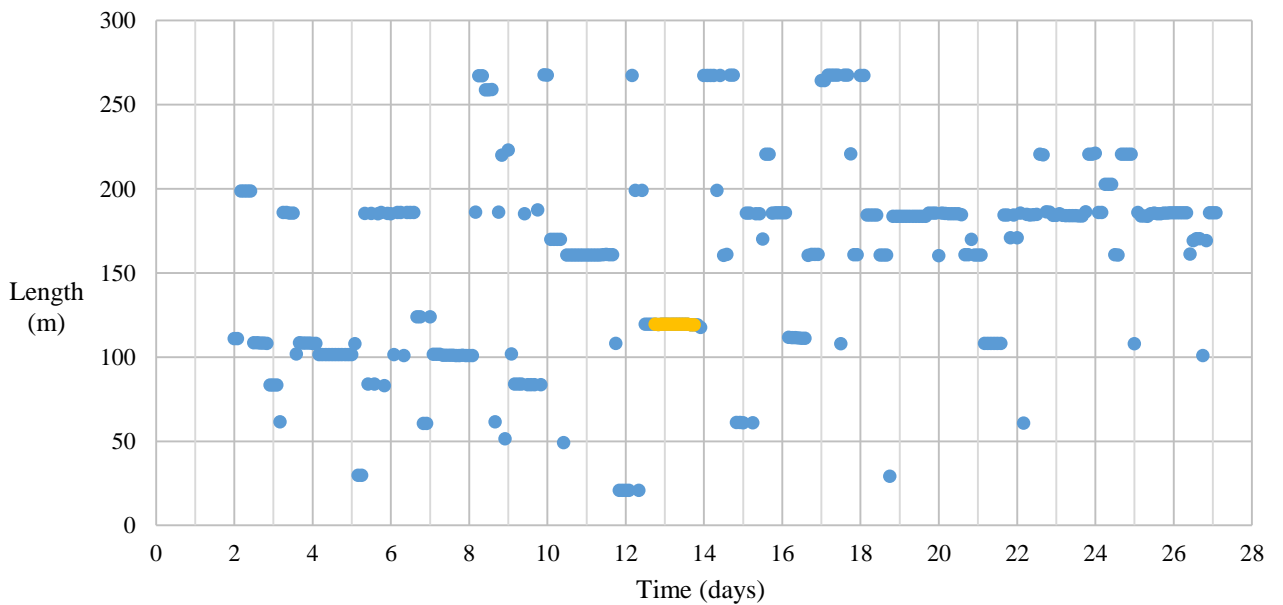


Figure 4.53. Replot of Figure 4.51 highlighting the 24 hours surrounding the leak (2F-TB).

The highlighted peak in Figure 4.52 lies outside of the expected maximum  $\Delta BFS$  values and it is complimented by the maximum  $\Delta BFS^2$  occurring constantly over the 24 hour period in the region of the

length-ordinate  $L = 120\text{m}$ . The simultaneous occurrence of a maximum  $\Delta\text{BFS}$  response being greater than the expected maximum  $\Delta\text{BFS}$ , and the maximum occurring in a single region of the 24 hour period of the peak are good indicators that the leak occurred in the flagged region. This simultaneous occurrence of a maximum  $\Delta\text{BFS}$  value exceeding the expected maximum occurring in the same region over an extended period of time would be a valid check to incorporate into a BFS FO cable leak detection system algorithm.

By plotting a 3-Dimensional (3D) graph of the  $\Delta\text{BFS}^2$ , using time and length as the two horizontal axes, the behaviour of the  $\Delta\text{BFS}^2$  can be assessed over the whole cable length across the entire timeframe in question. The 3D plot of the  $\Delta\text{BFS}^2$  for the 2F-TB cable is shown in Figure 4.54.

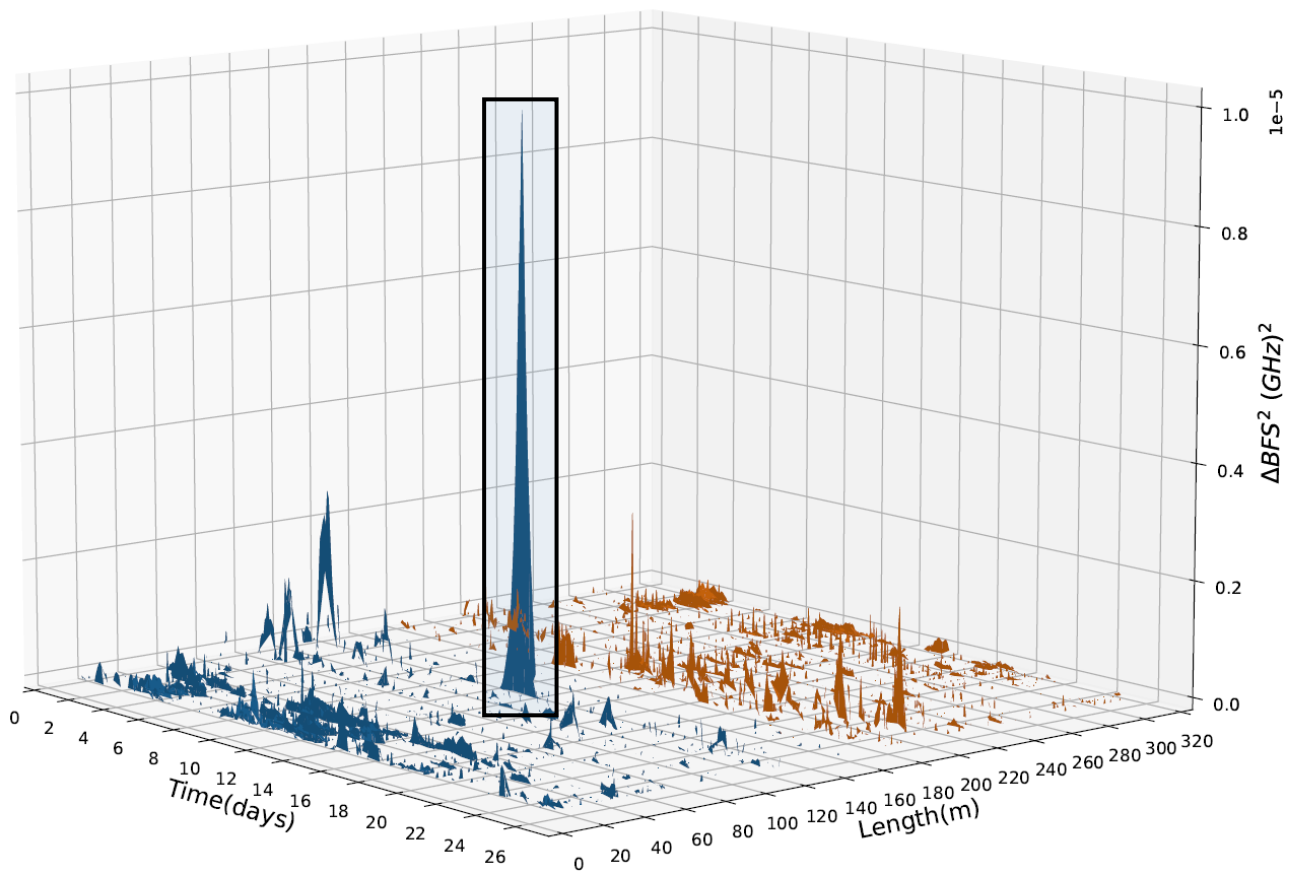


Figure 4.54. 3D plot of the  $\Delta\text{BFS}^2$  for the 2F-TB cable plotted against time and length, excluding  $\Delta\text{BFS}^2$  values below  $1\text{e-}7$  (GHz) $^2$ . The detected leak is highlighted by the rectangle. The blue section corresponds to the first 150m of the cable and the red section to the second 150m of the cable.

From Figure 4.54 the time of origin and location of occurrence of the  $\Delta\text{BFS}^2$  leak peak can be seen relative to the  $\Delta\text{BFS}^2$  outputs at different times and length ordinates. This provides a good visual representation of how the  $\Delta\text{BFS}^2$  produced by the leak stands out clearly from the  $\Delta\text{BFS}^2$  obtained where no leak occurred.

By investigating how the BFS behaves at the length-ordinates where the leak is being detected, a deeper understanding of what is happening to the BFS because of the leak can be acquired. The BFS at the length-ordinate  $L = 119.53$  is plotted in Figure 4.55.

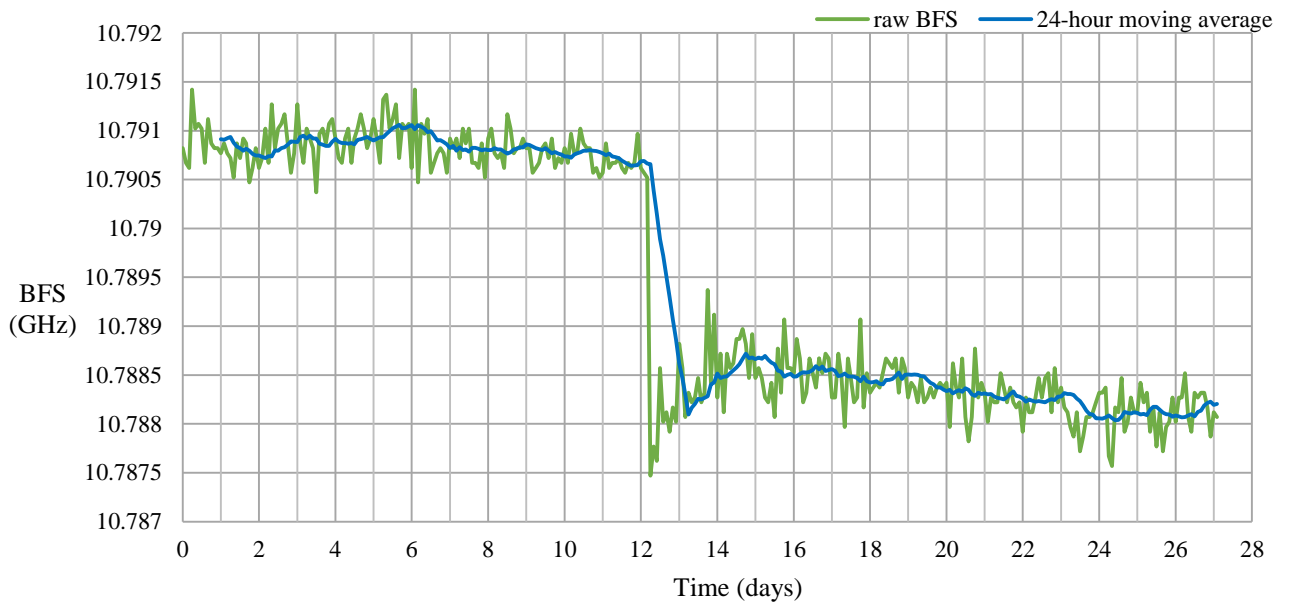


Figure 4.55. Raw BFS output and a 24-hour moving average computed at the length-ordinate  $L = 119.53\text{m}$ .

The BFS undergoes a noticeable change at time  $t = 12$  days when the leak was imposed. This drastic change in the BFS is what gives rise to the waxing and waning peak. By plotting the difference between each BFS value separated by 24 hours, Figure 4.56 is generated.

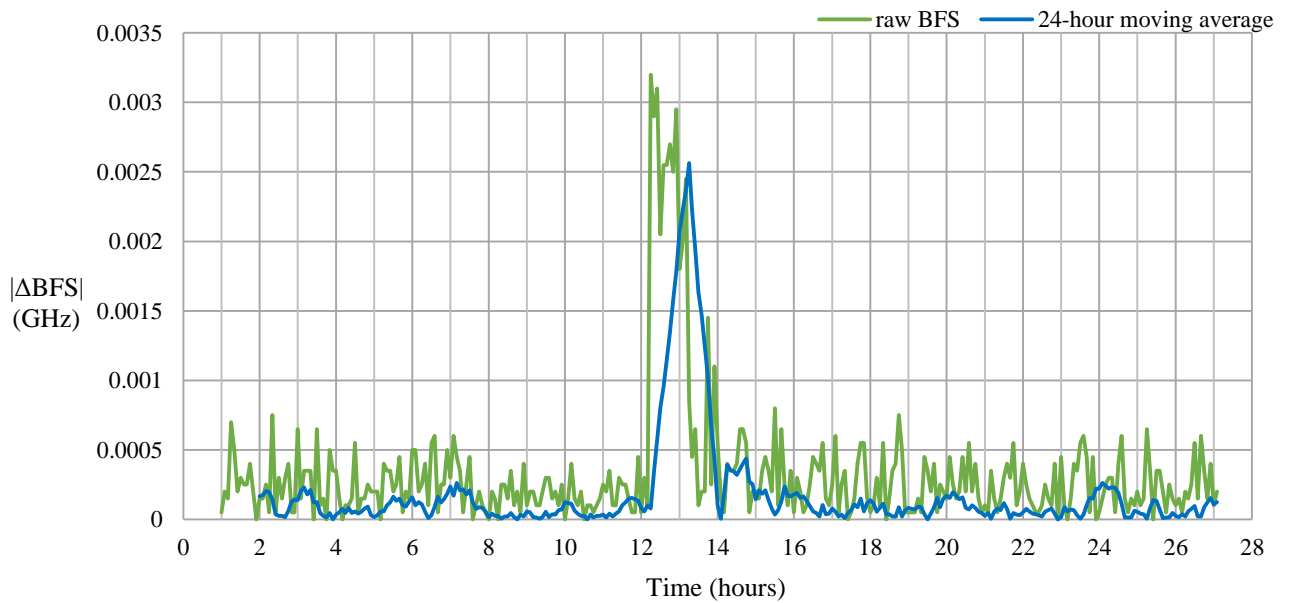


Figure 4.56. 24 hour difference computed for the raw BFS and 24-hour moving average shown in Figure 4.55.

The peaks for the two curves plotted in Figure 4.56 show the timing of when the leak took place. It is this computation of subtracting previous BFS readings from current BFS readings that is used to detect the time at which a leak occurs.

## 4.6.2 COMPARISON OF PERFORMANCE OF DIFFERENT CABLES

### 4.6.2.1 STRAIN TO 72F-6C-LC CABLE

Due to the fact that the strain cable only reached to standpipe 4 and the blind leak was imposed at standpipe 8, the strain cable did not take part in the blind leak test. Thus the 72F-6C-LC cable acted as the sensor along the strain-to-72F-6C-LC cable loop. As can be seen in Figure 4.57, the 72F-6C-LC cable was able to detect when the leak occurred as a deviation from the maximum expected  $\Delta\text{BFS}^2$  centred about the time of  $t = 13.25$  days.

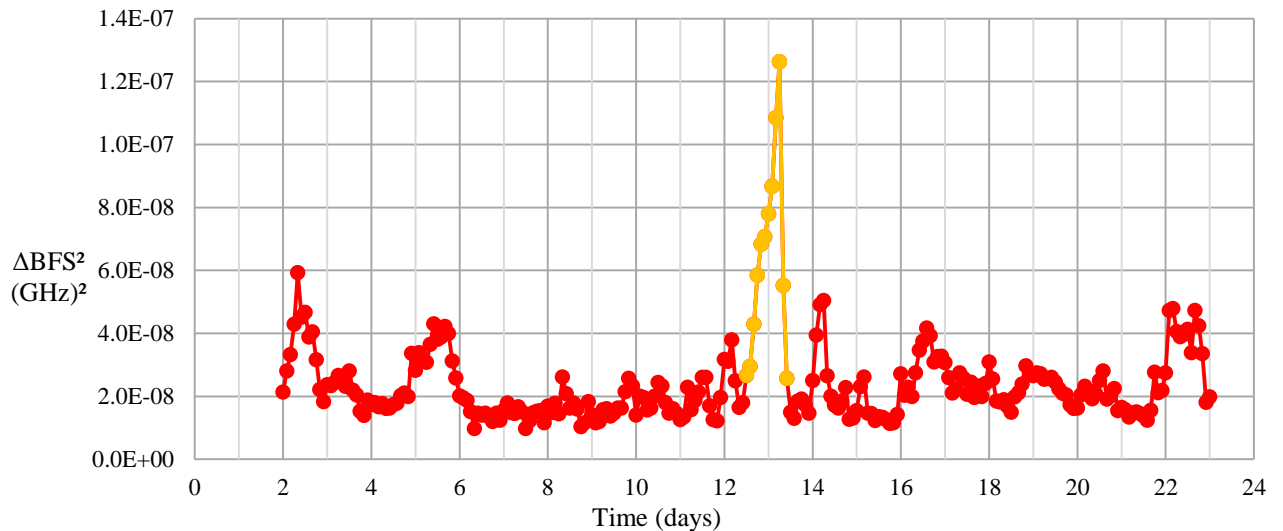


Figure 4.57. Maximum  $\Delta\text{BFS}^2$  for each time step along the 72F-6C-LC cable segment.

In comparison to the 2F-TB, the peak  $\Delta\text{BFS}^2$  value registered by the 72F-6C-LC cable, relative to the expected  $\Delta\text{BFS}^2$  value, grows to a lesser extent. This shows the reduced sensitivity of a LC cable to an imposed leak due to the reduced influence that soil strains have on the cable.

The 72F-6C-LC cable registered the maximum  $\Delta\text{BFS}^2$  around the length-ordinate  $L = 127\text{m}$ , shown in Figure 4.58, over the period of the waxing and waning of the peak in Figure 4.57.

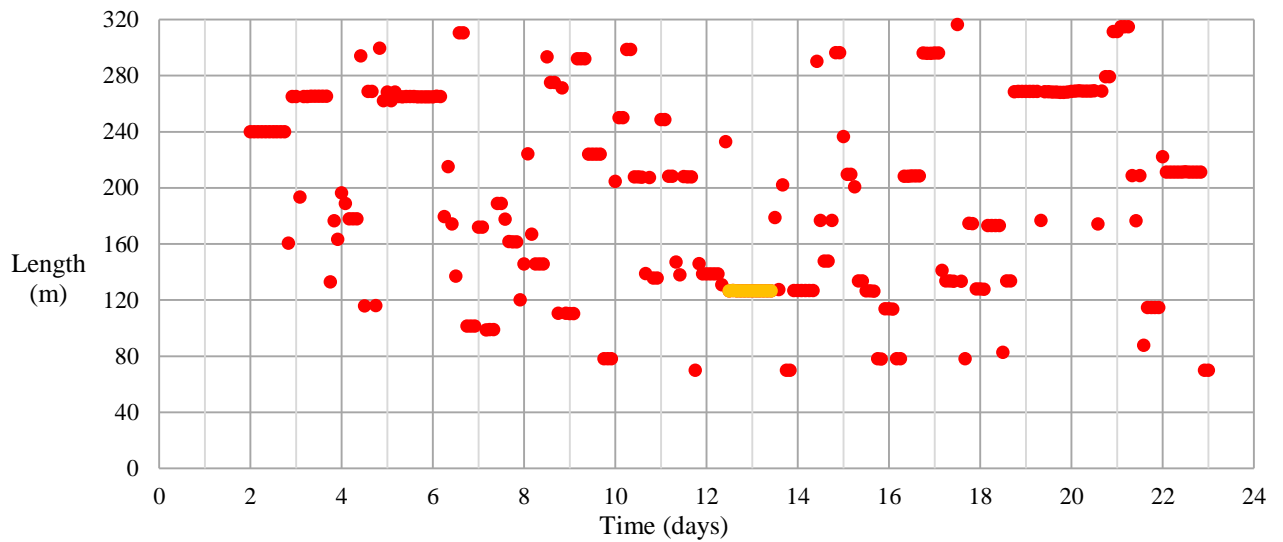


Figure 4.58. Length-ordinate of the maximum  $\Delta\text{BFS}^2$  at each time step along the 72F-6C-LC cable segment.

Observing the  $\Delta\text{BFS}$  along the length of the cable at time  $t = 13.25$  days the peak in the  $\Delta\text{BFS}$  value caused by the leak is clearly evident at length-ordinate  $L = 127\text{m}$ . There is an additional peak around  $L = 195\text{m}$ , due to the double response nature of the setup, but it is not as great as the peak registered at  $L = 127\text{m}$ . This is because the opposite end of the trench to where the standpipe was installed will experience less temperature and strain variation than the end at which the standpipe was installed.

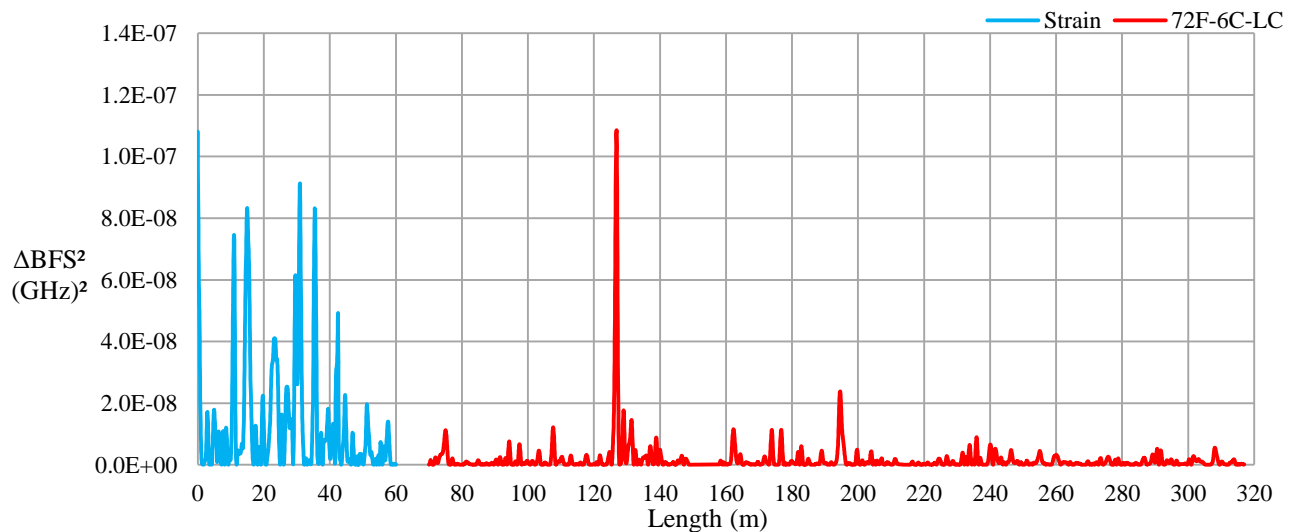


Figure 4.59.  $\Delta\text{BFS}^2$  along the 72F-6C-LC cable at time  $t = 13.25$  days.

Despite being a LC cable, the 72F-6C-LC cable was able to give a satisfactory result as a leak detection sensor, being able to both confidently detect when the leak occurred, and find its location. It can be inferred that temperature effects do play a significant role in the  $\Delta\text{BFS}$  cause by water ingress into the soil surrounding a FO cable. A FO leak detection system could therefore operate solely by detection temperature changes caused by water propagation through the surrounding soil.

#### 4.6.2.2 4F-DC-LC CABLE

The maximum  $\Delta\text{BFS}$  measured along the length of the 4F-DC-LC cable is shown in Figure 4.60.

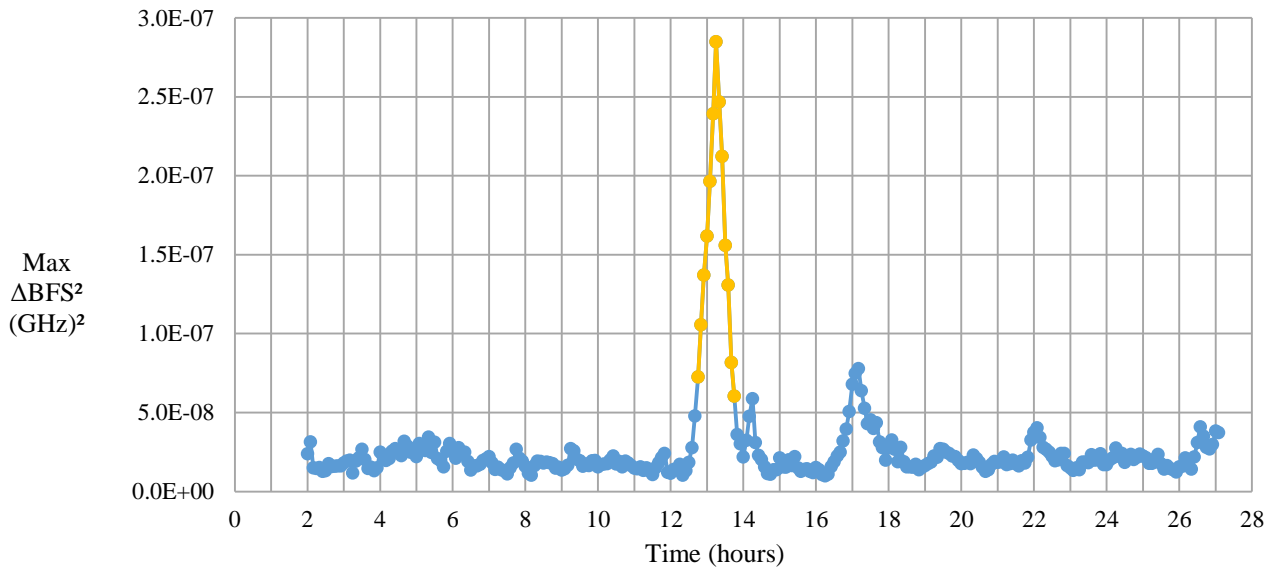


Figure 4.60. Maximum  $\Delta\text{BFS}^2$  for each time step along the 4F-DC-LC cable.

The 4F-DC-LC cable was able to register a strong deviation from the expected maximum  $\Delta\text{BFS}$  along its length in response to the imposed leak, centred about time  $t = 13.25$  days. The ratio of the peak maximum  $\Delta\text{BFS}$  output to the baseline maximum  $\Delta\text{BFS}$  output is more similar to that of the 2F-TB cable than to the 72F-6C-LC cable. The  $\Delta\text{BFS}^2$  output range of the LC and TB cables also seem to differ by an order of magnitude, both with respect to baseline and imposed leak output.

The location of the maximum  $\Delta\text{BFS}$  along the length of the 4F-DC-LC cable is shown in Figure 4.61.

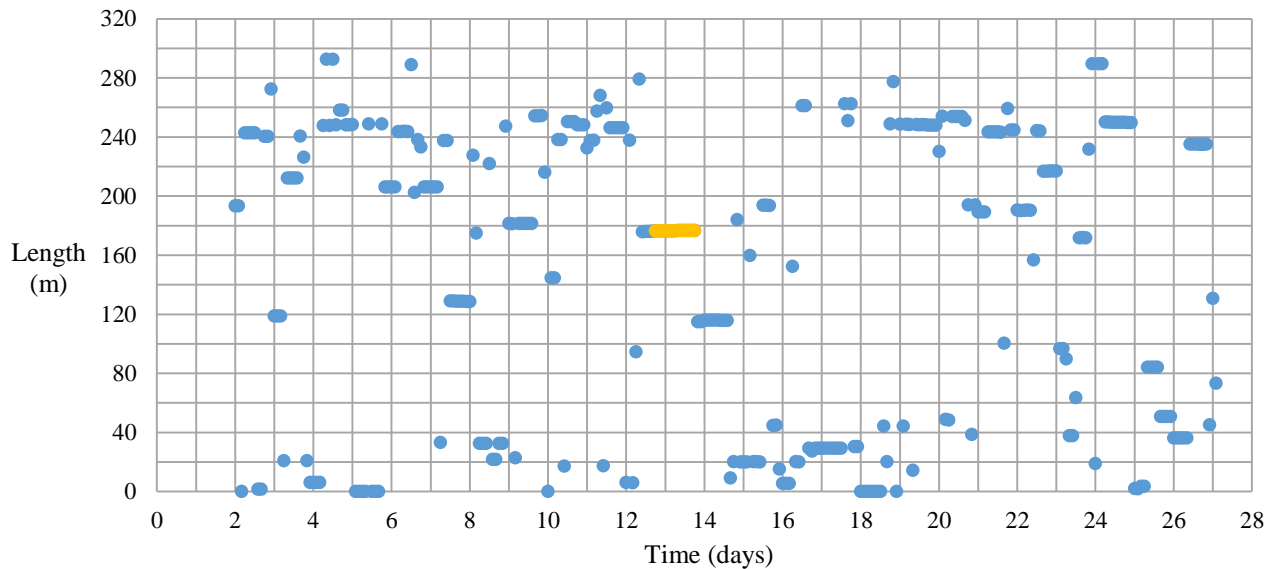


Figure 4.61. Length-ordinate of the maximum  $\Delta\text{BFS}^2$  at each time step along the 4F-DC-LC cable.

As can be seen in Figure 4.61, the length-ordinate at which the maximum  $\Delta\text{BFS}$  occurs during the waxing and waning of the leak-peak in Figure 4.60 is about length-ordinate  $L = 176.5\text{m}$ . This length-ordinate is in agreement with that obtained from the 72F-6C-LC cable and the 2F-TB cable, i.e. that the leak occurred at standpipe 8. Observing the  $\Delta\text{BFS}$  in the length domain along the length of the 4F-DC-LC cable, shown in Figure 4.62, two peaks can be seen about  $L = 115.5\text{m}$  and  $L = 176.5\text{m}$ .

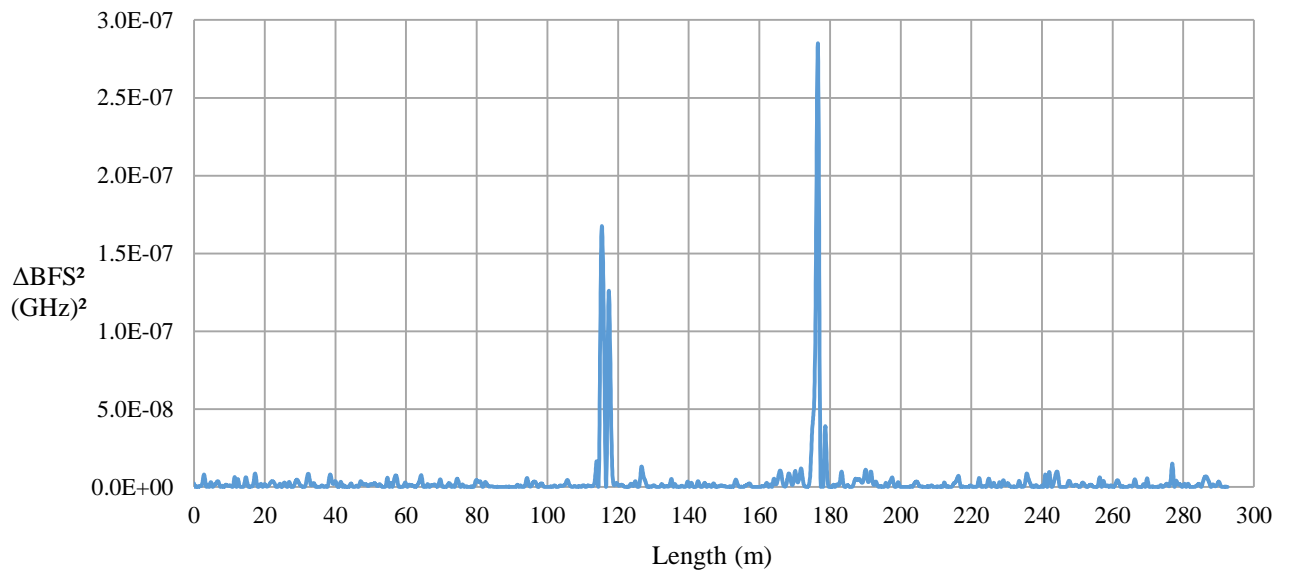


Figure 4.62. .  $\Delta\text{BFS}^2$  along the 4F-DC-LC cable at time  $t = 13.25$  days.

Again, the result acquired from the 4F-DC-LC cable shows that LC cables are indeed able to acts as leak detection sensors, and quite proficiently at that.

#### 4.6.2.3 2F-TB CABLE

As was stated, the 2F-TB cable produced both a baseline and a leak-peak that is an order of magnitude greater than the outputs given by the LC cables. However, this greater sensitivity of the 2F-TB cable over the LC cables does not necessarily give the 2F-TB cable an advantage over the LC cables. It has been shown that the 72F-6C-LC cable, the 4F-DC-LC cable and the 2F-TB cable are all capable of detecting a leak imposed on the system.

#### 4.6.2.4 6F-TB TO 72F-6C-LC CABLES

As the 72F-6C-LC cable has already been discussed, this section will focus on the 6F-TB cable.

The 6F-TB cable did not perform well in this test. As can be seen in Figure 4.63, the noise that is produced during the baseline operation of the cable was similar in magnitude to that of the maximum  $\Delta\text{BFS}$  leak-peak imposed about time  $t = 318$  hours.

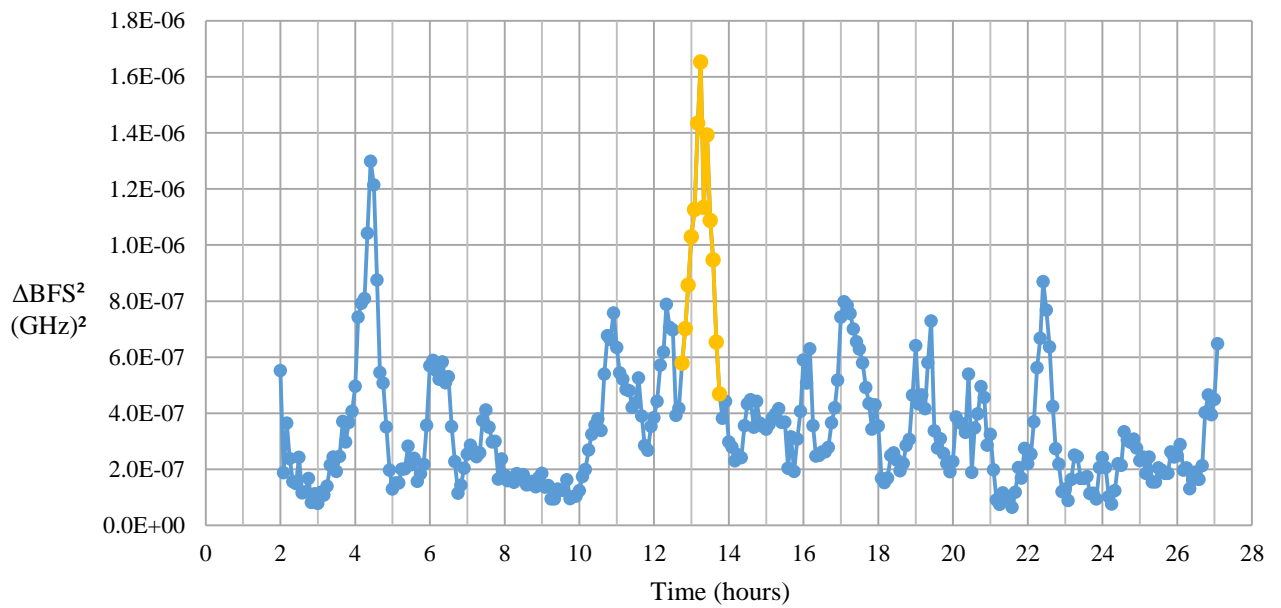


Figure 4.63. Maximum  $\Delta\text{BFS}^2$  for each time step along the 6F-TB to 72F-6C-LC cable.

In addition, during the waxing and waning of the leak-peak, the length-ordinate of the maximum  $\Delta\text{BFS}$  did not remain constant as expected. This is shown in Figure 4.64.

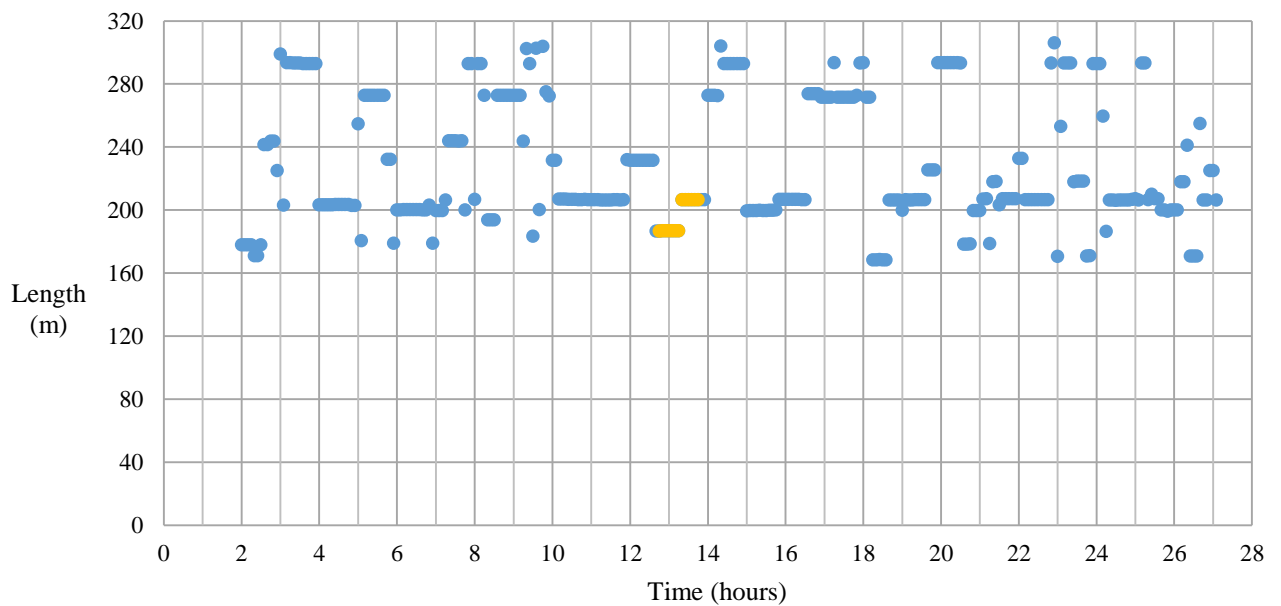


Figure 4.64. Length-ordinate of the maximum  $\Delta\text{BFS}^2$  at each time step along the 6F-TB to 72F-6C-LC cable.

The change in length-ordinate during the waxing and waning of the leak-peak would cause the leak to pass undetected by a leak detection software utilising the correlation between the leak-peak and time of constant length-ordinate. By assessing the  $\Delta\text{BFS}$  in the length domain along the 6F-TB cable shown in Figure 4.65, it becomes clear why there was a change in length-ordinate during the leak-peak phase.

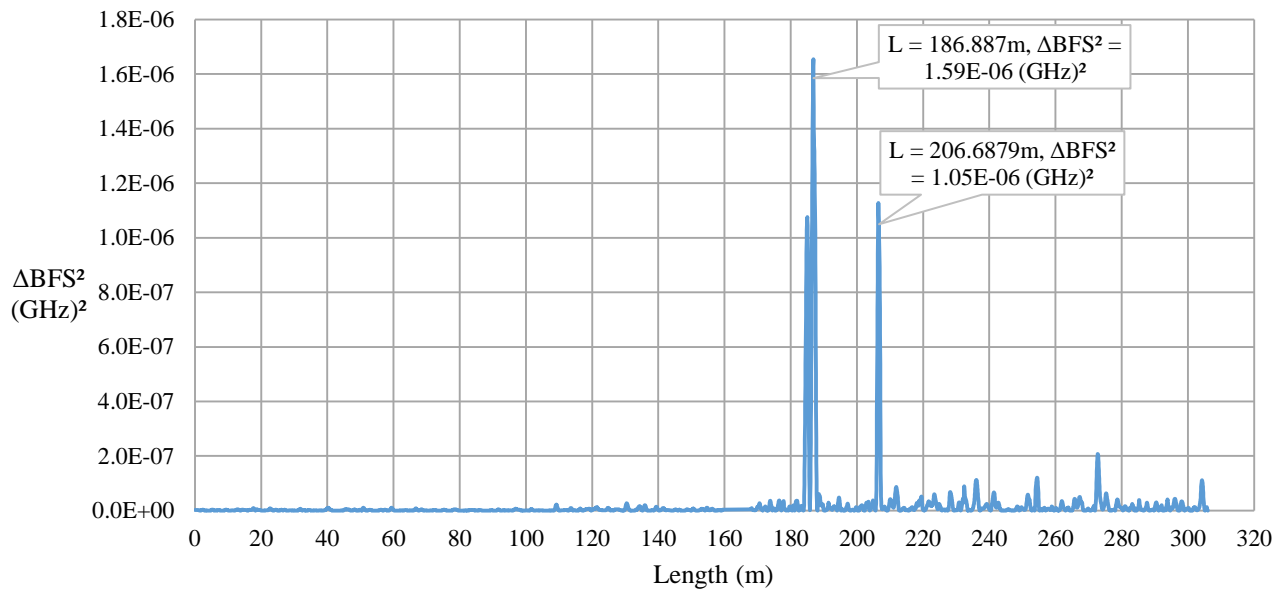


Figure 4.65.  $\Delta\text{BFS}^2$  along the 6F-TB to 72F-6C-LC cable at time  $t = 13.25$  days.

A peak arose about the length-ordinate  $L = 206.5\text{m}$  which should not have developed. By comparing Figure 4.63 and Figure 4.64, this region about  $L = 206\text{m}$  can be viewed as a problem region. Whenever the peak maximum  $\Delta\text{BFS}$  is high, the peak  $\Delta\text{BFS}$  is occurring around  $L = 206\text{m}$ , signifying that this region of the cable experiences more variation than the rest of the cable. The 6F-TB cable was thus able to detect the leak, as seen by the peak around length-ordinate  $L = 187\text{m}$ , but it was hindered by the overly active  $\Delta\text{BFS}$  of the cable around  $L = 206\text{m}$ .

The results of the blind leak test showed that both TB and LC cables were able to detect the leaks. The difference comes from the strength of the leak detection signal of the different cable types. The 2F-TB had a leak detection signal with an order of magnitude of  $10^{-6} (\text{GHz})^2$ , whereas the 4F-DC-LC cable signal was of the order of magnitude  $10^{-7} (\text{GHz})^2$ . The different signal strength is attributed to the TB cable registering both a strain and temperature change response, whereas the LC cable registers only a temperature change response.

## 4.7 PROLONGED LEAK TEST

The leaks described above amounted to releasing 50 litres of water at a given leak point and then assessing whether such a leak can be detected. In reality, leaks will commence and are unlikely to stop, resulting in a much larger volume of water being spilled and over a much longer time frame. For the prolonged/continuous leak test conducted, the standpipe used was standpipe number 5 at the mid-point along the length of the trench. Due to standpipe 5 being used for the first test, the FO strain cable was not included in the first prolonged leak experiment as it only reaches up to standpipe 4. The strain cable was, however, included in the second prolonged leak experiment using standpipe 2.

The flow rate of the continuous stream of water discharged into standpipes 5 and 2 was 40L/hour. The test was continued over the timeframe of 7 days. Thus the total volume of water used in each test is calculated as 6720L of water.

The data collected for the analysis of the test results consists of BFS profiles of the FO cables which were logged every 2 hours from the 11<sup>th</sup> of May 2021 to the 22<sup>nd</sup> of July 2021, and then again from the 22<sup>nd</sup> of July until the 25<sup>th</sup> of August. The prolonged leak tests was started on the 26<sup>th</sup> of May, and in order to determine the time of origin of the impose leak, the 24-hour-average-maximum- $\Delta\text{BFS}^2$  that occurred along the length of each cable was determined for each recorded time step. The time at which the maximum  $\Delta\text{BFS}^2$  deviates from the expected range is when the leak was induce. Thereafter, in order to locate the leak, the length-ordinate of the maximum  $\Delta\text{BFS}$  was extracted from the  $\Delta\text{BFS}$  vs length profiles after the leak had occurred. This methodology was used to process the BFS output given by the cables and the results thereof are compared among the different cable types.

#### 4.7.1 LONG TERM LEAK BFS BEHAVIOUR

Before data manipulation can take place to isolate a leak event, the raw BFS output at a leak point must be observed to understand how the BFS responds to a leak. By comparing the BFS at a leak point against a length-ordinate where no leak was induced it can be seen how a leak influences the BFS as opposed to the expected BFS non-leak output. The raw BFS output produced at standpipe 5 and another length ordinate 11m away, before, during and after the first prolonged leak test, is displayed in Figure 4.66.

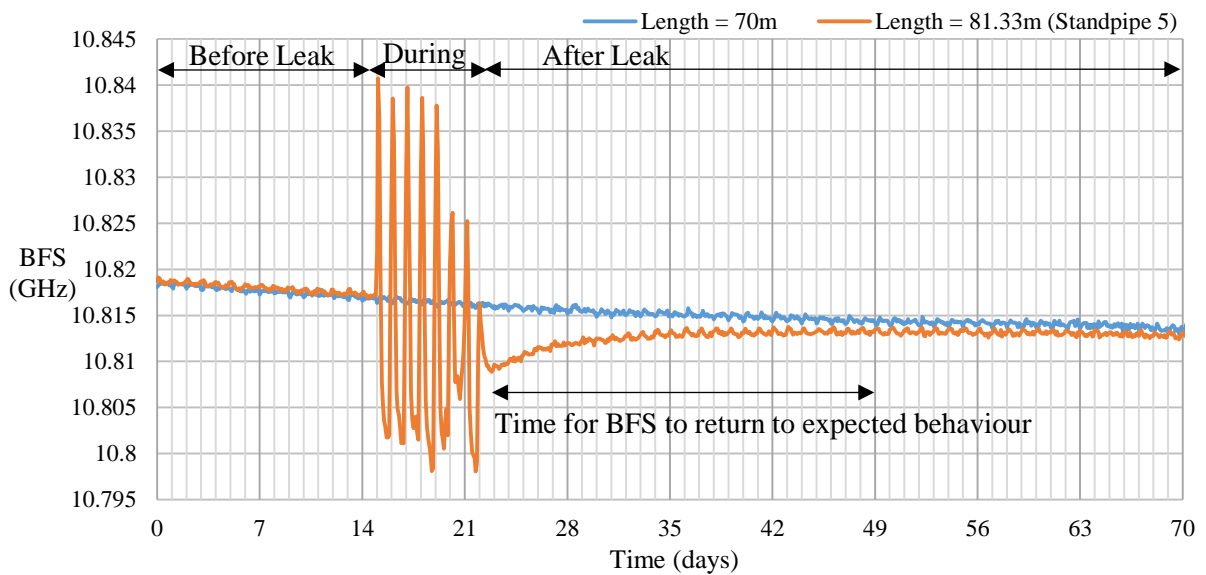


Figure 4.66. The BFS for 72F-6C-LC cable segment of the 72F-6C-LC to strain cable that occurs at standpipe 5 and another length ordinate 10m away before, during and after the first prolonged leak test.

The leak was imposed into standpipe 5 at time = 15 days and ended at time = 22 days. From Figure 4.66 it is easy to see where the leak begins and where it ends due to the wide fluctuation in the BFS output as opposed to the rest of the BFS vs time plot. The fluctuation in BFS during the time of the leak has a daily repeating cycle. This is because the water that is being poured into the standpipe undergoes daily temperature fluctuations, the warmest being in the afternoon and the coldest at night. This fluctuation in water temperature produces changes in BFS that are significant relative to the minor fluctuations that occur when no leak is happening.

After the leak has ended, there is a period of time where the BFS is different to what it is expected to be. In this timeframe the BFS tends back toward the BFS output that is expected. This is demonstrated by the Length = 81.33m curve in Figure 4.66 tending toward the L = 70m curve as time progresses after the leak has ended. The 72F-6C-LC cable does not seem to experience a permanent  $\Delta$ BFS after the leak once a significant amount of time has elapsed. This is to be expected, as a permanent  $\Delta$ BFS after a leak has occurred would be attributed to a permanent strain being imposed upon the FO cable and the 72F-6C-LC cable is primarily influenced by temperature effects.

A graph depicting the BFS at standpipe 2 (L = 25.36m) and L = 40.0m for the 72F-6C-LC segment of the 72F-6C-LC-to-strain cable during the second prolonged leak test is shown in Figure 4.67.

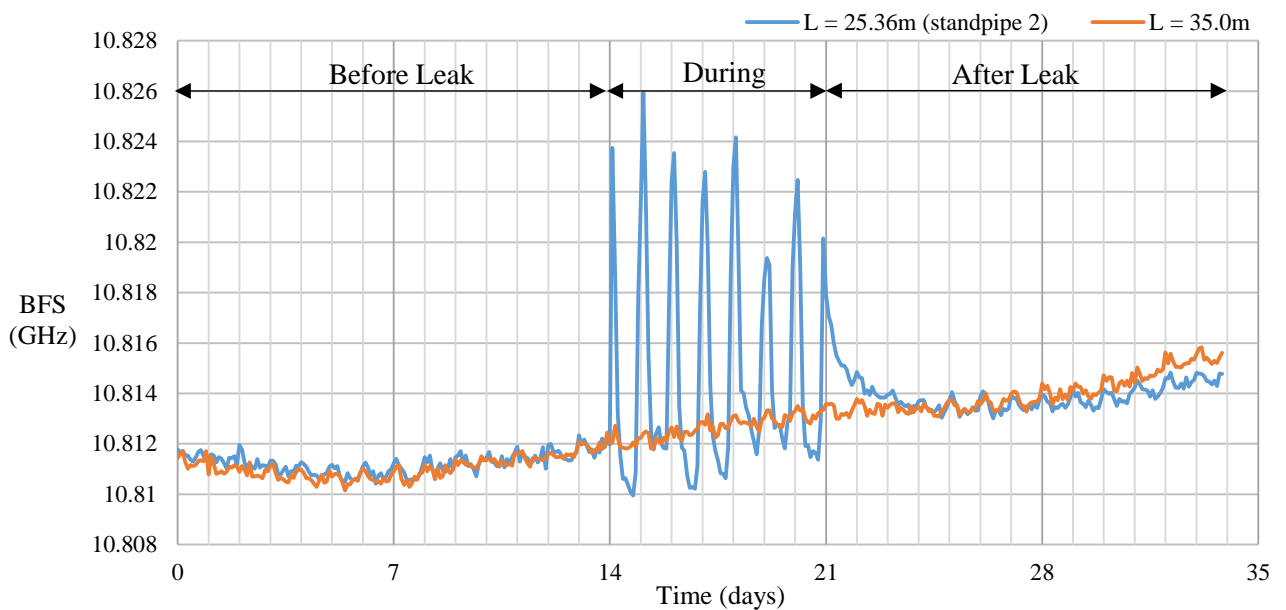


Figure 4.67. The BFS for 72-6C-LC cable segment of the 72F-6C-LC-to-strain cable that occurs at standpipe 2 and another length ordinate 15m away before, during and after the second prolonged leak test.

As can be seen in Figure 4.67 there is no residual permanent strain effect experienced by the 72F-6C-LC cable. Once the leak test has ended the BFS at the affected length-ordinate returns to following the standard behaviour expected by the 72F-6C-LC cable. In contrast to Figure 4.66, after the completion of the second leak test, Figure 4.67, the BFS returns back to its expected behaviour after only one day as opposed to the estimate of 26 days shown in Figure 4.66.

The 4F-DC-LC cable did not register a permanent, residual strain effect as it is mostly insensitive to mechanical strain. However, by observing the BFS output by the strain cable in Figure 4.68 a residual strain effect registered by the strain cable can be seen.

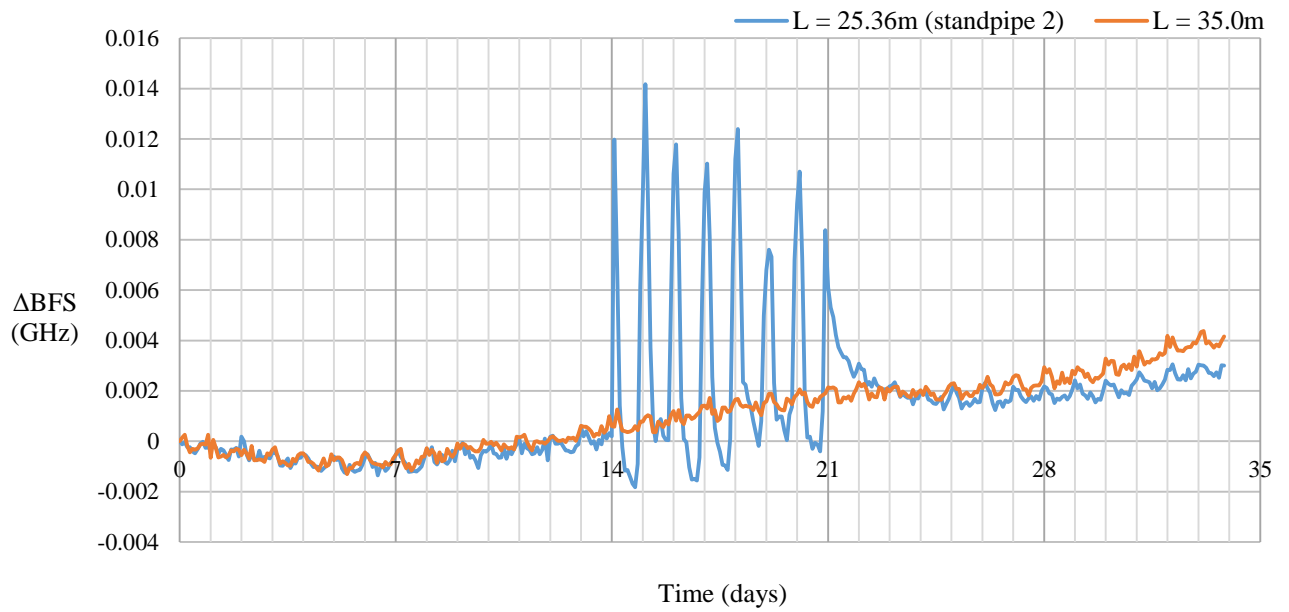


Figure 4.68. BFS output by the strain cable segment of the 72F-6C-LC-to-strain cable at standpipe 2 and a length-ordinate 10m away during the second prolonged leak test.

The strain effect can be made distinctive by normalising the two curves shown in Figure 4.68 with respect to their respective BFS output values at time  $t = 0$  days. This is shown in Figure 4.69.

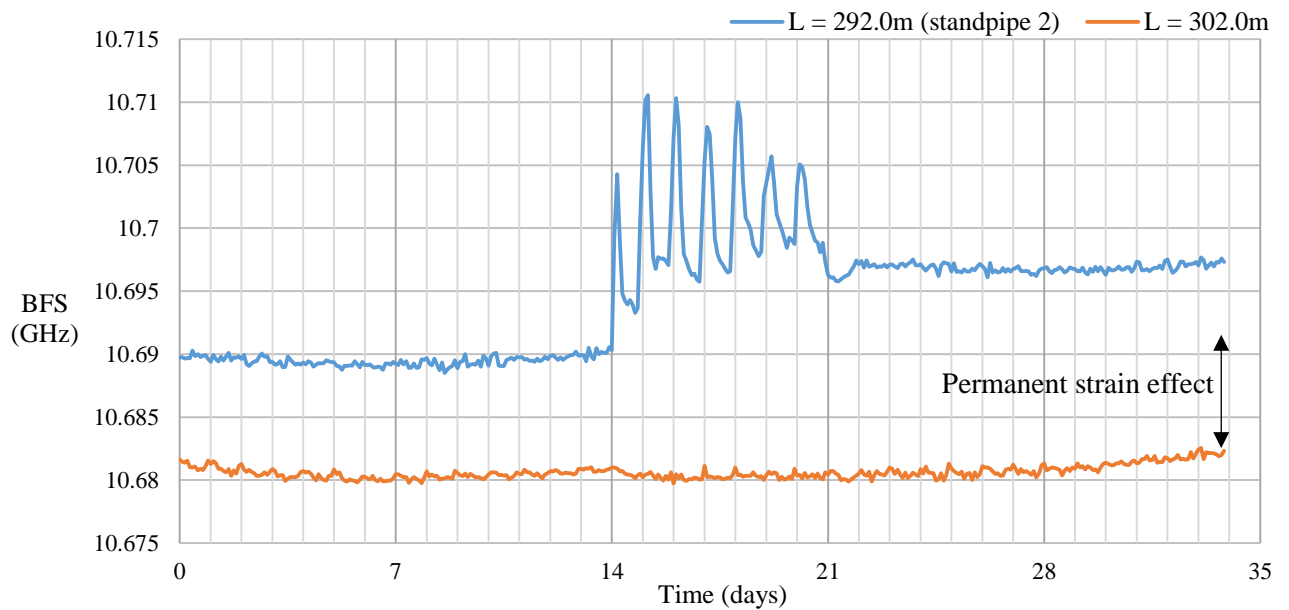


Figure 4.69. Zeroed BFS output by the strain cable segment of the 72F-6C-LC-to-strain cable at standpipe 2 and a length-ordinate 10m away during the second prolonged leak test.

From Figure 4.69 a clear residual strain effect can be seen by the difference in the BFS at the leak point as opposed to the non-leak point.

The two prolonged leak tests can be compared to each other by observing the BFS recorded from the 23<sup>rd</sup> of February to the 25<sup>th</sup> of October as shown in Figure 4.70.

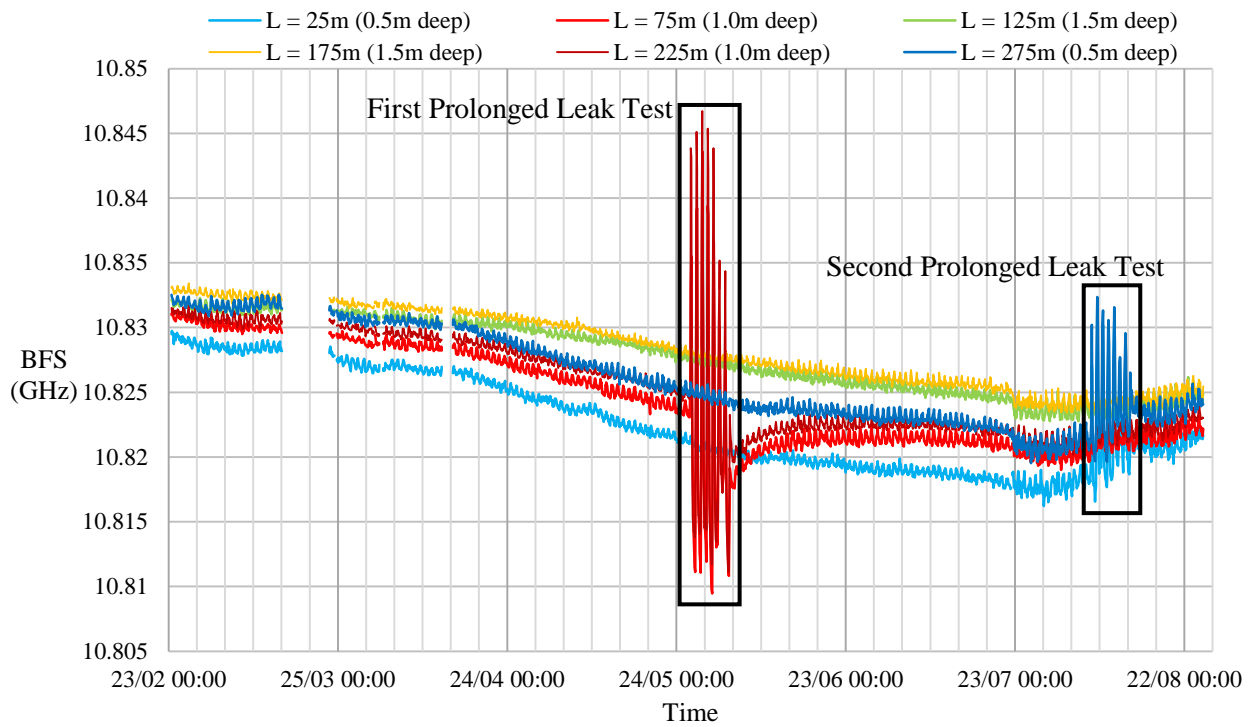


Figure 4.70. BFS recorded by the 4F-DC-LC cable at standpipes 2, 5, and 8 from the 23<sup>rd</sup> of February 2021 until the 25<sup>th</sup> of August 2021.

From Figure 4.70 the influx of water during the first leak test created much wider variation in the BFS than that of the second leak test. The BFS output that the 4F-DC-LC FO cable produced in response to an influx of water into the surrounding soil is therefore not consistent. Two similar leak events are able to create two different responses with variable magnitudes. With that being said, both leak events are easily visible in comparison to the rest of the BFS output history.

The BFS recorded by the 2F-TB cable from the 23<sup>rd</sup> of February to the 25<sup>th</sup> of October is shown in Figure 4.71.

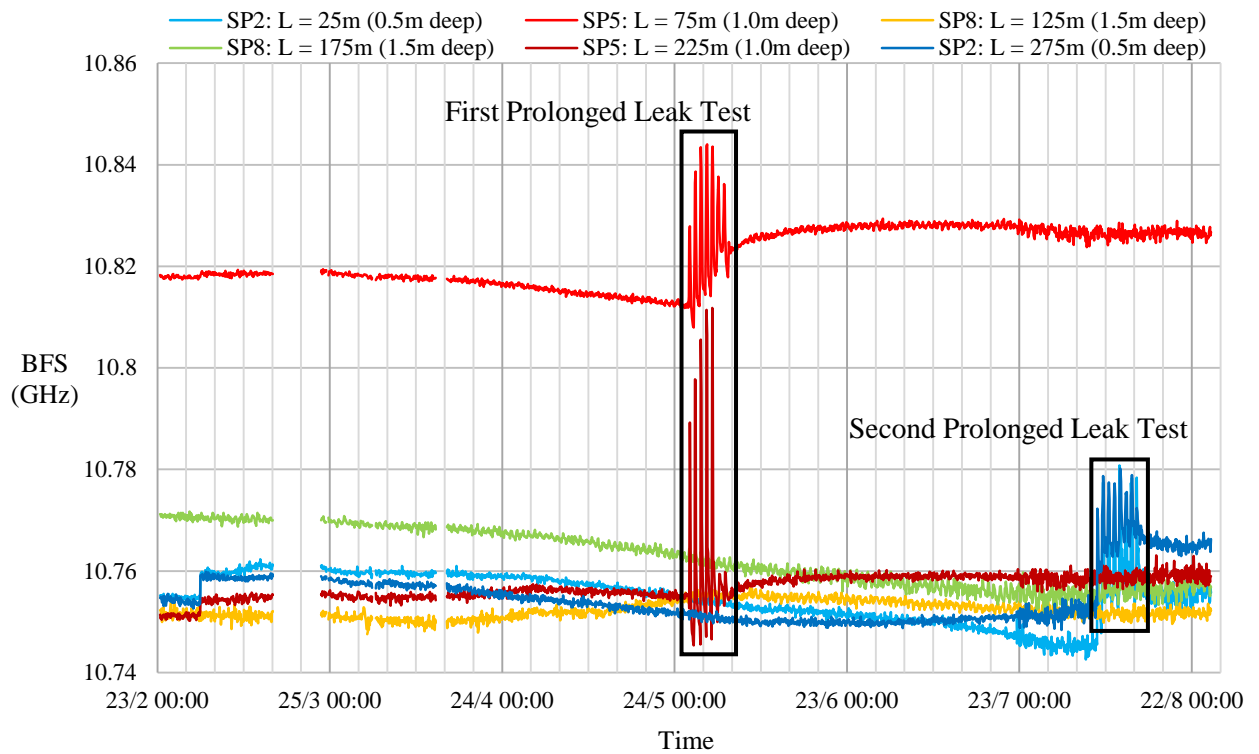


Figure 4.71. BFS recorded by the 2F-TB cable at standpipes 2, 5, and 8 from the 23<sup>rd</sup> of February 2021 until the 25<sup>th</sup> of August 2021.

Just like the 4F-DC-LC cable results shown in Figure 4.70 the 2F-TB cable registered a stronger response during the first prolonged leak test than the second prolonged leak test. In addition the permanent strain effect can be seen at the respective length ordinates after the two leak tests have ended.

In both the 4F-DC-LC cable and the 2F-TB cable, the BFS of the FO cables change due to the influx of water with a different temperature to that of the surrounding soil, or a combination of temperature and soil strain changes. These changes in BFS that occur during a leak are what a leak detection system must search for in order to detect leaks. By processing the BFS output as explained in Figure 4.48, these changes can be exploited to reveal the location and time of origin of a leak that occurs along a FO cable.

#### 4.7.2 EFFECT OF PROLONGED LEAK ON THE CHANGE IN BFS

To detect the influx of water into the soil surrounding the FO cables, the algorithm outlined in Figure 4.48 can be used. The result of applying the algorithm to the 72F-6C-LC-to-strain cables is shown in Figure 4.72.

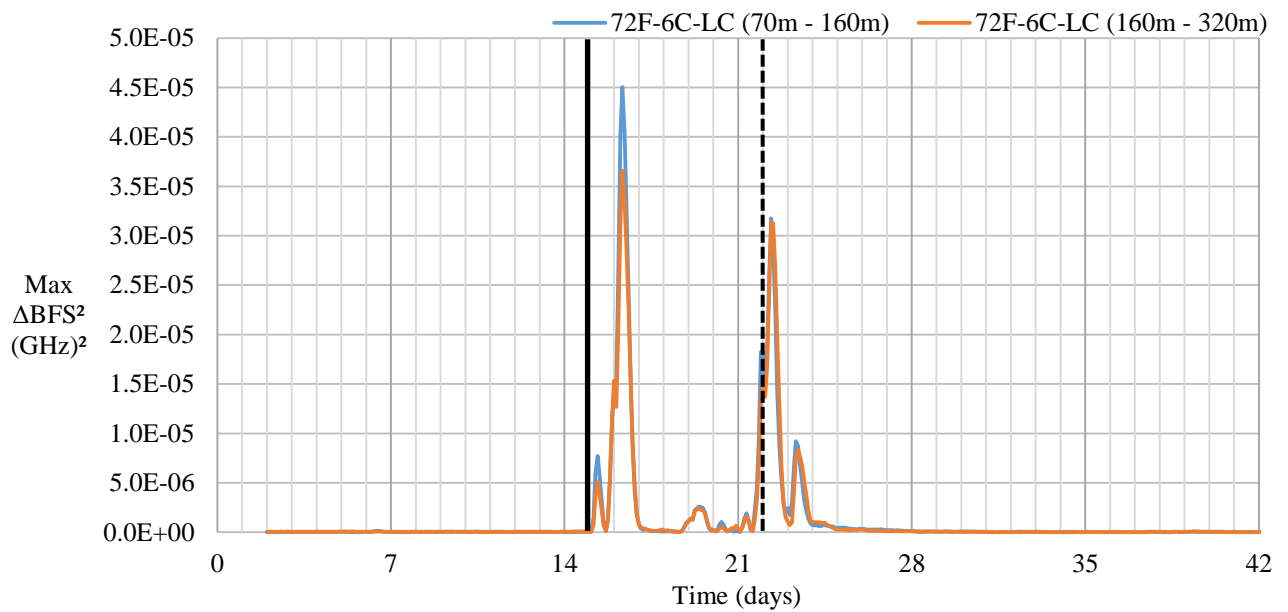


Figure 4.72. Maximum  $\Delta\text{BFS}^2$  vs time plot for the strain to 72F-6C-LC cable during the first prolonged leak test. The solid black line signifies the start of the leak test, and the dashed line represents the end of the leak test.

The maximum  $\Delta\text{BFS}$  preceding the time of 15 days is consistently close to zero relative to the greatest maximum  $\Delta\text{BFS}$  response that occurs on day 16. The time  $t = 15$  days corresponds to the 26<sup>th</sup> of May when the leak was imposed. This indicates that the stark change in maximum  $\Delta\text{BFS}$  was caused by the imposed leak. The maximum  $\Delta\text{BFS}$  output by the cable, however, does not increase and stays at the peaked value. Instead it reaches a peak value and then decreases back down to the  $\Delta\text{BFS}$  values produced by the optical fibre before the leak was imposed. This is due to the system (soil temperature and imposed strain) reaching an equilibrium after much water has been added to the system. Once the soil temperature and strain state have ceased changing, equilibrium of the system has been reached. Once the system has reached equilibrium, it becomes relatively stable once again, and the maximum  $\Delta\text{BFS}$  output range decreases to its former range.

It is unclear in Figure 4.72 how the maximum  $\Delta\text{BFS}$  varies with time before the leak is imposed. By plotting Figure 4.72 using a logarithmic vertical axis, the variation of the maximum  $\Delta\text{BFS}$  before the leak can be seen. Figure 4.72 is plotted using a logarithmic vertical axis and is shown in Figure 4.73.

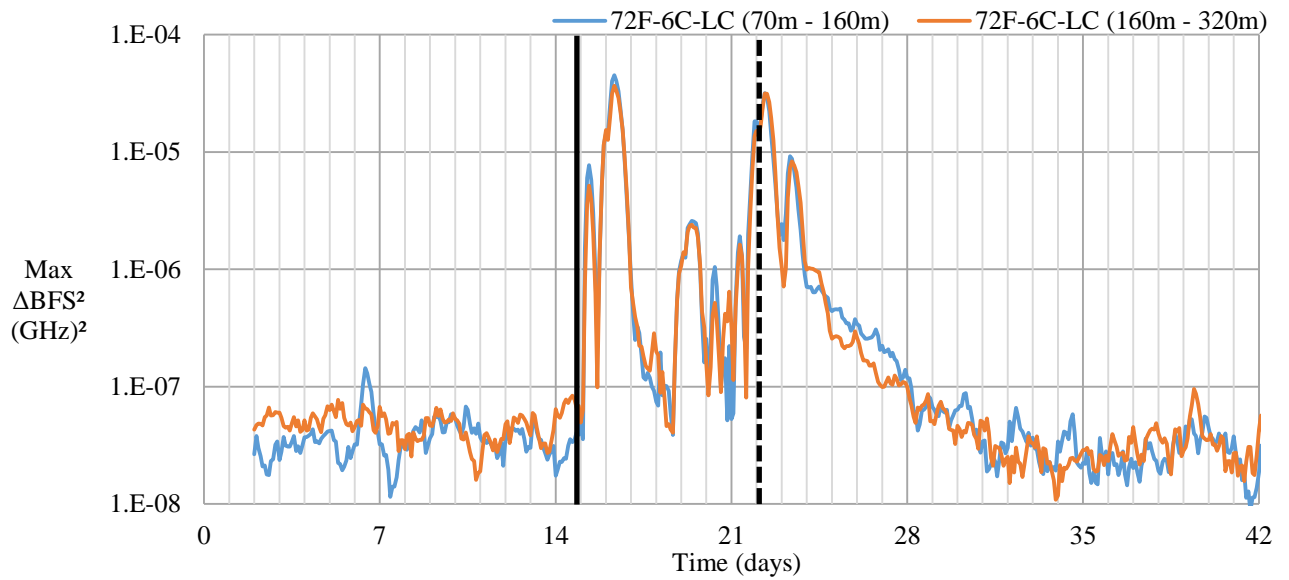


Figure 4.73. Maximum  $\Delta\text{BFS}^2$ , plotted using a logarithmic scale, vs time for the strain to 72F-6C-LC cable.

From Figure 4.73, the maximum  $\Delta\text{BFS}^2$  preceding the imposed leak, from  $t = 15$  days and onwards, occurs between the bounds of  $\Delta\text{BFS}^2 = 7\text{E-}8 \text{ (GHz)}^2$ , and  $\Delta\text{BFS}^2 = 3\text{E-}7 \text{ (GHz)}^2$ . These boundaries, if well-established, could form a range in which the maximum  $\Delta\text{BFS}^2$  can be expected to occur. Moreover, the maximum  $\Delta\text{BFS}^2$  changes by two orders of magnitude from the time when the leak is imposed to the greatest maximum  $\Delta\text{BFS}^2$  occurrence during the conduction of the leak test. Therefore, if the expected maximum  $\Delta\text{BFS}$  along the FO cable is known and well-established, then any value exceeding the expected maximum  $\Delta\text{BFS}$  would indicate that an event, such as a leak, has occurred somewhere along the FO cable.

To determine where the maximum  $\Delta\text{BFS}$  occurs along the cable, the length-ordinate of the maximum  $\Delta\text{BFS}$  can be extracted at each time step. A plot of the length-ordinate of the maximum  $\Delta\text{BFS}$  is shown in Figure 4.74.

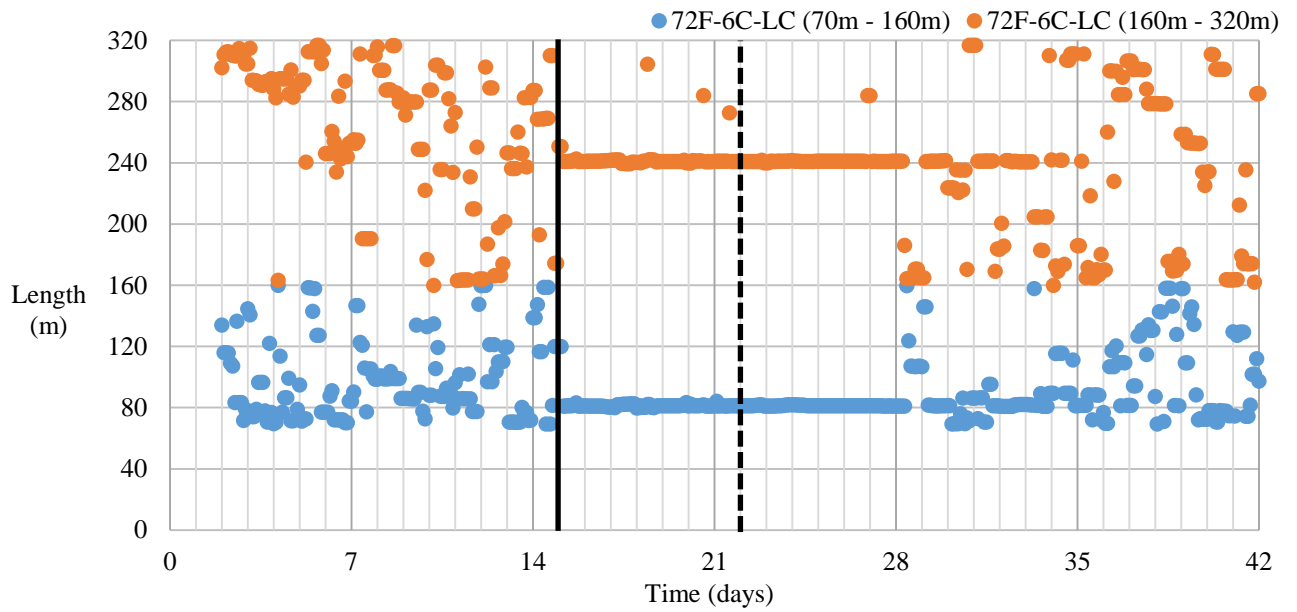


Figure 4.74. Length-ordinate of the maximum  $\Delta\text{BFS}$  along the strain to 72F-6C-LC cable after being separated into two segments (excluding the strain cable segment).

Figure 4.74 shows how the maximums  $\Delta\text{BFS}$  varies randomly along the length of the FO cable as time progresses before a leak occurs. Once the leak has been initiated the length-ordinate of the maximum  $\Delta\text{BFS}$  becomes constant and reveals the location of the leak. However, once the leak has ended the length-ordinate of the maximum  $\Delta\text{BFS}$  does not return to occurring randomly, but remains constant for some time after the leak ends. This is due to a residual  $\Delta\text{BFS}$  that decays for some time after the leak has ended. The residual  $\Delta\text{BFS}$  that decays with time can be seen in Figure 4.66.

By plotting the  $\Delta\text{BFS}^2$  of the strain to 72F-6C-LC cable along the length of the cable at the time instant  $t = 16$  days and 6 hours, the effect that the change in soil moisture content has on the FO cable can be seen, as depicted in Figure 4.75.

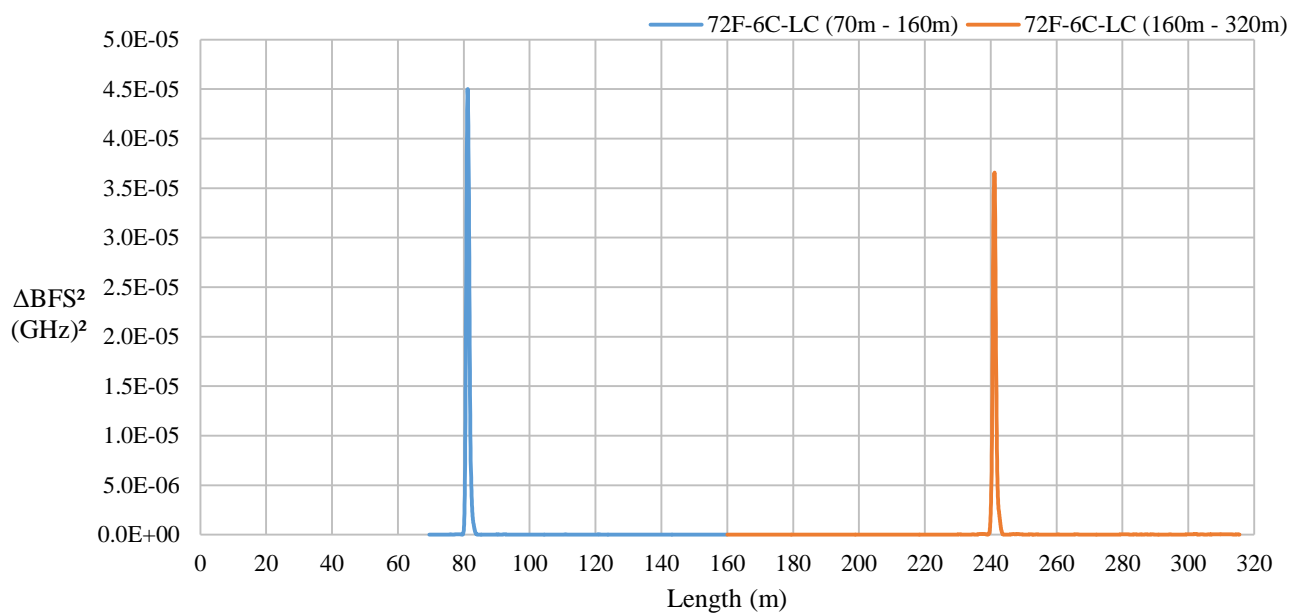


Figure 4.75.  $\Delta\text{BFS}^2$  plotted along the length of the strain to 72F-6C-LC FO cable at time = 16 days and 6 hours.

Given that the length of the FO cable is 320m, and the peaks occur around length-ordinates  $L = 80\text{m}$  and  $L = 240\text{m}$ , both being equidistant from the midpoint:  $L = 160\text{m}$ , it can be concluded that the FO cable successfully detected the location of the leak.

To compare the leak-peaks against the surrounding  $\Delta\text{BFS}^2$  values produced by processing the BFS data, the  $\Delta\text{BFS}^2$  can be visualized against both time and FO cable length using a 3-Dimensional plot. This is shown in Figure 4.76.

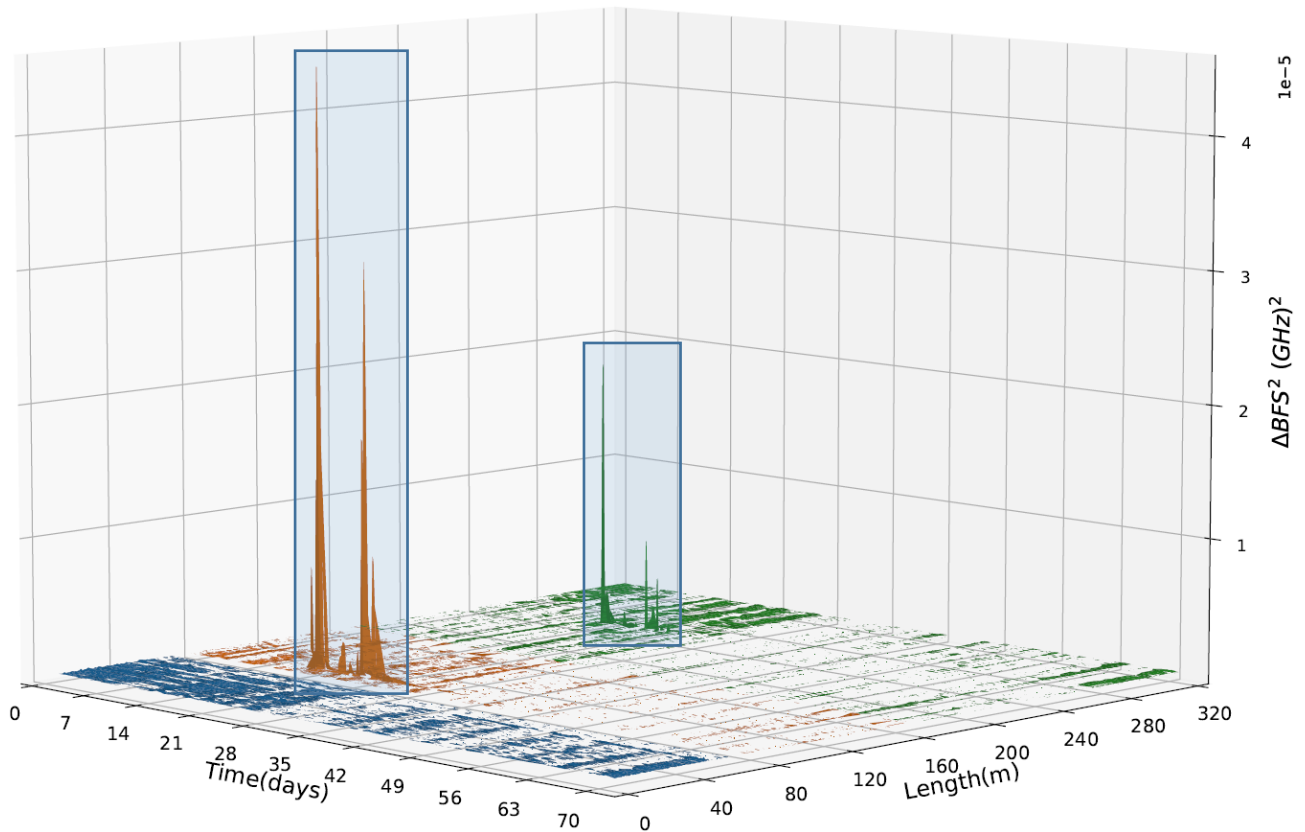


Figure 4.76. A 3-Dimensional plot of the  $\Delta\text{BFS}^2$  output (excluding values less than  $1\text{e-}8 \text{ (GHz)}^2$ ) from the 72F-6C-LC to strain cable against time and length during the first prolonged leak test. The detected leak is highlighted by the blue boxes. Blue corresponds to the strain cable, and the orange and green plots are the output of the 72F-6C-LC cable.

The  $\Delta\text{BFS}^2$  leak-peaks that arise from the prolonged leak test stand out significantly when compared against the surrounding  $\Delta\text{BFS}^2$  values. This phenomenon would suggest that the  $\Delta\text{BFS}$  caused by a leak would be easily detectable since the  $\Delta\text{BFS}$  peaks caused by the influx of water are prominent over the unaltered  $\Delta\text{BFS}$  that is expected along the rest of a FO cable's length.

### 4.7.3 COMPARISON OF THE DIFFERENT FO CABLE TYPES

#### 4.7.3.1 STRAIN TO 72F-6C-LC

The maximum  $\Delta\text{BFS}^2$  plotted against time for the second prolonged leak test conducted at standpipe 5 for the strain to 72F-6C-LC cable are shown in Figure 4.77. The second prolonged leak test was used as it was done specifically to capture the strain cable's response to a prolonged leak event.

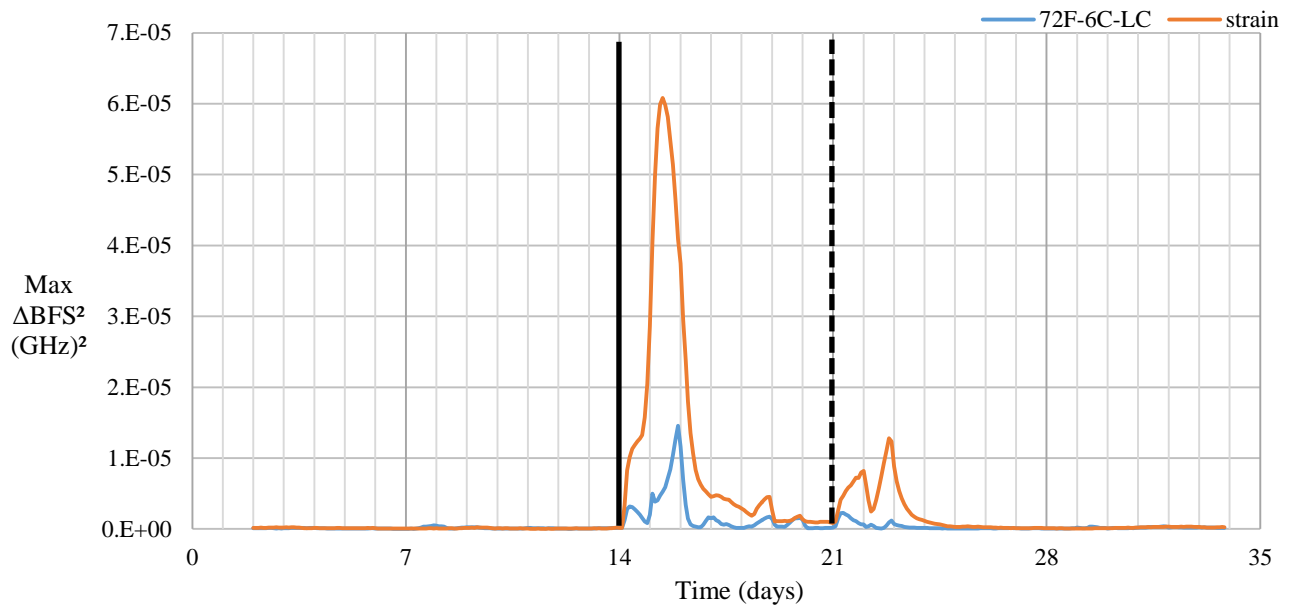


Figure 4.77. Maximum  $\Delta\text{BFS}^2$  plotted against time for the strain to 72F-6C-LC cable during the second prolonged leak test.

It is immediately noticeable that the two different cable types give distinct  $\Delta\text{BFS}$  responses induced by the leak. The strain cable undergoes a much greater  $\Delta\text{BFS}$  than the 72F-6C-LC cable in response to the leak. This is due to the strain cable being affected by strain as well as temperature effects, whereas the 72F-6C-LC cable is primarily influenced by temperature effects.

By plotting the  $\Delta\text{BFS}^2$  on a logarithmic scale the behaviour of the  $\Delta\text{BFS}$  for the two cables before the leak occurs seem to be very similar. This is shown in Figure 4.78.

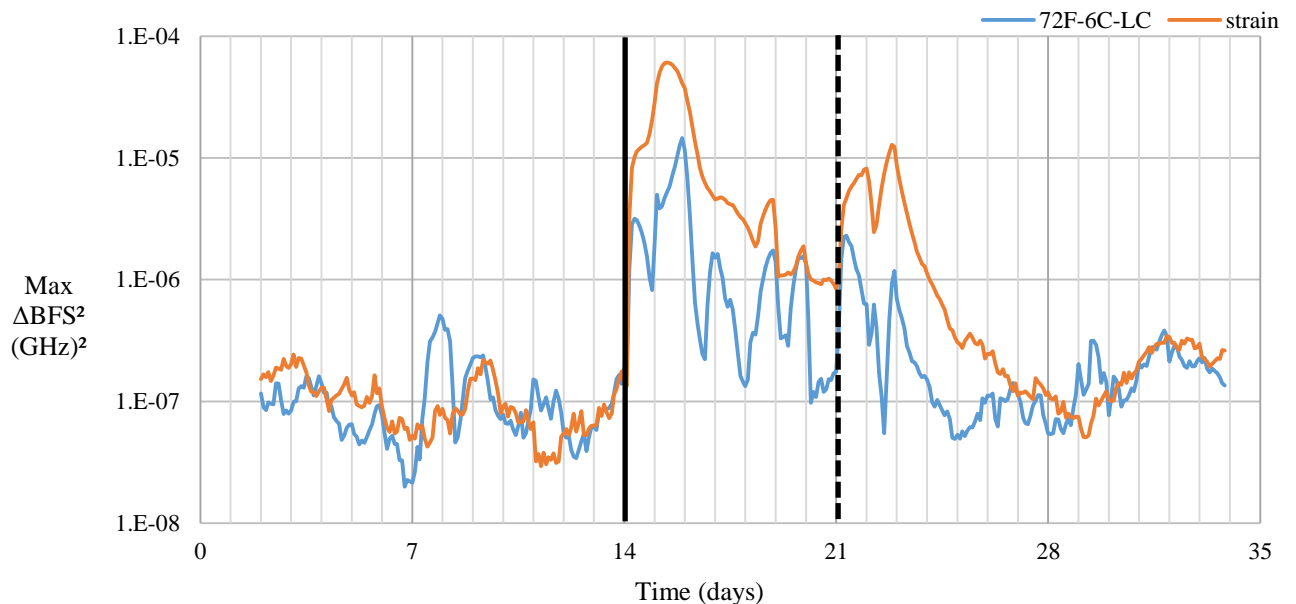


Figure 4.78. Maximum  $\Delta\text{BFS}^2$  plotted on logarithmic scale against time for the strain to 72F-6C-LC cable during the second prolonged leak test.

Interestingly, the maximum  $\Delta\text{BFS}^2$  produced by both cables during baseline conditions did not differ significantly at all. It would be expected that the  $\Delta\text{BFS}$  baseline behaviour of the strain cable would

produce greater  $\Delta\text{BFS}$  outputs influenced by the strains that occur due to random soil movements. The lack of large  $\Delta\text{BFS}$  outputs for the strain cable relative to the 72F-6C-LC cable could be attributed to the stiffness of the cable, i.e. that the cable is too stiff to undergo any strains due to random soil movement, but that soil strains induced by a significant soil moisture content change can impose significant strains upon the strain cable. This characteristic of the strain cable might make it superior as a leak detection sensor as it undergoes large  $\Delta\text{BFS}$  when affected by a leak and undergoes very little  $\Delta\text{BFS}$  during baseline conditions.

The length-ordinates of the maximum  $\Delta\text{BFS}^2$  along the length of the strain to 72F-6C-LC cable are shown in Figure 4.79.

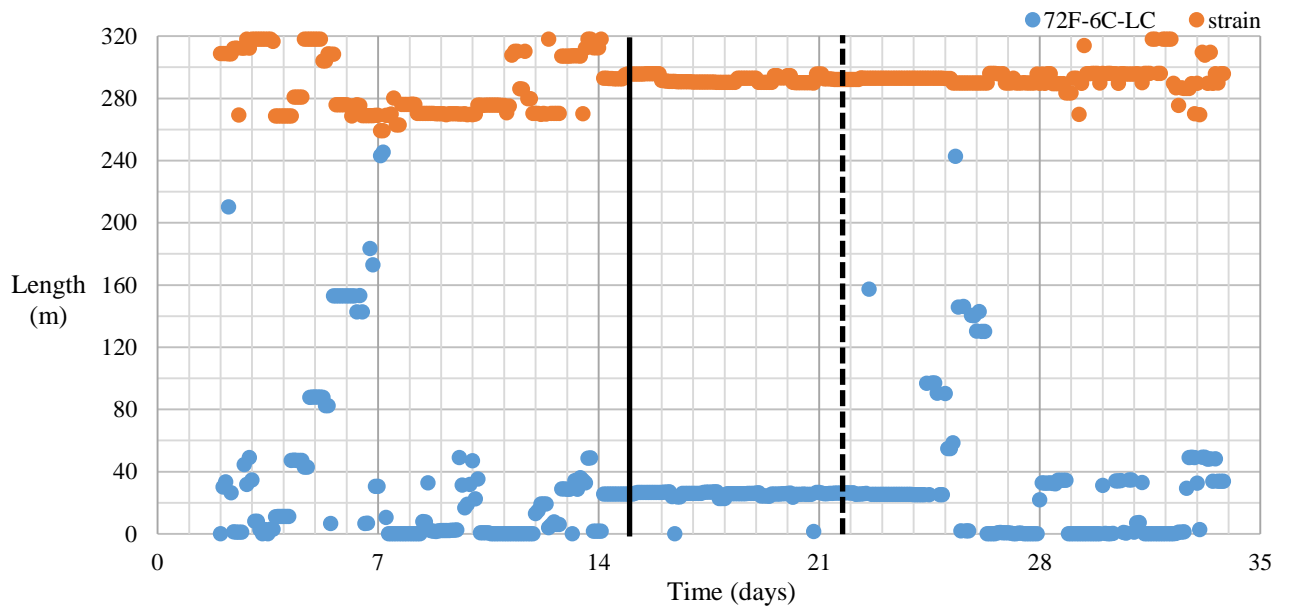


Figure 4.79. Length-ordinate of the maximum  $\Delta\text{BFS}$  occurring along the strain to 72F-6C-LC cable during the second prolonged leak test.

As expected the length-ordinate of the maximum  $\Delta\text{BFS}$  registered by the FO cable remains fairly constant during the leak test. The 72F-6C-LC cable registered the location of the leak at 25.6m and the strain cable registered the leak occurring at 293.0m. These two length-ordinates correspond with standpipe 2's location, meaning that each FO cable was successful in the detection of the leak location.

By plotting the  $\Delta\text{BFS}$  against the length of the FO cable at the time instant  $t = 15$  days and 10 hours, the  $\Delta\text{BFS}^2$  that each cable produced in response to the leak can be seen. This is shown in Figure 4.80.

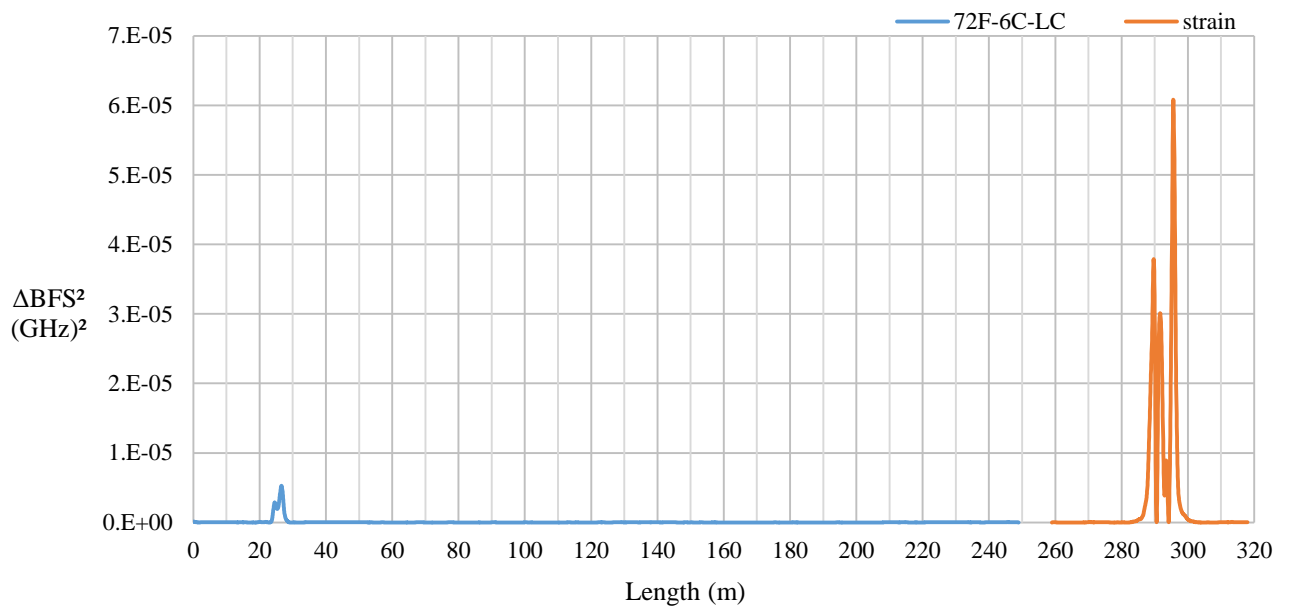


Figure 4.80.  $\Delta\text{BFS}^2$  plotted against the length of the 4F-DC-LC cable at time:  $t = 15$  days and 10 hours from the second leak test.

From Figure 4.80 the difference in performance as a leak detection sensor can be seen. The strain cable is able to produce a much greater  $\Delta\text{BFS}^2$  output in response to the induced leak. The 72F-6C-LC cable's  $\Delta\text{BFS}^2$  response is much weaker, only a 10<sup>th</sup> of the strain cable's response. Given the composition of each cable type, the strain cable being both strain and temperature sensitive and the 72F-6C-LC cable being mostly temperature sensitive, the difference in each  $\Delta\text{BFS}^2$  response to a leak is to be expected.

Examining the  $\Delta\text{BFS}^2$  in three dimensions, the  $\Delta\text{BFS}^2$  due to the leak can again be compared to the  $\Delta\text{BFS}^2$  that occurs along the cable throughout the time of the second leak test. The 3-Dimensional plot of  $\Delta\text{BFS}^2$  for the strain to 72F-6C-LC cable against time and length is shown in Figure 4.81.

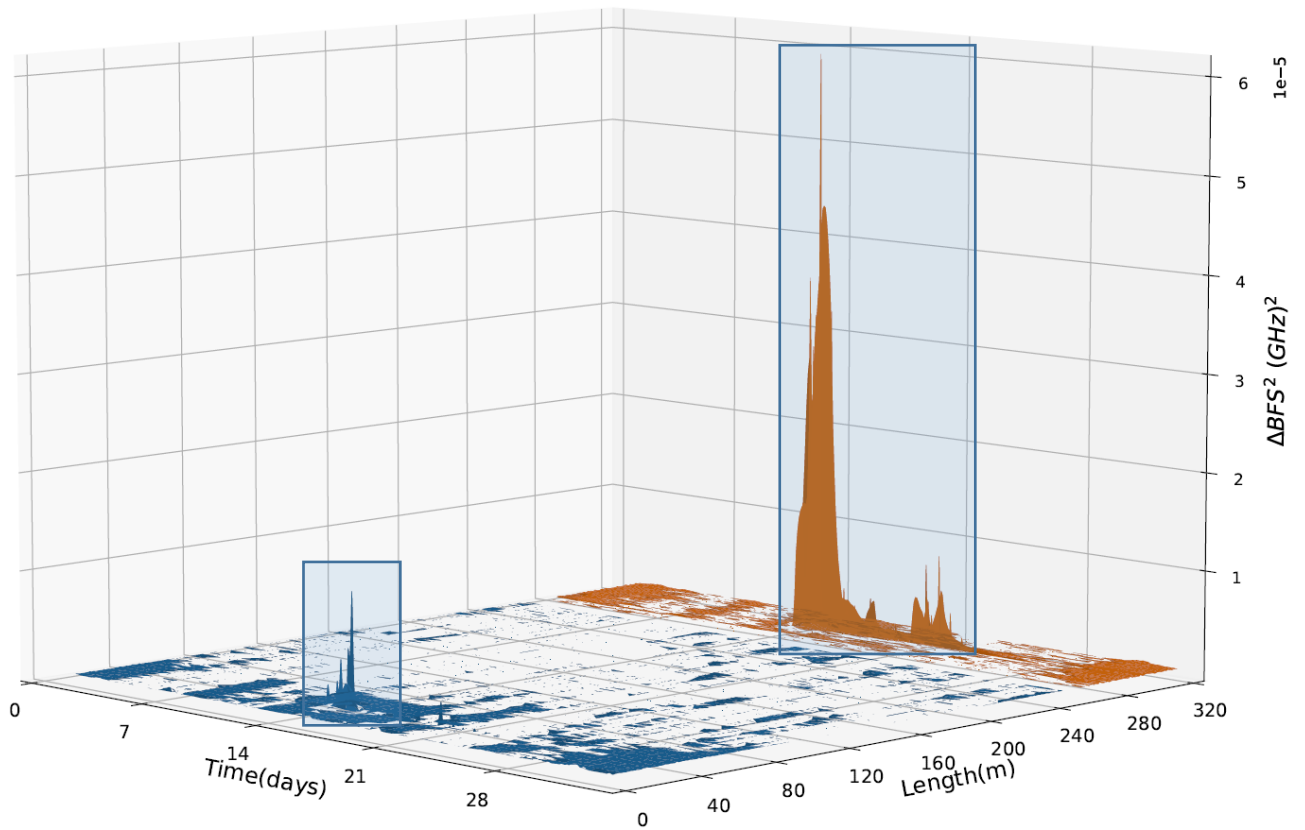


Figure 4.81. A 3-Dimensional plot of the  $\Delta\text{BFS}^2$  against time and length produced by the strain to 72F-6C-LC cable during the second leak test. The detected leak is highlighted by the blue boxes. The blue portion represents the 72F-6C-LC cable, and the red the strain cable.

Again the greater response that the strain cable has over the 72F-6C-LC cable is seen in Figure 4.81. However, whether this increased sensitivity is needed is debatable. Both FO cable types are conclusively able to detect the leak's time of origin and location of occurrence.

#### 4.7.3.2 4F-DC-LC

The maximum  $\Delta\text{BFS}^2$  along the 4F-DC-LC cable is plotted against time during the first prolonged leak test is shown in Figure 4.82.

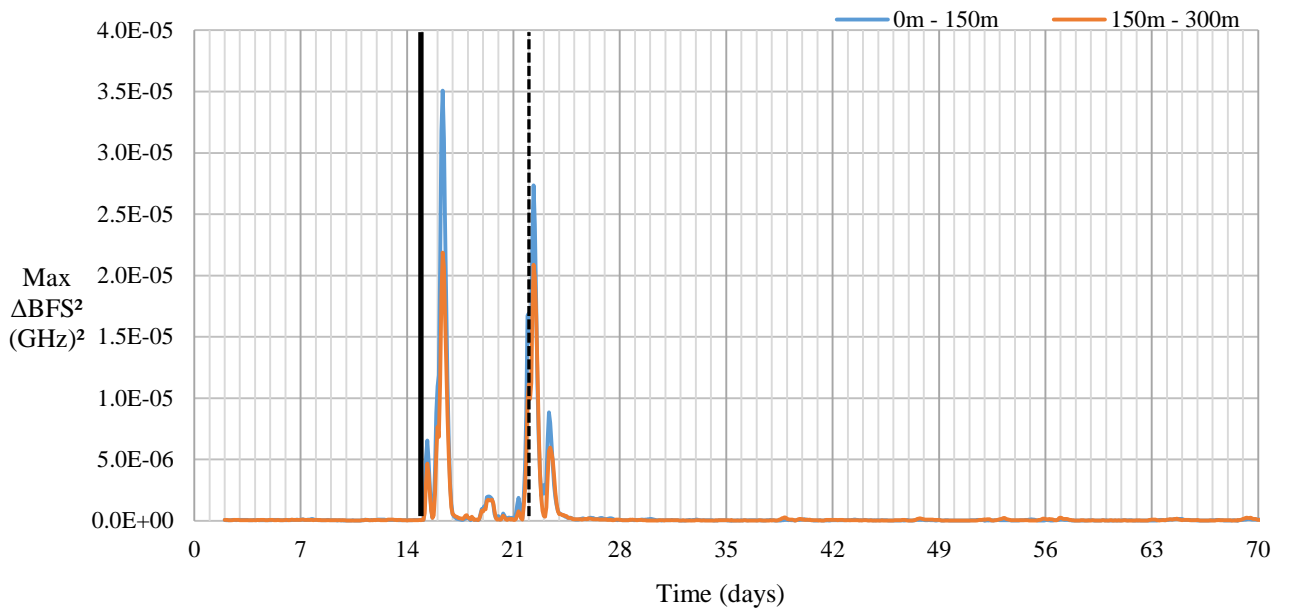


Figure 4.82. Maximum  $\Delta\text{BFS}^2$  plotted against time for the 4F-DC-LC cable during the first prolonged leak test.

The 4F-DC-LC cable output at maximum  $\Delta\text{BFS}^2$  response of  $\Delta\text{BFS}^2 = 3.51\text{E-}5 \text{ (GHz)}^2$ , which is comparable with the response output by the 72F-6C-LC cable of  $\Delta\text{BFS}^2 = 4.50\text{E-}5 \text{ (GHz)}^2$ . This is because both the 4F-DC-LC and the 72F-6C-LC cables are loose core (LC) cables. Therefore, the similar output given by the two cables is indicative of them both experiencing a similar temperature change due to the ingress of water into the soil surrounding the FO cables. The  $\Delta\text{BFS}^2$  of the 4F-DC-LC cable plotted on a logarithmic vertical scale is shown in Figure 4.83.

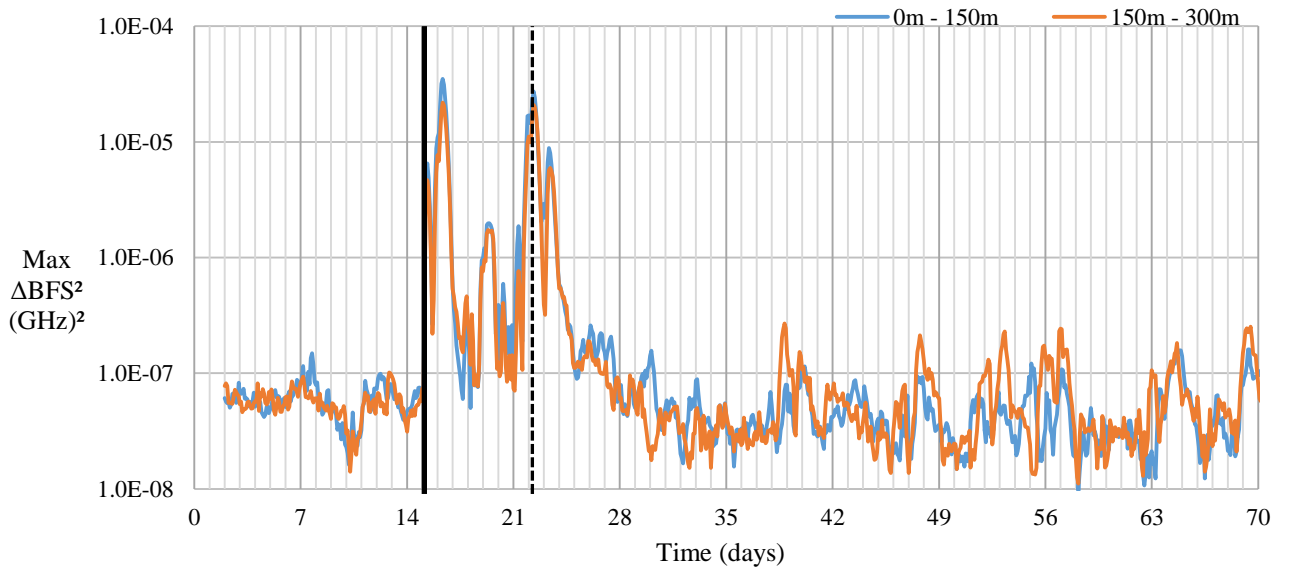


Figure 4.83. Maximum  $\Delta\text{BFS}^2$  plotted against time for the 4F-DC-LC cable using a logarithmic vertical scale during the first prolonged leak test.

Analysing where the maximum  $\Delta\text{BFS}$  occurred along the length of the 4F-DC-LC cable reveals the location of the leak, as is depicted in Figure 4.84.

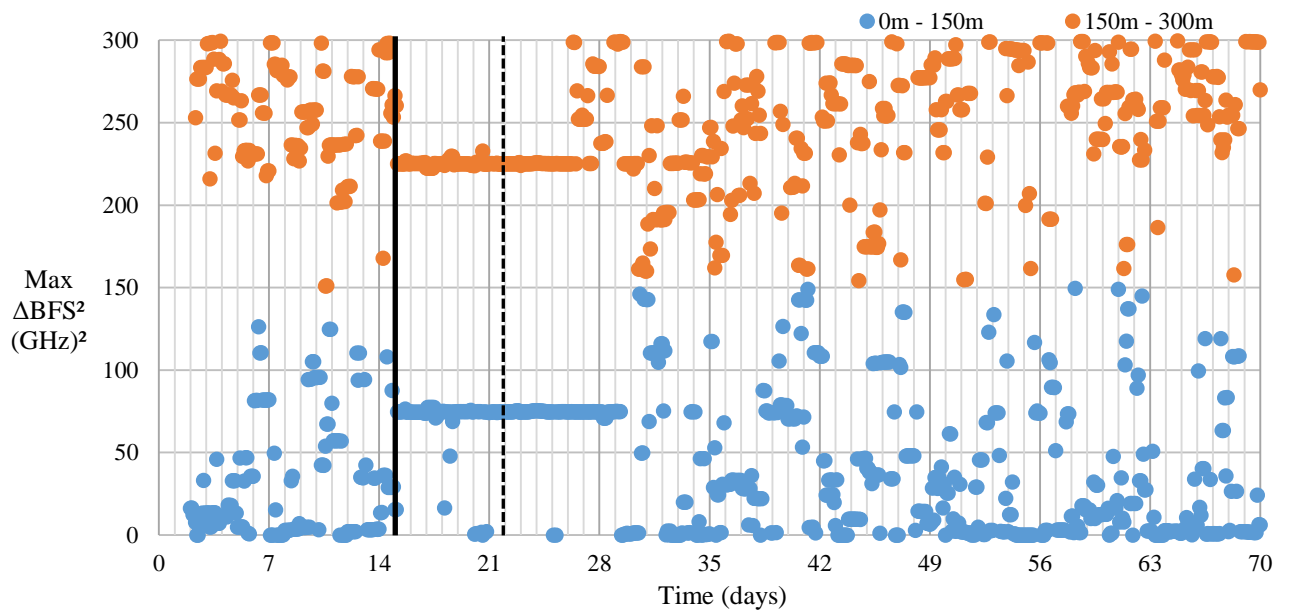


Figure 4.84. Length-ordinate of the maximum  $\Delta\text{BFS}^2$  occurring along the 4F-DC-LC cable during the first prolonged leak test.

From Figure 4.84 it can be seen that the leak has been detected around the length-ordinates  $L = 75\text{m}$  and  $L = 225\text{m}$ , both equidistant from the cable midpoint,  $L = 150\text{m}$ . As was the case with the 72F-6C-LC cable, after the leak was induced the length-ordinate at which the maximum  $\Delta\text{BFS}^2$  occurred alternated on the 4F-DC-LC cable between  $L = 75\text{m}$  and  $L = 225\text{m}$ .

Observing the  $\Delta\text{BFS}^2$  vs length profile at the time of the greatest  $\Delta\text{BFS}^2$ ,  $t = 16.25$  days, the  $\Delta\text{BFS}^2$  around the leak regions can be compared against the  $\Delta\text{BFS}^2$  of the unaffected regions. The  $\Delta\text{BFS}^2$  vs length profile is shown in Figure 4.85.

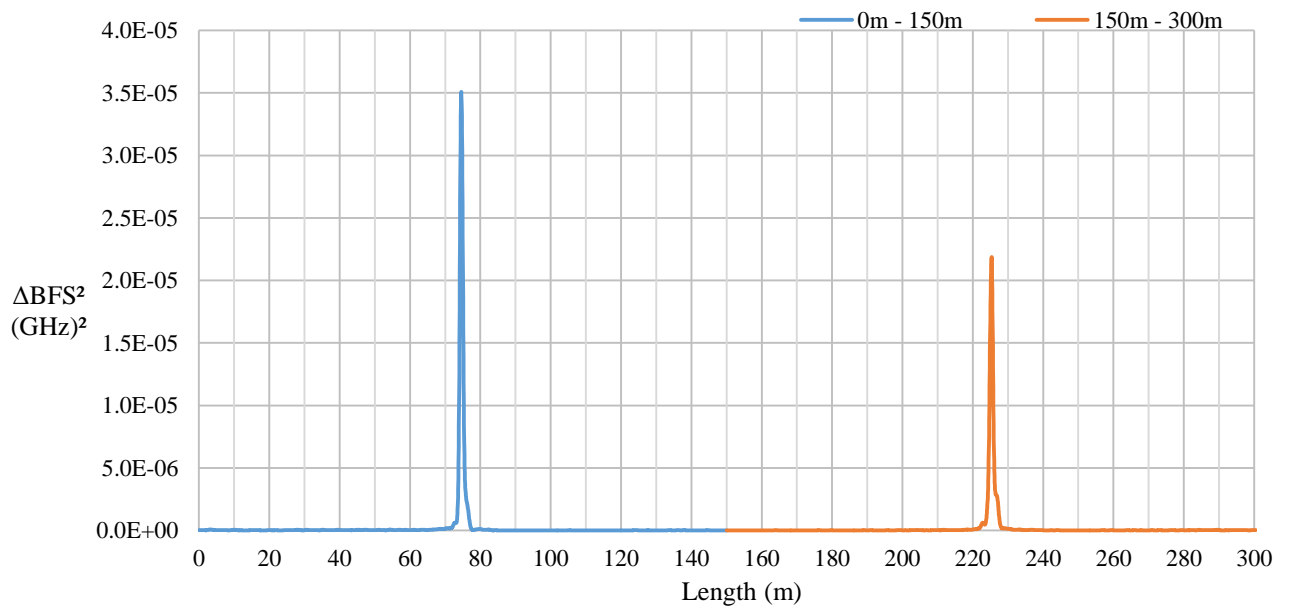


Figure 4.85.  $\Delta\text{BFS}^2$  plotted against the length of the 4F-DC-LC cable at time:  $t = 16$  days and 6 hours during the first prolonged leak test.

From Figure 4.85 and Figure 4.75 the peaks associated with the detection of the leak are very prominent. The curve of the  $\Delta\text{BFS}^2$  in the regions that are unaffected by the leak appear flat, and very close to zero relative to the peaks. This indicates that the response that the FO cables are able to output, by registering a change in  $\Delta\text{BFS}$  caused by water ingress into the soil, is significantly greater than what can be caused by any other environmental factors. By plotting Figure 4.85 using a logarithmic vertical scale the difference between the  $\Delta\text{BFS}^2$  in the leak regions and the unaffected regions can be fully realised. This is shown in Figure 4.86.

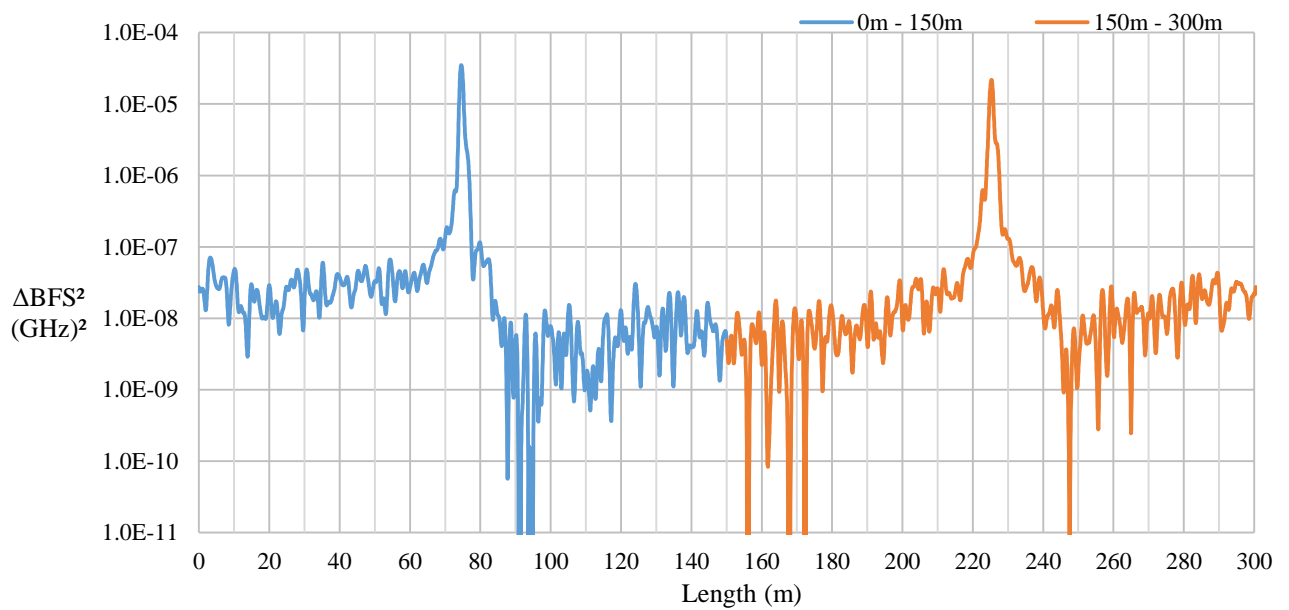


Figure 4.86.  $\Delta\text{BFS}^2$  plotted on a logarithmic scale against the length of the 4F-DC-LC cable at time:  $t = 16$  days and 6 hours during the first prolonged leak test.

Figure 4.86 shows that the peaks caused by the leaks are in the region of the order of magnitude of  $10^{-5}$  (GHz)<sup>2</sup>. The greatest  $\Delta\text{BFS}^2$  in the unaffected regions is in the range of the order of magnitude of  $10^{-8}$  (GHz)<sup>2</sup>. Thus, the contrast between the regions affected by the leak and the unaffected regions is three orders of magnitude.

The 3-Dimensional plot of the  $\Delta\text{BFS}^2$  of the 4F-DC-LC cable is shown in Figure 4.87

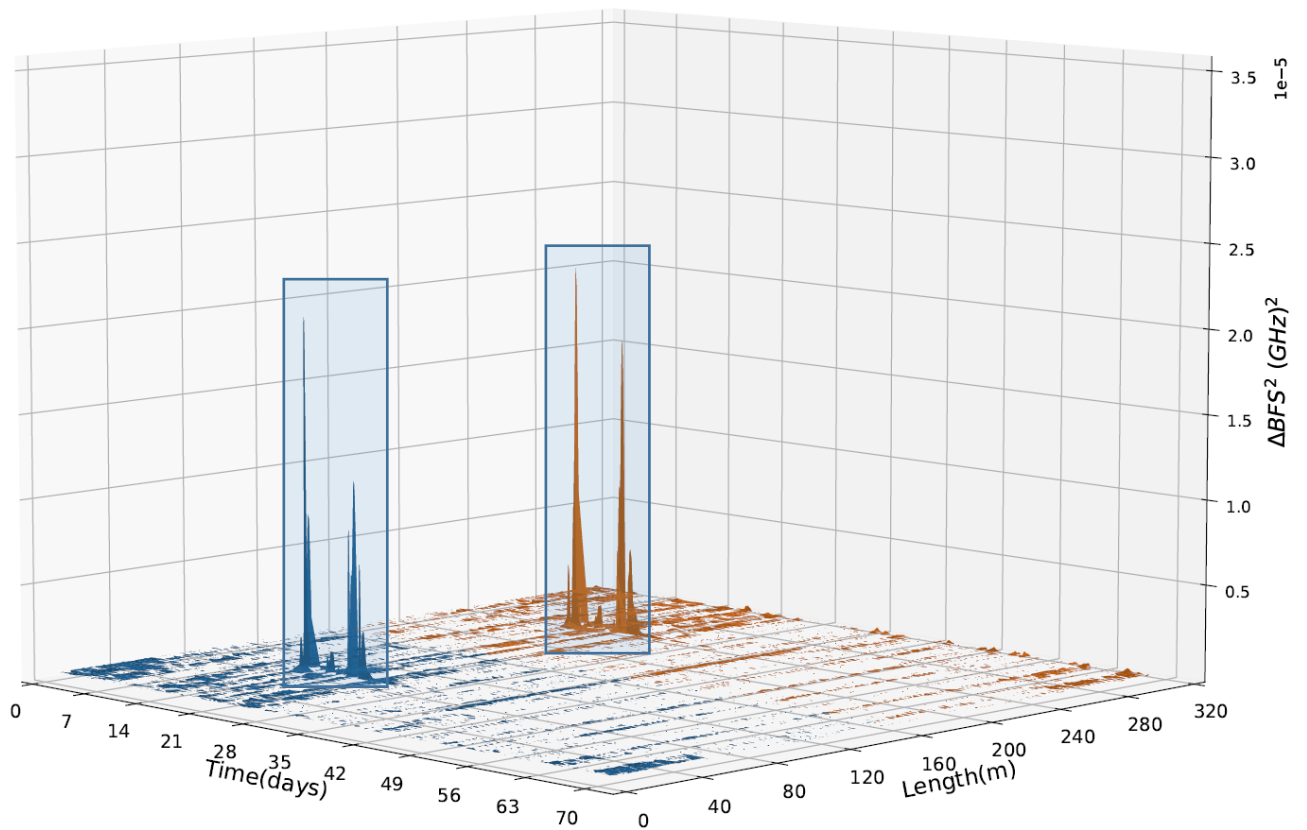


Figure 4.87. A 3-Dimensional plot of the  $\Delta\text{BFS}^2$  (excluding values less than  $1\text{e-}8$  (GHz) $^2$ ) against time and length for the 4F-DC-LC cable during the first prolonged leak test.

It is interesting to note that both halves of the cable gave extremely similar responses to the induced leak. The responses were within the same order of magnitude indicating that the FO cables were experiencing similar temperature changes due to the influx of water into the surrounding soil.

Even though the strain effect is negligible in the 4F-DC-LC cables, the  $\Delta\text{BFS}^2$  leak-peak that it produces in response to the water influx is clearly visible over the  $\Delta\text{BFS}^2$  that occurs throughout time over the rest of the cable length. This further alludes to a conclusion that the type of FO cable used as a leak detection sensor is irrelevant, as it has been shown that both strain insensitive LC cables and a mechanical strain measuring cable are both conclusively able to detect an influx of water into the surrounding soil.

### 4.7.3.3 2F-TB

Considering the data output given by the tight buffered (TB) cables, the maximum  $\Delta\text{BFS}^2$  output by the 2F-TB cable over the analysed time period is shown in Figure 4.88.

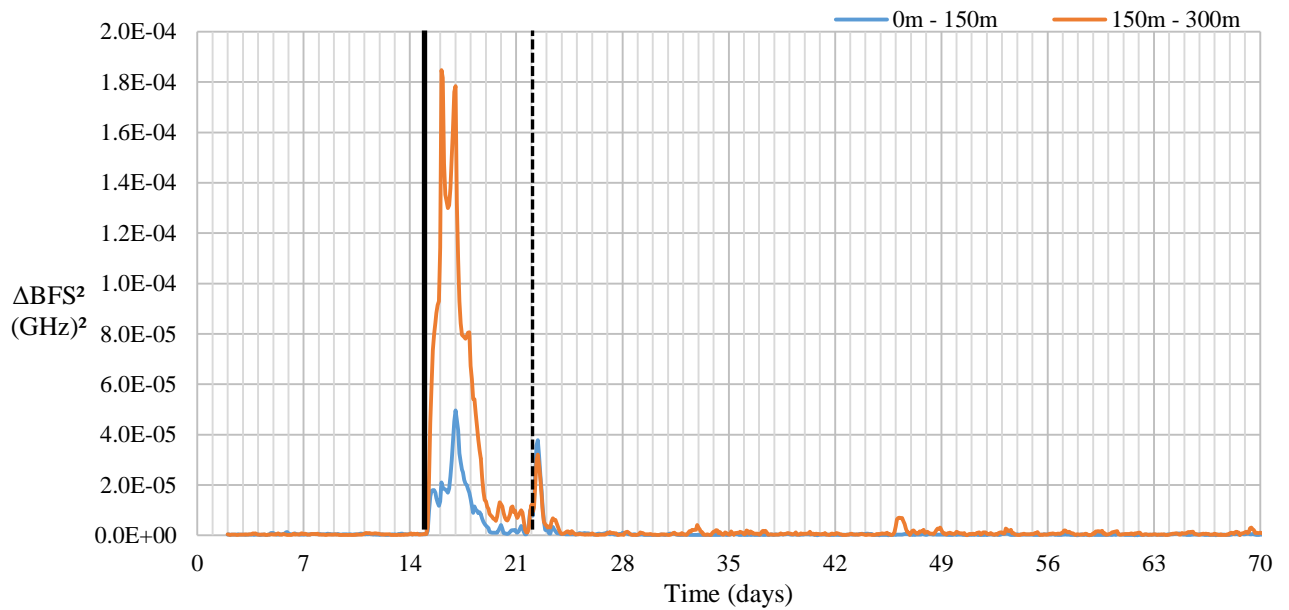


Figure 4.88. Maximum  $\Delta\text{BFS}^2$  output by the 2F-TB cable plotted against time.

It is immediately noticeable from Figure 4.88 that the 2F-TB cable output a maximum  $\Delta\text{BFS}^2$  for the leak test that is of the order of  $10^{-4}$ . This is an order of magnitude greater than the  $\Delta\text{BFS}^2$  response that was output by the 72F-6C-LC and the 4F-DC-LC cables. However, as shown in Figure 4.89, the maximum  $\Delta\text{BFS}^2$  that the 2F-TB cable outputted before the leak was imposed was between the values of  $2\text{E-}7$  and  $2\text{E-}6$  (GHz)<sup>2</sup>, which is an order of magnitude greater than the pre-leak maximum  $\Delta\text{BFS}^2$  output range of the 4F-DC-LC cable. Thus for both the LC and TB cable, the  $\Delta\text{BFS}^2$  between pre-leak and post-leak conditions was around two to three orders of magnitude.

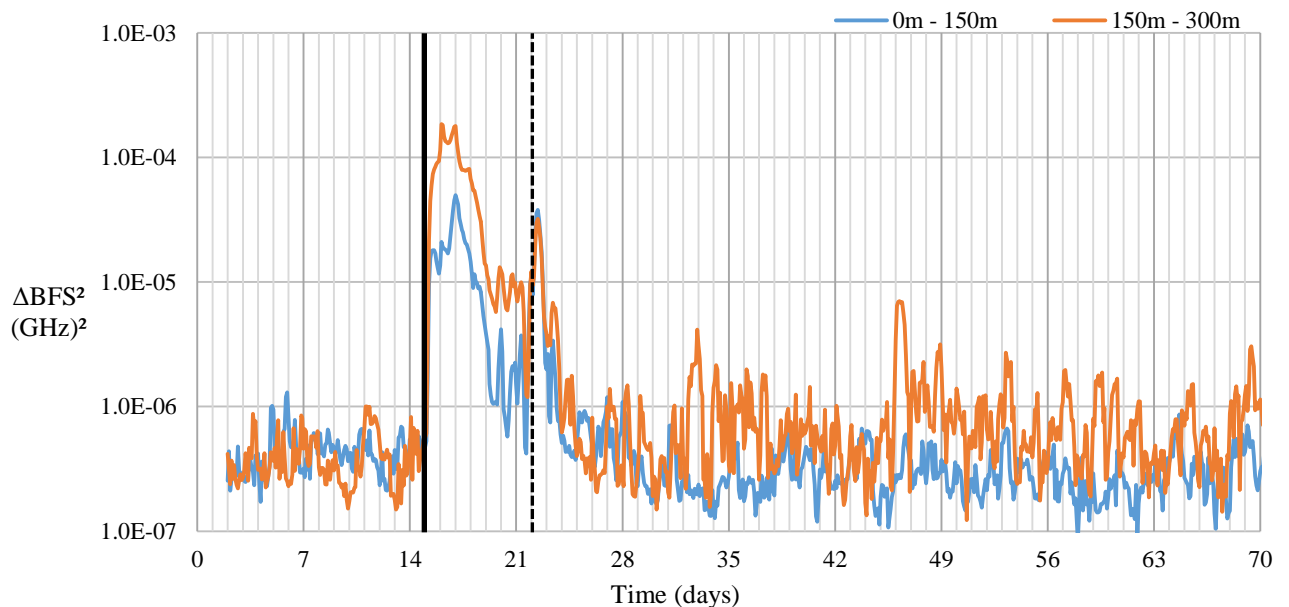


Figure 4.89. Maximum  $\Delta\text{BFS}^2$ , plotted on a logarithmic scale, produced by the 2F-TB cable against time.

The length-ordinate of the maximum  $\Delta\text{BFS}$  for each time step, along the 2F-TB cable, is shown in Figure 4.90.

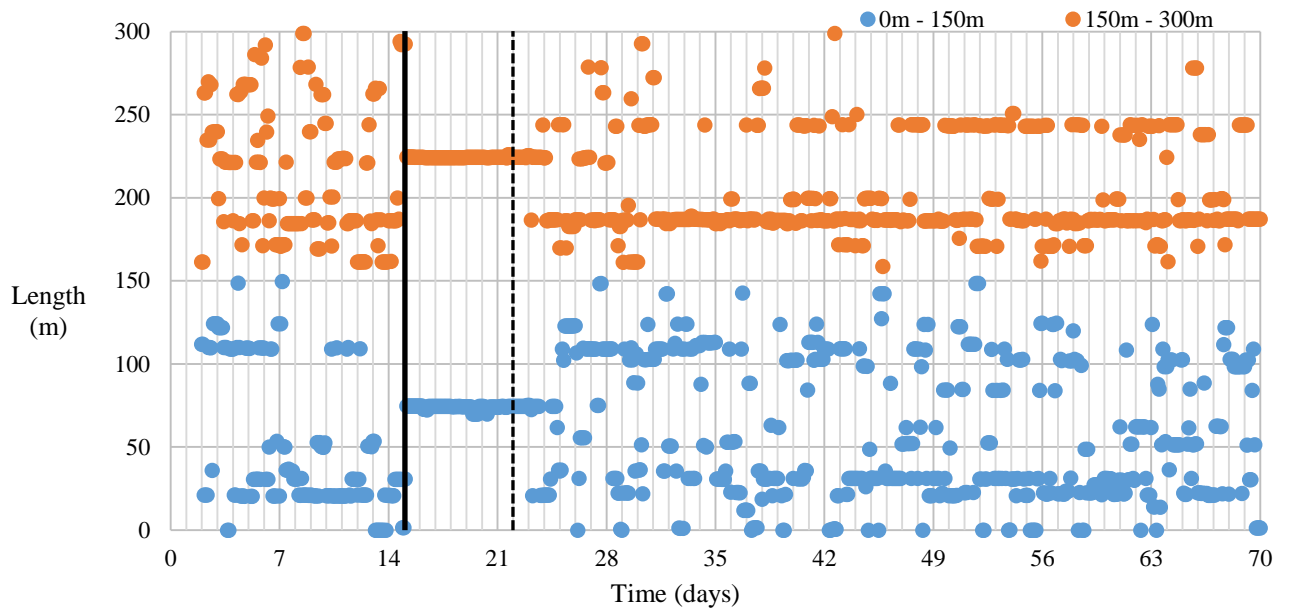


Figure 4.90. Length-ordinate of the Maximum  $\Delta\text{BFS}$  output by the 2F-TB cable for each time step.

Unlike the LC cables, the length-ordinate of the maximum  $\Delta\text{BFS}$  for the 2F-TB cable, after the leak had been imposed, remains mostly constant. This is because the 2F-TB cable is influenced by strain and temperature effects within the soil. Therefore, referring to the experimental setup, the part of the cable on the side of the trench where the standpipe is installed will experience a greater  $\Delta\text{BFS}$  as the surrounding soil will receive more water. This is because the strain in the soil on the standpipe-side of the trench will be greater than that of the opposite side. This is evidenced by the  $\Delta\text{BFS}^2$  vs length profile shown in Figure 4.91.

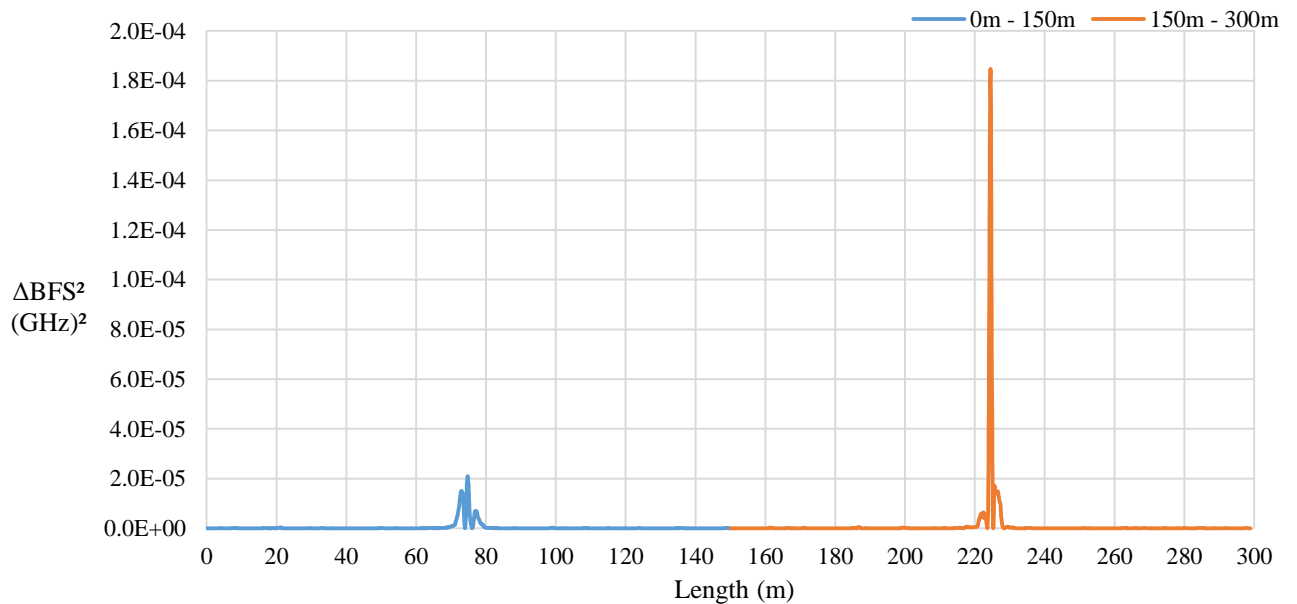


Figure 4.91.  $\Delta\text{BFS}^2$  plotted against length for time instant,  $t = 16$  days and 2 hours along the 2F-TB cable. There was greater strain in the soil corresponding to  $L = 225\text{m}$  than at  $L = 75\text{m}$ .

The  $\Delta\text{BFS}$  is biased toward the 225m length-ordinate over the 75m length-ordinate. This is because the 2F-TB cable length-ordinate of 225m is on the side of the trench on which the standpipe is installed.

The  $\Delta\text{BFS}$  response, however, is strong at both length-ordinates, meaning that even if the fibre is not right next to the point of water ingress it is still able to conclusively detect the leak.

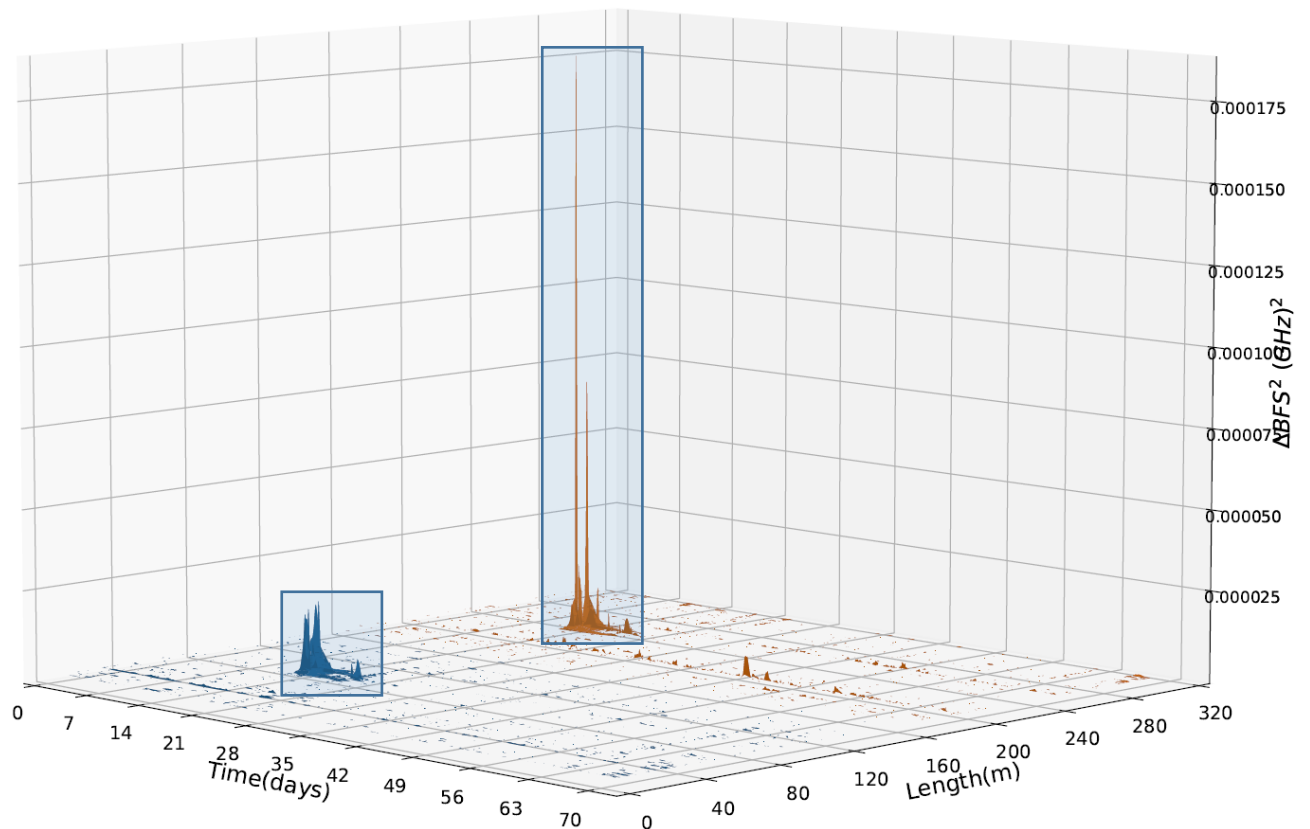


Figure 4.92. A 3-Dimensional plot of the  $\Delta\text{BFS}^2$  (excluding values less than  $1\text{e-}8$   $(\text{GHz})^2$ ) against time and length for the 2F-TB cable during the first prolonged leak test.

Unlike the 4F-DC-LC cable, the two halves of the 2F-TB cable responded very differently to the induced leak. As can be seen in Figure 4.92 the first half, 0m -150m, of the 2F-TB cable produced a much lesser  $\Delta\text{BFS}^2$  response to the leak than the second half, 150m-300m, of the cable. This is due to asymmetrical soil strain conditions that develop in the trench due to the influx of water from the standpipe.

The standpipe is positioned on one side of the trench. Thus, when the water is introduced at this point there is an asymmetrical distribution of water at the base of the trench where the standpipe is located. This asymmetrical water distribution leads to the asymmetrical soil strain conditions in the trench which is detected by the strain sensitive 2F-TB cable.

The detection of the leak by the 2F-TB cable shows that all three cable types used in the experiment, i.e. the strain cable, the LC cables, and the TB cables, all conclusively function as leak detection sensors.

#### 4.7.3.4 6F-TB TO 72F-6C-LC

The 6F-TB and 72F-6C-LC cables analysed side-by-side, provides a good comparison between the performance of the TB and the LC cable types. By separating the cable into its two segments, analysing them individually and comparing them, the differences and similarities in their behaviour as leak

detection sensors can be evaluated. The maximum  $\Delta\text{BFS}^2$  occurring within the two segments, 6F-TB and 72F-6C-LC, for each time step is plotted in Figure 4.93.

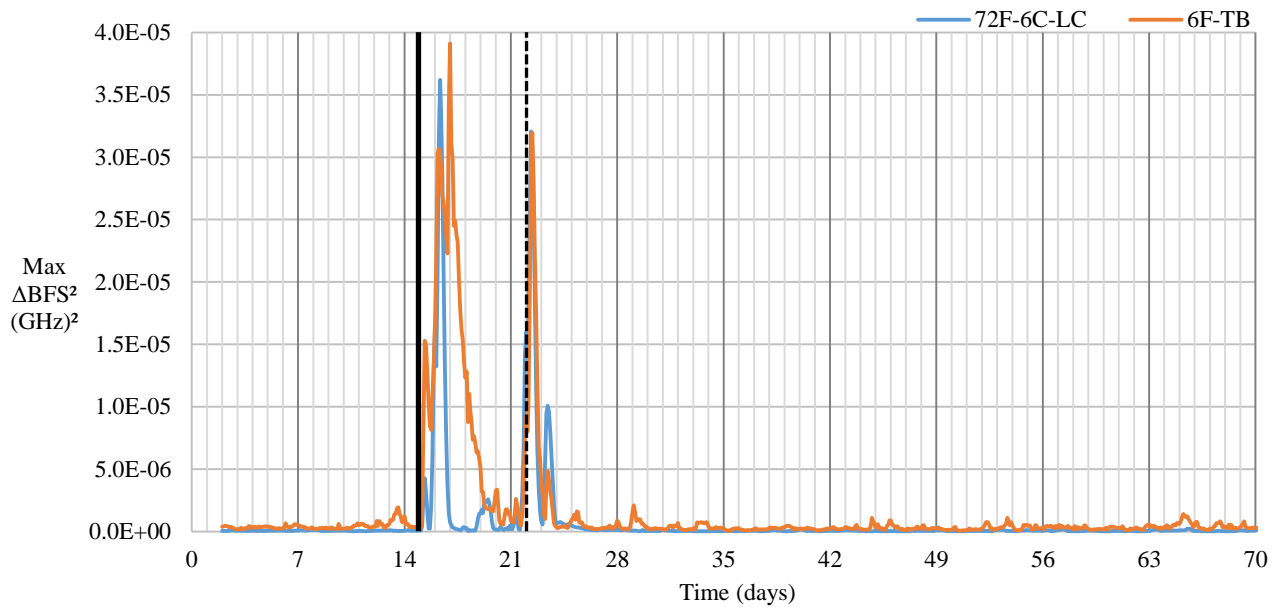


Figure 4.93. Maximum  $\Delta\text{BFS}^2$  output by the 6F-TB to 72F-6C-LC cable plotted against time.

The  $\Delta\text{BFS}$  in both cables deviated at the same time instant,  $t = 15$  days and 2 hours, as expected, however they reached their peak  $\Delta\text{BFS}$  at different time instances. The 72F-6C-LC cable obtained a maximum  $\Delta\text{BFS}$  at time  $t = 16$  days and 4 hours, and the 6F-TB cable had its peak  $\Delta\text{BFS}$  at time  $t = 17$  days. Interestingly, the difference between the maximum  $\Delta\text{BFS}^2$  values output by each cable during the leak test was not very large, only  $0.29 \times 10^{-5}$   $(\text{GHz})^2$ . The maximum  $\Delta\text{BFS}^2$  values for each cable were therefore of the same order of magnitude,  $10^{-5}$ , in contrast to the 2F-TB cable which output a  $\Delta\text{BFS}^2$  response with an order of magnitude of  $10^{-4}$ . This shows that there is variability in output ranges even among cables of the same type. Throughout the experiment, all cables were able to output a  $\Delta\text{BFS}^2$  response greater than  $10^{-5}$ . This value could be taken as a lower bound for the  $\Delta\text{BFS}^2$  output due to a leak event.

Regarding the increase and decrease surrounding the peaks, the maximum  $\Delta\text{BFS}$  of the 72F-6C-LC cable increases to its peak and decreases back to its original state over a period of 2 days. The maximum  $\Delta\text{BFS}$  of the 6F-TB cable increases similarly to the 72F-6C-LC cable, but the 6F-TB cable's  $\Delta\text{BFS}$  decreases at a slower rate than that of the 72F-6C-LC cable, taking about 5 days to return to its former state. This could be attributed to the strain effects taking place in the soil during the ingress of water, causing a longer duration of greater  $\Delta\text{BFS}$  values to occur as equilibrium is reached in the soil for both temperature and strain states.

By plotting the  $\Delta\text{BFS}^2$  from Figure 4.93 on a logarithmic scale, Figure 4.94 is obtained.

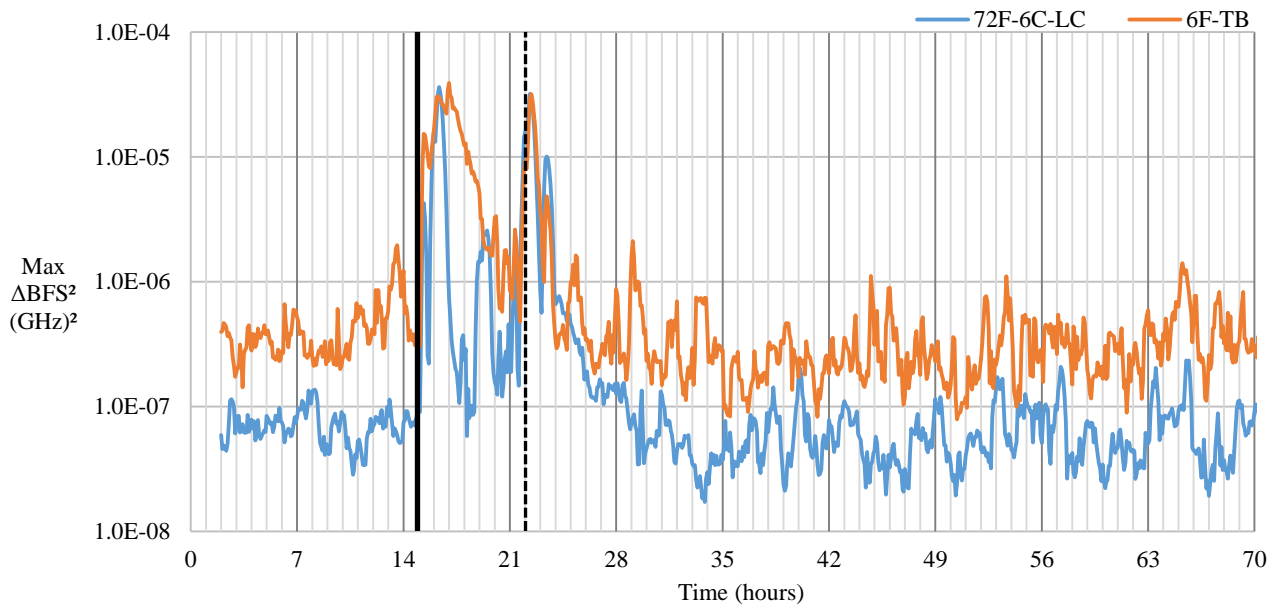


Figure 4.94. Maximum  $\Delta BFS^2$ , plotted on a logarithmic scale, output by the 6F-TB to 72F-6C-LC cable, against time.

Comparing the behaviour of the 6F-TB and the 72F-6C-LC cable before the leak takes place it is clear that the expected maximum  $\Delta BFS^2$  for the 6F-TB cable is above  $10^{-7}$ , and sometimes even goes above  $10^{-6}$ . The expected maximum  $\Delta BFS^2$  of the 72F-6C-LC cable lies mostly beneath  $10^{-7}$ , sometimes exceeding  $10^{-7}$  slightly. This highlights the increased effect than strain effects can impose onto a cable's baseline behaviour that is both strain and temperature sensitive, as opposed to only being temperature sensitive, even under normal conditions.

By comparing the length-ordinates of the maximum  $\Delta BFS$  that occurred along each cable for each time step, Figure 4.95 is generated.

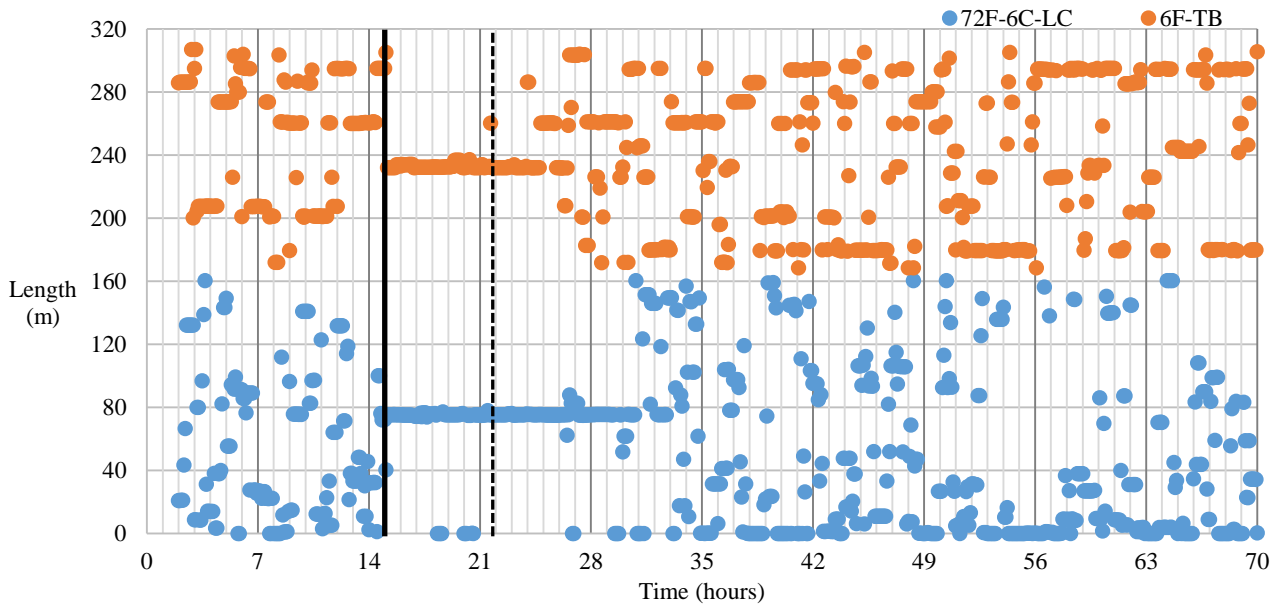


Figure 4.95. Length-ordinate of the Maximum  $\Delta BFS$  output by the 6F-TB to 72F-6C-LC cable for each time step.

From Figure 4.95, the length-ordinate of the maximum  $\Delta\text{BFS}$  seems to be more random in the 72F-6C-LC cable than in the 6F-TB cable. The length-ordinate of the 6F-TB cable appears to remain in one region for extended periods of time before switching to a different region. The length-ordinate of the 72F-6C-LC cable appears to be more scattered, with the length-ordinate remaining in a single position for an extended period less frequently than the 6F-TB cable. After the leak has been imposed however, both cables are conclusively able to detect the leak's location, as is shown by the length-ordinate residing around 75m for the 72F-6C-LC cable, and around 230m for the 6F-TB cable. By plotting the  $\Delta\text{BFS}^2$  for the two cables along their lengths the peaks due to the leak can be seen in Figure 4.96.

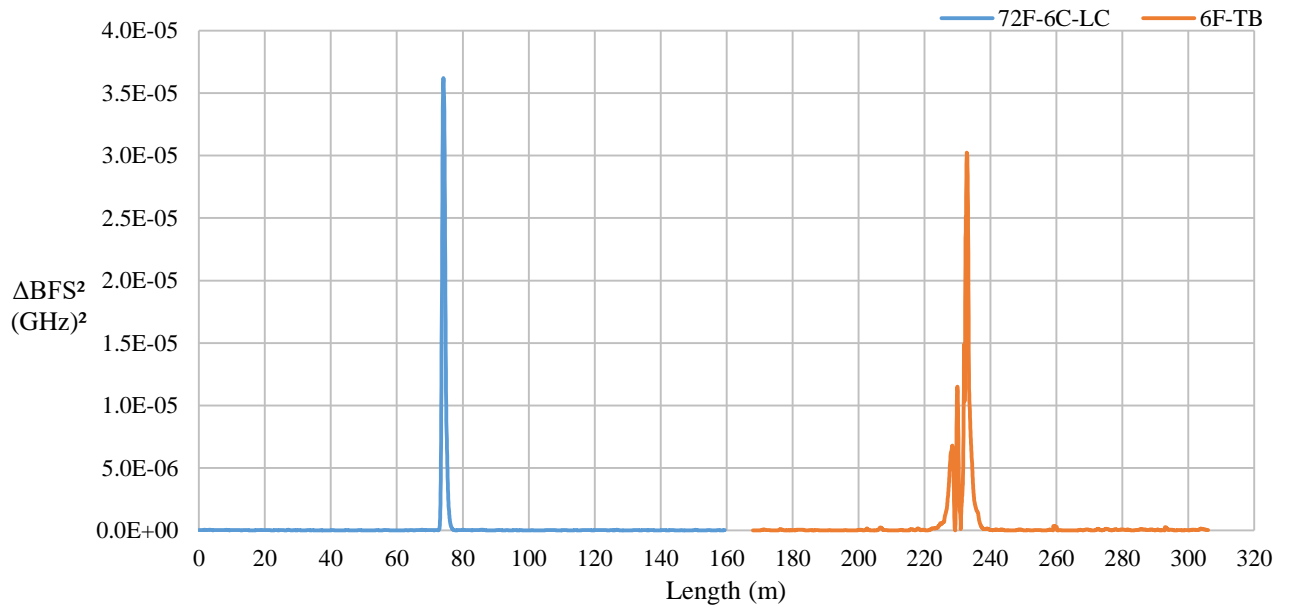


Figure 4.96.  $\Delta\text{BFS}^2$  plotted against length for the 6F-TB and the 72F-6C-LC cables at time instant,  $t = 16$  day and 8 hours.

Even though the  $\Delta\text{BFS}^2$  for the 6F-TB cable in the region of the leak was only of the order of magnitude of  $10^{-5}$ , the peak in the  $\Delta\text{BFS}^2$  vs length profile is clearly distinguishable from the  $\Delta\text{BFS}^2$  in the unaffected regions surrounding the peak of the 6F-TB cable. As shown in Figure 4.96, both the 72F-6C-LC and the 6F-TB cables gave good  $\Delta\text{BFS}$  responses to the imposed leak, which indicates that both LC and TB cables types, when compared directly as seen in Figure 4.96, are suitable to use as leak detection sensors.

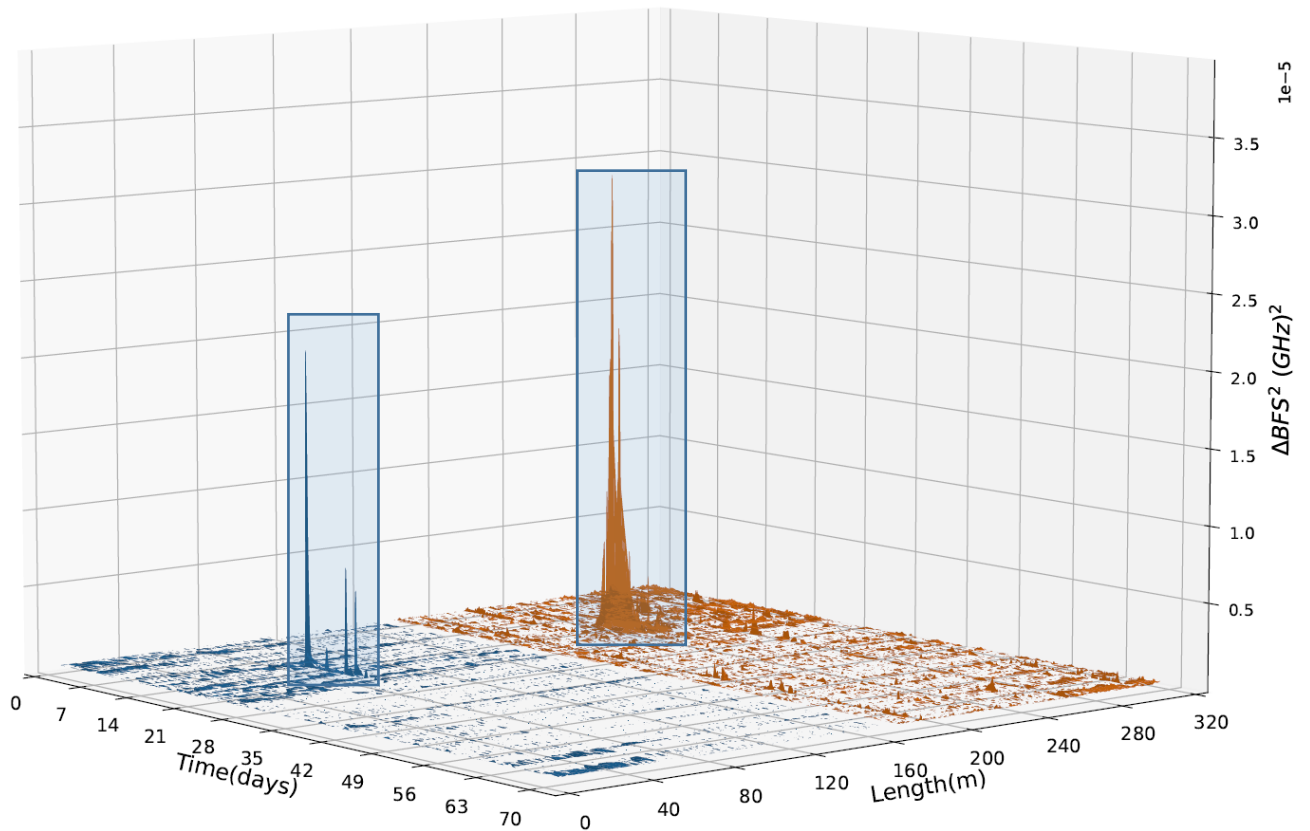


Figure 4.97. A 3-Dimensional plot of the  $\Delta\text{BFS}^2$  (excluding values less than  $1\text{e-}8$  ( $\text{GHz}^2$ )) against time and length for the 6F-TB to 72F-6C-LC cable during the first prolonged leak test.

Considering Figure 4.96 and Figure 4.97, a comparison of the 6F-TB against the 72F-6C-LC cable shows that the 6F-TB cable has a wider region of length over which it is affected than the 72F-6C-LC cable. This wider length of influence is likely caused by soil strains developing further away from point of water influx which is detected by the strain sensitive TB cable. The narrower length of influence seen by the LC cable is due to it being affected locally by the changing temperature conditions caused by the water influx. The change in temperature is localised to the close vicinity about the standpipe base and is nullified by the surrounding soil so that the temperature change does not migrate laterally.

## 4.8 BURIED PIPELINE CONDITIONS

Thus far only the results of the FO cables buried in the trench on the University of Pretoria Hillcrest Campus have been discussed. Although similar to a buried pipeline these results from the Hillcrest Campus trench could be further verified by assessing how a FO cable responds to a change in surrounding soil moisture content when buried along a real pipeline. The FO cable was fully installed and buried with the pipe. The pipeline was not carrying water when this test was carried out however. The maximum  $\Delta\text{BFS}^2$  along the FO cable buried in Tom Jenkins plotted against time is shown in Figure 4.98.

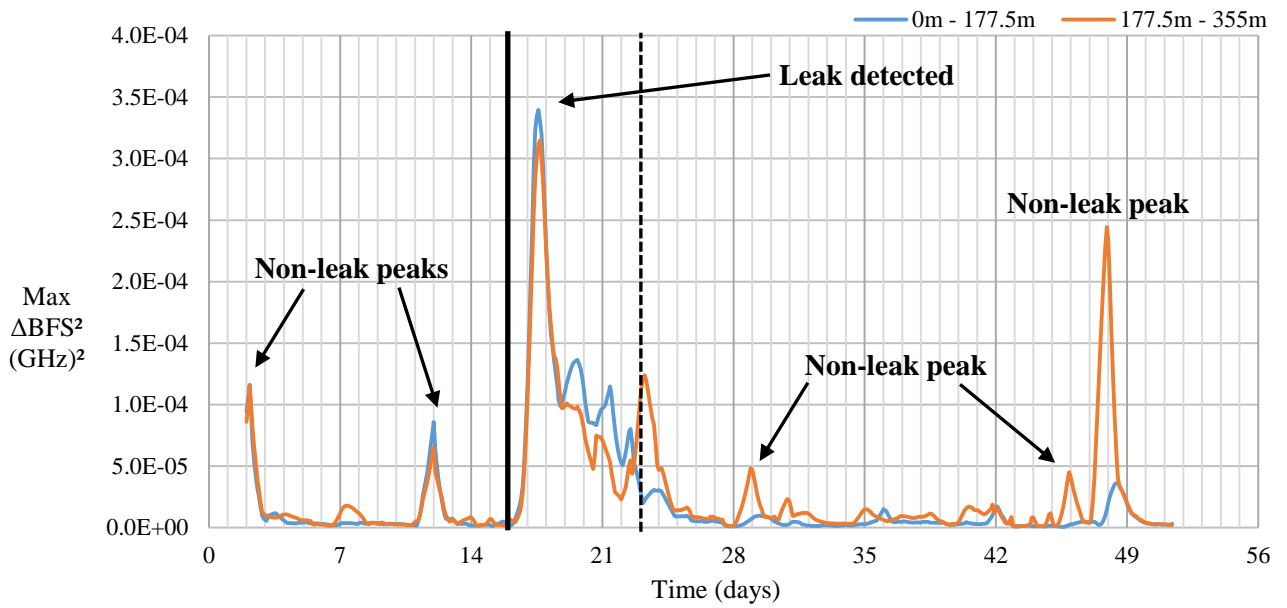


Figure 4.98. Maximum  $\Delta BFS^2$  measured along Tom Jenkins Drive plotted against time. The solid line corresponds to the start of the influx of water, and the dashed line to the end of the induced leak.

As depicted in Figure 4.98 there is a definite  $\Delta BFS$  which was caused by the influx of water into the surrounding soil. There are, however, other peaks that appear in the maximum  $\Delta BFS^2$  vs time curve that occur outside of the realm of the leak test. These peaks could be attributed to the pipeline itself having leaks developing after installation (the pipe would need to be excavated to confirm this), or it could be another occurrence due to the different environment compared to the trench on the Hillcrest Campus.

The length-ordinates of the maximum  $\Delta BFS^2$  that occur along the FO cable, plotted against time, is shown in Figure 4.99.

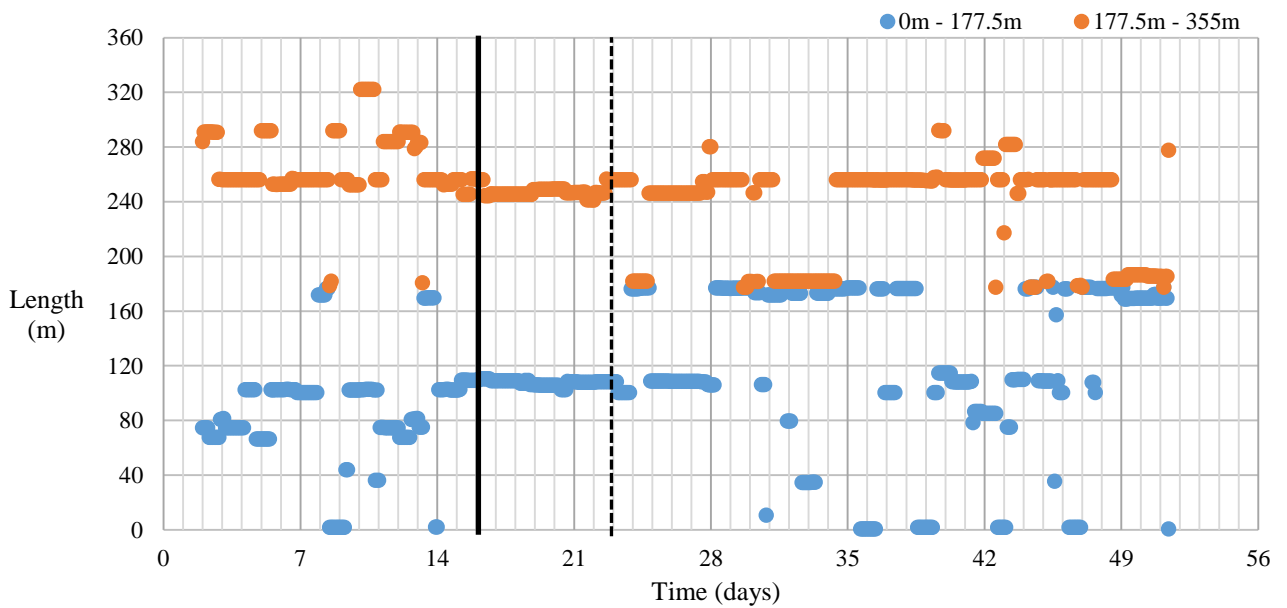


Figure 4.99. Length-ordinate of the maximum  $\Delta BFS^2$  that occurred along Tom Jenkins Drive plotted against time.

The length-ordinates of the maximum  $\Delta BFS^2$  do not vary as randomly as those measured in the Hillcrest Campus trench. It is possible that the lack of variability is due to the cable not being buried deep enough

to minimise the effect that daily ambient temperature changes have on the FO cable's BFS. Once the leak was induced into the system, the length-ordinate of the maximum  $\Delta\text{BFS}$  was concurrent with the location of the standpipe used for the leak test. This is evidenced by the plot of  $\Delta\text{BFS}^2$  vs length at time  $t = 17$  days and 4 hours, the time of occurrence of the maximum  $\Delta\text{BFS}$ . This is shown in Figure 4.100.

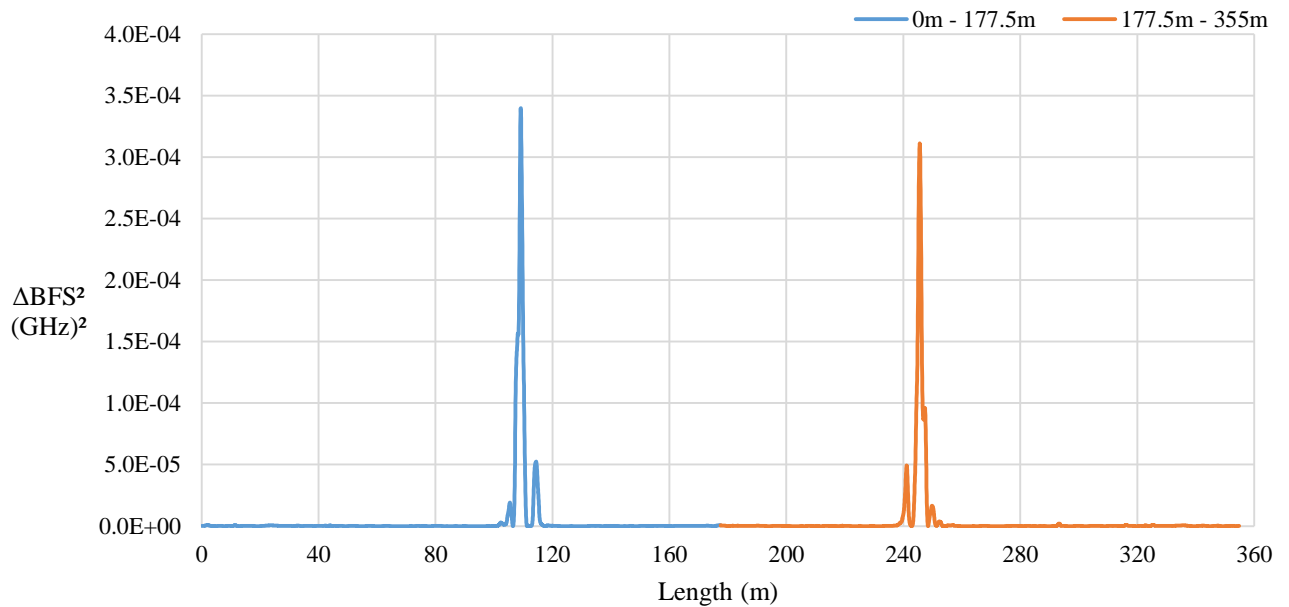


Figure 4.100. Plot of the  $\Delta\text{BFS}^2$  plotted against distance at time  $t = 17$  days and 14 hours along at Tom Jenkins Drive.

Thus the 2F-TB cable buried in Tom Jenkins Drive along the pipeline was indeed able to detect the leak induced into the surrounding soil. The problem, however, is that the peak due to the induced leak was not the only peak that was detected by the FO cable during the period of observation. Looking at the 3-Dimensional plot of the  $\Delta\text{BFS}^2$  plotted against time and length in Figure 4.101 three other peak events can be seen other than the one caused by the induced leak.

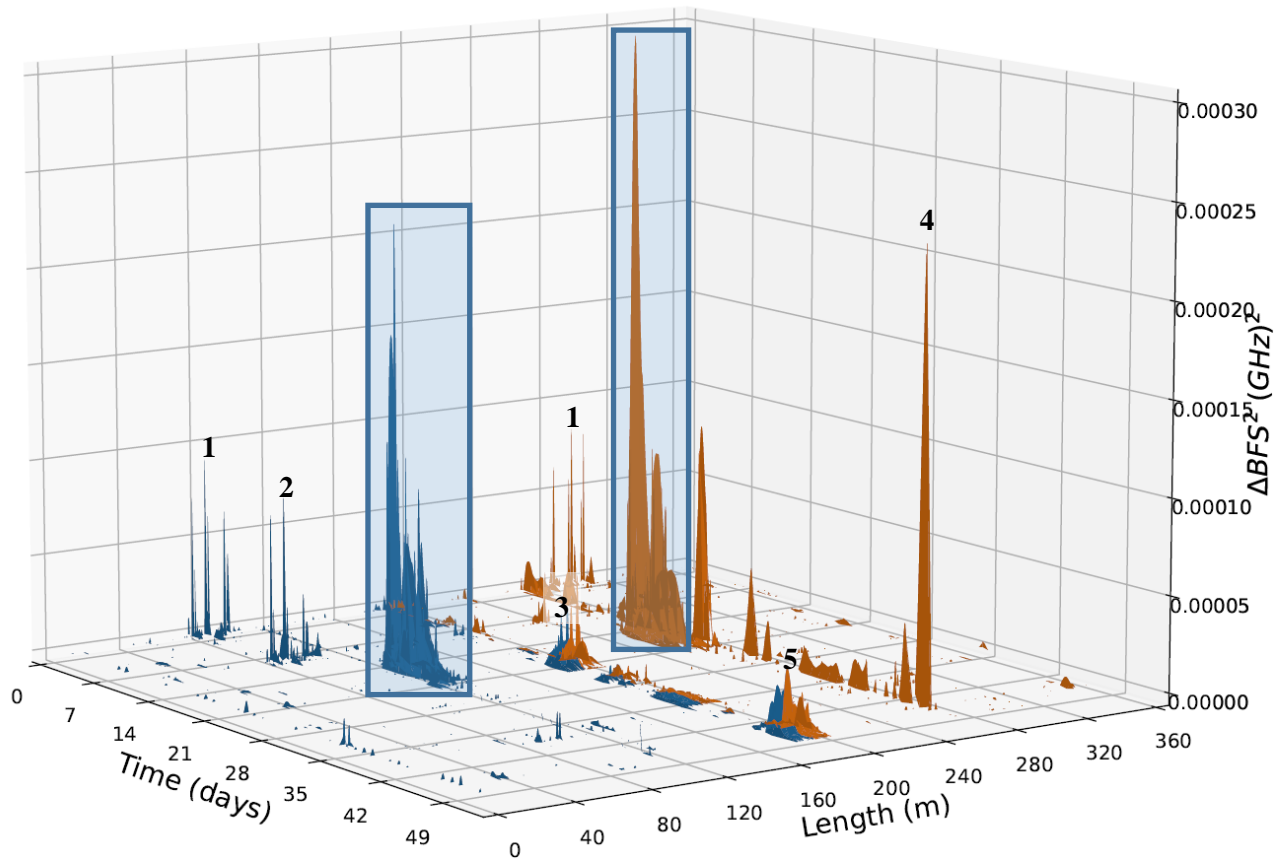


Figure 4.101. 3-Dimensional plot of the  $\Delta\text{BFS}^2$  (excluding values below  $1\text{e-}6$  (GHz) $^2$ ) produced at Tom Jenkins Drive plotted against both time and length. The  $\Delta\text{BFS}^2$ -peaks due to the induced leak are highlighted by blue boxes. The five other non-induced-leak events are numbered chronologically.

From Figure 4.101 there seems to be more factors that are able to influence the  $\Delta\text{BFS}$  produced by the FO cable in a working pipeline environment than in the experimental trench setup. The FO cable seems to be more active when buried along a working pipeline as evidenced by the five other non-induced-leak events. With that being the case, the FO cable proved successful in its endeavour as a leak detection sensor to detect a soil moisture content change along a working pipeline.

## 4.9 DISCUSSION OF RESULTS

The behaviour of the BFS occurring in a FO cable is a function of the strain state and the temperature that the optical fibres experience. The FO cables experience both temperature and strain variations while buried in ground under baseline conditions, from which the expected FO cable behaviour can be formulated. In addition, cables buried deeper undergo less temperature variation than those buried in shallower ground.

The mechanism driving the leak detection system presented is a stark change in the BFS registered by the FO cable in a specific region of the cable. The introduction of water into the soil surrounding the FO cable causes the temperature of the soil to change, and the soil also undergoes strain due to changes in matric suction. The temperature change is most easily imposed onto the FO cable, regardless of its type. If the FO cable is strain sensitive then the effect of the soil strains can be imposed onto the FO cable as

well. Both the change in temperature and strain of the FO cable cause the BFS at the affected location to alter. This alteration is what is detected once the BFS output from the cable is processed to expose the  $\Delta$ BFS leak-peaks.

It is evident that different FO cable types experience different ranges of  $\Delta$ BFS under baseline conditions. The LC cables tested experienced  $\Delta$ BFS<sup>2</sup> in the region of  $10^{-8}$  (GHz)<sup>2</sup>, while the TB cables experienced  $\Delta$ BFS<sup>2</sup> in the region of  $10^{-7}$  (GHz)<sup>2</sup>. It is helpful to rid the BFS output of periodic temperature variations encountered throughout the day. In conjunction therewith, cleaning the BFS output profiles using CMAs proves useful to rid the data of unwanted noise anomalies.

The performance of the FO cables as leak detection sensors varies from cable to cable. However, it has been proven that each FO cable type tested was suitable to detect water ingress into the surrounding soil. It seems from the leak tests that the depth to which the FO cables are buried does not have any effect on the detectability of the leaks. The leaks imposed in each depth region were conclusively able to be detected. No clear relationship between FO cable burial depth and leak-imposed  $\Delta$ BFS was discovered.

TB cables, due to their increased sensitivity to strain effects, register larger  $\Delta$ BFS when used as leak detection sensors than LC cables. When the data output by TB is processed, the TB cables also output a longer peak waning period after the leak has occurred before returning back to normal. However, due to the difference in baseline behaviour of the TB and LC cables, the ratio of the  $\Delta$ BFS leak-peak values to the  $\Delta$ BFS baseline values are fairly similar.

The amount of water that is allowed to ingress into the soil surrounding a FO cable has a significant influence of the  $\Delta$ BFS output by the cable at the location of water ingress. In the tests that used 50L of water as a bulk volume the  $\Delta$ BFS due to the ingress of water into the soil was noticeable, but not as substantial as those caused by prolonged leaks. These leaks were able to be detected by each cable, but the output was not as strong as that of a prolonged leak.

The results of the prolonged leak test, in which a large volume of water was used, produced very clear and unmistakable leak-test results. The time of origin and location of the prolonged leak was detected by each cable.

When placed along a real pipeline, the 2F-TB cable behaved differently to how it behaved in the experimental Hillcrest Campus trench. The length-ordinate of the maximum  $\Delta$ BFS<sup>2</sup> did not vary as randomly as in the experimental trench and there were five other non-induced-leak peaks detected by the cable, the causes of which are uncertain. The FO cable, however, was able to detect the leak as in the experiments in the Hillcrest campus trench signifying that the FO cable leak detection system along an actual working pipeline is indeed viable.

From the results obtained on the Hillcrest Campus the 2F-TB cable is best suited as a leak detection sensor due to its strong leak detection signal output. However, when the 2F-TB cable was tested along Tom Jenkins Drive it yield results which were unforeseen at the Hillcrest Campus setup. The random

non-leak peak events must further be investigated so that a clearer understanding of the FO cable behaviour along a working pipeline can be obtained.

## **5 CONCLUSIONS AND RECOMMENDATIONS**

### **5.1 CONCLUSIONS**

A study has been conducted investigating the validity of a FO leak detection system based upon Brillouin Frequency Shift Fibre Optic Distributed Sensing. Leaking pipes are responsible for 25.4% of the NRW that is lost in South Africa, with similar losses happening in many countries around the world. Leak detection technologies are in existence, such as acoustic leak detection sensors. However, these are implemented as discrete measurement techniques which require processing of their output data to pinpoint the location of a potential detected leak.

FO cables consist of a small diameter light transmitting glass fibre surrounded and protected by a sheath. The sheath can either be attached to the optical fibre or separated from it by a gel matrix. Optical fibres are highly durable due to their protective sheaths and are immune to interference from all types of radiation.

Some of the light that is transmitted by the optical fibre is reflected/backscattered with different photonic properties to the original input light signal. The altered properties of these backscattered light signals are dependent upon the stress and temperature states of the optical fibres. Backscattered light can be used to create distributed sensors from FO cables by measuring the backscattered light from many length-ordinates along an optical fibre, with small spatial resolutions.

The BFS is a backscatter phenomenon that occurs in FO cables which is co-dependent upon the strain and temperature state of the optical fibre. It can be measured along a fibre optic cable with a spatial resolution as small as 5cm and can monitor FO cable lengths of up to 100km. By measuring the BFS multiple times along a FO cable and then comparing the readings, changes in temperature and strain state can be detected. This methodology can be implemented to produce a pipe leak detection system by monitoring for changes in BFS that occur in a FO cable buried along a pipeline.

Water flowing out of a break point of a buried pipeline into the surrounding soil will interact with the soil causing the temperature and strain state of the soil to change. If a FO cable is buried in the affected soil the change in temperature and strain states experienced by the soil are in turn imposed onto the buried FO cable. The state change experienced by the FO cable is registered by the change in BFS response that the optical fibre produces.

A field experimental setup was created to mimic the conditions that a buried working pipeline instrumented with a FO cable would be subjected to. Five FO cables (strain, 72F-6C-LC, 4F-DC-LC, 2F-TB, 6F-TB), consisting of three different cable types (strain, LC and TB) were buried within a 150m long trench with nine standpipes spaced along the trench for the introduction of water into the soil. This

was included in the study to investigate which FO cable type is best suited to operate as a leak detection sensor.

The depth to which a FO cable is buried has an influence on how the BFS of the FO cable output varies through seasonal/temperature variations throughout the year. The raw BFS of the FO cable is at a peak during the summer and at a low during the winter. The FO cable type, however, also plays a role in the seasonal variation of the BFS. LC cables show the greatest change in BFS throughout the year, being primarily affected by temperature effects. The TB cables, due to their susceptibility to soil strain influences, show less variation in BFS throughout the year as the optical fibre cables are held in place in their sheaths and in the soil. Thus, their expansion and contraction potential in response to a temperature change is hindered.

The leak test experimentation consisted of inducing artificial leaks at chosen standpipe points and analysing the response of the BFS that occurred over time in the different FO cables in the field setup. Specifically, the change in BFS occurring in the FO cables was analysed to see how the FO cables would respond to the imposed water influx down the standpipe. The results of the tests showed great changes in the BFS occurring at the FO cable length-ordinates corresponding to the used standpipes, while the FO cable did not register any significant changes at the unaffected FO cable length-ordinates.

It was also concluded that each cable that was tested in this study was capable of functioning as a leak detection sensor. Each cable produced a stark change in its BFS at the length-ordinate of the induced influx of water down the active standpipe as compared to the rest of the  $\Delta$ BFS vs length profile. Each cable was also able to determine the time of origin of the leak in conjunction with the leak length-ordinate.

Both a small leak amounting to 50L in total, and prolonged leaks were induced into the field setup to investigate how the FO cables perform as leak detection sensors. It was concluded that small leaks were detectable by the FO cables, but with less certainty as the  $\Delta$ BFS leak-response was in some cases masked by the  $\Delta$ BFS baseline output of the FO cable. However, prolonged leaks are able to be conclusively detected by the FO cables as these leaks produced changes in BFS that far exceed the baseline  $\Delta$ BFS behaviour of the FO cable.

An experimental setup was also created along a working pipeline installed along Tom Jenkins Road in Rietondale, Pretoria. A length of 2F-TB was buried along the pipeline to assess the working conditions of a live pipeline in the field. Water was introduced at the level of the FO cable, again using a standpipe, and it was proven that a  $\Delta$ BFS was indeed registered by the FO cable in response to a leak under working pipeline conditions. It was also noted, however, that the FO cable registered other events, appearing like leaks, and taking place along its length that were not induced during the experiment. Further investigation and research are required on active pipelines to determine what these unknown  $\Delta$ BFS events are caused by.

The depth to which FO cables are buried does not have an influence on the detectability of a leak. The change in soil strain and temperature state are the main factors that contribute to the  $\Delta$ BFS response that occurs due to a leak. However, the effect that a buried leaking pipe has on the  $\Delta$ BFS of a FO cable has not been tested in this study. The water introduced into the standpipes was above ground and thus was influenced by daily temperature fluctuations which may differ from the temperature fluctuations that exist within a working buried pipeline.

## **5.2 RECOMMENATIONS**

It is recommended that any further study of the topic be conducted on a working pipeline. As this study has not incorporated data acquired from monitoring the BFS of a FO cable in a working pipeline environment, monitoring an operational pipeline would be the next step to validating the proposed BFS FO leak detection system.

Throughout this study the BFS interrogator was stopped and reset each time a new phase of the study was entered. It would be advantageous to run the interrogator at a fixed logging rate without restarting the logging process. This would allow for a continuous flow of BFS data to be collected and analysed without gaps in the time history of the data.

The use of LC FO cables as a means of investigating the temperature effect was satisfactory. However, recording the actual temperature using thermistors at a location where a leak occurs could be used to quantify the exact temperature change that occurs in the soil where a leak is happening.

In addition, due to the water introduction pipes being above ground during the artificial leak tests, the temperature fluctuation was heavily influenced by the ambient air temperature. During a real leak event the water in a leaking pipe would not be affected by the ambient air temperature. The temperature fluctuation that the water in a pipe network undergoes must therefore be quantified if further research using live pipelines is to be conducted.

Within a water distribution network there is pressure variation as a result of end customer usage levels. When the usage is high the pressure is lower, and when the usage abates the pressure increases. This pressure variation could impose other stresses upon the FO cables which have not been accounted for in this study. It is recommended therefore that the pressure within a working pipeline be quantified and investigated to determine how the pressure variation influences the  $\Delta$ BFS response that a FO cable produces.

## REFERENCES

- Adem, H. Vanapalli, S. 2014. Soil–environment interactions modelling for expansive soils. *Environmental Geotechnics*, Volume 3, No 3, May, pp 178-187.
- Bhagwan, J. Wegelin, W. Mckenzie, R. Wensley, A. 2014. Counting the lost drops: South Africa’s study into non-revenue water. *Water Practice & Technology*. Volume 9, No 2, December.
- Blazevic, M. Samardzic, I. Kolombic, Z. 2005. Leak Detection in Underground Pipelines of Municipal Water Distribution. *International Conference on Advanced Technologies for Developing Countries, Conference 4*, September.
- Burn, S. DeSilva, D. Eiswirth, M. Hunaidi, O. Speers, A. Thornton, J. 1999. Pipe Leakage – Future Challenges and Solutions. *Pipes Wagga Wagga*, January.
- Cheng-Yu, H. Yi-Fan, Z. Guo-Wei, L. Meng-Xi, Z. Zi-Xiong, L. 2017. Recent progress of using Brillouin distributed fiber optic sensors for geotechnical health monitoring. *Sensors and Actuators A: Physical*, Volume 258, March, pp 131-145.
- Clayton, C.R.I. Xu, M. Whiter, J.T. Ham, A. Rust, M. 2010. Stresses in cast-iron pipes due to seasonal shrink-swell of clay soils. *Water Management*, Volume 163, No 3, pp 157-162.
- Curran, M. Shirk, B. 2018. Basics of Fibre Optics. Communication
- Galindez-Jamioy, C.A. López-Higuera, J.M. 2012. Brillouin Distributed Fibre Sensors: An Overview and Applications. *Journal of Sensors*. Volume 2012, No 1, August, 17 pages.
- Gens, A. Alonso, E.E. 1992. A framework for the behaviour of unsaturated expansive clays. *Canadian Geotechnical Journal*, Volume 29, August.
- Georgia Environmental Protection Division Watershed Protection Branch. 2007. Leak Detection and Repair Programs. *Communication*, August.
- Gong, J. Png, G.M. Arkwright, J.W. Papageorgiou, A.W. Cook, P.R. Lambert, M.F. Simpson, A.R. Zecchin, A.C. 2018. In-pipe fibre optic pressure sensor array for hydraulic transient measurement with application to leak detection. *Measurement*, Volume 126, May, pp 309-317.
- González-Gómez, F. García-Rubio, M.A. Guardiola, J. 2011. Why Is Non-revenue Water So High in So Many Cities? *Water Resources Management*, Volume 27, No 2, June, pp 345-360.
- Grattan, K.T.V. Sun, T. 1999. Fibre Optic Sensor Technology: An Overview. *Sensors and Actuators*, Volume 82, November, pp 41-60.
- Jacobsz, S.W. Jahnke, S.I. 2020. Leak detection on water pipelines in unsaturated ground by discrete fibre optic sensing. *Structural Health Monitoring*, Volume 19, No 4, pp 1219-1236.
- Jennings, J.E. Kerrich, J.E. 1962. The Heaving Of Buildings and the Associated Economic Consequences, With Particular Reference to the Orange Free State Goldfields. *Die Siviele Ingenieur in Suid Afrika*, November.
- Jiang, L. Wang, Y. Yang, P. Zhang, L. Yang, L. Dai, S. Lou, C. 2020. Brillouin scattering behaviour in acoustically guiding single-mode optical fibres with different core diameters. *Optics Communications*, Volume 459, November.
- Khademi, F. Budiman, J. 2016. Expansive Soil Causes and Treatments. *I-manager’s Journal on Civil Engineering*, Volume 6, No 3, June, pp 1-14.

- Kingdom, B. Liemberger, R. Marin, P. 2006. The Challenge of Reducing Non-Revenue Water (NRW) in Developing Countries. *Water Supply and Sanitation Sector Board Discussion Paper Series*, Paper No 8, December.
- Li, J. Cameron, D.A. Ren, G. 2013. Case study and back analysis of a residential building damaged by expansive soils. *Computers and Geotechnics*, Volume 56, December.
- Li, P. Vanapalli, S. Li, Tonglu, L. 2016. Review of collapse triggering mechanism of collapsible soils due to wetting. *Journal of Rock Mechanics and Geotechnical Engineering*, Volume 8, January, pp 256-274.
- Li, W. Ling, W. Liu, S. Zhao, J. Liu, R. Chen, C. Qiang, Z. Qu, J. 2011. *Journal of Environmental Sciences*, Volume 23.
- Martínez-Espiñeira, R. Garcia-Rubio, M. A. Gonzalez-Gomez, F. 2017. Which factors, and to what extent, influence the condition of urban water distribution networks. An empirical analysis of the Spanish case. *Water Resources and Economics*, Volume 18, February, pp 20-33.
- Mckenzie, R. Siquilaba, Z.N. Wegelin, W.A. 2012. The State Of Non-Revenue Water in South Africa. *Communication*, August.
- Mokhtari, M. Dehghani, M. 2012. Swell-Shrink Behaviour of Expansive Soils, Damage and Control. *Edge*, Volume 17, No 1, pp 1-10.
- Motil, A. Bergman, A. Tur, M. 2015. State of the art of Brillouin fibre-optic distributed sensing. *Optics & Laser Technology*, Volume 78, No 1, October, pp 81-103.
- Osama, H. 2000. Detecting Leaks in Water-Distribution Pipes. *Construction Technology Update*, Volume 40, October.
- Pedersen, J. Baadsgaard (Ed.) & Klee, P. (Ed.in C.), 2013. Meeting an increasing demand for water by reducing urban water loss - Reducing Non-Revenue Water in water distribution. *The Rethink Water network and Danish Water Forum White Papers*, Copenhagen. Available at [www.rethinkwater.dk](http://www.rethinkwater.dk)
- Ren, L. Jiang, T. Jia, Z.G. Li, D.S. Yuan, C.L. Li, H.N. 2018. Pipeline corrosion and leakage monitoring based on the distributed optical fiber sensing technology. *Measurement*, Volume 122, March, pp 57-65.
- Ross, G.J. 1978. Relationships of specific surface area and clay content to shrink-swell potential of soils having different clay mineralogical compositions. *Canadian Journal of Soil Science*, Volume 58, May, pp 159-166.
- Sandberg, C. Holmes, J. McCoy, K. Koppitsch, H. 1989. The Application of a Continuous Leak Detection System to Pipelines and Associated Equipment. *Transactions on Industry Applications*, Volume 25, No 5, September.
- Schenato, L. Galtarossa, A. Pasuto, A. Palmieri, L. 2020. Distributed optical fiber pressure sensors. *Optical Fiber Technology*, Volume 58, April.
- Tanimola, F. Hill, D. 2009. Distributed fibre optic sensors for pipeline protection. *Journal of Natural Gas Science and Engineering*, Volume 1, November.
- Van Zyl, J.E. Alsaydalani, M.O.A. Clayton, C.R.I. Bird, T. Dennis, A. 2013. Soil fluidisation outside leaks in water distribution pipes - preliminary observations. *Water Management*, Volume 166, No 1, November, pp 546-555.
- Van Zyl, J.E. Clayton, C.R.I. 2007. The effect of pressure on leakage in water distribution systems. *Water Management*, Volume 000, No 1, January, pp 1-6.

- Vanapalli, S.K. Fredlund, D.G. Pufahl, D.E. Clifton, A.W. 1996. Model for the prediction of shear strength with respect to soil suction. *Canadian Geotechnical Journal*, Volume 33, January, pp 379-392.
- Wang, F. Lin, W. Liu, Z. Qui, X. 2019. Pipeline Leak Detection and Location Based on Model-Free Isolation of Abnormal Acoustic Signals. *Energies*, Volume 12, August.
- Water Wheel. 2004. Big Savings through Leakage Detection as Part of Water Demand Management. *Municipal Water Management*, Volume 1, July.
- Zeng, W. Gong, J. Cook, P.R. Arkwright, J.W. Simpson, A.R. Cazzolato, B.S. Zecchin, A.C. Lambert, M.F. 2020. Leak Detection for Pipelines using In-Pipe Optical Fiber Pressure Sensors and a Paired-IRF Technique. *Journal of Hydraulic Engineering*, October.
- Zheng, Y. Chen, C. Liu, T. Shao, Y. Zhang, Y. 2020. Leakage detection and long-term monitoring in diaphragm wall joints using fiber Bragg grating sensing technology. *Tunnelling and Underground Space Technology*, Volume 98, February.
- Zou, L. Landolsi, T. 2014. Pipeline Leakage Detection Using Fiber-Optic Distributed Strain and Temperature Sensors. *OZ Optics*, White Paper, October.

**APPENDIX A SGS MATROLAB HILLCREST CAMPUS  
CLAY TEST RESULTS**

SGS MATROLAB (PTY) LTD  
 - CIVIL ENGINEERING SERVICES -  
 Reg No.: 2003/021980/07 - VAT. Reg.No.: 4040210587

256 Brander Street, Jan Niemand Park, Pretoria  
 P.O. Box 912387, Silverton, 0127  
 Tel. : (012) 800 1299  
 Fax :  
 Email : martinus.schwartz@sgs.com

a SANAS Accredited Testing Laboratory, No. T0025

## TEST RESULTS

UNIVERSITY OF PRETORIA  
 THE DIRECTOR OF FINANCE  
 PRIVATE BAG X20  
 HATFIELD, PRETORIA 0028  
 Attention: Mr SW Jacobz

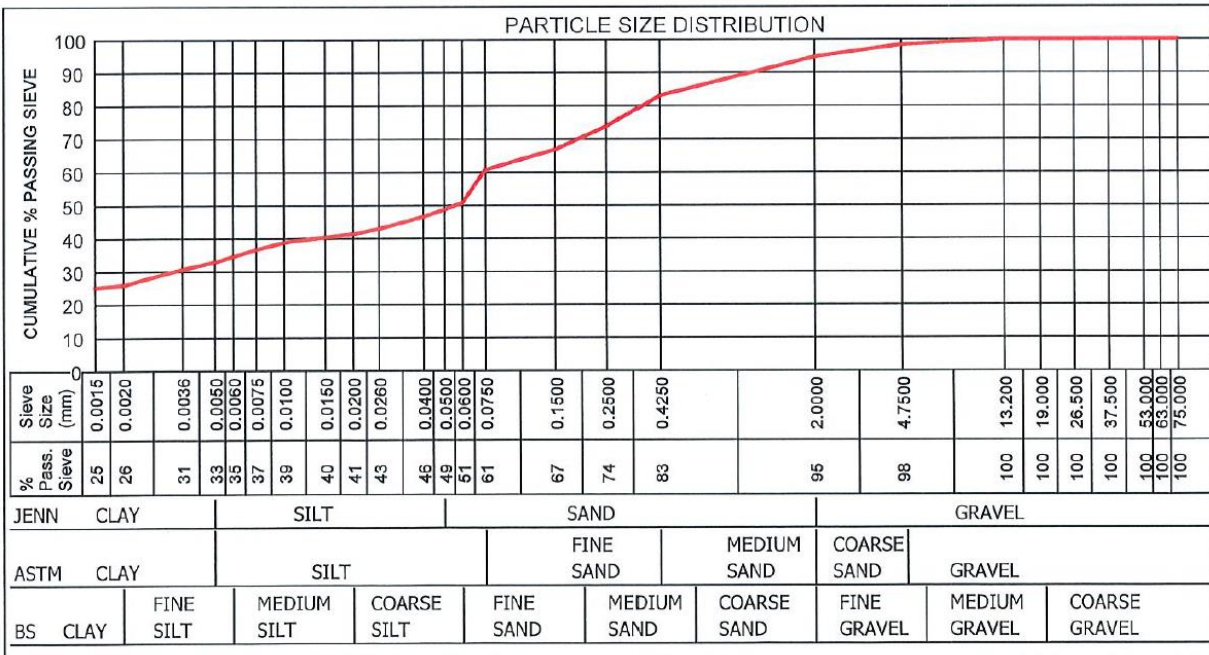
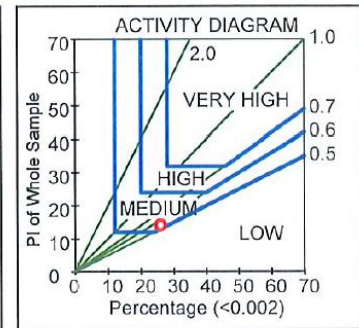
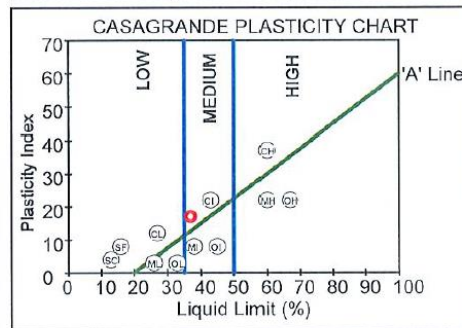
Project : Jason Barry  
 : Hillcrest Campus  
 Your Ref :  
 Our Ref : PL/45815  
 Date Reported : 29.09.2021

### FOUNDATION INDICATOR (ASTM: D422)

Sample No. : A21/3070  
 Hole No. :  
 Depth :  
 Liquid Limit (%) : 37  
 Plasticity Index : 17  
 Linear Shrinkage (%) : 9.0  
 PI of Whole Sample : 14  
 P.R.A. Classification : A-6(8)  
 Unified Soil Classificati: CL  
 Activity : 0.54  
 Heave Classification : MEDIUM  
 Grading Modulus : 0.61  
 Percentage (<0.002) : 26.0  
 Moisture Content (%) : 7.9

Material Description : Dark red SANDY CLAY

	Clay (%)	Silt (%)	Sand (%)	Gravel (%)	Classification
Jennings	32.9	15.7	46.1	5.3	SANDY CLAY
Astm	32.9	27.7	37.7	1.7	SANDY CLAY
British Standard	25.9	24.9	43.9	5.3	CLAYEY SAND



Remarks : Sampled by client.

FORM: A6

4.4.1(SGS)(2019.12.04)

Technical Signatory : Martinus Schwartz/Lizette Breiting

MATROLAB IS NOW PART OF SGS, THE WORLD'S LEADING INSPECTION, VERIFICATION, TESTING AND CERTIFICATION COMPANY.

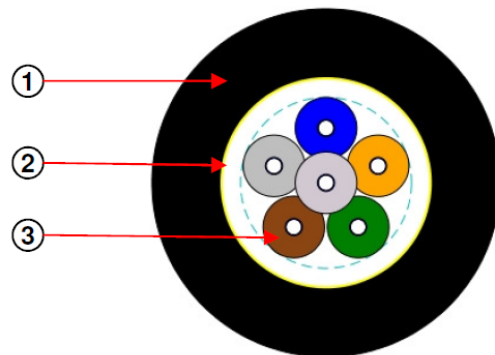
This document is issued by the Company under its General Condition of Service accessible at [http://www.sgs.com/en/Terms\\_and\\_Conditions.aspx](http://www.sgs.com/en/Terms_and_Conditions.aspx). Attention is drawn to the limitation of liability, indemnification and jurisdiction issues defined therein.

# **APPENDIX B 6F-TB AND 2F-TB CABLE SPEC SHEET**

# DATA SHEET

## Field Deployable Cable (Tight Buffered Cable For Re-usable, Temporary or Mobile Links)

CABLE DESCRIPTION	
1	Hytrel Sheath
2	Aramid Yarn Overall Strength Member
3	Colour Coded " Easy Strip" Tight Buffer Optical Fibres



FIBRE COUNT	ELEMENTS PER LAYER (na)												FIBRES	
	1	2	3	4	5	6	7	8	9	10	11	12		
6														6 Fibres

**Optical Fibres** are coloured in accordance with TIA/EIA-598  
**Colour sequence:** Blue, Orange, Green, Brown, Grey and White.

PRODUCT FEATURES
* The CBI-Electric Telecom cables "field deployable " cable is a compact, tight buffered cable specially designed for military applications, to provide fast communication links.
* As a temporary measure, the reusable cable can be used like a jumper, skirting the damaged section to a fixed optical installation in double quick time with the use of mechanical splices. This allows a maintenance team time to repair or replace damaged cable at leisure, and to link in this repaired cable with permanent fusion splices, outside of peak times.
* The cable is however suitable for a vast variety of applications where quick deployment and recovery is necessary, and has also been found to be ideal for mobile links.
* The cable will tolerate vertical installations and can support its own weight for considerable drops, making it ideal for risers, mine shafts, boreholes, etc.
* Ideally suited for point to point links, eliminating the need for fibre patch cords in many instances.
* The cable is small, lightweight, flexible, and will tolerate small bend radii, yet is surprisingly resistant to kinking, making it ideal for easy deployment and recovery.
* The special sheathing compound has been specially chosen for its excellent abrasion and cut resistance, in order to withstand damage when deployed over hostile terrain.
* The sheath is well dosed with Carbon Black to give the cable excellent UV resistance.
* The fibres are protected by a tough easy strip, tight buffered nylon jacket.
* The fibres are individually coloured for easy of identification.

Note: the 2F-TB specifications are identical to the 6F-TB cable except for the number of fibres housed within the sheath.

# DATA SHEET



DATA SHEET: CBI Telecom-OFC-FIELD DEPLOYABLE-01

PHYSICAL PROPERTIES		
Parameter	Fibre Count	Test Method
	6	
Cable diameter (nominal)	5.1 mm	
Cable weight (nominal)	24 kg/km	
Maximum tensile load- Short Term(N)*	800 N	
Maximum tensile load- Long Term(N)**	300	IEC 60794-1-21
Minimum bend radius	100 mm	IEC 60794-1-21
Crush Resistance (via 100mm plates)	800 N	IEC 60794-1-21
Impact resistance (25mm anvil / 10 blows)	2 Nm Blows	IEC 60794-1-21
Temperature Performance	-20°C to +70°C	IEC 60794-1-22
Maximum unsupported vertical drop (m)	1000m	
Note: *Short term load is the load at which the fibre strain is less than one third of the fibre proof strain. ** Long term load load is the load at which no fibre strain occurs.		

# DATA SHEET



## DATA SHEET: CBI Telecom-OFC-FIELD DEPLOYABLE-01

OPTICAL PROPERTIES (Single-Mode Optical Fibres) (Alternative fibre types/properties are available on request)	
Specification	ITU-T G.652.D/G.657.A1
Attenuation	$\leq 0.35$ dB/km @ 1310 nm $\leq 0.22$ dB/km @ 1550 nm $\leq 0.24$ dB/km @ 1625 nm
Chromatic Dispersion [ps/(nm.km)]	
1285-1330 nm	$\leq 3$
1550 nm	$\leq 18$
1625 nm	$\leq 22$
Polarisation Mode Dispersion (PMD <sub>D</sub> )	$\leq 0.1$ ps/ $\sqrt{\text{km}}$
Mode Field Diameter	$9.2 \pm 0.4$ $\mu\text{m}$ @ 1310 nm $10.4 \pm 0.5$ $\mu\text{m}$ @ 1550 nm
Cladding Diameter	$125 \pm 0.7$ $\mu\text{m}$
Coating Diameter	$242 \pm 5$ $\mu\text{m}$
Core-Clad Concentricity	$\leq 0.5$ $\mu\text{m}$
Cladding Non-circularity	$\leq 0.7$ %
Cable Cut-off Wavelength	$\leq 1260$ nm
Macro-bend loss	$\leq 0.5 / 1.5$ dB @ <b>10mm Radius</b> , 1 turn @ 1550/1625 nm $\leq 0.05 / 0.3$ dB @ <b>15 mm Radius</b> , 10 turns @ 1550/1625 nm

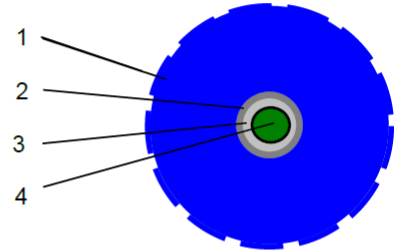
## **APPENDIX C STRAIN CABLE SPEC SHEET**

## BRUsens strain V9

3\_50\_2\_005

Flexible, mini armored fiber optic strain sensing cable with central metal tube, structured PA outer sheath, one optical fiber, strain range up to 1% (10000 µstrain)

LLK-BSST V9 3.2 mm



**Construction:**

- 1) PA outer sheath, with structured surface with interlocking system
- 2) Metal tube SS316L for protection and hermetic seal
- 3) Multi layer buffer and strain transfer layer with interlocking system
- 4) Special strain sensing optical single mode fiber

**Description:**

- Central metal tube with 1 optical fiber
- Good tensile strength
- Longitudinally and laterally watertight
- Good rodent protection
- High strain sensitivity
- Compact design, good flexibility, small bending radius
- Abrasion resistant structured sheath, for better strain transfer
- Halogen-free cable sheath

**Temperature range:**

- Operating temperature: - 30° C ... +70° C
- Storage temperature: - 40° C ... +70° C
- Installation temperature: - 10° C ... +50° C
- Short term temperature (60 min) +150°C (during installation)

**Cable sheath color:**

- Blue, similar RAL 5005
- Other colors upon request

**Standards:**

- Cable tests complying with IEC 60794-1-2

**Remarks:**

- Fiber colored
- Final test reports OTDR and BOTDA measurement
- Other cable designs and temperature ranges available
- Standard cable marking with meter marks, special labeling of outer sheath upon request
- Preassembled cable sets available, special field termination kit available
- Accessories such as anchors, loops, fan-outs, splice enclosures, connectors, etc. available
- Deployment training upon request
- For improved UV resistance, black cable sheath available upon request

**Applications:**

- Distributed strain sensing
- Sensing technologies: Brillouin, FBG
- Precision measurement and alarm systems
- Soil movement, ground monitoring
- Pipeline monitoring
- Structural monitoring
- Direct burial in soil, concrete
- Harsh environment, subsea, outdoors

**Standard optical fiber:**

- Single-mode fiber: ITU-T G.657
- Other fiber types and fiber quality available upon request

**Technical data:**

Type	Max. no. of fibres units	Cable ø mm	Weight kg/km	Max. tensile strength installation N	Typical Load at 1% elongation N
1F	1	3.2	10.5	260	470

Type	Min. bending radius		Max. crush resistance N/cm
	with tensile mm	without tensile mm	
1F	64 (20xD)	48 (15xD)	250

**Optical fiber data (cabled) at 20°C**

Fiber Type	Attenuation, dB/km 1550 nm	Typical Brillouin parameters BOTDR or BOTDA at 1550 nm		
		Temperature sensitivity $df_B / dT$	Strain sensitivity $df_B / d\epsilon$	Centr. Brillouin Freq.
SMF	≤ 0.5	1.1 MHz/°C	450 MHz/%	10.6 GHz

© Copyright 2016 by Brugg Cables AG. THE INFORMATION CONTAINED IN THIS DOCUMENT IS THE SOLE PROPERTY OF BRUGG KABEL AG. ANY REPRODUCTION IN PART OR AS A WHOLE WITHOUT THE PERMISSION OF BRUGG KABEL AG IS PROHIBITED.

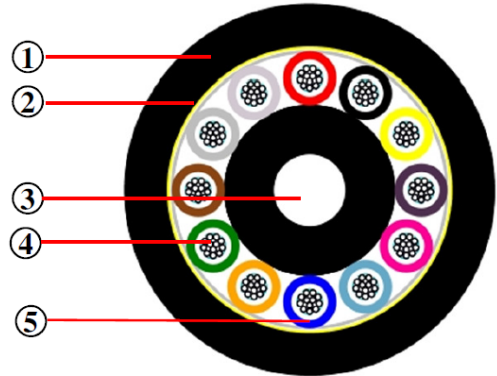
Subject to changes without notice

2016/06/07 Rev. 02 TH

## **APPENDIX D 72F-6C-LC CABLE SPEC SHEET**

## Aerial Self Support ( Industrial Strength)

CABLE DESCRIPTION	
1	UV resistant Polyethylene outer sheath (Black)
2	Aramid yarn peripheral strength member (Optimized load transfer between aramid & sheath)
3	Glass reinforced plastic centre strength member (GRP) (Over-sheathed in some cases)
4	Optical fibres
5	PBT loose tube (Thixotropic gel filled)



The drawing depicts a 144 fibre cable

FIBRE COUNT	ELEMENTS PER LAYER													
	1	2	3	4	5	6	7	8	9	10	11	12		
4	BE	FL	FL	FL	4 Fibres per Ø 2.2mm tube									
12	BE	FL	FL	FL	12 Fibres per Ø 2.2mm tube									
24	BE	OE	FL	FL	12 Fibres per Ø 2.2mm tube									
48	BE	OE	GN	BN	12 Fibres per Ø 2.2mm tube									
72	BE	OE	GN	BN	GY	WE	12 Fibres per Ø 2.2mm tube							
96	BE	OE	GN	BN	GY	WE	RD	BK	12 Fibres per Ø 2.2mm tube					
144	BE	OE	GN	BN	GY	WE	RD	BK	YW	VT	PK	TE	12 Fibre per Ø2.2mm tube	

The loose tubes contain 12 fibres per tube.  
 The fibre colours follows the TIA/EIA-598 colour coding scheme: Blue, Orange, Green, Brown, Grey, White, Red, Black, Yellow, Violet, Pink and Turquoise.  
 The loose tubes colours follows TIA/EIA-598 colour coding scheme: Blue, Orange, Green, Brown, Grey and White, Red, Black, Yellow, Violet, Pink and Turquoise.  
 Fillers are Black in colour

PRODUCT FEATURES
<ul style="list-style-type: none"> <li>* The CBI Telecom "short span" series are compact loose tube aerial self-supporting cables specifically designed for installation on pole routes with spans up to 70m.</li> <li>* The cable's main feature is its low installation cost, and the speed with which this can be effected due to its lightweight and self-supporting characteristics.</li> <li>* A non-metallic construction ensures lightning immunity.</li> <li>* The series is furnished with high modulus, creep resistant, aramid strength members which enable the cable to withstand sustained Every Day Stress (EDS), as well as high loading during environmental extremes. The aramid is applied contra-helicly in layers to eliminate torsional stress.</li> <li>* The cable's smooth circular profile inhibits galloping, and the gel in the tubes provides additional protection against vibration, ensuring excellent optical reliability for all service conditions.</li> <li>* The sheathing material is well dosed with Carbon Black to give the cable excellent UV resistance.</li> </ul> <p style="font-size: x-small;">             Extensive cable/clamp compatibility tests were carried out to ensure optimum load transfer properties over a wide temperature range. It is recommended that only installation hardware verified according to the ATC CLAMP-APPROVAL SPECIFICATION be used (Please contact the CBI Telecom Technical Department in this regard).           </p> <ul style="list-style-type: none"> <li>* Printing (Indelible printing)  <b>CBI TELECOM "NO OF FIBRES" (G657A INDUSTRIAL STRENGTH BEND TOLERANT) FIBRE OPTIC CABLE + LENGTH MARK + UNIQUE NUMBER</b> </li> </ul>

# DATA SHEET OPTICAL FIBRE CABLE



DATA SHEET : ADSS-Industrial

TYPICAL PROPERTIES					
Parameter	Property / Pass criteria				Test Method
	Fibre Count				
	4 - 48 Fibre Cables	72 Fibre Cables	96 Fibre Cable	144 Fibre Cable	
Number of elements	4	6	8	12	
Cable diameter (nominal)	9.4mm	10.5mm	12mm	15.3mm	
Cable weight (nominal)	65 kg/km	87 kg/km	117 kg/km	184 kg.km	
Maximum load using the formula (0.6*9.81*2*Weight)	765N	1024N	1150 N	2166 N	IEC 60794-1-E1
Maximum installation load (aerial self-support, based on 70m span, 0.8m sag)	618 N	850 N	1562 N	1810 N	
Maximum working load (anticipating no ice, but winds up to 125 km/h)	1200 N	1530 N	1840 N	2500 N	
Crush resistance (via 100 mm plates)	1200 N	1500 N	2000 N	2000 N	IEC 60794-1-E3
Long term creep test (10 days)	< 0.1% cable length increase				ATC Internal
Cable / Termination clamp compatibility (up to 70 °C)	100% load transfer				ATC Internal
Minimum bend radius	12 x Cable Diameter				IEC 60794-1-11
Impact resistance (25mm anvil / 10 blows)	2 Nm Blows				IEC 60794-1-E4
Temperature performance	-10 to +70° C				IEC 60794-1-F1
Drip test (300 mm sample of loose tube @ 80 °C)	No leakage				IEC 60794-1-14

# DATA SHEET OPTICAL FIBRE CABLE



DATA SHEET : ADSS-Industrial

**OPTICAL PROPERTIES** *(Alternative fibre types/properties are available on request)*

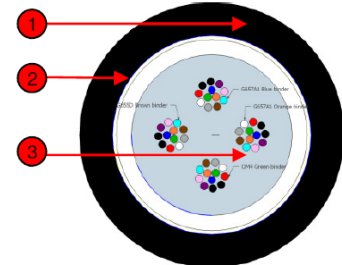
Fibre Type	SSMF
Specification	ITU-T G.657A
Attenuation	0.35 dB/km @ 1310 nm 0.20 dB/km @ 1550 nm 0.23 dB/km @ 1625 nm
Mode Field Diameter	9.2 ± 0.4 µm @ 1310 nm 10.4 ± 0.5 µm @ 1550 nm
Polarisation Mode Dispersion (PMD <sub>D</sub> )	≤ 0.06 ps/√km
Dynamic and static fatigue (Unaged and aged)	N <sub>d</sub> ≥ 20
Cladding Diameter	125 ± 0.7 µm
Core Concentricity Error	≤ 0.6 µm
Cladding Non-circularity	≤ 0.7 %
Chromatic Dispersion (ps/√[nm.km]) 1285-1330nm 1550nm 1625nm	≤ 3  ≤18 ≤22
Cable Cut-off Wavelength	≤ 1260 nm
Macro-bend loss *	≤ 0.75 / 1.5 dB @ <b>10mm Radius</b> , 1 turn @ 1550/1625 nm ≤ 0.25 / 1.0 dB @ <b>15 mm Radius</b> , 10 turns @ 1550/1625 nm
Proof strain	0.7 GPa

# APPENDIX E 4F-DC-LC SPEC SHEET

# DATA SHEET MICRO FIBRE OPTIC CABLE

## MICRO BLOWN FIBRE OPTIC CABLE (Drop Cable- Multi Fibre )

CABLE DESCRIPTION	
1	Black UV Stabilized Hytrel Sheath
2	Glass Composite Oval strength members
3	Polycarbonate mono tube (Thixotropic gel filled) with 48 Colour coded optical Fibres, bundled/binded in 4 units of 12 Fibers each.



Drawing depicts a 48Fibre construction

FIBRE COUNT	ELEMENTS PER LAYER												Fibres per tube	
	1	2	3	4	5	6	7	8	9	10	11	12		
Blue Binder	G657A1	G657A1	G657A1	G657A1	G657A1	G657A1	G657A1	G657A1	G657A1	G657A1	G657A1	G657A1	G657A1	12 Fibres per bundle
Orange Binder	G657A1	G657A1	G657A1	G657A1	G657A1	G657A1	G657A1	G657A1	G657A1	G657A1	G657A1	G657A1	G657A1	12 Fibres per bundle
Green Binder	OM4	OM4	OM4	OM4	OM4	OM4	OM4	OM4	OM4	OM4	OM4	OM4	OM4	12 Fibres per bundle
Brown Binder	G655D	G655D	G655D	G655D	G655D	G655D	G655D	G655D	G655D	G655D	G655D	G655D	G655D	12 Fibres per bundle

Each bundle contain up to 12 individually coloured fibres. The fibre colours follows the TIA/EIA-598 colour coding scheme: Blue, Orange, Green, Brown, Grey, White, Red, Black, Yellow, Violet, Pink and Turquoise.  
 Blue binder: G657A1  
 Orange binder: G657A1  
 Green binder: OM4  
 Brown binder: G655D

PRODUCT FEATURES
<ul style="list-style-type: none"> <li>The cable design is such that cables may be installed by means of hauling or pushing techniques into (6 ID mm micro ducts).</li> <li>The thixotropic jell filled tube allows for excellent sustained reliability over a wide temperature range, and is engineered to ensure the optical fibres remain stress free over the designated temperature range.</li> <li>Resistance to moisture ingress is achieved though dry water blocking GCO materials. The design facilitates in the hand ability of the fibre optic duct cable during installation, termination and splicing.</li> <li>The Black TPE (Hytrel ) is UV stabilised for outdoor applications including aerial installations.</li> <li>The fibre optic cable is a totally non-metallic construction and immune to any RF interference.</li> <li>The cable is designed for flexibility in dynamic conditions.</li> <li>Printing: CBI TELECOM SKA SA (12F A1-BE)+(12F A1-OE) +(12F 55D-BN)+(12F OM4-BN)+DROP CABLE+“DATE”+ “LENGTH MARK” + UNIQUE NUMBER</li> </ul>

## DATA SHEET MICRO FIBRE OPTIC CABLE

<b>PHYSICAL PROPERTIES</b>		
Parameter	Fibre Count	Test Method
	48	
Number of elements	1	
Cable diameter (nominal)	less than 5.8 mm	
Cable weight (nominal)	37 kg/km	
Installation load ( fibre strain reversible)	400 N	
Minimum bend radius (long term/short term )	12 x Cable diameter	IEC 60794-1-11
Crush Resistance (via 100mm plates)	500 N	IEC 60794-1-E3
Impact resistance	1 Joule	IEC 60794-1-E4
Torsion (20N load, 1meter sample)	10 Cycles 180° apart	IEC 60794-1-2-E7
Flexing through 90 degrees	60 000 cycles	IEC 60794-1-2-E8
Repeated Bending (20N load)	35 Cycles R=20xD	IEC 60794-1-2-E6
Cable kink test	Pass: Bending radius of 25mm	IEC 60794-1-2-E10
Temperature Performance	-10°C to +70°C	IEC 60794-1-F1
Water penetration (3m cable, 1m head of water)	No leakage	IEC 60794-1-5B
Drip test (300 mm sample of loose tube @ 80°C)	No leakage	IEC 60794-1-14
Ageing Test: See Flexing and Temperature Performance	2000 Cycles 85° C for 14 days 2000 Cycles	CBI internal

## DATA SHEET MICRO FIBRE OPTIC CABLE

<b>OPTICAL PROPERTIES</b> <small>(Alternative fibre types/properties are available on request)</small>		
<b>FIBRE TYPE</b>	<b>Multi Mode 50/125 µm OM4</b>	
Specification	ITU-T G. 651	
Fibre core size	50 µm	
Cladding diameter	125 ± 0.7 µm	
Primary coating diameter	245 µm	
Operating wavelength	850 nm	1300 nm
Max. Attenuation	2.5 dB/km	0.7 dB/km
Overfilled modal Bandwidth	3500 MHz.km	500 MHz.km

<b>OPTICAL PROPERTIES</b>		
<b>Fibre Type</b>	<b>NZDSF</b>	<b>SSMF</b>
Specification	ITU-T G.655D	ITU-T G.657A1
Effective Area	72 µm <sup>2</sup>	N/A
Attenuation	0.25 dB/km @ 1550 nm 0.28 dB/km @ 1625 nm	0.36 dB/km @ 1310 nm 0.24 dB/km @ 1550nm 0.25 dB/km @ 1625 nm
Mode Field Diameter	9.6 ± 0.4 µm @ 1550 nm	9.2 ± 0.4 µm @ 1310 nm 10.4 ± 0.5 µm @ 1550 nm
Polarisation Mode Dispersion (PMD <sub>0</sub> )	≤ 0.05 ps/vkm	≤ 0.06 ps/vkm
Cladding Diameter	125 ± 0.7 µm	125 ± 0.7 µm
Core Concentricity Error	≤ 0.5 µm	≤ 0.5 µm
Cladding Non-circularity	≤ 0.7 %	≤ 0.8 %
Cable Cut-off Wavelength	≤ 1450 nm	≤ 1260 nm
Macro-bend loss	≤ 0.50 dB @ 16mm Radius, 1 turn @ 1550 nm ≤ 0.05 dB @ 30 mm Radius, 100 turns @ 1550 nm	≤ 0.5 dB @ 10 mm Radius, 1 turn @ 1550 nm ≤ 1.5 dB @ 10 mm Radius, 1 turn @ 1625 nm ≤ 0.05 dB @ 15 mm Radius, 10 turns @ 1550 nm ≤ 0.3 dB @ 15 mm Radius, 10 turns @ 1625 nm
Proof strain	0.7 Gpa	0.7 GPa

**APPENDIX F FIBRISTERRE FTB SERIES FIBRE-OPTIC  
SENSING BFS INTERROGATOR SPECIFICATION SHEET**

## Performance, features and technical data

Fiber type	Standard single-mode		
Optical connectors	E-2000 / APC		
Sensor configuration	loop		
Distance range (fiber loop)	50 km <sup>(1)</sup>		
Spatial resolution	up to 1 km fiber	0.2 m <sup>(2)</sup>	
	up to 25 km fiber	0.5 m	
	up to 50 km fiber	1.0 m	
Spatial accuracy	0.05 m		
Dynamic range <sup>(3)</sup>	> 20 dB		
Measurable parameters	Brillouin frequency shift, temperature, strain		
Accuracy and Range		Accuracy	Range
	strain	< 2 $\mu\epsilon$	-3% to +3% <sup>(4)</sup>
	temperature	< 0.1°C	-273 to +1000°C <sup>(4)</sup>
	Brillouin freq. shift	< 100 kHz	10 – 13 GHz
Acquisition time <sup>(5)</sup>	0.2 km fiber	20 seconds	
	2 km fiber	1 minute	
	10 km fiber	8 minutes	
	25 km fiber	25 minutes	
Communication interface	Ethernet		
Data export formats	binary, ASCII		
Measurement modes	Single measurements on demand; continuous monitoring Automatic detection of fiber length and attenuation		
Remote operation	Remote measurements, system diagnostics		
Operating temperature	5 - 40°C		
Dimensions	L x W x H	495 x 482 x 145 mm (19" rack case)	
Weight	10.5 kg		
Power consumption	60 W		
Laser class	1M		

(1) Standard distance range is 25 km. Distance range enhancement to 50 km available upon request.

(2) Software resolution enhancement selectable in user interface

(3) High optical losses along the sensing fiber may degrade the strain / temperature accuracy.

(4) Limited by optical fiber

(5) Estimated for typical measurements. Measurement time will vary with resolution, accuracy and strain / temperature range.



r